Particles and Fields in Superfluid Turbulence: Numerical and Theoretical Studies

A thesis submitted for the degree of
Doctor of Philosophy
in the Faculty of Science

Vishwanath Shukla

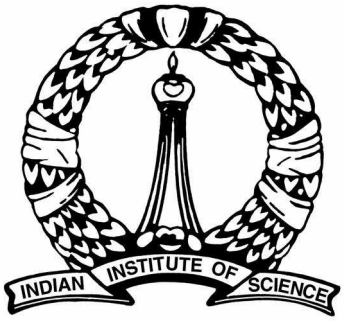

Department of Physics
Indian Institute of Science
Bangalore - 560012
India

August 2014

Declaration

The work reported in this thesis is original and was carried out by me during my tenure as a PhD student at the Department of Physics, Indian Institute of Science, Bangalore. This thesis has not formed the basis for the award of any degree, diploma, associateship, membership or similar title of any university or institution.

(**Vishwanath Shukla**)
August, 2014

Department of Physics,
Indian Institute of Science,
Bangalore - 560012,
India

Acknowledgement

Life is a beautiful journey on which we tread to realize our dreams and expectations and chance encounters with wonderful people on the way makes the experience more benign.

The PhD journey begins with a search for a "guide" (*thesis advisor*). I am fortunate enough to get an opportunity to work with Professor Rahul Pandit. His willingness to work on new ideas and his beautiful mix of professional and personal touch, which he provides to the relationship that he shares with his students, make him the best "guide". It is due to him that the last five years have been very satisfying and productive on the research-work front. I am grateful to Professor Marc Brachet, ENS, Paris, for more than half of the work presented in this thesis, has been done in collaboration with him. His constant encouragement, detailed and insightful discussions, and much needed suggestions have helped immensely in the timely completion of the present work.

I would like to take this opportunity to thank Professor Abhik Basu, SINP, Kolkata, for several useful discussions on our joint work and arranging my visits to SINP. I would also like to thank Samriddhi Sankar Ray, ICTS, Bangalore, for many discussions and suggestions on several topics presented in this thesis. Brief encounters with Dhrubaditya Mitra, Nordita, Stockholm, Sweden and Prasad Perlekar, TCIS, Hyderabad, were always motivating. I am thankful to Professor Madan Rao, NCBS, Bangalore, for his useful comments on a part of work included in this thesis and also for the discussions on our joint work. I would also like to thank Professor Sergey Nazarenko, Warwick, UK, for the intense and insightful discussions, which Marc and I had with him, based on a part of work presented in this thesis. I am especially indebted to Edith Brachet (and Marc) for making me feel at home, on my visits to ENS, Paris. They graciously allowed me to stay in their home for more than a week on my first visit and helped me to navigate through an unfamiliar city. I am enormously thankful for their hospitality.

The liberal and the work conducive environment of the Physics Department, at IISc lets you to be what you are and at the same time helps you to grow professionally. I am grateful to all my teachers, Professor Rahul Pandit, Professor Prabal Maiti, Professor Subroto Mukerjee, Professor Chandan Das Gupta, Professor Vijay Shenoy, and Professor G. Rangarajan (mathematics department), for their guidance and excellent courses, which has helped tremendously in my research work. I am especially grateful to Professor Prabal Maiti for allowing me to walkin anytime into his office for a quick discussion. On several occasions, I had detailed discus-

sions with Professor Subroto Mukerjee, which were very valuable. I would also like to extend my gratitude to Professor H. R. Krishnamurthy for several impromptu discussions and especially for a detailed chat, which I had with him in the first week of my joining research work. Chats with Professor Manish Jain were always informative and refreshing.

My senior and best friend Anupam, was the one who helped me to get off the ground, when I was struggling in the initial days. Anupam, Alok, and Akshay were always there for me and without them it would have been a difficult journey. I owe all my technical *gyan* (knowledge) to them. I would like to thank my past and present group members Chirag Kalelkar, Ganapati Sahoo, Debarghaya Banerjee, Rupamanjari Majumdar, Jamshid M. Kurdestani, K.V. Rajany, Sabyasachi, Nairita, and Soling Zimik for their support and providing a work conducive environment in the group. I would like to mention Sumilan, Subhro, and Vijay for their help and discussions during the first-year course work. I also thank all the CCMT memebers (past and present) and my batch-mates Pramod, Tarakh, Kingshuk, Soumyakanti, and Baban, for without them the stay here would have not been so enjoyable.

I am grateful to my teachers at IIT Delhi and Banaras Hindu University; it was at these places that I became familiar with physics research. I would like to thank Professor Sankalp Ghosh (IIT Delhi) for instilling in me the ability to work in a disciplined way on research problems during my M.Sc. project work.

I acknowledge the efficient help of department staff members, especially, Mr. Srinivas, Ms. Shanta Kumari, Ms. Meena, Mr. Srivatsa, Ms. Rakma, Ms. Bhargavi, and Mr. Prabhakar.

I thank Council for Scientific Research (CSIR), India, for the five-year research fellowship and Indo-French Centre for Applied Maths (IFCAM) for providing the financial support during my research visits to ENS, Paris.

My stay at IISc became more comfortable, enjoyable, and memorable because of several good friends. The vast BHU gang was always chirpy, whether it was while having meals together in the mess or otherwise. I would especially like to mention Alok (BHU), Kirtiman, V. Akshay Shiva, Abhay, Prabhat, Rahul, Dipankar, Pushpendra, Rahman, and Gaurav for their great company. Harsh, Nitin, Ketan, Apurba, Hemant, Satyendra, Pranab, Arvind, Gyan, SRK, Manohar, Himanshu, Manisha, Debobrata, and Ranjan will always be remembered. I met Bodhi and Pankaj here, in IISc and since then they have been my close friends, who made the IISc experience more colorful and joyful.

At a get-together at Rahul's house, I got a chance to meet his wonderful family, Shobha and Mrinalika who welcomed me wholeheartedly in their family, filling the absence of my loved ones. Since then, we have met on several occasions and forever in my life I will cherish those meetings and memories. I am grateful to them for their affection, warmth, and caring concern.

My decision of pursuing a PhD would have not materialized without the love and support of my family. I am grateful to two very special persons in my life, in the form of my parents- Professor M.B. Shukla and Nirmala Shukla, for instilling in me faith and courage to take up with this endeavor. I had almost carefree five years because of my parents, wife, adoring sisters - Kanchan, Gunjan and Keerti, Saurabh (brother-in-law) in the role of elder brother and my sweet nephew Pragyan. I am grateful to my in-laws for their constant support and encouragement. Words cannot express my affection and gratitude for my friend, philosopher and life partner Namrata who always shouldered our responsibilities with a smile and for being there with me during my life's most crucial stage.

Preface

In this thesis we study a variety of problems in superfluid turbulence, principally in two dimensions. A summary of the main results of our studies is given below; we indicate the Chapters in which we present these.

In Chapter 1, we provide an overview of several problems in superfluid turbulence with special emphasis on background material for the problems we study in this thesis. In particular, we give: (a) a brief introduction of fluid turbulence; (b) an overview of superfluidity and the phenomenological two-fluid model; (c) a brief overview of experiments on superfluid turbuelnce; (d) an introductory accounts of the phenomenological models used in the study of superfluid turbuelnce. We end with a summary of the problems we study in subsequent Chapters of this thesis.

In Chapter 2, we present a systematic, direct numerical simulation of the two-dimensional, Fourier-truncated, Gross-Pitaevskii equation to study the turbulent evolutions of its solutions for a variety of initial conditions and a wide range of parameters. We find that the time evolution of this system can be classified into four regimes with qualitatively different statistical properties. First, there are transients that depend on the initial conditions. In the second regime, power- law scaling regions, in the energy and the occupation-number spectra, appear and start to develop; the exponents of these power laws and the extents of the scaling regions change with time and depend on the initial condition. In the third regime, the spectra drop rapidly for modes with wave numbers $k > k_c$ and partial thermalization takes place for modes with $k < k_c$; the self-truncation wave number $k_c(t)$ depends on the initial conditions and it grows either as a power of t or as $\log t$. Finally, in the fourth regime, complete thermalization is achieved and, if we account for finite-size effects carefully, correlation functions and spectra are consistent with their nontrivial Berezinskii-Kosterlitz-Thouless forms. Our work is a natural generalization of recent studies of thermalization in the Euler and other hydrodynamical equations; it combines ideas from fluid dynamics and turbulence, on the one hand, and equilibrium and nonequilibrium statistical mechanics on the other.

In Chapter 3, we present the first calculation of the mutual-friction coefficients α and α' (which are parameters in the Hall-Vinen-Bekharevich-Khalatnikov two-fluid model that we study in chapter 5) as a function of temperature in a homogeneous Bose gas in two-dimensions by using the Galerkin-truncated Gross-Pitaevskii equation, with very special initial conditions, which we obtain by using

the advective, real, Ginzburg-Landau equation (ARGLE) and an equilibration procedure that uses a stochastic Ginzburg-Landau equation (SGLE). We also calculate the normal-fluid density as a function of temperature.

In Chapter 4, we elucidate the interplay of particles and fields in superfluids, in both simple and turbulent flows. We carry out extensive direct numerical simulations (DNSs) of this interplay for the two-dimensional (2D) Gross-Pitaevskii (GP) equation. We obtain the following results: (1) the motion of a particle can be chaotic even if the superfluid shows no sign of turbulence; (2) vortex motion depends sensitively on particle charateristics; (3) there is an effective, superfluid-mediated, attractive interaction between particles; (4) we introduce a short-range repulsion between particles, with range $r_{\rm SR}$, and study two- and many-particle collisions; in the case of two-particle, head-on collisions, we find that, at low values of $r_{\rm SR}$, the particle collisions are inelastic with coefficient of restitution $e = 0$; and, as we increase $r_{\rm SR}$, e becomes nonzero at a critical point, and finally attains values close to 1; (5) assemblies of particles and vortices show rich, turbulent, spatio-temporal evolution.

In Chapter 5, we present results from our direct numerical simulations (DNSs) of the Hall-Vinen-Bekharevich-Khalatnikov (HVBK) two-fluid model in two dimensions. We have designed these DNSs to study the statistical properties of inverse and forward cascades in the HVBK model. We obtain several interesting results that have not been anticipated hitherto: (1) Both normal-fluid and superfluid energy spectra, $E^n(k)$ and $E^s(k)$, respectively, show inverse- and forward-cascade regimes; the former is characterized by a power law $E^s(k) \sim E^n(k) \sim k^{-\alpha}$ whose exponent is consistent with $\alpha \simeq 5/3$. (2) The forward-cascade power law depends on (a) the friction coefficient, as in 2D fluid turbulence, and, in addition, on (b) the coefficient B of mutual friction, which couples normal and superfluid components. (3) As B increases, the normal and superfluid velocities, $\mathbf{u}_n$ and $\mathbf{u}_s$, respectively, get locked to each other, and, therefore, $E^s(k) \simeq E^n(k)$, especially in the inverse-cascade regime. (4) We quantify this locking tendency by calculating the probability distribution functions (PDFs) $\mathcal{P}(\cos(\theta))$ and $\mathcal{P}(\gamma)$, where the angle $\theta \equiv (\mathbf{u}_{\rm n} \cdot \mathbf{u}_{\rm s})/(|\mathbf{u}_{\rm n}||\mathbf{u}_{\rm s}|)$ and the amplitude ratio $\gamma = |\mathbf{u}_{\rm n}|/|\mathbf{u}_{\rm s}|$; the former has a peak at $\cos(\theta) = 1$; and the latter exhibits a peak at $\gamma = 1$ and power-law tails on both sides of this peak. (4) This locking increases as we increase B, but the power-law exponents for the tails of $\mathcal{P}(\gamma)$ are universal, in so far as they do not depend on B, ρ_n/ρ, and the details of the energy-injection method. (5) We characterize the energy and enstrophy cascades by computing the energy and enstrophy fluxes and the mutual-friction transfer functions for all wave-number scales k.

In Chapter 6, we examine the multiscaling of structure functions in three-dimensional superfluid turbulence by using a shell-model for the three-dimensional HVBK equations. Our HVBK shell model is based on the GOY shell model. In particular, we examine the dependence of multiscaling on the normal-fluid fraction and the mutual-friction coefficients.

We hope our *in silico* studies of 2D and 3D superfluid turbulence will stimulate new experimental, numerical, and theoretical studies.

List of Publications

- Turbulence in the two-dimensional Fourier-truncated Gross-Pitaevskii equation, Vishwanath Shukla, Marc Brachet and Rahul Pandit, New J. Phys. **15** 113025 (2013).
- Superfluid Mutual-friction Coefficients from Vortex Dynamics in the Two-dimensional Galerkin-truncated Gross-Pitaevskii Equation, Vishwanath Shukla, Marc Brachet and Rahul Pandit, manuscript in preparation.
- Particles and Fields in Superfluids: Insights from the Two-dimensional Gross-Pitaevskii Equation, Vishwanath Shukla, Marc Brachet and Rahul Pandit, manuscript in preparation.
- Homogeneous Isotropic Superfluid Turbulence in Two Dimensions: Inverse and Forward Cascades in the Hall-Vinen-Bekharevich-Khalatnikov model, Vishwanath Shukla, Anupam Gupta and Rahul Pandit, manuscript in preparation.
- Superfluid Turbulence: A shell-model approach, Vishwanath Shukla and Rahul Pandit, manuscript in preparation.

Contents

1 Introduction **1**

1.1 Turbulence 1
1.2 Fluid turbulence 3
1.2.1 Conservation laws 5
1.2.2 Classical turbulence phenomenology 6
1.3 Superfluid hydrodynamics 10
1.3.1 Superfluid equations of motion 13
1.3.2 Mutual friction 18
1.4 Superfluid turbulence 21
1.4.1 Experiments 24
1.4.2 Phenomenological Models 33
1.5 Outline of chapters 39

2 Turbulence in the two-dimensional Fourier-truncated Gross-Pitaevskii equation **50**

2.1 Introduction 50
2.2 Model, Initial Conditions, and Numerical Methods 53
2.2.1 The Gross-Pitaevskii Equation 53
2.2.2 Numerical Methods and Initial Conditions 55
2.3 Results 57
2.3.1 Evolution of energies, velocity PDFs, and the zero-wave-number population 57
2.3.2 Initial transients and the onset of thermalization 62
2.3.3 Partial thermalization and self-truncation 67
2.3.4 Complete thermalization 73
2.4 Conclusions 77
1 Supplementary Material 80

Appendix A **83**
A.1 Note on units . . . 83
A.2 Standard results on the BKT transition . . . 83
A.2.1 Low-temperature thermodynamical computations . . . 84
A.2.2 Low-temperature results at given density . . . 86
A.2.3 Results expressed in terms of energy increase . . . 87

3 Superfluid Mutual-friction Coefficients from Vortex Dynamics in the Two-dimensional Galerkin-truncated Gross-Pitaevskii Equation **96**
3.1 Introduction . . . 96
3.2 Model, Initial Conditions, and Numerical Methods . . . 97
3.3 Results . . . 99
3.4 Conclusion . . . 105
3.5 Video Captions . . . 107

Appendix B Determination of the mutual-friction coefficients **108**
B.1 Mutual friction coefficients α and α' . . . 108
B.1.1 Determination of α by using the initial configuration `IC1` . . . 108
B.1.2 Determination of α and α' by using the initial configuration `IC2` 109

Appendix C **112**
C.1 Note on Units . . . 112
C.2 Advective real Ginzburg-Landau equation (ARGLE) . . . 112
C.3 Stochastic Ginzburg-Landau equation (SGLE) . . . 114

Appendix D Low-temperature phenomenological model **116**
D.1 Standard results on the BKT transition . . . 116
D.2 Low-temperature thermodynamical computations with counterflows 117
D.3 Low-temperature results at a given density . . . 118

4 Particles and Fields in Superfluids: Insights from the Two-dimensional Gross-Pitaevskii Equation **124**
4.1 Introduction . . . 124
4.2 Model, Initial Conditions, and Numerical Methods . . . 125
4.3 Results . . . 128
4.3.1 Single particle dynamics: Constant external force on the particle 129
4.3.2 Two-particle dynamics . . . 136
4.3.3 Many-particle dynamics . . . 144

4.3.4 Interaction of a single particle with a vortex-antivortex pair . 146
4.3.5 Interaction of two particles with a vortex-antivortex pair . . . 153
4.3.6 Single particle dynamics in the presence of counter-rotating vortex clusters 157
4.3.7 Many-particle dynamics in the presence of counter-rotating vortex clusters 162
4.4 Conclusions 166
4.5 Video Captions 168

Appendix E **171**
E.1 Note on Units 171
E.2 Preparation of counter-rotating vortex clusters 171

5 Homogeneous Isotropic Superfluid Turbulence in Two Dimensions: Inverse and Forward Cascades in the Hall-Vinen-Bekharevich-Khalatnikov model **176**
5.1 Introduction 176
5.2 Model and Numerical Methods 177
5.3 Results 178
5.3.1 Vorticity fields 179
5.3.2 Spectra 179
5.3.3 Fluxes 182
5.3.4 PDFs 184
5.4 Conclusions 188
5.5 Video Captions 189

6 Superfluid turbulence: A shell-model approach **193**
6.1 Introduction 193
6.2 Models and Numerical Simulations 195
6.3 Results 199
6.4 Conclusions 208

Chapter 1

Introduction

1.1 Turbulence

Turbulence is a common phenomena in fluid flows. Turbulence occurs in atmospheric flows, ocean currents, Earth's molten core, the solar atmosphere, convective zones in stars, interstellar clouds, arms of spiral galaxies. Cyclones (Fig. 1.1 (a)), ash plumes from volcano eruptions (Fig. 1.1 (b)), jet streams, rapids in rivers, and winds past high land-masses (Fig. 1.1 (c)) are all examples of naturally occurring turbulent flows on Earth. The Great Red Spot of Jupiter (Fig. 1.2 (a)) and solar flares (Fig. 1.2 (b)) are two examples of extraterrestrial turbulent motion. Turbulence can also be created in superfluid flows and is believed to be present in the superfluid cores of neutron stars (Fig. 1.2 (c)) [1, 2].

The above examples and pictures Figs. 1.1 (a)-(c) and 1.2 (a)-(c) show manifestations of turbulence in vastly different systems, so it becomes difficult to give a precise definition of turbulence. Therefore, we adopt a working definition from a recent review on Quantum Turbulence [3], "Despite the abundant examples of turbulence, there is no consensus definition of the term. Here, we define turbulence as a dynamic field that is spatially complex, aperiodic in time, and involves processes spanning several orders of magnitude in spatial extent and temporal frequency." In this thesis we present our results from studies of various statistical properties of superfluid turbulence in two-(2D) and three-dimensions (3D). In Chapter 2, we present a systematic, direct numerical simulation (DNS) of the 2D, Fourier-truncated, Gross-Pitaevskii equation to study the turbulent evolutions of its solutions for a variety of initial conditions. Chapter 3 contains our calculations of the mutual-friction coefficients as a function of temperature in a homogeneous Bose gas in 2D by using the Galerkin-truncated Gross-Pitaevskii equation. Chapter 4 is devoted to the study of the interplay of particles and fields in superfluids, in both simple and turbulent flows. Chapter 5 contains results from our DNSs of the

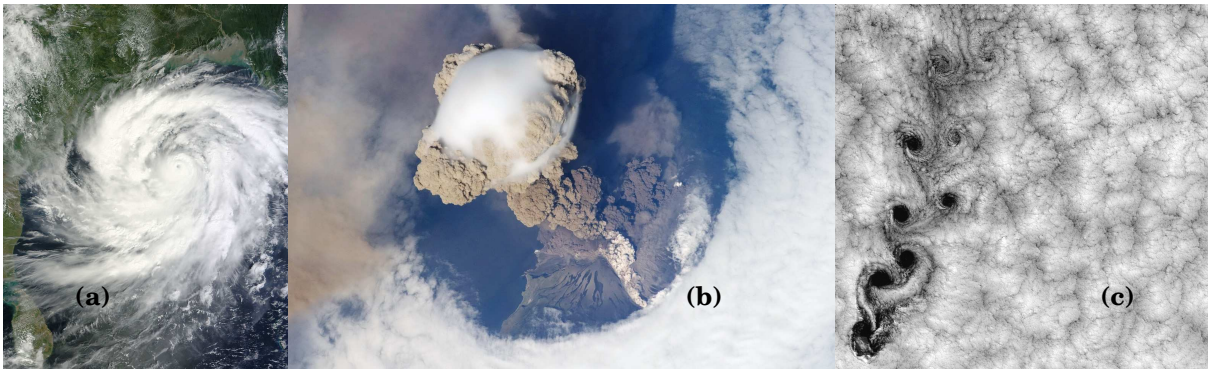

Figure 1.1: (a) Cyclone Phailin (near peak intensity on October 11, 2013), a severe, tropical cyclone over the Bay of Bengal. Source:http://en.wikipedia.org/wiki/Cyclone_Phailin. (b) A view of Sarychev Volcano (Kuril Islands, northeast of Japan), in an early stage of eruption on June 12, 2009; turbulent plume was a combination of brown ash and white steam (photograph by the Expedition 20 crew on the International Space Station). Source:http://earthobservatory.nasa.gov/IOTD/view.php?id=38985. (c) von Kármán vortex street, formed by wind-driven clouds when they encountered Selkirk Island in the southern Pacific Ocean (Image acquired by Landsat 7 on September 15, 1999). Source:http://earthobservatory.nasa.gov/IOTD/view.php?id=625.

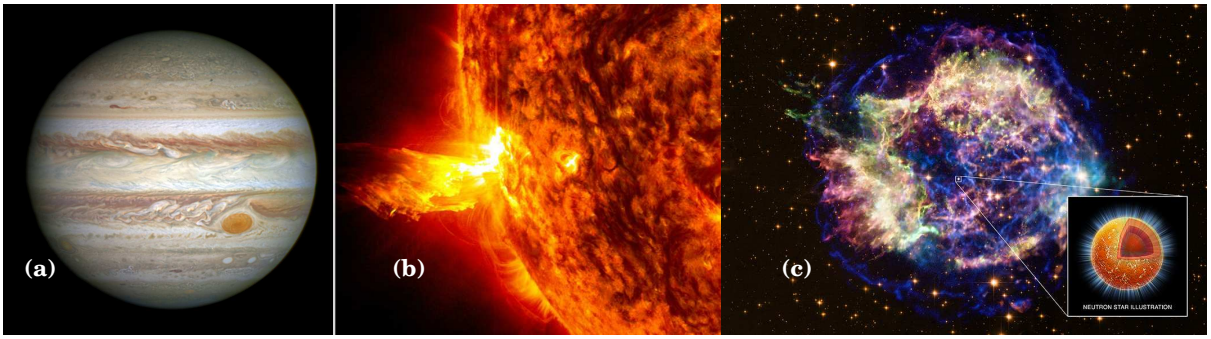

Figure 1.2: (a) The Great Red Spot (in the south-eastern corner), a giant swirling storm system in the Jupiter's banded atmosphere, which has existed for more than 300 years; the spot rotates anticlockwise, with a period of six Earth days. Image taken on April 21, 2014 by NASA's Hubble Space Telescope (Credit: NASA, ESA, and A. Simon (Goddard Space Flight Center)). Source:http://hubblesite.org/newscenter/archive/releases/2014/24/image/b. (b) The bright light of a solar flare on the left side of the sun and an eruption of solar material shooting through the sun's atmosphere; this is called a prominence eruption. Shortly thereafter, this same region of the sun sent a coronal mass ejection out into space. The image was taken on June 20, 2013, at 11:15 p.m. EDT; credit: Solar Dynamics Observatory (SDO), NASA. Source: http://www.nasa.gov/mission_pages/sunearth/news/News062013-cme.html. (c) This composite image shows a beautiful X-ray and optical view of Cassiopeia A (Cas A), a supernova remnant located in our Galaxy about 11,000 light years away. These are the remains of a massive star that exploded about 330 years ago, as measured in Earth's time frame. X-rays from Chandra (NASA's Chandra X-ray Observatory) are shown in red, green, and blue, along with optical data from the Hubble-Space Telescope in gold. At the center of the image is a neutron star, an ultra-dense star created by the supernova. This was the first direct evidence for a superfluid, a friction-free state of matter, at the core of a neutron star. Source:http://chandra.harvard.edu/photo/2011/casa/.

Hall-Vinen-Bekharevich-Khalatnikov (HVBK) two-fluid model in 2D. In Chapter 6, we examine the multiscaling of structure functions in 3D superfluid turbulence by using a shell model for the 3D HVBK equations.

The remaining part of this Chapter is organized as follows. In Sec. 1.2 we present an introduction to three- and two-dimensional fluid turbulence. In Sec. 1.3 we give an overview of superfluidity and the phenomenological two-fluid model. Section 1.4 is devoted to superfluid turbulence; here we give a brief introduction, followed by an overview of important experiments and phenomenological models.

1.2 Fluid turbulence

The spatiotemporal evolution of the velocity field $\mathbf{u}(\mathbf{x},t)$ associated with an incompressible and charge-neutral fluid flow is governed by the Navier-Stokes (NS) equations

$$\frac{\partial \mathbf{u}(\mathbf{x},t)}{\partial t} + \mathbf{u}(\mathbf{x},t)\cdot\nabla\mathbf{u}(\mathbf{x},t) = -\frac{1}{\rho}\nabla p + \nu\nabla^2\mathbf{u}(\mathbf{x},t) + \mathbf{f}_{\rm ext}, \tag{1.1a}$$

$$\nabla\cdot\mathbf{u}(\mathbf{x},t) = 0; \tag{1.1b}$$

where ρ is the fluid density, ν the kinematic viscosity, and $\mathbf{f}_{\rm ext}$ represents the forces driving the fluid flow. The Eqs. (1.1a) and (1.1b) result from the momentum and the density conservation laws, respectively. The NS Eqs. (1.1) are an example of a nonlinear, partial differential equations with a quadratic nonlinearity in the variable $\mathbf{u}(\mathbf{x},t)$. The nonlinearity in the Eq. (1.1) manifests itself in the form of a wide variety of complex phenomena in its solutions, with turbulence being one of them, where the velocity field $\mathbf{u}(\mathbf{x},t)$ fluctuates randomly in time and varies across a wide range of length scales. The Eq. (1.1) themselves are deterministic, i.e., it is possible to integrate them for given initial conditions, but its solutions are unpredictable in the sense that an infinitesimal variation in the initial state may lead to a completely different realization. Strictly speaking, the regularity of the solutions of the Navier-Stokes equation, for arbitrary initial data, has not been established; and this continues to be a grand challenge for mathematicians [4]. Thus, turbulence is a dynamic phenomenon, in which fields, such as the velocity of a fluid, display spatiotemporal chaos. Therefore, while characterizing the turbulent flows, we are interested not in one realization of the fields associated with the flow, but the statistical properties of the fields, which are well behaved and reproducible.

Reynolds number

To understand the onset of turbulence in the fluid flows, we make use of a nondimensional parameter, referred to as the Reynolds number $Re \equiv UL/\nu$, where U and L are the characteristic velocity and length scales of the flow, respectively. At low values of Re the fluid flow is laminar; if Re is progressively increased then, at a critical value of $Re = Re_c$, the flow starts becoming unstable and at $Re \gg Re_c$ it displays fully developed turbulence. Reynolds number can also be viewed as the ratio of the nonlinear, advective term $\mathbf{u} \cdot \nabla \mathbf{u}$ and the dissipation term $\nu \nabla^2 \mathbf{u}$.

Velocity-vorticity formulation

We can obtain an equation for the dynamical evolution of the vorticity field $\omega = \nabla \times \mathbf{u}$, by taking the curl of the NS Eqs. (1.1), given by

$$\partial_t \omega + (\mathbf{u} \cdot \nabla)\omega = (\omega \cdot \nabla)\mathbf{u} + \nu \nabla^2 \omega + \mathbf{f}_\omega; \tag{1.2a}$$

$$\nabla^2 \mathbf{u} = -\nabla \times \omega; \tag{1.2b}$$

here $\mathbf{f}_\omega$ is the forcing term for the vorticity field. In three-dimensional (3D) turbulent flows, the "vortex stretching term" $(\omega \cdot \nabla)\mathbf{u}$ can either amplify or reduce the vorticity locally. The global measure of the vorticity content of the flow, the mean-squared vorticity, referred to as the enstrophy, can also get amplified or reduced by this mechanism, but it does not affect the integrated vorticity.

Two-dimensional NS equation and vorticity-stream function formulation

All fluid flows whether, naturally occurring or produced in laboratories are three-dimensional; even then, an idealized two-dimensional (2D) flow is relevant in the following cases: (a) the spatial extent of the fluid flow is much smaller in one direction than in the other two and the typical sizes of the features of interest, in such flows; (b) there may be other constraints, which render the fluid motion a quasi two-dimensional. Two-dimensional flows are described by the NS Eqs. (1.1), but now the velocity field $\mathbf{u}(\mathbf{r}, t)$ is constrained to two-dimensions with $\mathbf{r} \equiv (x, y)$:

$$\partial_t \mathbf{u} + (\mathbf{u} \cdot \nabla)\mathbf{u} = -\frac{1}{\rho}\nabla p + \nu \nabla^2 \mathbf{u} - \mu \mathbf{u} + \mathbf{f}, \tag{1.3a}$$

$$\nabla \cdot \mathbf{u} = 0; \tag{1.3b}$$

here μ is the linear-friction force coefficient. The linear-friction term is included to model the boundaries of the quasi-2D flows with the surrounding medium or air-drag induced friction in a fluid soap film [5–7].

The curl of Eq. (1.3) gives the following equation

$$\partial_t \omega + \mathbf{u} \cdot \nabla \omega = \nu \nabla^2 \omega - \mu \omega + \mathbf{f}_\omega, \tag{1.4a}$$

$$\nabla^2 \psi = -\omega, \tag{1.4b}$$

$$\mathbf{u} = \Big(\partial_y \psi, -\partial_x \psi\Big); \tag{1.4c}$$

here ψ is the stream-function. Furthermore, by using Eq. (1.4c) we can rewrite the 2D NS Eq. (1.4) in the vorticity-stream-function formulation as

$$\partial_t \omega + (\partial_x \omega \partial_y \psi - \partial_y \omega \partial_x \psi) = \nu \nabla^2 \omega - \mu \omega + \mathbf{f}_\omega, \tag{1.5a}$$

$$\omega = -\nabla^2 \psi, \tag{1.5b}$$

where the incompressibility condition Eq. (1.3b) is satisfied by construction.

1.2.1 Conservation laws

In the discussion below, we use periodic boundary conditions for the solutions of the NS Eqs. (1.1) describing an incompressible fluid flow, so that $\mathbf{u}(\mathbf{x}, t)$ is spatially periodic, with period L. First, we define the important quantities (per unit mass) characterizing the flow, which we use extensively later in the thesis: $E \equiv \langle \frac{1}{2}|\mathbf{u}|^2 \rangle$ is the mean energy, $\Omega \equiv \langle \frac{1}{2}|\omega|^2 \rangle$ is the mean enstrophy, $H \equiv \langle \frac{1}{2}\mathbf{u} \cdot \omega \rangle$ is the mean helicity, and $H_\omega \equiv \langle \frac{1}{2}\omega \cdot \nabla \times \omega \rangle$ is the mean vortical helicity, where the angular brackets denote spatial average over the entire volume occupied by the fluid $\langle \cdot \rangle \equiv (1/L^3) \int_{L^3} d\mathbf{x}$.

The quantities defined above satisfy the following balance equations:

$$\frac{dE}{dt} = -2\nu\Omega; \tag{1.6a}$$

$$\frac{dH}{dt} = -2\nu H_\omega; \tag{1.6b}$$

these become conservation laws only when the viscosity is set equal to zero. In the presence of an external forcing, the energy balance Eq. (1.6a) is modified to

$$\frac{dE}{dt} = -\epsilon_\nu + \epsilon_{\text{inj}}, \tag{1.7}$$

where $\epsilon_\nu \equiv 2\nu\Omega$ is the mean energy dissipation and $\epsilon_{\text{inj}} \equiv \frac{1}{L^3} \int_{L^3} \mathbf{f}_{\text{ext}} \cdot \mathbf{u}$ the energy-injection rate. In a statistically-steady state $\langle dE/dt \rangle = 0$ and $\epsilon_\nu = \epsilon_{\text{inj}}$.

In two-dimensional systems the helicity vanishes identically and we have a conservation law for the enstrophy (if $\nu = 0$)

$$\frac{d\Omega}{dt} = -2\nu\mathcal{P}, \tag{1.8}$$

where $\mathcal{P} = \langle \frac{1}{2}|\nabla \times \omega|^2 \rangle$ is the palinstrophy.

1.2.2 Classical turbulence phenomenology

As mentioned earlier, we are interested in the statistical description of the turbulent flows; to further simplify our problem, we assume that the flows which we consider are statistically homogeneous and isotropic; thus, the turbulence is statistically invariant under translation, rotation and reflection of coordinate axes. We begin with the pictorial description of turbulence, based on the concept of energy cascade introduced by L. F. Richardson, who wrote, "Big whorls have have little whorls that feed on their velocity, and little whorls have lesser whorls and so on to viscosity" [8]. Thus, we can identify the Richardson-cascade picture with three different regions of spatial scales (ℓ): (1) the energy-injection scales ($\ell \sim l_I$), where the energy driving the turbulent flow is injected into the system at large length scales and the eddies ($\sim$ curl of velocity) formed are comparable to the system size (l_I is also called the integral scale); (2) the region of intermediate length scales ($l_I \gg \ell \gg l_d$), also called the inertial scales, through which the energy flows down by the transformation of the large-scale eddies into successively small-scale eddies by nonlinear interactions, represented by the advection term in the NS Eqs. (1.1); (3) dissipation scales $\ell \ll l_d$, where l_d is the dissipation-scale below which the finer eddies are removed from the system by viscous dissipation.

Now, we give a more systematic, phenomenological description of turbulence in terms of statistical quantities; we follow Ref. [9] closely and at places we quote verbatim from it. The following two basic empirical laws of fully developed turbulence, seem to be valid, at least approximately for any turbulent flow:

- *Two-thirds law.* In a turbulent flow at very high Reynolds number, the mean square velocity increment $\langle(\delta u(l))^2\rangle$ between two-points separated by a distance ℓ behaves approximately as the two-thirds power of the distance in the inertial range.

- *Law of finite energy dissipation.* If, in an experiment on turbulent flow, all the control parameters are kept the same, except for the viscosity, which is lowered as much as possible, the energy dissipation per unit mass dE/dt behaves in a way consistent with a finite positive limit.

We now state hypotheses, originally due to Kolmogorov [10, 11], compatible with the above two laws, to make more predictions about the turbulent flows.

- **H1** As $Re \to \infty$, all the possible symmetries of the Navier-Stokes equation, usually broken by the mechanisms producing the turbulent flow, are restored in a statistical sense at small scales ($\ell \ll l_I$) and away from boundaries.

- **H2** With the same assumptions of H1, the turbulent flow is self-similar at small scales, i.e. it possesses a unique scaling exponent.
- **H3** With the same assumptions of H1, the turbulence has a finite, nonvanishing mean rate of dissipation ϵ per unit mass.

The velocity increments over length ℓ are

$$\delta\mathbf{u}(\mathbf{r},\boldsymbol{\ell}) \equiv \mathbf{u}(\mathbf{r}+\boldsymbol{\ell}) - \mathbf{u}(\mathbf{r}). \tag{1.9}$$

We define the property of small-scale homogeneity by assuming that $\delta\mathbf{u}(\mathbf{r}+\boldsymbol{\varrho},\ell) \overset{Law}{=} \delta\mathbf{u}(\mathbf{r},\boldsymbol{\ell})$, for all increments $\ell \ll l_I$ and all displacements $\varrho \ll l_I$, where the symbol $\overset{Law}{=}$ implies same statistical properties. Similarly, we regard isotropy as the invariance of the statistical properties of $\delta\mathbf{u}(\mathbf{r},\boldsymbol{\ell})$ under simultaneous rotations of $\boldsymbol{\ell}$ and $\delta\mathbf{u}$. The self-similarity (H2) is $\delta\mathbf{u}(\mathbf{r},\lambda\boldsymbol{\ell}) \overset{Law}{=} \lambda^h\delta\mathbf{u}(\mathbf{r},\boldsymbol{\ell})\ \forall\ \lambda \in \mathbb{R}_+$ and $h \in \mathbb{R}$, for all $\mathbf{r}$ and all increments $\boldsymbol{\ell} \ll l_I$ and $\lambda\boldsymbol{\ell} \ll l_I$.

Kolmogrov's four-fifths law, one of the most important and the only exact result in the theory of fully developed turbulence [12], states that, as $Re \to \infty$

the third order (longitudinal) structure function of homogeneous isotropic turbulence, evaluated for increments ℓ small compared to the integral scale, is

$$\langle\big(\delta u_\parallel(\ell)\big)^3\rangle = -\frac{4}{5}\epsilon\ell. \tag{1.10}$$

The order-p longitudinal structure functions of the velocity fluctuations $\delta\mathbf{u}(\boldsymbol{\ell})$ are

$$S_p(\ell) \equiv \Big\langle\Big[\big(\mathbf{u}(\mathbf{r}+\boldsymbol{\ell}) - \mathbf{u}(\mathbf{r})\big)\cdot\frac{\boldsymbol{\ell}}{\ell}\Big]^p\Big\rangle = \Big\langle\Big[\delta\mathbf{u}(\boldsymbol{\ell})\cdot\frac{\boldsymbol{\ell}}{\ell}\Big]^p\Big\rangle, \tag{1.11}$$

where the order $p > 0$ and the increment $\ell \ll l_I$. The three hypotheses H1, H2, H3 and the *four-fifths law*, together can be used to show that the unique scaling exponent (H2) is $h = 1/3$, which implies that the structure functions S_p behave as

$$S_p(\ell) \propto \ell^{\zeta_p} \tag{1.12}$$

with $\zeta_p = p/3$ and ℓ in the inertial range. Because $(\epsilon\ell)^{p/3}$ has the same dimensions as S_p, we rewrite the above equation as

$$S_p(\ell) = C_p\epsilon^{p/3}\ell^{\zeta_p}, \tag{1.13}$$

where C_p's are dimensionless. These predictions were made by Kolmogorov in the year 1941, therefore, we refer to this phenomenological approach as K41.

The second-order structure function $S_2(\boldsymbol{\ell})$ can be related to the energy spectrum $E(k)$ defined in the Fourier space, which shows the distribution of energy across the length scales:

$$E(k) \equiv \int_{\Omega_s} d\Omega_s|\mathbf{u}(\mathbf{k})|^2; \tag{1.14}$$

here $\mathbf{u}(\mathbf{k})$ is the Fourier-space representation of the velocity field $\mathbf{u}$, $k = |\mathbf{k}|$, $\mathbf{k}$ the wave vector, and Ω_s the d-dimensional solid angle. In the K41 description $S_2 \sim \ell^{2/3}$, so

$$E^{K41}(k) \sim k^{-5/3}, \tag{1.15}$$

which is in good agreement with the experimental results.

We briefly give the estimates of some of the length scales, which are frequently used in this phenomenological description. The integral scale

$$l_I \simeq \frac{\sum_k k^{-1} E(k)}{\sum_k E(k)}; \tag{1.16}$$

the Taylor-microscale

$$\lambda \simeq \Big(\frac{\sum_k E(k)}{\sum_k k^2 E(k)}\Big)^{1/2}; \tag{1.17}$$

and the dissipation length scale

$$l_d \simeq \Big(\frac{\nu^3}{\epsilon}\Big)^{1/4}. \tag{1.18}$$

Based on l_I and λ we can define the integral-scale Reynolds number $Re_I = u_{\rm rms} l_I/\nu$ and the Taylor-microscale Reynolds number $Re_\lambda = u_{\rm rms}\lambda/\nu$, respectively, where $u_{\rm rms}$ is the root-mean-square velocity.

Intermittency

The phenomenological picture presented above is incomplete. Experiments and numerical simulations show that the structure-function (multi)scaling exponents ζ_p deviate significantly from the ζ_p^{K41}. Thus, these are anomalous. This arises because of small-scale intermittency in turbulent flows, both in temporal and the spatial domains: (a) in the temporal domain intermittency shows up as short bursts in the time series of an observable, e.g., the velocity component measurement at a point, separated by relatively quiescent periods; (b) in the spatial domain it is characterized by the occurrence of isolated regions of high-amplitude fluctuations, once again, separated by relatively quiescent regions. These extreme events become more pronounced as Re increases. Intermittency is also reflected in the probability distribution functions (PDFs) of the increments of the fluid velocity $\delta\mathbf{u}$ in the form of extended, length-scale-dependent tails, whose extent is much more than that of a Gaussian PDF. This signifies that extreme or rare events are far more probable than can be expected from a Gaussian distribution; and it results because of the uneven spatial distribution of the small-scales; therefore, the small-scale universality assumption in the K41 is not completely true as it assumes that the energy

transfer across the inertial scales occur only because of the interactions between the neighboring scales.

The scaling exponents ζ_p of structure functions must satisfy certain constraints as discussed in Ref. [9], which we follow closely here. In summary, the structure functions of even order follow power-laws with exponents ζ_{2p} and, if the incompressibility approximation does not break down as $Re \to \infty$, the graph of ζ_{2p} versus p is concave and nondecreasing. A precise discussion (see Ref. [9]) of these constraints proceeds as follows:

- **S1** In the limit $Re = l_I u_0/\nu \to \infty$, the structure functions of even order $2p > 0$ possess the exponents ζ_{2p}, i.e., for $\ell \to 0$,

$$\frac{\langle \big(\delta u_{\|}(\ell)\big)^{2p} \rangle}{u_0^{2p}} \approx A_{2p} \big(\frac{\ell}{l_I}\big)^{\zeta_{2p}}, \tag{1.19}$$

  where A_{2p} is a positive numerical constant (not necessarily universal).

- **S2** For large but finite Re, the scaling above Eq. (1.19) still holds over the inertial range of scales increasing with Re at least as a power-law:

$$1 \gg \frac{\ell}{l_I} \gg Re^{-\alpha}, \tag{1.20}$$

  where $\alpha > 0$.

u_0 is root-mean-square velocity fluctuation associated to length scales l_I. Below we state the following constraints on the ζ_p without their proofs:

- **P1** For any three positive integers $p_1 \leq p_2 \leq p_3$, we have the convexity inequality:

$$(p_3 - p_1)\zeta_{2p_2} \geq (p_3 - p_2)\zeta_{2p_1} + (p_2 - p_1)\zeta_{2p_3}. \tag{1.21}$$

- **P2** Under assumption S1, if there exist two consecutive even numbers $2p$ and $2p + 2$ such that

$$\zeta_{2p} > \zeta_{2p+2}, \tag{1.22}$$

  then the velocity of the flow (measured in the reference frame of the mean flow) cannot be bounded.

Energy cascades in 2D turbulence

The conservation of energy and enstrophy, in the inviscid unforced case in the 2D Navier-Stokes equation, gives the 2D fluid turbulence one of its most characteristic feature namely, two cascades (as opposed to the forward cascade of energy, from

large to small length scales, in 3D fluid turbulence). In 1967, Kraichnan had suggested that, if energy is injected into a 2D flow at an intermediate length scale l_0, at a constant rate ϵ, then kinetic energy flows towards larger length scales $\ell > l_0$, until the largest scale is reached [13]. This *inverse cascade* of energy was conjectured by Kraichnan based on 'absolute equilibrium' for the Galerkin-truncated Euler equation, in the absence of any forcing and viscous dissipation; the Galerkin truncation makes the Euler equation a finite-dimensional Hamiltonian system because, only a finite number of Fourier-modes are retained [14]. The inverse-cascade regime is associated with an energy spectrum $E(k) \sim k^{-5/3}$, for the wave-number range $k_E < k < l_0^{-1}$, where the peak $E(k_E)$ depends on the balance between the nonlinear energy transfer and the energy sink at the largest scales; thus, the energy spectrum at very low wave numbers depends on the presence (and the nature) or the absence of an energy sink [15, 16]. For example, in many experimental realizations like soap films, the inverse cascade is cut off at large length scales by air-drag-induced friction [7, 17, 18].

The forward-cascade regime, with $E(k) \sim k^{-3}$ for the wave number range $l_0^{-1} < k < l_d^{-1}$, is associated with the cascade of enstrophy from the energy-injection length scale to smaller length scales [13, 19, 20]. In the presence of linear-friction, at small wave numbers, the energy spectrum $E(k) \sim k^{-3-\delta}$, where $\delta > 0$ depends on the coefficient of friction. The enstrophy spectra behaves as $\Omega(k) \sim k^{-1-\delta}$ in the forward-cascade regime [16, 21, 22].

1.3 Superfluid hydrodynamics

Superfluidity is a phenomenon in which quantum-mechanical behavior is manifested on a macroscopic level. It was first discovered in the year 1937 in helium, which, when cooled below the critical transition temperature $T_\lambda = 2.17\mathrm{K}$, becomes a *superfluid*. The transition temperature T_λ is called the 'lambda point' because of the characteristic shape of the specific-heat versus temperature curve, which looks like a Greek letter λ. The phases of liquid helium, above and below T_λ, are also referred to as helium I and helium II, respectively. At temperatures below T_λ, the de-Broglie wavelength of the helium atoms is comparable to the interatomic distances, so it has quantum properties and, thus, it is not a classical, but a quantum liquid. In helium II, the ability of the superfluid to flow, without friction, through narrow capillaries is one of the several remarkable properties of the superfluidity.

Many of the flow properties of superfluid helium II at low velocities can be described within the framework of a phenomenological, two-fluid model, proposed by

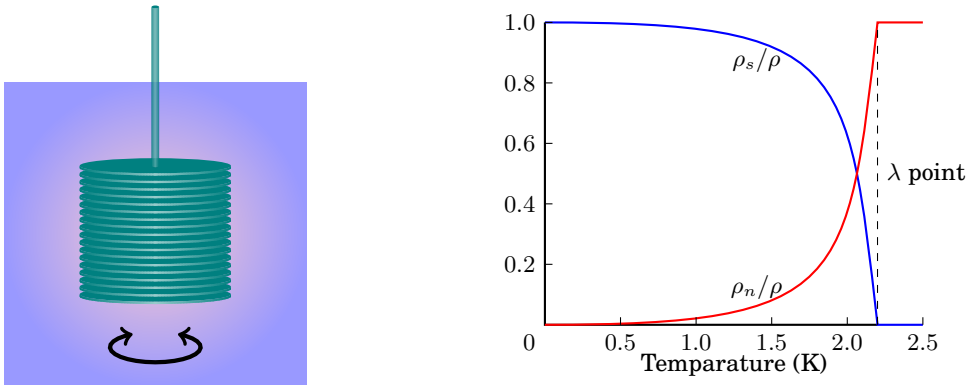

Figure 1.3: Direct measurement of ρ_n/ρ as function of temperature. (a) Schematic of the experiment reported in Ref. [23]: A pile of equally-spaced metal discs, suspendend by a torsion fibre performs torsion oscillations in liquid helium. For $T > T_\lambda$ all the fluid between the discs is dragged, however, at temperatures below T_λ not all the fluid is dragged with discs resulting in the sharp decrease in the oscillation period. (b) Variation of ρ_n/ρ and ρ_s/ρ with temperature. The above schematic diagrams are based on Fig.1.7 in Ref. [24].

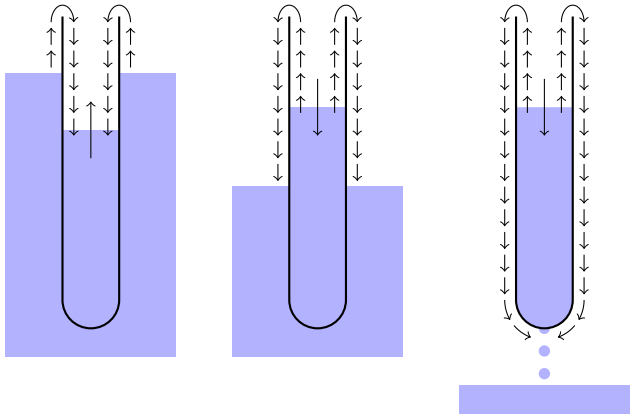

Figure 1.4: Film flow of superfluid fraction of helium II through the film in the presence of height difference between two bulk liquids. The above schematic diagram is based on Fig.1.8 in Ref. [24].

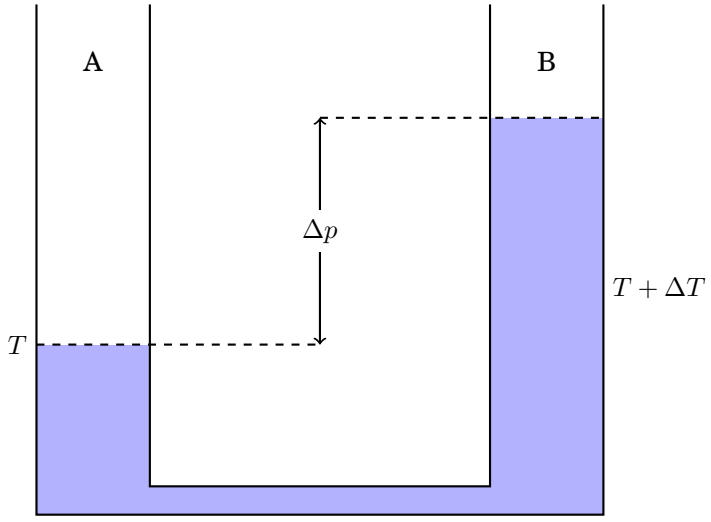

Figure 1.5: Temperature difference between two columns of bulk helium II connected by a superleak, which clamps the normal fluid flow, is accompanied by a pressure head. The column at higher temperature has a reduced ρ_s/ρ fraction, so the superfluid fraction moves to through the superleak to minimize the temperature gradient. The above schematic diagram is based on Fig.1.9 in Ref. [24].

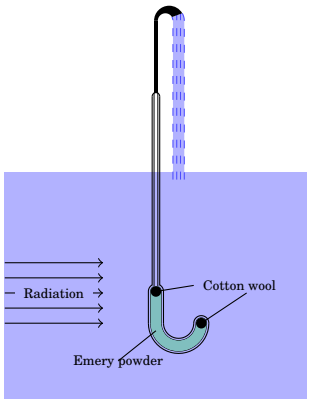

Figure 1.6: The helium fountain: When the emry powder in the superleak is heated, the superfluid fraction flows into the superleak with such a large speed that helium II is forced out of the capillary tube in the form of a jet (for details we refer the reader to Refs. [25, 26]. The above schematic diagram is based on Fig.1.10 in Ref. [24].

L. Tisza [27,28] and L. Landau [29], independently. In the two-fluid model, Helium II is regarded as a physically inseparable mixture of two fluids, one the superfluid and the other the normal fluid; the former has no viscosity or entropy and can flow in a dissipationless manner past obstacles and through extremely narrow channels; the latter has viscosity and carries the entire entropy of the flow. The total density ρ of helium II is the sum of the superfluid density ρ_s and the normal fluid density ρ_n; ρ, ρ_s, and ρ_n depend on the temperature T. At $T = T_\lambda$, $\rho = \rho_n$; and at $T = 0$, the normal fluid density is zero, so $\rho = \rho_s$. Both the superfluid and the normal fluid are assumed to have their own velocity fields $\mathbf{v}_s$ and $\mathbf{v}_n$, respectively. Thus, the total current density is $\mathbf{j} = \mathbf{j}_s + \mathbf{j}_n = \rho_s \mathbf{v}_s + \rho_n \mathbf{v}_n$, where $\mathbf{j}_s$ and $\mathbf{j}_n$ are the superfluid and the normal fluid current densities, respectively. In Figs. 1.3, 1.4, 1.5, and 1.6 we illustrate some of the remarkable properties of superfluids, which were demonstrated in the early experiments on liquid helium.

Superfluidity is associated with a phenomenon of Bose-Einstein condensation (BEC) exhibited by bosons at low-enough temperatures, in which a quantum state, corresponding to the lowest single-particle energy level, has a macroscopic population; the particles constituting the macroscopic population are together regarded as a condensate. In liquid helium there are interactions between atoms and these interactions cause a depletion of the condensate by raising some particles to slightly higher energy levels. Therefore, the higher energy levels have a finite population at absolute zero temperature because of depletion and at temperatures $T > 0$ because of the combined effects of depletion and thermal excitations. The excitations form the elementary excitations of the entire system. Thus, at the simplest level of description, these can be treated as non-interacting quasiparticles. At $T = 0$, helium II is a pure superfluid, leading to the identification that superfluid density includes both the condensate and the depleted particles; and at $T > 0$, thermal excitations constitute the normal fluid.

1.3.1 Superfluid equations of motion

The discussion below closely follows that in Refs. [24, 30–32], for the heuristic derivation of the equation of motions for superfluid and normal fluid. Let us postulate that the condensate behaviour is governed by a single wave function $\psi(\mathbf{r}, t)$ with coherent phase $\theta(\mathbf{r}, t)$, i.e.,

$$\psi(\mathbf{r}, t) = \psi_0(\mathbf{r}, t) \exp\Big[i\theta(\mathbf{r}, t)\Big], \tag{1.23}$$

which is a solution of the Schrödinger equation

$$i\hbar \frac{\partial \psi}{\partial t} = -\frac{\hbar^2}{2m}\nabla^2\psi + \overline{V}(r)\psi, \tag{1.24}$$

where m is the mass of the condensate atoms and $\overline{V}(r)$ is the potential energy. The wave function ψ is normalized such that

$$|\psi|^2 = |\psi_0(\mathbf{r}, t)|^2 = \frac{\rho_s}{m}. \tag{1.25}$$

A thermodynamic description of superfluidity is possible, if the superfluid density ρ_s and the potential $\overline{V}(r)$ are slowly varying functions of space and the volume elements in which ρ_s is uniform are macroscopic in size. $\overline{V}(r)$ is a thermodynamic parameter, since it is the potential energy of each one of the macroscopically large number of atoms in the volume element about $\mathbf{r}$. By using the first law of thermodynamics, a reversible change in the total energy U_0 of a fluid at rest can be expressed as

$$dU_0 = Td\Sigma + \mu dN - pdV, \tag{1.26}$$

where the independent variables entropy Σ, number of particles N and volume V determine the state of the system; T is the temperature, μ the chemical potential, and p the pressure. Thus,

$$\mu = \Big(\frac{\partial U_0}{\partial N}\Big)_{\Sigma,V} \tag{1.27}$$

is the energy gained by the fluid when one single particle is added to it. If the superfluid has kinetic energy $U_{s,K}$, then the total energy of the fluid becomes

$$U = U_{s,K} + U_0. \tag{1.28}$$

Consider the motion of a volume element, with ΔN superfluid atoms in thermodynamic equilibrium with the rest of the fluid, from point A to point B in a superfluid flow, in which the total energy and the entropy do not change; for such a motion the change in the total energy is

$$\Delta U = \Delta U_{s,K} + \left[\Big(\frac{\partial U_0}{\partial N}\Big)^B_{\Sigma,V} - \Big(\frac{\partial U_0}{\partial N}\Big)^A_{\Sigma,V}\right]\Delta N = 0; \tag{1.29}$$

whence

$$\frac{\Delta U_{s,K}}{\Delta N} = -\big(\mu_B - \mu_A\big). \tag{1.30}$$

Therefore the chemical potential of the whole fluid plays the role of the potential energy per particle of the supefluid; also, Eq. (1.30) shows that the superfluid is accelerated when it flows from a region of high to a region of low chemical potential. Thus, by replacing the $\overline{V}(\mathbf{r})$ by μ in Eq. (1.24), we obtain

$$i\hbar\frac{\partial\psi}{\partial t} = -\frac{\hbar^2}{2m}\nabla^2\psi + \mu\psi. \tag{1.31}$$

The substitution of Eqs. (1.23) and (1.25) in the above equation yields, for the condensate phase θ,

$$\hbar\frac{\partial\theta}{\partial t} = -\mu + \frac{\hbar^2}{2m}\big(\nabla\theta\big)^2 + \frac{\hbar^2}{2m}\frac{\nabla^2\sqrt{\rho_s}}{\sqrt{\rho_s}}. \tag{1.32}$$

By using Eq. (1.24) and its complex conjugate, the equation of continuity for the probability density $|\psi|^2$ can be written as

$$\frac{\partial|\psi|^2}{\partial t} = -\nabla\cdot\mathbf{J}_p, \tag{1.33}$$

where

$$\mathbf{J}_p = -\frac{i\hbar}{2m}\Big(\psi^*\nabla\psi - \psi\nabla\psi^*\Big), \tag{1.34}$$

is the probability current density. Substitution of Eq. (1.23) and (1.25) in the Eq. (1.33) gives the following equation of continuity for the superfluid density:

$$\frac{\partial\rho_s}{\partial t} = -\nabla\cdot\mathbf{j}_s, \tag{1.35}$$

where

$$\mathbf{j}_s = \frac{\hbar}{m}\rho_s\nabla\theta \equiv \rho_s\mathbf{v}_s \tag{1.36}$$

is the superfluid current density with

$$\mathbf{v}_s = \frac{\hbar}{m}\nabla\theta \tag{1.37}$$

the superfluid velocity. The gradient of Eq. (1.32), along with Eq. (1.37) gives the following equation of motion for the superfluid

$$m\frac{\partial\mathbf{v}_s}{\partial t} = -\nabla\Big(\mu + \frac{1}{2}m\mathbf{v}_s^2\Big) + \frac{\hbar^2}{2m}\nabla\frac{\nabla^2\sqrt{\rho_s}}{\sqrt{\rho_s}}. \tag{1.38}$$

The last term in equation 1.38 contributes significantly only when there is a rapid variation in ρ_s, e.g., near a wall or inside a vortex; it can be neglected while describing a bulk superfluid. Therefore, the equation of motion for the superfluid becomes

$$\frac{D\mathbf{v}_s}{Dt} = \frac{\partial\mathbf{v}_s}{\partial t} + \mathbf{v}_s\cdot\nabla\mathbf{v}_s = -\frac{1}{m}\nabla\mu, \tag{1.39}$$

which is the Euler's equation for an ideal fluid.

The Gibbs energy for a fluid at rest is $G = U_0 - T\Sigma + pV$, thus, the differential change in G after substituting for dU_0 is $dG = \mu dN - \Sigma dT + V dp$, which gives, after integration,

$$N\mu(p,T) = G(N,p,T); \tag{1.40}$$

therefore, the chemical potential can also be interpreted as the Gibbs energy per particle for given values of p and T. By using Eq. (1.40), a small reversible change

in μ, at constant N, can be obtained as

$$N d\mu = \left(\frac{\partial G}{\partial p}\right)_{N,T} dp + \left(\frac{\partial G}{\partial T}\right)_{N,p} dT, \tag{1.41a}$$

$$= V dp - \Sigma dT, \tag{1.41b}$$

where we have identified $\left(\frac{\partial G}{\partial p}\right)_{N,T}$ and $\left(\frac{\partial G}{\partial T}\right)_{N,p}$ with V and $-\Sigma$, respectively. Thus, Eq. (1.41b), when expressed for a gradient of μ, becomes

$$\nabla \mu = \frac{V}{N} \nabla p - \frac{\Sigma}{N} \nabla T, \tag{1.42}$$

which yields, with Eq. (1.39),

$$\frac{D\mathbf{v}_s}{Dt} = \frac{\partial \mathbf{v}_s}{\partial t} + \mathbf{v}_s \cdot \nabla \mathbf{v}_s = -\frac{1}{\rho} \nabla p + \sigma \nabla T, \tag{1.43}$$

where Nm/V is the total density of the superfluid and $\sigma = \Sigma / Nm$ the total entropy per unit mass.

The total density and the total mass current density are given by

$$\rho = \rho_s + \rho_n \tag{1.44}$$

and

$$\mathbf{j} = \rho_s \mathbf{v}_s + \rho_n \mathbf{v}_n, \tag{1.45}$$

respectively. The conservation of the total mass of the fluid, is expressed by the continuity equation

$$\frac{\partial \rho}{\partial t} = -\nabla \cdot \mathbf{j}. \tag{1.46}$$

In the limit of small velocities the viscous dissipation in the normal fluid can be neglected and the total entropy of the fluid is conserved. Thus, the equation of continuity for the entropy density $\rho\sigma$ can be written as

$$\frac{\partial \rho\sigma}{\partial t} = -\nabla \cdot \big(\rho\sigma \mathbf{v}_n\big), \tag{1.47}$$

where $\rho\sigma\mathbf{v}_n$ is the entropy-current density, (all the entropy is carried by the normal fluid). Thus, for an incompressible flow, where ρ, ρ_s, ρ_n and σ are all constant, Eq. (1.47) gives $\nabla \cdot \mathbf{v}_n = 0$, which in turn yields $\nabla \cdot \mathbf{v}_s = 0$ by virtue of Eqs. (1.45) and (1.46). The Navier-Stokes equation is used to describe the motion of the whole fluid:

$$\rho_s \frac{D\mathbf{v}_s}{Dt} + \rho_n \frac{D\mathbf{v}_n}{Dt} = -\nabla p + \nu_n \nabla^2 \mathbf{v}_n, \tag{1.48}$$

where ν_n is the viscosity of the normal fluid. By multiplying Eq. (1.43) by ρ_s and, subsequently, subtracting it from Eq. (1.48) gives the following equations of motion

for the superfluid and the normal fluid velocities:

$$\rho_s\Big(\frac{\partial \mathbf{v}_s}{\partial t} + \mathbf{v}_s \cdot \nabla \mathbf{v}_s\Big) = -\frac{\rho_s}{\rho}\nabla p + \rho_s \sigma \nabla T; \tag{1.49a}$$

$$\rho_n\Big(\frac{\partial \mathbf{v}_n}{\partial t} + \mathbf{v}_n \cdot \nabla \mathbf{v}_n\Big) = -\frac{\rho_n}{\rho}\nabla p + \rho_n \sigma \nabla T + \nu_n \nabla^2 \mathbf{v}_n; \tag{1.49b}$$

these are valid at small velocities.

As mentioned earlier, in the two-fluid model the gas of thermal excitations constitute the normal fluid; moreover, because the total number of excitations is not conserved, we use Planck's distribution function

$$n(\varepsilon_n) = \frac{1}{\exp(\varepsilon_n/k_B T) - 1}, \tag{1.50}$$

where ε_n is the thermal-excitation energy in the normal-fluid rest frame. The creation of an excitation, with momentum $\mathbf{p}$ and energy ε_n in the normal-fluid rest frame, is equivalent to an excitation with momentum $\mathbf{p}$ and energy $\varepsilon_n + \mathbf{p}\cdot(\mathbf{v}_n - \mathbf{v}_s)$ in the superfluid rest frame; clearly, $\mathbf{v}_n - \mathbf{v}_s$ is the relative velocity of the normal-fluid rest frame with respect to the superfluid rest frame; $\mathbf{v}_n$ and $\mathbf{v}_s$ are defined with respect to the laboratory frame. The distribution function Eq. (1.50) can be written as

$$n(\varepsilon) = \left[\exp\Big(\frac{\varepsilon(p) - \mathbf{p}\cdot(\mathbf{v}_n - \mathbf{v}_s)}{k_B T}\Big) - 1\right]^{-1}, \tag{1.51}$$

where $\varepsilon(p)$ is the energy spectrum measured in the superfluid rest frame. The discussion above shows that $(\mathbf{v}_n - \mathbf{v}_s)$, is an extra thermodynamic parameter for the helium II. Relative to the superfluid rest frame, the drift momentum density of the excitations is

$$\mathbf{j}_d = \rho_n(\mathbf{v}_n - \mathbf{v}_s), \tag{1.52}$$

and the change in the total energy density is given by

$$dU_{SRF} = T d(\rho\sigma) + \frac{\mu}{m} d\rho + (\mathbf{v}_n - \mathbf{v}_s)\cdot d\mathbf{j}_d, \tag{1.53}$$

which can be compared with Eq. (1.26); the subscript SRF denotes superfluid rest frame. Thus the thermodynamic relation Eq. (1.53) can be used to determine the chemical potential as follows:

$$\frac{1}{m}\mu(p, T, \mathbf{v}_n - \mathbf{v}_s) = \frac{1}{m}\mu(p, T, 0) - \frac{\rho_n}{2\rho}(\mathbf{v}_n - \mathbf{v}_s)^2, \tag{1.54}$$

where $\mu(p, T, 0)$ is the chemical potential in the absence of relative motion. Use of $\mu(p, T, \mathbf{v}_n - \mathbf{v}_s)$ in Eq. (1.39) gives the following equation for the superfluid velocity

$$\rho_s\Big(\frac{\partial \mathbf{v}_s}{\partial t} + \mathbf{v}_s \cdot \nabla \mathbf{v}_s\Big) = -\frac{\rho_s}{\rho}\nabla p + \rho_s \sigma \nabla T + \frac{\rho_s \rho_n}{2\rho}\nabla(\mathbf{v}_n - \mathbf{v}_s)^2, \tag{1.55}$$

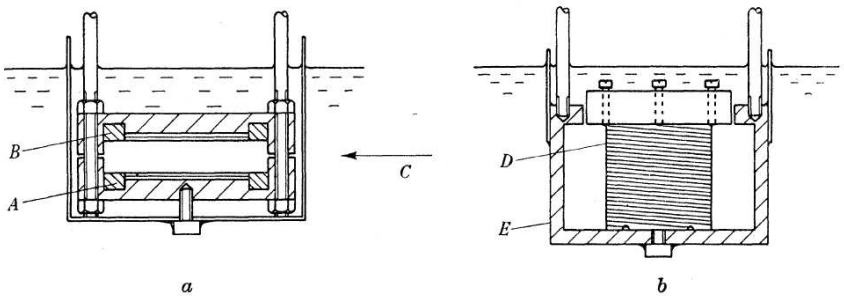

Figure 1.7: Sketch of the experimental setup used by H. E. Hall and W. F. Vinen to determine the existence of the mutual friction force. The resonators: (a) axial mode resonator; (b) radial mode resonator. In each resonator the heater consists of about 60 cm 50 s.w.g eureka wire and the thermometer about 60cm 0.003 in. phosphor-bronze wire, wound across the rings A and B in the axial mode resonator and round the cylinder D in the radial mode resonator. The arrow C indicates the axis of rotation for the axial mode resonator on its side; when rotation is about this axis the second sound propagation direction is normal to the axis of rotation, as with the radial mode resonator. Our caption follows the caption of Fig.1 in Ref. [33].

which, when subtracted from the Navier-Stokes Eq. (1.48), yields an equation for the normal fluid

$$\rho_n\Big(\frac{\partial \mathbf{v}_n}{\partial t} + \mathbf{v}_n \cdot \nabla \mathbf{v}_n\Big) = -\frac{\rho_n}{\rho}\nabla p + \rho_n \sigma \nabla T - \frac{\rho_s \rho_n}{2\rho}\nabla(\mathbf{v}_n - \mathbf{v}_s)^2 + \nu_n \nabla^2 \mathbf{v}_n; \qquad (1.56)$$

Eqs. (1.55) and (1.56) are valid at higher velocities as compared to Eqs. (1.49a) and (1.49b). At higher velocities the normal fluid can become turbulent and then there can be interaction between the fluids.

1.3.2 Mutual friction

For $T < T_\lambda$, the scattering of the thermal excitations, constituting the normal fluid, by the quantized superfluids vortices results in a force of interaction between the two fluids known as mutual friction. In experiments performed in helium II, it has been observed that in the temperature range $1\text{K} < T < T_\lambda$ the collision of the rotons with the vortices is the major contributor to the mutual friction. The collision cross-section for the above scattering depends strongly on the direction of the relative velocity between the drifting rotons and the quantized vortex line: it is maximum for perpendicularly incident rotons and almost zero if their incidence is parallel incidence.

Experimental determination of mutual friction

Hall and Vinen performed experiments on the propagation of second sound in uniformly rotating helium II to determine the existence of mutual friction [33, 34].

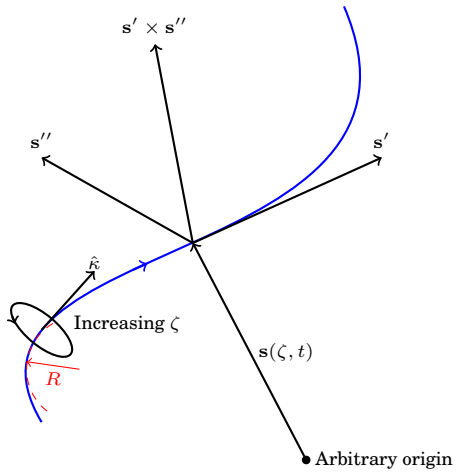

Figure 1.8: The instantaneous local configuration of the vortex filament at point s, represented by a parametrised curve $\mathbf{s}(\zeta, t)$, can be characterized by a triad of mutually perpendicular vectors $\mathbf{s}'(= d\mathbf{s}/d\zeta \sim 1)$, $\mathbf{s}''(= d^2\mathbf{s}/d^2\zeta \sim R^{-1})$, and $\mathbf{s}' \times \mathbf{s}''(\sim R^{-1})$, which are directed along the local tangent (in turn, it points in the direction of the circulation), the principal normal, and the binormal, respectively. The local induced velocity at a point in the fluid approximately points in the direction of $\mathbf{s}' \times \mathbf{s}''$.

They used two resonant cavities, each immersed in a vessel containing helium II and rotating about a particular axis; in one the second sound was propagated in a direction parallel to the axis of rotation; in the other it was propagated perpendicular to the rotation axis. They found that the second sound suffered an appreciable excess attenuation when propagating perpendicular to the axis of rotation, for uniformly rotating helium II, in comparison to the non-rotating case. Thus, they concluded that the attenuation of second sound, in uniformly rotating helium II, arises because of a volume force and depends on the orientation of the velocity $(\mathbf{v}_s - \mathbf{v}_n)$ in the second-sound wave relative to the axis of rotation. Moreover, the mutual friction force F_{sn} per unit volume acting on the normal fluid must be proportional to both (a) $(\mathbf{v}_s - \mathbf{v}_n)$, (b) $\mathbf{\Omega}$ the angular velocity of rotation, and, to a first approximation is

$$\mathbf{F}_{sn} = -B\frac{\rho_s\rho_n}{\rho}\frac{\mathbf{\Omega} \times [\mathbf{\Omega} \times (\mathbf{v}_s - \mathbf{v}_n)]}{|\mathbf{\Omega}|} - B'\frac{\rho_s\rho_n}{\rho}\mathbf{\Omega} \times (\mathbf{v}_s - \mathbf{v}_n); \tag{1.57}$$

B and B' are dimensionless coefficients and are measured in experiments; $(\mathbf{v}_s - \mathbf{v}_n)$ is the instantaneous counterflow velocity. The parameter B depends on the direction of $(\mathbf{v}_s - \mathbf{v}_n)$ relative to the rotation axis; it is a constant for all orientations of $(\mathbf{v}_s - \mathbf{v}_n)$ that lie in a plane perpendicular to the axis of rotation and is zero along it. The B term in Eq. (1.57) is responsible for the excess attenuation and the B' term produces a shift in the second-sound frequency.

At finite temperatures the Magnus force acting on a quantized vortex line is

$$\mathbf{f}_M = \rho_s \kappa \mathbf{s}' \times (\mathbf{v}_L - \mathbf{v}_{sl}), \tag{1.58}$$

where $\mathbf{v}_L$ and $\mathbf{v}_{sl}$ are the macroscopically averaged vortex-line velocity and the local superfluid velocity, respectively. The drag force acting on the vortex line due to the interaction with the normal fluid can be written as

$$\mathbf{f}_D = -\alpha \rho_s \kappa \mathbf{s}' \times \big[\mathbf{s}' \times (\mathbf{v}_n - \mathbf{v}_{sl})\big] - \alpha' \rho_s \kappa \mathbf{s}' \times (\mathbf{v}_n - \mathbf{v}_{sl}), \tag{1.59}$$

with α and α' being the temperature-dependent coefficients. If the vortex is regarded as a true line or filament and the inertia associated with its core is neglected, then the sum of the Magnus and the drag force, must add up to zero

$$\mathbf{f}_M + \mathbf{f}_D = \rho_s \kappa \mathbf{s}' \times \Big[(\mathbf{v}_L - \mathbf{v}_{sl}) - \alpha \mathbf{s}' \times (\mathbf{v}_n - \mathbf{v}_{sl}) - \alpha' (\mathbf{v}_n - \mathbf{v}_{sl})\Big] = 0, \tag{1.60}$$

because these being the only forces acting on the vortices. For Eq. (1.60) to be satisfied, the terms in the square bracket must either be in the direction of s' or equal to zero; the latter condition gives the following expression for the velocity of any point on the vortex line (see Fig. 1.8):

$$\mathbf{v}_L = \mathbf{v}_{sl} + \alpha \mathbf{s}' \times (\mathbf{v}_n - \mathbf{v}_{sl}) - \alpha' \mathbf{s}' \times \big[\mathbf{s}' \times (\mathbf{v}_n - \mathbf{v}_{sl})\big]. \tag{1.61}$$

In rapidly rotating helium II at finite temperatures, a uniform array of vortices is produced parallel to the rotation axis; thus, in the equilibrium the sum of the force per unit volume on the normal fluid plus the drag force per unit volume on the quantized vortices must vanish

$$\mathbf{F}_{ns} + n_0 \mathbf{f}_D = 0, \tag{1.62}$$

where $n_0 = \nabla \times \mathbf{v}_s / \kappa = 2\Omega/\kappa$ is the number of vortices per unit area. Hence, the mutual friction force is given by

$$\mathbf{F}_{ns} = \omega_s \rho_s \mathbf{s}' \times \big[\mathbf{s}' \times (\mathbf{v}_n - \mathbf{v}_s)\big] + \omega_s \rho_s \alpha' \mathbf{s}' \times (\mathbf{v}_n - \mathbf{v}_s), \tag{1.63}$$

where $\omega_s = \nabla \times \mathbf{v}_s$ is the superfluid vorticity and $\mathbf{v}_s = \mathbf{v}_{sl}$, assuming the vortex lines to be straight, so that the self-induced velocity is zero. If the vortex lines are curved, then the self-induced velocity $\mathbf{v}_{si}$ is not zero. If the curvature of the vortex lines is small enough, then the self-induced velocity $\mathbf{v}_{si} \approx (\kappa/4\pi R) \ln(L/a) \mathbf{s}' \times \mathbf{s}''$, where a is the size of the vortex core and L is some characteristic microscopic length whose choice depends on the details of the vortex configuration, e.g., the radius of curvature or the inter-vortex separation. We can rewrite $\mathbf{v}_{si} \approx \varpi (\mathbf{s}' \cdot \nabla) \mathbf{s}'$, where $\varpi = (\kappa/4\pi) \ln(L/a) = \varepsilon/\rho_s \kappa$ with ε being the kinetic energy per unit length of the

potential flow around a vortex core and $\mathrm{s}' \times \mathrm{s}'' = (\mathrm{s}' \cdot \nabla)\mathrm{s}'$ (for details we refer to [30, 35]). Furthermore, if the density of vortex lines is high, then they can be assumed to form a continuum. If we use

$$\mathbf{v}_{sl} = \mathbf{v}_s + \mathbf{v}_{si} = \mathbf{v}_s + \varpi(\mathbf{s}' \cdot \nabla)\mathbf{s}', \tag{1.64}$$

under such conditions in Eqs. (1.59) and (1.62) we obtain the following generalized form for the mutual friction force:

$$\begin{aligned} \mathbf{F}_{ns} = \omega_s \rho_s \mathbf{s}' \times \big[\mathbf{s}' \times (\mathbf{v}_n - \mathbf{v}_s)\big] + \omega_s \rho_s \alpha' \mathbf{s}' \times (\mathbf{v}_n - \mathbf{v}_s) \\ + \rho_s \omega_s \alpha \varpi \nabla \times \mathbf{s}' + \rho_s \omega_s \alpha' \varpi (\mathbf{s}' \cdot \nabla)\mathbf{s}', \end{aligned} \tag{1.65}$$

where the last two terms come from the self-induced velocity and in the third term the vector relation $(\mathrm{s}' \cdot \nabla)\mathrm{s}' = -\mathrm{s}' \times \nabla \mathrm{s}'$ has been used. Moreover, the self-induced velocity also introduces a term $\varpi\omega_{\mathrm{s}}(\mathrm{s}' \cdot \nabla)\mathrm{s}'$ in the equation of motion of v_s Eq. (1.38). Therefore, the generalized equations of motion for the superfluid and the normal fluid are given by

$$\rho_s \frac{D\mathbf{v}_s}{Dt} = -\frac{\rho_s}{\rho}\nabla p + \rho_s \sigma \nabla T + \frac{\rho_s \rho_n}{2\rho}\nabla(\mathbf{v}_n - \mathbf{v}_s)^2 + \rho_s \varpi \omega_{\mathrm{s}} (\mathbf{s}' \cdot \nabla)\mathbf{s}' - \mathbf{F}_{ns} \tag{1.66}$$

and

$$\rho_n \frac{D\mathbf{v}_n}{Dt} = -\frac{\rho_n}{\rho}\nabla p + \rho_n \sigma \nabla T - \frac{\rho_s \rho_n}{2\rho}\nabla(\mathbf{v}_n - \mathbf{v}_s)^2 + \mathbf{F}_{ns} + \nu_n \nabla^2 \mathbf{v}_n, \tag{1.67}$$

respectively. The Eqs. (1.65), (1.66) and (1.67) are together known as the Hall-Vinen-Bekarevich-Khalatnikov (HVBK) equations [30, 32].

Before proceeding further, we present a brief overview of the important experiments and their outcomes, performed in liquid ^{4}He and BECs of alkali atoms to study the properties of superfluid turbulence in Sec. 1.4.1; we do not discuss experiments done on ^{3}He-B, which exhibits superfluidity at extremely low temperatures. In Sec. 1.4.2 we give an outline of the important phenomenological models used in the field of superfluid turbulence. For details we refer to excellent reviews on the subject [3, 36–45].

1.4 Superfluid turbulence

Fluid turbulence invariably involves rotational motion; the same is true in superfluid turbulence, but there are important differences, between normal fluid turbulence and superfluid turbulence, which we briefly outline below. Superfluids can sustain rotational motion only through the formation of vortices, where the circulation Γ around a vortex is quantized in units of κ, i.e.,

$$\Gamma = \oint_C \mathbf{u}_s \cdot d\mathbf{l} = n\kappa, \tag{1.68}$$

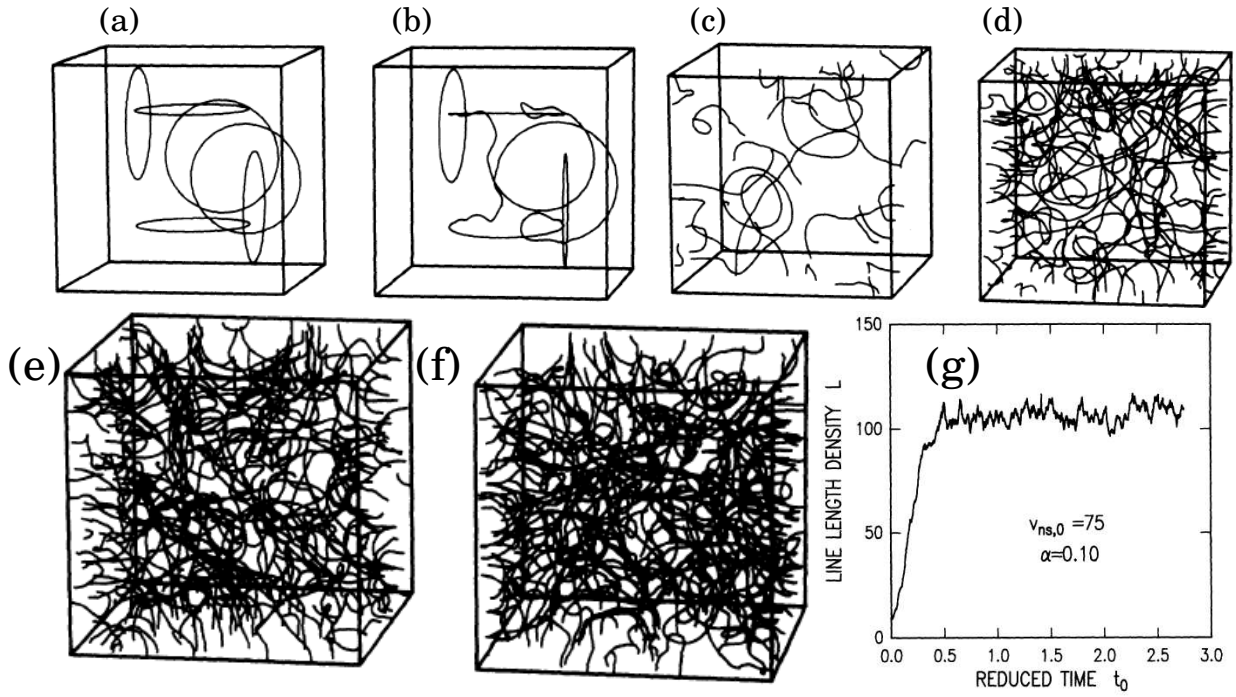

Figure 1.9: (a)-(f) Development of a vortex tangle in a channel starting with an initial configuration of six vortex rings under the influence of a pure superflow driving field; (g) time evolution of the vortex-line length per unit volume. Images (a)-(f) and (g) taken from Figs.1 and 2 in Ref. [50], respectively.

where $\kappa \equiv h/m$; $\mathbf{u}_s$ is the superfluid velocity, m the mass of the superfluid atom, and h the Planck's constant. A superfluid vortex is an example of a topological defect, unlike vortices in classical fluids, which can have any value of circulation. A superfluid vortex can not decay by the process of viscous diffusion of vorticity. Moreover, the vortices in superfluids are extremely thin, with a core size $\xi \simeq 10^{-10}\mathrm{m}$ in helium II, and are distinctly identifiable. Historically, Feynman had discussed the possibility that helium II flow can become turbulent by forming a dynamic, random, tangle of interacting quantized vortices [1], this was subsequently confirmed in experiments [46–49]. Superfluid turbulence is also referred to as *quantum turbulence* because of the presence of quantized vortices; and superfluid motion is influenced by quantum mechanical effects.

Most of the early understanding about the superfluid turbulence came from the thermal-counter-flow experiments in helium II, where at temperatures above $1\mathrm{K}$ homogeneous turbulence, in the form of a tangle of quantized vortices, was produced and sustained by the relative motion between the superfluid and the normal fluid [46–49]. The findings of the thermal counterflow experiments were reproduced in the pioneering simulation studies of K. W. Schwarz, who demonstrated the

existence of a dynamically self-sustaining random tangle of quantized vortex lines in helium II by including a mutual friction between the two fluids and requiring that two vortices undergo a reconnection event when they come very close together; he used a vortex-filament model (VFM) along with a local-induction approximation (see the subsection on VFM below), in which the vortices are treated as filaments with velocity at any point on it given by Eq. (1.61) [50–52]. Figure 1.9 shows the development of a vortex tangle in a channel starting with an initial configuration of six vortex rings under the influence of a pure superflow driving field; for details we refer the reader to Ref. [50]. In view of Fig. 1.9(f) we can introduce a length scale ℓ_v denoting the inter-vortex separation. The existence of a turbulent state in superfluids provides enough motivation to explore the similarities and differences with classical counterpart. Counterflow-turbulence experiments, do not have any classical analogue. Therefore, many experiments have been performed on helium II by adopting turbulence-production schemes similar to those used in turbulence experiments on classical fluids [40, 43]. These experiments have shown that, on length scales $\ell \gg \ell_v$, superfluid and classical-fluid turbulence are similar. This is supported by the following observations: (a) the existence of Kolmogorov-like regime with $E(k) \sim k^{-5/3}$ form in the inertial range [53–55]; (b) a classical decay of the vorticity $\omega \sim \kappa L$ as $\omega \sim t^{-3/2}$, independent of the turbulence-production mechanism, with an effective dissipation $\epsilon = \nu' \langle \kappa^2 L^2 \rangle$, where $L \sim \ell_v^{-2}$ is the vortex-line density, ν' the effective kinematic viscosity, and the quantity $\langle \kappa^2 L^2 \rangle$ is the measure of the effective mean square vorticity due to vortex lines [56–58]. In the superfluid-turbulence literature, the standard symbol for the vortex-line density is L. In our numerical simulations L denotes the box size. The meaning of this symbol should be clear from the context in which it is used. Hence, for length scales $\ell \gg \ell_v$ turbulence in superfluids is also referred to as the *quasi-classical turbulence*.

In helium II at finite temperatures the dissipation occurs because of the combined effects of (a) viscous processes in the normal fluid and (b) the mutual friction; the dissipation from the mutual friction is effective only at length scales $\ell \lesssim \ell_v$. The mechanism of energy dissipation at very low temperatures, in the limit $\rho_n \to 0$, is still an area of active research; at these temperatures the dissipation due to the mutual friction becomes ineffective and we have to look for other dissipative mechanisms. The reconnection of a pair of quantized vortices occurs naturally, when they are within a distance of the order of few core lengths, as first shown by Koplik and Levine in the nonlinear Schrödinger equation model for the superfluids [59]; this reconnection involves acoustic-wave emission [60, 61]; moreover, oscillatory motion of the vortex core can also radiate phonons, but these

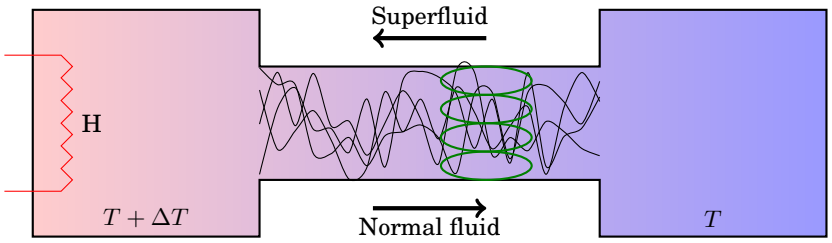

Figure 1.10: Schematic view of the experimental design to produce counterflow turbulence in helium II and its detection using the second sound attenuation method (green curve), for details see text 1.4.1.

two process together are insufficient to account for the decay of superfluid turbulence at low temperatures. According to the current understanding, during the reconnection events small-scale structures ("kinks") are formed on the vortices and Kelvin waves are excited on the vortex lines; the nonlinear coupling of these waves produces high-frequency oscillations that eventually radiate phonons into the surrounding fluid (for details we refer the reader to the references contained in the reviews Refs. [3, 36, 38, 62]).

1.4.1 Experiments

Thermal-counterflow turbulence

Experiments on counterflows of helium II were the earliest attempts to demonstrate the existence of a turbulent state in superfluids. The first detailed investigations of such counterflow turbulence were performed by W. F. Vinen, in an influential series of papers in 1957 [46–49]. Thermal counterflow is a special feature of superfluid flow, which relies on its two-fluid nature; Fig. 1.10 shows a schematic experimental set up, where counterflow can be generated by passing a direct current through a resistor located at the closed end of a channel open to a helium II bath at the opposite end. In helium II at finite temperatures heat and entropy are transported by the normal fluid; therefore, when heat is generated at the closed end of the channel the normal fluid flows from the heat source to the sink, which in the present case is the helium II bath. The superfluid flows in the opposite direction to conserve the total mass; this establishes a relative/counterflow velocity $\mathrm{v}_{ns} = \mathrm{v}_n - \mathrm{v}_s$ along the length of the channel. It was observed that at relatively small values of v_{ns}, the heat transport is affected by the resulting superfluid turbulent state in the form of a disordered tangle of vortex lines, whose intensity can be characterized by a vortex line density L, the total length of vortex lines in a

unit volume. Assuming an approximately homogeneous vortex line density, Vinen proposed the following phenomenological model for its time evolution, based on the dimensional arguments:

$$\frac{dL}{dt} = \frac{\rho_n B}{2\rho}\chi_1 v_{ns} - \frac{\kappa}{2\pi}\chi_2 L^2, \tag{1.69}$$

where χ_1 and χ_2 are undetermined dimensionless constants. The first term in Eq. 1.69 describes the production and the growth of the vortex tangle and the second term its decay. In the steady state, the Eq. 1.69 predicts that

$$L = \frac{\pi\rho_n B\chi_1}{\rho\kappa\chi_2} v_{ns}^2. \tag{1.70}$$

The quantity L is adequate to describe most of the phenomena observed in steady-state counterflow turbulence and the length scale associated with it, $\ell_v = 1/\sqrt{L}$, is the average distance between the quantized vortices. Steady-state counterflow turbulence has no analogues in classical-fluid flows, except its relatively unexplored similarity with the turbulent thermal convection; turbulent heat transport in both displays a power-law dependence on the temperature difference with an exponent close to $1/3$ [58].

Superfluid turbulence driven by two counter-rotating disks

Maurer and Tabeling [53] investigated turbulent flow in liquid helium confined in a cylinder driven by two counter-rotating disks with blades, in a range of temperatures between 1.4 and $2.3\mathrm{K}$; thus, the measurements were done in both the superfluid and the classical-turbulence regimes. The Fig. 1.11(a) shows a sketch of the experimental set up. In the experiment the local pressure fluctuations were measured by using a small, total-head pressure tube in the region with non-zero axial mean flow; the pressure fluctuations at the total-head tube are due to the velocity fluctuations, so the measurements can be used to construct the energy spectra, as shown in Fig. 1.11(b) for three different temperatures: (a) at $2.3\mathrm{K}$, above the superfluid transition temperature T_λ, (b) at $2.08\mathrm{K}$, just below T_λ, and (c) at $1.4\mathrm{K}$, below T_λ with large superfluid fraction. The experiment showed that: (1) the form of the energy spectra are similar both above and below T_λ with a Kolmogorov-like scaling regime, revealing a similarity between ordinary and superfluid turbulence; (2) the cascade processes are ubiquitous, independent of the energy dissipation mechanism at small scales, as different dissipation mechanisms dominate at temperatures above T_λ and much below it; (3) the inertial range-intermittency is present even at temperatures below T_λ.

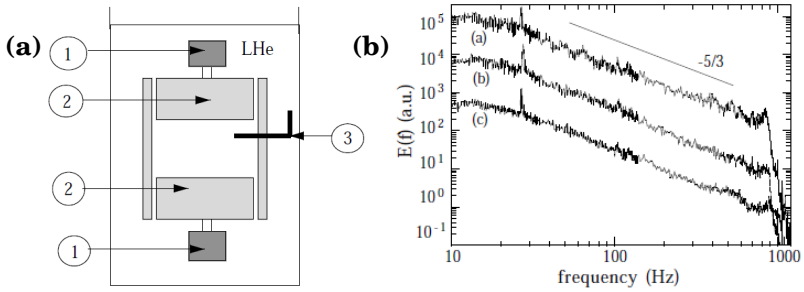

Figure 1.11: Superfluid turbulence driven by two counter-rotating disks: (a) sketch of the experimental set up; 1: DC Motor, 2: propeller, 3: probe; (b) energy spectra obtained in the same conditions, but at different temperatures: (a) $2.3\mathrm{K}$; (b) $2.08\mathrm{K}$; (c) $1.4\mathrm{K}$. The spectra have been shifted vertically so as to make their representation clear. Images in (a) and (b) are from Figs.1 and 2 in Ref. [53], respectively.

Grid turbulence in helium II

In classical fluids grid experiments have been used to study the properties of both the fully developed and the decaying homogeneous and isotropic turbulence produced behind the grid. Figure 1.12(A) shows a sketch of the experimental set up used by R. J. Donnolly and his collaborators to study decaying, homogeneous turbulence produced in a stationary sample of helium II by towing a grid [63]. To probe the vortex line density, L, produced in the turbulent state, the second-sound-attenuation technique was used. Superfluid vorticity was defined in terms of the vortex line density as $\omega_s(t) = \kappa L$. The experiments showed that there is no appreciable difference in the decay of the $\omega_s(t)$ curves, obtained over a temperature range of 1.4 to $2.15\mathrm{K}$, which corresponds to an order-of-magnitude difference in the normal fluid fraction ρ_n/ρ; after the saturation of the energy-containing length scale at the size of the channel, the superfluid vorticity decays as $\omega_s(t) \propto t^{-3/2}$ (see Fig. 1.12(B)) [56]. Thus, the study of the grid-generated decaying helium II turbulence experiments can used to understand classical-fluid turbulence.

Flow visualization around a cylinder in counteflow helium II

Visualization of the superfluid flow in helium II is a challenging problem, but it can yield direct evidence about the existence of turbulent structures. Figure 1.13 shows the use of the particle-image-velocimetry (PIV) technique to visualize the counterflow in helium II over a circular cylinder [64]. Counterflow was generated in a one-dimensional rectangular channel ($200-\mathrm{mm}$ long, cross-section $38.9\times19.5-\mathrm{mm}^2$), which was immersed in a constant-temperature helium II bath; the flow was seeded with polymer particles of diameter $1.7\mu\mathrm{m}$ and specific gravity equal to 1.1.

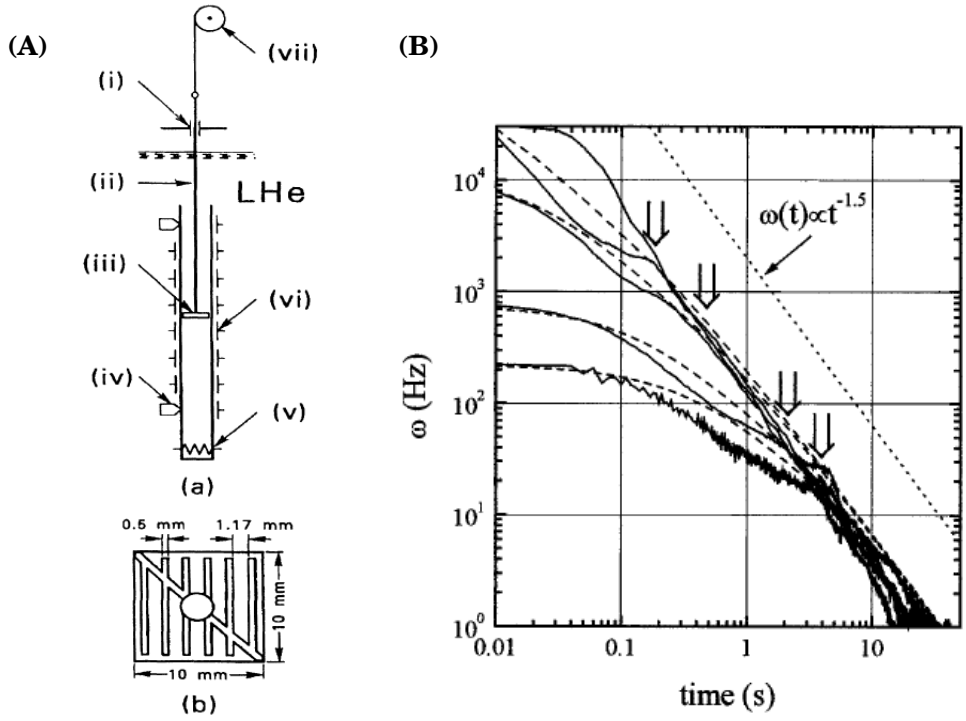

Figure 1.12: Grid turbulence in helium II: (A) (a) Lay out of the apparatus to study grid turbulence. (i) Vacuum seal, (ii) $5/16$ rod, (iii) grid, (iv) germanium thermometer, (v) counterflow heater, (vi) second sound transducer pair, and (vii) stepper motor. (b) Detail of grid construction. Our caption follows the caption of Fig.1 in Ref. [63]. (B) Decay of vorticity for grid velocities of 5, 10, 50, 100, and 200cms (top curve) at 1.5K. Our caption follows the caption of Fig.2 in Ref. [56].

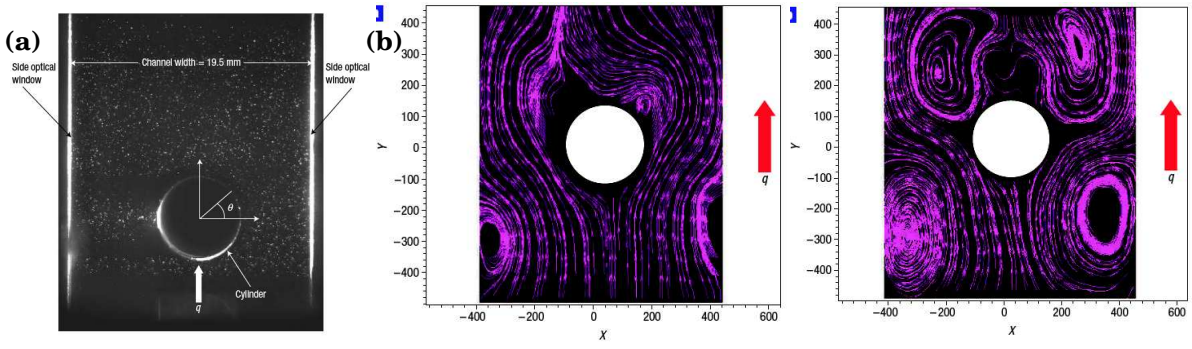

Figure 1.13: Flow visualization around a cylinder in counteflow helium II. (a) Raw data produced by the PIV experiment, showing suspended particles in the helium II channel at $T = 2.03$K; (b) and (c) velocity streamlines for particle motion at $T = 1.6$K, $q = 4\text{kWm}^{-2}$ and $T = 2.03$K, $q = 11.2\text{kWm}^{-2}$, respectively. Images (a) and (b) are from Figs.1 and 2 in Ref. [64], respectively.

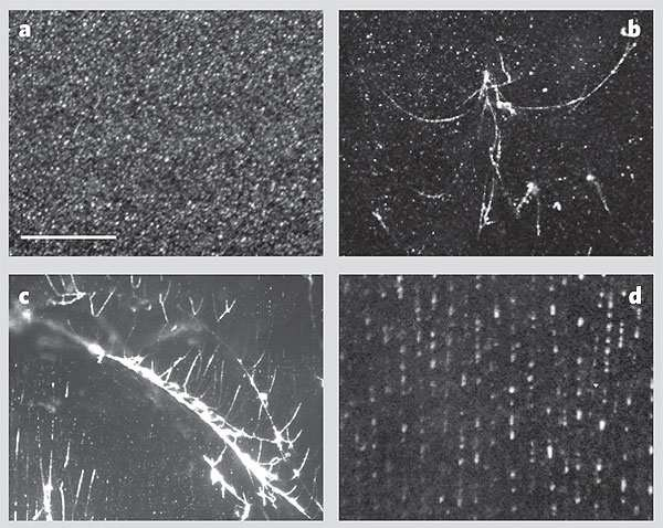

Figure 1.14: Quantized vortex cores in liquid helium. (a)-(d), Images of particles (light against dark background) obtained with a camera and $105 - \mathrm{mm}$ lens under different conditions: (a), just above the transition temperature, when they are uniformly dispersed; (b), (c), on branching filaments at tens of millikelvin below the transition temperature; and (d), regrouping along vertical lines for steady rotation about the vertical axis. In (b) and (c), the particles on lines are evenly separated in small regions. Scale bar, $1\mathrm{mm}$. Our caption follows the caption of Fig.1 in Ref. [65].

As typical in counterflow channels, heat flux was applied at the closed end and the top end was open to the helium II bath. A transparent cylinder of diameter $6.35 - \mathrm{mm}$ was placed inside the channel spanning the full width and orthogonal to the counterflow (for details see Ref. [64]). The experiment demonstrated the existence of large turbulent structures in the counterflow around a cylinder; moreover, in contrast to the classical-fluid case in which macroscopic eddies are present downstream of the cylinder, the particle motion driven by the counterflow in helium II showed such structures, both downstream and in front of the cylinder, thus indicating that both the fluids may be undergoing a kind of flow separation while passing over the cylinder.

Visualization of quantized vortices

Superfluids can sustain rotational motion only by forming quantized vortices. Visualization of these vortices can help to understand the geometries and the interactions between them, which is of prime importance in the studies of superfluid turbulence. In a series of experiments Bewley et al. have used small particles of solid hydrogen to image the cores of quantized vortices in their three-dimensional environment of helium II [65, 66]. They generated smaller hydrogen particles by injecting a premixed gaseous solution of hydrogen, greatly diluted with helium,

into liquid helium I; the suspension was then cooled to below the superfluid transition temperature. The subsequent visualization procedure showed that apart from tracing the fluid motion, the particles get trapped on slender filaments, which many a times are several millimetres long (see Fig. 1.14). The experiments have conclusively shown that: (1) the vortex filaments appear only in the superfluid phase of helium, upon rotation of the vessel containing helium; (2) the particles arrange themselves along the uniformly spaced vortex filaments; (3) the number density of lines per unit area normal to the axis of rotation, for a series of rotation rates, is consistent with Feynmans rule, which predicts about $2,000\Omega$ lines per cm^2, where Ω is the angular velocity of the vessel in radians per second. In subsequent experiments they were able to visualize directly the reconnection processes [66] and emission of Kelvin waves [67].

Helium wind-tunnel experiments

Homogeneous and isotropic turbulent flows were generated in liquid helium by continuous driving by using propellers (see Refs. [54,55,69,70]), which allowed better statistical convergence and improved stationarity than measurements in non-stationary flows. In Fig. 1.15(a) we show the schematic diagram of the TOUPIE wind tunnel used in the study of Ref. [55]. The wind tunnel was operated down to $1.56\mathrm{K}$ and up to Taylor-microscale-based Reynold's number $R_\lambda = 1640$. Local-velocity measurements were made in the far wake of a disc (see Fig. 1.15(a)). The experiments showed the following (see Figs. 1.15 (b)-(d)): (i) the Kolmogorov $4/5-$law of classical turbulence remains valid in superfluid turbulence, at least at the largest inertial scales; (ii) energy spectra exhibit a Kolmogorov scaling regime $E(K) \sim k^{-5/3}$ both above and below the superfluid transition temperature T_λ; (iii) the velocity-component PDFs are nearly Gaussian below T_λ.

Turbulence in three-dimensional BECs

Bose-Einstein condensates (BECs) of bosonic atoms in traps can be prepared in a controlled manner by tuning parameters like the interactions between the atoms, atomic density, and trapping configurations. Trapped BECs exhibit superfluidity, thus they provide us a means of studying superfluid turbulence. Dynamics of quantized vortices is an area of active study in such systems, in which it is also possible to visualize these vortices by optical means, upon the expansion of the cold-atom system after it has been released from the trap. Recently, a vortex tangle was created in a magnetically trapped BEC of ^{87}Rb atoms by the application of an external perturbation in the form of an oscillating magnetic field [71]. Figure 1.16(a)

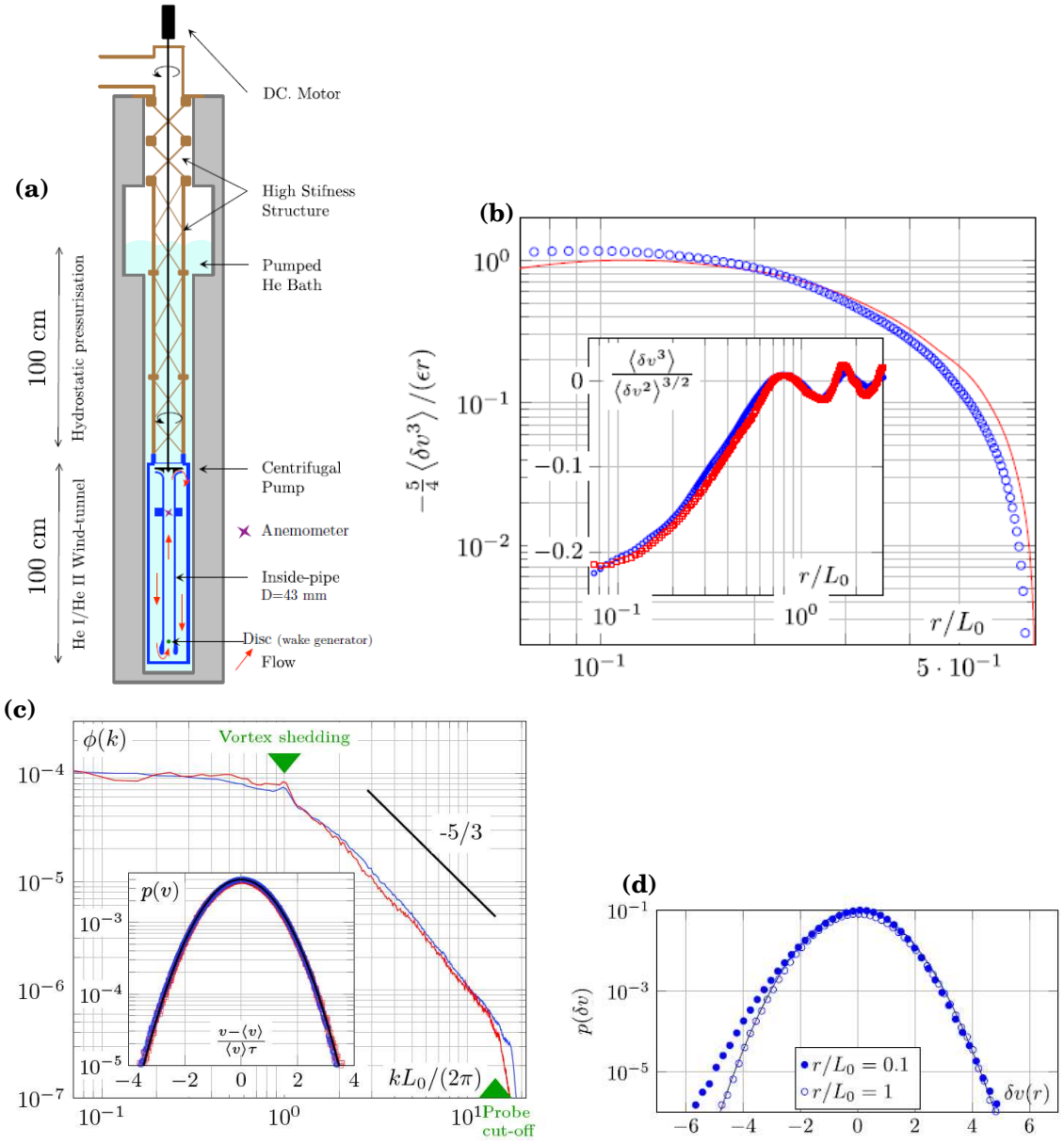

Figure 1.15: Helium wind tunnel experiments. (a) Wind tunnel (in blue) in the cryostat (in grey) (Figure taken from Ref. [68]). (b) Experimental third-order velocity structure function compensated by the $4/5-$law obtained in superfluid helium at T =1.56K (blue circles) and in classical liquid helium at T =2.2K (red squares). Inset: skewness of the distribution of longitudinal velocity increments (same color code). The smallest abscissa $r/L_0 = 710^2$ corresponds to the probe cut-off. The oscillation at large scales is related to the frequency of the vortex shedding (Our caption follows caption of Fig.4 in Ref. [55]). (c) Experimental 1D velocity power spectrum above and below the superfluid transition. Red line: $T = 2.2\text{K} > T_\lambda$ at $R_\lambda \approx 1640$. Blue line: $T = 1.56\text{K} < T_\lambda$. Inset: velocity probability density distribution above and below the superfluid transition. Black line: Gaussian distribution (Our caption follows caption of Fig.2 in Ref. [55]). (d) Experimental histogram of the longitudinal velocity increments at large and intermediate scales in a superfluid turbulent flow ($T = 1.56\text{K}$). Solid black line: Gaussian PDF (Our caption follows caption of Fig.3 in Ref. [55]).

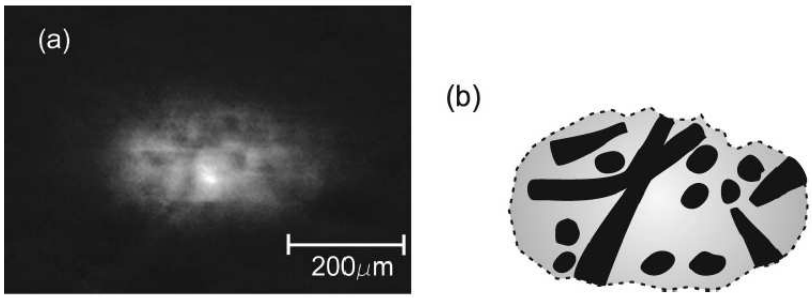

Figure 1.16: Turbulence in a 3D BEC. (a) Atomic optical density after 15 ms of free expansion showing vortex structures spread all around the cloud resembling a vortex tangle, and (b) schematic diagram showing the inferred distribution of vortices as obtained from the image shown in (a). Our caption follows the caption of Fig. 2 in Ref. [71].

shows the vortex structures in the atomic optical density and Fig. 1.16(b) shows the schematic distribution of the vortices in (a). Experiments have shown that the turbulent regime, with tangled vortices, changes the hydrodynamic behaviour of the atomic cloud, where the aspect-ratio (ratio of axial and radial widths) inversion is suppressed during the free-expansion of the cloud.

Turbulence in two-dimensional BEC

In BEC experiments the geometry and the dimensionality of the confining potentials can be varied in a controlled fashion to create two-dimensional (2D) condensates; the generation of turbulence in such condensates is an exciting possibility, which can aid in the understanding of 2D superfluid turbulence (also referred to as quantum turbulence). Neely et al. [72] generated a two-dimensional quantum turbulence (2DQT) in highly oblate BECs, produced by utilizing optical and magnetic confinement. BECs of up to $\sim 2 \times 10^6$ ^{87}Rb atoms were produced in a harmonic potential with radial (r) and axial (z) trapping frequencies $(\omega_r/2\pi, \omega_z/2\pi) = (8, 90)$; 2D vortex dynamics was achieved by the tight confinement, along the $z-$axis, which suppressed the bending and the tilting motion of the vortices. Moreover, the trap was made annular by passing a blue-detuned Gaussian laser beam along the trap axis. A large number of vortices were nucleated by moving the harmonic trap center, but not the central barrier, with the help of a magnetic bias field; the vortices so produced were distributed in a disordered fashion, which was identified with a 2D turbulent state similar to the vortex-tangle in 3D superfluid turbulence. Figure 1.17 shows the experimental procedure and the observed vortex distribution. The BEC was retained in the annular trap for a varying period of time allowing the turbulence to decay, before ramping off the central barrier and releasing the atoms

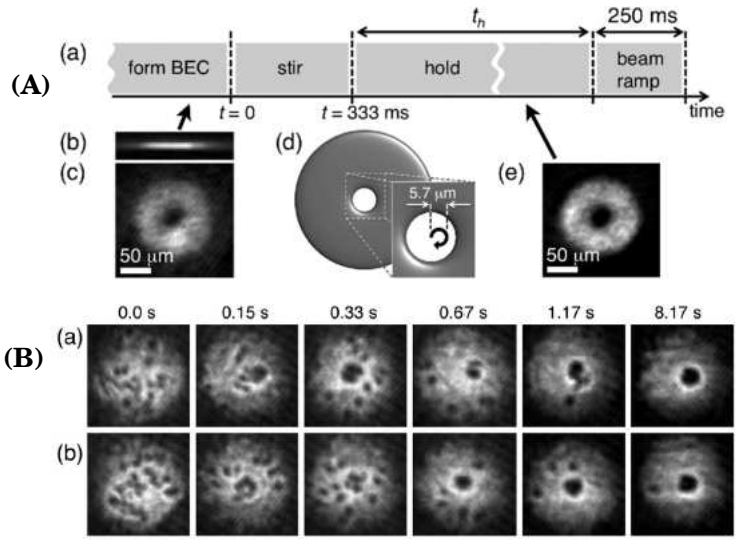

Figure 1.17: Turbulence in a 2D BEC. (A): (a) Timing sequence. (b,c) In situ BEC column-density images prior to the stir, shown (b) in the plane of 2D trapping and (c) along the z axis. Lighter shades indicate larger column densities, as in subsequent data. (d) Stirring illustration. The black arrow shows the trap center trajectory relative to the larger fluid-free region created by the laser barrier. (e) In situ BEC image 10 s after stirring. Our caption follows the caption of Fig. 1 in Ref. [72]. (B): (a,b) $200-\mu m$-square experimental column-density images acquired at the hold times t_h indicated. BECs undergo $\sim 50-ms$ ballistic expansion immediately after barrier removal. Each image is acquired from a separate experimental run. Our caption follows the caption of Fig. 2 (a,b) in Ref. [72]

from the trap to perform the absorption imaging of vortices on the expanding cloud. In the experiments it was observed that the disordered vortex distribution of 2DQT, following small-scale forcing, can be robust against immediate vortex-antivortex annihilation and decay into large-scale flow as manifested by a persistent current, which was interpreted as an experimental signature of the energy transport from small to large length scales during the 2DQT forcing and decay.

1.4.2 Phenomenological Models

Three important phenomenological approaches have been used to investigate the properties of turbulence in superfluids. Superfluidity occurs in a wide variety of system e.g., ^{4}He II, ^{3}He-B, BECs of bosonic atoms in traps, neutron stars [2] etc.; at the moment there is no single theory which encompasses all the systems and is capable of predicting all dynamical effects across all length scales. Therefore, we have to rely on phenomenological models, which are at times better suited for one type of problem than for others. In our overview below, we focus on the concepts needed for this thesis; for a more comprehensive introduction of the phenomenological models popularly used in the study of superfluid turbulence we refer the reader to the following excellent reviews [36, 40, 43–45].

Gross-Pitaevskii description

At finite temperatures, below the Bose-Einstein transition temperature T_c, the condensate coexists with the thermally excited particles, which form the thermal cloud. In the $T \to 0$ limit, the effect of the thermal cloud can be neglected and the hydrodynamic description of a weakly interacting Bose gas is given by the Gross-Pitaevskii equation (GPE)

$$i\hbar\frac{\partial\psi(\mathbf{x},t)}{\partial t} = -\frac{\hbar^2}{2m}\nabla^2\psi(\mathbf{x},t) + g|\psi|^2\psi(\mathbf{x},t), \tag{1.71}$$

where $\psi(\mathbf{x},t)$ is a complex, classical field and g is the effective interaction strength [73, 74]. The Eq. (1.71) is a nonlinear Schrödinger equation and it can be derived using the following action principle with a Lagrangian $\mathcal{L}$:

$$\delta\int_{t1}^{t2}\mathcal{L}dt = \delta\int_{t1}^{t2}\left[\int d^3x\frac{i\hbar}{2}\left(\psi^*\frac{\partial\psi}{\partial t} - \psi\frac{\partial\psi^*}{\partial t}\right) - H\right]dt = 0; \tag{1.72}$$

where H is the Hamiltonian of the system

$$H = \int d^3x\big(\frac{\hbar^2}{2m}|\nabla\psi|^2 + \frac{g}{2}|\psi|^4\big). \tag{1.73}$$

The dynamical evolution of the GP Eq. (1.71), conserves the total energy H (Eq. (1.73)), the total number of particles

$$N = \int |\psi|^2 d^3x, \tag{1.74}$$

and the momentum

$$\mathbf{P} = \int \frac{i\hbar}{2}(\psi\nabla\psi^* - \psi^*\nabla\psi)d^3x. \tag{1.75}$$

We can express the GP Eq. (1.71) in terms of hydrodynamical variables by the use of the Madelung transformation

$$\psi(\mathbf{x},t) = \sqrt{\frac{\rho(\mathbf{x},t)}{m}}\exp[i\frac{m}{\hbar}\phi(\mathbf{x},t)], \tag{1.76}$$

where $\rho(\mathbf{x},t)$ is the particle density and $\phi(\mathbf{x},t)$ the phase of ψ, which also acts as a velocity potential. Therefore, we rewrite the Eq. (1.71) as

$$\frac{\partial\rho}{\partial t} + \nabla\cdot(\rho\nabla\phi) = 0; \tag{1.77}$$

and

$$\frac{\partial\phi}{\partial t} + \frac{1}{2}(\nabla\phi)^2 + \frac{g}{m^2}\rho - \frac{\hbar^2}{2m^2}\frac{\nabla^2\sqrt{\rho}}{\sqrt{\rho}} = 0; \tag{1.78}$$

Eq. (1.77) is the continuity equation and Eq. (1.78) is the equation of motion for the field ϕ. The condensate velocity is

$$\mathbf{u}(\mathbf{x},t) = \nabla\phi(\mathbf{x},t), \tag{1.79}$$

which shows that the condensate motion is irrotational in the absence of any singularities in the field ϕ:

$$\nabla\times\mathbf{u} = \nabla\times\nabla\phi = 0. \tag{1.80}$$

We can find the equation of motion for the velocity $\mathbf{u}$ by taking the gradient of Eq. (1.78) as

$$\frac{\partial\mathbf{u}}{\partial t} = -\nabla\Big(\tilde{\mu} + \frac{1}{2}mu^2\Big), \tag{1.81}$$

where

$$\tilde{\mu} = \frac{g}{m^2}\rho - \frac{\hbar^2}{2m^2}\frac{\nabla^2\sqrt{\rho}}{\sqrt{\rho}}. \tag{1.82}$$

The last term in the Eq. (1.82) is referred to as the *quantum-pressure term*; it arises due to the spatial variations in the magnitude of the condensate wave function.

Healing length: If a condensate is confined in a box with infinitely hard walls, then at the walls the condensate density must go to zero, and in the interior it should be equal to its bulk value ρ_0. The distance over which the condensate density recovers its bulk value is referred to as the *healing length*, which can be estimated by the competition between the interaction energy term $g\rho_0$ and the kinetic

energy term in the GP Eq. (1.71). If ξ is the spatial scale of variation, then the kinetic energy per particle is of order $\hbar^2/2m\xi^2$; by equating it to the interaction term we get $\xi = \sqrt{\hbar^2/2g\rho_0}$. ξ is also the length scale associated with the vortex core.

Elementary excitations: Linearization of the Eqs. (1.77), (1.81), and (1.82) around the equilibrium state with $\rho = \rho_0 + \delta\rho$ and $\tilde{\mu} = \tilde{\mu}_0 + \delta\tilde{\mu}$, where the fluctuations in density $\delta\rho$ and velocity are treated to be small gives the following equation of motion:

$$\frac{\partial^2 \delta\rho}{\partial t^2} = \nabla \cdot \Big(\rho_0 \nabla \delta\tilde{\mu}\Big), \tag{1.83}$$

where

$$\delta\tilde{\mu} = \frac{g}{m^2}\delta\rho - \frac{\hbar^2}{4m^2}\frac{\nabla^2\delta\rho}{\rho_0}. \tag{1.84}$$

For a uniform system, if we consider travelling-wave solutions, proportional to $\exp(i\mathbf{k}\cdot\mathbf{r} - i\omega t)$, where k is the wave vector and ω the frequency, then Eq. (1.83) leads to the Bogoliubov dispersion relation

$$\omega(k) = \Big[\frac{g\rho_0 k^2}{m^2} + \frac{\hbar^2 k^4}{4m^2}\Big]^{1/2}. \tag{1.85}$$

For small wave numbers k the spectrum $\omega(k) \sim ck$ is sound-like, with sound velocity $c = \sqrt{g\rho_0/m^2}$; for large k the spectrum is quadratic and a free-particle behavior is observed; this crossover occurs when the quantum pressure term dominates over the usual pressure at around $k \sim \xi^{-1}$. Thus, on length scales larger than ξ, we observe collective motion, whereas, on smaller length scales, excitations behave as free particles.

Finite temperatures: The discussion that follows, is not comprehensive; we present material that is directly needed for this thesis. The inclusion of finite-temperature effects into the condensate dynamics, in the presence of the thermal cloud, is a challenging problem and it is still an area of active research; for a comprehensive review we refer the reader to Refs. [44, 75–78]. If $n(k) = \langle|\hat{\psi}(k)|^2\rangle \gg 1$, where $\hat{\psi}$ denotes the Fourier transform of ψ, then quantum fluctuations can be neglected in comparison to classical thermal fluctuations, and these modes may be represented by a coherent wave function. This approximation becomes poor for high-energy modes, whose occupation number is low at equilibrium. For even higher-energy modes, the criterion $n(k) \gg 1$ does not hold; for such modes a kinetic-equation-based approach is appropriate. The GP Eq. (1.71) and its variants have been used to describe the formation of a BEC and its various stages of evolution, starting with different initial configurations for weakly interacting Bose gases [79–85].

In this thesis, we use the truncated Gross-Pitaevskii equation (TGPE) [86], in which we truncate the Fourier transform of the wave function for $|\mathbf{k}| > k_{\max}$, so

that only highly occupied modes are retained. The spatiotemporal evolution of the complex, classical, wave function $\psi(\mathbf{x},t)$ describing the superfluid is given by

$$i\hbar\frac{\partial\psi(\mathbf{x},t)}{\partial t}=\mathcal{P}_G\left[\Big(-\frac{\hbar^2}{2m}\nabla^2+g\mathcal{P}_G[|\psi|^2]\Big)\psi(\mathbf{x},t)\right], \tag{1.86}$$

where g is the effective interaction strength, $\mathcal{P}_G$ the Galerkin projector, i.e., $\mathcal{P}_G[\hat{\psi}(k)]=\theta(k_{\max}-k)\hat{\psi}(k)$, with $\hat{\psi}$ the spatial Fourier transform of ψ and $\theta(\cdot)$ the Heaviside function. The Eq. (1.86) exactly conserves the energy

$$H=\int d\mathbf{x}\Big[\frac{\hbar^2}{2m}|\nabla\psi|^2+\frac{g}{2}\big[\mathcal{P}_G[|\psi|^2]\big]^2\Big], \tag{1.87}$$

and the number of particles

$$N=\int d\mathbf{x}|\psi|^2. \tag{1.88}$$

By using Fourier pseudospectral methods, we can show that the momentum

$$\mathbf{P}=\int d\mathbf{x}\frac{i\hbar}{2}(\psi\nabla\psi^*-\psi^*\nabla\psi) \tag{1.89}$$

is also conserved, provided the dealiasing is performed by using the two-thirds rule ($k_{\max}=2/3\times N_c/2$ at resolution N_c).

The GP-equation-based approach is an useful model of superfluid turbulence at low temperatures for weakly interacting Bose gases and applies only qualitatively to helium II, where the interactions are strong. This approach can be used to describe phenomena at the length scale ξ of the vortex core because it accounts for the existence of vortices, their finite core size, and nucleation [30]. The GP equation allows for the effects of compressibility, so it is able to describe the reconnection between vortices in a self-consistent manner [59]; these are associated with the emission of sound waves [60,61] and the generation of Kelvin-waves on the vortices.

Vortex-filament phenomenology

Quantized vortices in helium II can be regarded as *filament* in 3D, because the vortex core size $a\simeq 10^{-10}\mathrm{m}$; these filaments, can be treated as classical object in many physically relevant situations in superfluid flows, where the core size a is negligible in comparison to characteristic lengths in the hydrodynamic description of the flow, e.g, the mean inter-vortex separation ℓ_v or the radius of curvature R of the filaments. Therefore, while describing the large-scale motion of the superfluid, we distinguish between the individual filaments, but ignore the details of the vortex core. In such a description, each filament, with a fixed circulation κ, is represented by a curve in the parametric form $\mathrm{s}=\mathrm{s}(\zeta,t)$, where ζ is the arc length along the

filament. The superfluid flow outside the vortex-core region obeys Eulerian dynamics, and it is incompressible and irrotational. At $T = 0$ and in the absence of any external force on the vortex core, the filament moves with the superfluid; the velocity produced at a distance r from the core in an unbounded flow is given by the Biot-Savart expression [52]

$$\mathbf{v}_{\mathbf{s},\omega}(\mathbf{r},t) = \frac{\kappa}{4\pi}\int_{\mathcal{L}} \frac{(\mathbf{s}_1 - \mathbf{r}) \times d\mathbf{s}_1}{|\mathbf{s}_1 - \mathbf{r}|^3}, \tag{1.90}$$

where the integral is taken along the vortex filament $\mathcal{L}$ and s_1 refers to a point on the filament. The integral in Eq. (1.90) diverges as r approaches the point s_1 on the vortex filament; to avoid this divergence, the contribution to the velocity is divided into local and nonlocal parts [52].

The instantaneous local configuration of the vortex filament at point s, represented by a parametrised curve $\mathrm{s}(\zeta,t)$, can be characterized by a triad of mutually perpendicular vectors $\mathrm{s}'(= d\mathrm{s}/d\zeta \sim 1)$, $\mathrm{s}''(= d^2\mathrm{s}/d^2\zeta \sim R^{-1})$, and $\mathrm{s}' \times \mathrm{s}''(\sim R^{-1})$, which are directed along the local tangent (in turn, it points in the direction of the circulation), the principal normal, and the binormal, respectively (see Fig. 1.8). The local induced velocity at a point in the fluid points approximately in the direction of $\mathrm{s}' \times \mathrm{s}''$. In the absence of any friction force, the instantaneous velocity of any point on the vortex filament in an unbounded fluid is given by the expression [52]:

$$\mathbf{v}_L = \dot{\mathbf{s}_0} = \mathbf{v}_{s,a}(\mathbf{s}) + \frac{\kappa}{4\pi}\mathbf{s}' \times \mathbf{s}'' \ln\left(\frac{2(l_+ l_-)^{1/2}}{e^{1/4}a}\right) + \frac{\kappa}{4\pi}\int_{\mathcal{L}}' \frac{(\mathbf{s}_1 - \mathbf{s}) \times d\mathbf{s}_1}{|\mathbf{s}_1 - \mathbf{s}|^3}, \tag{1.91}$$

where $\mathbf{v}_{s,a}$ is the background superfluid velocity because of applied fields, a is the phenomenological cut-off parameter that models the core of the vortex, l_+ and l_- are the lengths of filament portions around the point s that are used in the calculation of the local contribution to the velocity at s, and the prime on the integral denotes that the regions of the vortex filament contributing to the local part of the velocity should be omitted. At finite temperatures, the gas of the elementary excitations, which constitutes the normal component, are scattered by the quantized vortices present in the superfluid. This, leads to the exchange of momentum between the two components; coupled with this, the drift velocity of the normal fluid relative to the superfluid $\mathbf{v}_n - \mathbf{v}_s$, results in a frictional force f that acts on the fluid in the neighbourhood of the core of the quantized vortex; $\mathbf{v}_n$ is the average velocity of the excitation gas constituting the normal fluid. Therefore, the modified expression for the instantaneous velocity of any point on the vortex filament at finite temperatures is given by Eq. (1.61).

In the vortex filament model (VFM) the normal-fluid velocity $\mathbf{v}_n$, which enters in Eq. (1.61), should be solved for self-consistently to allow for a two-way coupling

between the two fluids [87, 88]. However, a numerical implementation of such a scheme is computationally very expensive, thereby reducing the usefulness of the VFM. Therefore, the majority of studies that use the VFM assume an imposed normal-fluid velocity, which ignores the influence of the superfluid on the normal fluid. The major drawback of the VFM is that it can not model a vortex-reconnection event in a self-consistent manner. Such reconnections, have to be introduced by hand when two segments of vortical filaments come close to each other. The VFM does not support the generation of sound waves, which are allowed in the GPE; thus it can not model dissipation at very low temperatures, where the mutual friction is ineffective. Despite the above-mentioned weaknesses, the VFM has been successfully used to study counterflow turbulence [50, 89], quasi-classical superfluid tubulence [90–93], both forced and decaying, and the formation of coherent structures under rotation [45].

Hall-Vinen-Bekharavich-Khalatnikov (HVBK) two-fluid model

The two-fluid model of superfluidity, proposed independently by Tisza [27, 28] and Landau [29], lacked a vortex-dynamics description, as it came into existence before the discovery of quantized vortices in helium II. Therefore, it was modified to include the effects of vortex dynamics; and the result was a generalized two-fluid HVBK model; in Sec. 1.3.1 we have given a heuristic set of arguments to arrive at the equations of motion for the superfluid and normal fluid velocity fields Eq. (1.66) and (1.67), respectively. In the two-fluid HVBK model, we ignore the distinction between the individual quantized vortices present in helium II and deal with a coarse-grained model, the vortices form a continuum over any patch of the superfluid. Thus, if ℓ_v is the mean inter-vortex separation, then the HVBK model is valid only on length scales $\ell \gg \ell_v$. The HVBK prescription of coarse graining the superfluid vorticity field is most suited for the cases where the vortex lines are locally aligned, e.g., in laminar flows, where it is possible to define a macroscopic vorticity field ω_s by averaging out the length scales of the order of ℓ_v and smaller. The HVBK Eq. (1.66) and (1.67) have also given results in agreement with Taylor-Couette flows observed in helium II [94, 95].

The use of the HVBK, two-fluid model can be extended to provide a phenomenological description of superfluid turbulence in helium II, where the turbulent state is regarded as a random tangle of vortex lines. This HVBK treatment of superfluid turbulence can suffer from the drawback of underestimating (a) the superfluid vorticity ω_s and (b) the mutual-friction-induced interaction between normal and superfluid components of the fluid. This short-coming of the model is reme-

died, to some extent, in the case of fully developed turbulence, where the continuum approximation for the vorticity field is improved because of the presence of an extremely large number of vortex lines. Therefore, the two-fluid HVBK model, can provide a good description of the turbulent motion for length scales larger than ℓ_v. The HVBK equations have been used in large-eddy simulations [96], eddy damped quasi-normal Markovian simulations [97], and direct numerical simulations of the quasi-classical turbulence observed in helium II [98–100]. Recently, shell-model versions of the HVBK model have been used to study the statistical properties of 3D superfluid turbulence [101–103].

1.5 Outline of chapters

In this thesis we study a variety of problems in superfluid turbulence, principally in two dimensions. A summary of the main results of our studies is given below; we indicate the Chapters in which we present these.

In Chapter 2, we present a systematic, direct numerical simulation of the two-dimensional, Fourier-truncated, Gross-Pitaevskii equation to study the turbulent evolutions of its solutions for a variety of initial conditions and a wide range of parameters. We find that the time evolution of this system can be classified into four regimes with qualitatively different statistical properties. First, there are transients that depend on the initial conditions. In the second regime, power- law scaling regions, in the energy and the occupation-number spectra, appear and start to develop; the exponents of these power laws and the extents of the scaling regions change with time and depend on the initial condition. In the third regime, the spectra drop rapidly for modes with wave numbers $k > k_c$ and partial thermalization takes place for modes with $k < k_c$; the self-truncation wave number $k_c(t)$ depends on the initial conditions and it grows either as a power of t or as $\log t$. Finally, in the fourth regime, complete thermalization is achieved and, if we account for finite-size effects carefully, correlation functions and spectra are consistent with their nontrivial Berezinskii-Kosterlitz-Thouless forms. Our work is a natural generalization of recent studies of thermalization in the Euler and other hydrodynamical equations; it combines ideas from fluid dynamics and turbulence, on the one hand, and equilibrium and nonequilibrium statistical mechanics on the other.

In Chapter 3, we present the first calculation of the mutual-friction coefficients α and α' (which are parameters in the Hall-Vinen-Bekharevich-Khalatnikov two-fluid model that we study in chapter 5) as a function of temperature in a ho-

mogeneous bose gas in two-dimensions by using the Galerkin-truncated Gross-Pitaevskii equation, with very special initial conditions, which we obtain by using the advective, real, Ginzburg-Landau equation (ARGLE) and an equilibration procedure that uses a stochastic Ginzburg-Landau equation (SGLE). We also calculate the normal-fluid density as a function of temperature.

In Chapter 4, we elucidate the interplay of particles and fields in superfluids, in both simple and turbulent flows. We carry out extensive direct numerical simulations (DNSs) of this interplay for the two-dimensional (2D) Gross-Pitaevskii (GP) equation. We obtain the following results: (1) the motion of a particle can be chaotic even if the superfluid shows no sign of turbulence; (2) vortex motion depends sensitively on particle charateristics; (3) there is an effective, superfluid-mediated, attractive interaction between particles; (4) we introduce a short-range repulsion between particles, with range $r_{\rm SR}$, and study two- and many-particle collisions; in the case of two-particle, head-on collisions, we find that, at low values of $r_{\rm SR}$, the particle collisions are inelastic with coefficient of restitution $e = 0$; and, as we increase $r_{\rm SR}$, e becomes nonzero at a critical point, and finally attains values close to 1; (5) assemblies of particles and vortices show rich, turbulent, spatio-temporal evolution.

In Chapter 5, we present results from our direct numerical simulations (DNSs) of the Hall-Vinen-Bekharevich-Khalatnikov (HVBK) two-fluid model in two dimensions. We have designed these DNSs to study the statistical properties of inverse and forward cascades in the HVBK model. We obtain several interesting results that have not been anticipated hitherto: (1) Both normal-fluid and superfluid energy spectra, $E^n(k)$ and $E^s(k)$, respectively, show inverse- and forward-cascade regimes; the former is characterized by a power law $E^s(k) \sim E^n(k) \sim k^{-\alpha}$ whose exponent is consistent with $\alpha \simeq 5/3$. (2) The forward-cascade power law depends on (a) the friction coefficient, as in 2D fluid turbulence, and, in addition, on (b) the coefficient B of mutual friction, which couples normal and superfluid components. (3) As B increases, the normal and superfluid velocities, $\mathbf{u}_n$ and $\mathbf{u}_s$, respectively, get locked to each other, and, therefore, $E^s(k) \simeq E^n(k)$, especially in the inverse-cascade regime. (4) We quantify this locking tendency by calculating the probability distribution functions (PDFs) $\mathcal{P}(\cos(\theta))$ and $\mathcal{P}(\gamma)$, where the angle $\theta \equiv (\mathbf{u}_{\rm n} \cdot \mathbf{u}_{\rm s})/(|\mathbf{u}_{\rm n}||\mathbf{u}_{\rm s}|)$ and the amplitude ratio $\gamma = |\mathbf{u}_{\rm n}|/|\mathbf{u}_{\rm s}|$; the former has a peak at $\cos(\theta) = 1$; and the latter exhibits a peak at $\gamma = 1$ and power-law tails on both sides of this peak. (4) This locking increases as we increase B, but the power-law exponents for the tails of $\mathcal{P}(\gamma)$ are universal, in so far as they do not depend on B, ρ_n/ρ, and the details of the energy-injection method. (5) We characterize the

energy and enstrophy cascades by computing the energy and enstrophy fluxes and the mutual-friction transfer functions for all wave-number scales k.

In Chapter 6, we examine the multiscaling of structure functions in three-dimensional superfluid turbulence by using a shell-model for the three-dimensional HVBK equations. Our HVBK shell model is based on the GOY shell model. In particular, we examine the dependence of multiscaling on the normal-fluid fraction and the mutual-friction coefficients.

Bibliography

[1] R. P. Feynman. Application of quantum mechanics to liquid helium. In C. J. Gorter, editor, *Progress in Low Temperature Physics*, volume I, page 17. North-Holland, Amsterdam, 1955.

[2] G. Baym, C. Pethick, and D. Pines. Superfluidity in neutron stars. *Nature*, 224(5220):673–674, 1969.

[3] M. S. Paoletti and D. P. Lathrop. Quantum turbulence. *Annu. Rev. Condens. Matter Phys.*, 2(1):213–234, 2011.

[4] `http://www.claymath.org/millenium-problems/navier-stokes-equation`.

[5] J Sommeria. Experimental study of the two-dimensional inverse energy cascade in a square box. *J. Fluid Mech.*, 170:139–168, 1986.

[6] R. Salmon. *Lectures on geophysical fluid dynamics*, volume 378. Oxford University Press Oxford, 1998.

[7] M. Rivera and X. L. Wu. External Dissipation in Driven Two-Dimensional Turbulence. *Phys. Rev. Lett.*, 85:976–979, Jul 2000.

[8] L. F. Richardson. *Weather prediction by numerical process*. Cambridge University Press, 1922.

[9] U. Frisch. *Turbulence*, volume 1. Cambridge University Press, Cambridge, UK, 1996.

[10] A. N. Kolmogorov. The local structure of turbulence in incompressible viscous fluid for very large Reynolds numbers. *Dokl. Akad. Nauk SSSR*, 30:301–305, 1941.

[11] A. N. Kolmogorov. On degeneration of isotropic turbulence in an incompressible viscous liquid. *Dokl. Akad. Nauk SSSR*, 31:538–541, 1941.

[12] A. N. Kolmogorov. Dissipation of energy in locally isotropic turbulence. *Dokl. Akad. Nauk SSSR*, 32:16–18, 1941.

[13] R. H. Kraichnan. Inertial Ranges in Two–Dimensional Turbulence. *Phys. Fluids*, 10(7):1417–1423, 1967.

[14] R. H. Kraichnan and D. Montgomery. Two-dimensional turbulence. *Rep. Prog. Phys*, 43, 1980.

[15] M. Lesieur. *Turbulence in fluids*, volume 3. Kluwer academic publishers Dordrecht, 1997.

[16] G. Boffetta and R. E. Ecke. Two-dimensional turbulence. *Annu. Rev. Fluid Mech.*, 44:427–451, 2012.

[17] M. Rivera, X.-L. Wu, and C. Yeung. Universal Distribution of Centers and Saddles in Two-Dimensional Turbulence. *Phys. Rev. Lett.*, 87:044501, Jul 2001.

[18] W. B. Daniel and M. A. Rutgers. Topology of Two-Dimensional Turbulence. *Phys. Rev. Lett.*, 89:134502, Sep 2002.

[19] C. E. Leith. Diffusion approximation for two-dimensional turbulence. *Phys. Fluids*, 11(3):671–672, 1968.

[20] G. K. Batchelor. Computation of the energy spectrum in homogeneous two-dimensional turbulence. *Phys. Fluids*, 12(12):II–233, 1969.

[21] P. Perlekar and R. Pandit. Statistically steady turbulence in thin films: direct numerical simulations with Ekman friction. *New J. Phys.*, 11(7):073003, 2009.

[22] K. Nam, E. Ott, T. M. Antonsen, and P. N. Guzdar. Lagrangian Chaos and the Effect of Drag on the Enstrophy Cascade in Two-Dimensional Turbulence. *Phys. Rev. Lett.*, 84:5134–5137, May 2000.

[23] E. L. Andronikashvili. *J. Phys. U.S.S.R.*, 10:201, 1946.

[24] D. R. Tilley and J. Tilley. *Superfluidity and superconductivity*. CRC Press, 1990.

[25] J. F. Allen and H. Jones. New phenomena connected with heat flow in helium II. *Nature*, 141(3562):243–244, 1938.

[26] J. Wilks. The properties of liquid and solid helium. 1967.

[27] L. Tisza. Transport phenomena in helium II. *Nature*, 141:913, 1938.

[28] L. Tisza. Sur la Supraconductibilit e thermique de l'helium II liquide et la statistique de Bose-Einstein. *C. R. Acad. Sci*, 207(22):1035, 1938.

[29] L. D. Landau. The theory of superfluidity of helium ii. *J. Phys. U.S.S.R.*, 5(1):71–90, 1941.

[30] R. J. Donnelly. *Quantized vortices in helium II*, volume 2. Cambridge University Press, 1991.

[31] J. F. Annett. *Superconductivity, superfluids, and condensates*, volume 67. Oxford University Press Oxford, 2004.

[32] I. M. Khalatnikov. *An introduction to the theory of superfluidity*. WA Benjamin New York, 1965.

[33] H. E. Hall and W. F. Vinen. The rotation of liquid helium II. I. Experiments on the propagation of second sound in uniformly rotating helium II. *Proc. Roy. Soc. A*, 238(1213):204–214, 1956.

[34] H. E. Hall and W. F. Vinen. The rotation of liquid helium ii. ii. the theory of mutual friction in uniformly rotating helium ii. *Proc. Roy. Soc. A*, 238(1213):215–234, 1956.

[35] E. B. Sonin. Vortex oscillations and hydrodynamics of rotating superfluids. *Rev. Mod. Phys.*, 59(1):87, 1987.

[36] W. F. Vinen and J. J. Niemela. Quantum turbulence. *J. Low Temp. Phys.*, 128(5-6):167–231, 2002.

[37] L. Skrbek. Energy spectra of quantum turbulence in He II and ^{3}He-B: A unified view. *JETP Lett.*, 83(3):127–131, 2006.

[38] M. Tsubota. Quantum Turbulence. *J. Phys. Soc. Jpn.*, 77(11):111006, 2008.

[39] I. Procaccia and K. R. Sreenivasan. The state of the art in hydrodynamic turbulence: Past successes and future challenges. *Physica D*, 237(14):2167–2183, 2008.

[40] L. Skrbek and K. R. Sreenivasan. Developed quantum turbulence and its decay. *Phys. Fluids*, 24(1):011301, 2012.

[41] M. Brachet. Gross–Pitaevskii description of superfluid dynamics at finite temperature: A short review of recent results. *C. R. Physique*, 13(9):954–965, 2012.

[42] M. Tsubota, M. Kobayashi, and H. Takeuchi. Quantum hydrodynamics. *Phys. Rep.*, 522(3):191–238, 2013.

[43] C. F. Barenghi, V. S. Lvov, and P.-E. Roche. Experimental, numerical, and analytical velocity spectra in turbulent quantum fluid. *Proc. Natl. Acad. Sci. USA*, 111(Supplement 1):4683–4690, 2014.

[44] N. G. Berloff, M. Brachet, and N. P. Proukakis. Modeling quantum fluid dynamics at nonzero temperatures. *Proc. Natl. Acad. Sci. USA*, 111(Supplement 1):4675–4682, 2014.

[45] R. Hänninen and A. W. Baggaley. Vortex filament method as a tool for computational visualization of quantum turbulence. *Proc. Natl. Acad. Sci. USA*, 111(Supplement 1):4667–4674, 2014.

[46] W. F. Vinen. Mutual friction in a heat current in liquid helium II. I. Experiments on steady heat currents. *Proc. Roy. Soc. A*, 240(1220):114–127, 1957.

[47] W. F. Vinen. Mutual friction in a heat current in liquid helium II. II. Experiments on transient effects. *Proc. Roy. Soc. A*, 240(1220):128–143, 1957.

[48] W. F. Vinen. Mutual friction in a heat current in liquid helium II. III. Theory of the mutual friction. *Proc. Roy. Soc. A*, 242(1231):493–515, 1957.

[49] W. F. Vinen. Mutual friction in a heat current in liquid helium II. IV. Critical heat currents in wide channels. *Proc. Roy. Soc. A*, 243(1234):400–413, 1958.

[50] K. W. Schwarz. Three-dimensional vortex dynamics in superfluid He 4: Homogeneous superfluid turbulence. *Phys. Rev. B*, 38(4):2398, 1988.

[51] K. W. Schwarz. Turbulence in superfluid helium: Steady homogeneous counterflow. *Phys. Rev. B*, 18:245–262, Jul 1978.

[52] K. W. Schwarz. Three-dimensional vortex dynamics in superfluid He 4: Line-line and line-boundary interactions. *Phys. Rev. B*, 31(9):5782, 1985.

[53] J. Maurer and P. Tabeling. Local investigation of superfluid turbulence. *Europhys. Lett.*, 43(1):29, 1998.

[54] P.-E. Roche, P. Diribarne, T. Didelot, O. Français, L. Rousseau, and H. Willaime. Vortex density spectrum of quantum turbulence. *Europhys. Lett.*, 77(6):66002, 2007.

[55] J. Salort, B. Chabaud, E. Lévêque, and P.-E. Roche. Energy cascade and the four-fifths law in superfluid turbulence. *Europhys. Lett.*, 97(3):34006, 2012.

[56] S. R. Stalp, L. Skrbek, and R. J. Donnelly. Decay of Grid Turbulence in a Finite Channel. *Phys. Rev. Lett.*, 82:4831–4834, Jun 1999.

[57] L. Skrbek, J. J. Niemela, and R. J. Donnelly. Four regimes of decaying grid turbulence in a finite channel. *Phys. Rev. Lett.*, 85(14):2973, 2000.

[58] L. Skrbek, A. V. Gordeev, and F. Soukup. Decay of counterflow He II turbulence in a finite channel: Possibility of missing links between classical and quantum turbulence. *Phys. Rev. E*, 67:047302, Apr 2003.

[59] J. Koplik and H. Levine. Vortex reconnection in superfluid helium. *Phys. Rev. Lett.*, 71:1375–1378, Aug 1993.

[60] J. Koplik and H. Levine. Scattering of Superfluid Vortex Rings. *Phys. Rev. Lett.*, 76:4745–4748, Jun 1996.

[61] M. Leadbeater, T. Winiecki, D. C. Samuels, C. F. Barenghi, and C. S. Adams. Sound Emission due to Superfluid Vortex Reconnections. *Phys. Rev. Lett.*, 86:1410–1413, Feb 2001.

[62] W. F. Vinen. An introduction to quantum turbulence. *Philos. Trans. R. Soc. London Ser. A*, 366(1877):2925–2933, 2008.

[63] M. R. Smith, R. J. Donnelly, N. Goldenfeld, and W. F. Vinen. Decay of vorticity in homogeneous turbulence. *Phys. Rev. Lett.*, 71:2583–2586, Oct 1993.

[64] T. Zhang and S. W. Van Sciver. Large-scale turbulent flow around a cylinder in counterflow superfluid ^{4}He (He (II)). *Nat. Phys.*, 1(1):36–38, 2005.

[65] G. P. Bewley, D. P Lathrop, and K. R. Sreenivasan. Superfluid helium: Visualization of quantized vortices. *Nature*, 441(7093):588–588, 2006.

[66] G. P. Bewley, M. S. Paoletti, K. R. Sreenivasan, and D. P. Lathrop. Characterization of reconnecting vortices in superfluid helium. *Proc. Natl. Acad. Sci. USA*, 105(37):13707–13710, 2008.

[67] E. Fonda, D. P. Meichle, N. T. Ouellette, S. Hormoz, and D. P. Lathrop. Direct observation of Kelvin waves excited by quantized vortex reconnection. *Proc. Natl. Acad. Sci. USA*, 111(Supplement 1):4707–4710, 2014.

[68] J. Salort. *Quantum turbulence versus Classical turbulence*. PhD thesis, Université de Grenoble, 2011.

[69] J. Salort, B. Chabaud, E. Lévêque, and P.-E. Roche. Investigation of intermittency in superfluid turbulence. In *J. Phys. Conf. Ser.*, volume 318, page 042014. IOP Publishing, 2011.

[70] J. Salort, C. Baudet, B. Castaing, B. Chabaud, F. Daviaud, T. Didelot, P. Diribarne, B. Dubrulle, Yv. Gagne, F. Gauthier, et al. Turbulent velocity spectra in superfluid flows. *Phys. Fluids*, 22(12):125102, 2010.

[71] E. A. L. Henn, J. A. Seman, G. Roati, K. M. F. Magalhães, and V. S. Bagnato. Emergence of Turbulence in an Oscillating Bose-Einstein Condensate. *Phys. Rev. Lett.*, 103:045301, Jul 2009.

[72] T. W. Neely, A. S. Bradley, E. C. Samson, S. J. Rooney, E. M. Wright, K. J. H. Law, R. Carretero-González, P. G. Kevrekidis, M. J. Davis, and B. P. Anderson. Characteristics of Two-Dimensional Quantum Turbulence in a Compressible Superfluid. *Phys. Rev. Lett.*, 111:235301, Dec 2013.

[73] E. P. Gross. Structure of a quantized vortex in boson systems. *Il Nuovo Cimento Series 10*, 20(3):454–477, 1961.

[74] L. P. Pitaevskii. Vortex lines in an imperfect Bose gas. *Sov. Phys. JETP*, 13(2):451–454, 1961.

[75] N. P. Proukakis and B. Jackson. Finite-temperature models of Bose-Einstein condensation. *J. Phys. B: At. Mol. Opt. Phys.*, 41(20):203002, 2008.

[76] A. Griffin, T. Nikuni, and E. Zaremba. *Bose-condensed gases at finite temperatures*. Cambridge University Press, 2009.

[77] C. W. Gardiner, J. R. Anglin, and T. I. A Fudge. The stochastic Gross-Pitaevskii equation. *J. Phys. B: At. Mol. Opt. Phys.*, 35(6):1555, 2002.

[78] P. B. Blakie, A. S. Bradley, M. J. Davis, R. J. Ballagh, and C. W. Gardiner. Dynamics and statistical mechanics of ultra-cold Bose gases using c-field techniques. *Adv. Phys.*, 57(5):363–455, 2008.

[79] E. Levich and Yakhot V. The kinetics of Bose-condensation. *Ann Isr. Phys. Soc.*, 2:861–865, 1978.

[80] Yu. M. Kagan, B. V. Svistunov, and G. V. Shlyapnikov. Kinetics of Bose condensation in an interacting Bose gas. *Sov. Phys. JETP*, 75(2):387, August 1992.

[81] D. V. Semikoz and I. I. Tkachev. Kinetics of Bose Condensation. *Phys. Rev. Lett.*, 74:3093–3097, Apr 1995.

[82] K. Damle, S. N. Majumdar, and S. Sachdev. Phase ordering kinetics of the Bose gas. *Phys. Rev. A*, 54:5037–5041, Dec 1996.

[83] Yu. Kagan and B. V. Svistunov. Evolution of Correlation Properties and Appearance of Broken Symmetry in the Process of Bose-Einstein Condensation. *Phys. Rev. Lett.*, 79:3331–3334, Nov 1997.

[84] M. J. Davis, S. A. Morgan, and K. Burnett. Simulations of Bose Fields at Finite Temperature. *Phys. Rev. Lett.*, 87:160402, Sep 2001.

[85] N. G. Berloff and B. V. Svistunov. Scenario of strongly nonequilibrated Bose-Einstein condensation. *Phys. Rev. A*, 66:013603, Jul 2002.

[86] G. Krstulovic and M. Brachet. Energy cascade with small-scale thermalization, counterflow metastability, and anomalous velocity of vortex rings in Fourier-truncated Gross-Pitaevskii equation. *Phys. Rev. E*, 83:066311, Jun 2011.

[87] D. Kivotides, C. F. Barenghi, and D. C. Samuels. Triple vortex ring structure in superfluid helium II. *Science*, 290(5492):777–779, 2000.

[88] D. Kivotides. Spreading of superfluid vorticity clouds in normal-fluid turbulence. *J. Fluid Mech.*, 668:58–75, 2011.

[89] H. Adachi, S. Fujiyama, and M. Tsubota. Steady-state counterflow quantum turbulence: Simulation of vortex filaments using the full Biot-Savart law. *Phys. Rev. B*, 81(10):104511, 2010.

[90] T. Araki, M. Tsubota, and S. K. Nemirovskii. Energy spectrum of superfluid turbulence with no normal–fluid component. *Phys. Rev. Lett.*, 89(14):145301, 2002.

[91] A. W. Baggaley, L. K. Sherwin, C. F. Barenghi, and Y. A. Sergeev. Thermally and mechanically driven quantum turbulence in helium II. *Phys. Rev. B*, 86(10):104501, 2012.

[92] A. W. Baggaley, J. Laurie, and C. F. Barenghi. Vortex-density fluctuations, energy spectra, and vortical regions in superfluid turbulence. *Phys. Rev. Lett.*, 109(20):205304, 2012.

[93] D. Kivotides, C. J. Vassilicos, D. C. Samuels, and C. F. Barenghi. Velocity spectra of superfluid turbulence. *Europhys. Lett.*, 57(6):845, 2002.

[94] C. F. Barenghi. Vortices and the Couette flow of helium II. *Phys. Rev. B*, 45(5):2290, 1992.

[95] K. L. Henderson, C. F. Barenghi, and C. A. Jones. Nonlinear Taylor–Couette flow of helium II. *J. Fluid Mech.*, 283:329–340, 1995.

[96] L. Merahi, P. Sagaut, and M. Abidat. A closed differential model for large-scale motion in HVBK fluids. *Europhys. Lett.*, 75(5):757, 2006.

[97] J Tchoufag and P Sagaut. Eddy damped quasinormal Markovian simulations of superfluid turbulence in helium II. *Phys. Fluids*, 22(12):125103, 2010.

[98] P.-E. Roche, C. F. Barenghi, and E. Lévêque. Quantum turbulence at finite temperature: The two-fluids cascade. *Europhys. Lett.*, 87(5):54006, 2009.

[99] J. Salort, P.-E. Roche, and E. Lévêque. Mesoscale equipartition of kinetic energy in quantum turbulence. *Europhys. Lett.*, 94(2):24001, 2011.

[100] J. Salort, B. Chabaud, E. Lévêque, and P.-E. Roche. Energy cascade and the four-fifths law in superfluid turbulence. *Europhys. Lett.*, 97(3):34006, 2012.

[101] D. H. Wacks and C. F. Barenghi. Shell model of superfluid turbulence. *Phys. Rev. B*, 84(18):184505, 2011.

[102] L. Boué, V. L'vov, A. Pomyalov, and I. Procaccia. Energy spectra of superfluid turbulence in ^{3}He. *Phys. Rev. B*, 85:104502, Mar 2012.

[103] L. Boué, V. L'vov, A. Pomyalov, and I. Procaccia. Enhancement of intermittency in superfluid turbulence. *Phys. Rev. Lett.*, 110:014502, Jan 2013.

Chapter 2

Turbulence in the two-dimensional Fourier-truncated Gross-Pitaevskii equation

This Chapter is based on our published work [1].

In this Chapetr we undertake a systematic, direct numerical simulation (DNS) of the two-dimensional, Fourier-truncated, Gross-Pitaevskii equation to study the turbulent evolutions of its solutions for a variety of initial conditions and a wide range of parameters. We find that the time evolution of this system can be classified into four regimes with qualitatively different statistical properties. First, there are transients that depend on the initial conditions. In the second regime, power-law scaling regions, in the energy and the occupation-number spectra, appear and start to develop; the exponents of these power-laws and the extents of the scaling regions change with time and depended on the initial condition. In the third regime, the spectra drop rapidly for modes with wave numbers $k > k_c$ and partial thermalization takes place for modes with $k < k_c$; the self-truncation wave-number $k_c(t)$ depends on the initial conditions and it grows either as a power of t or as $\log t$. Finally, in the fourth regime, complete-thermalization is achieved and, if we account for finite-size effects carefully, correlation functions and spectra are consistent with their nontrivial Berezinskii-Kosterlitz-Thouless forms. Our work is a natural generalisation of recent studies of thermalization in the Euler and other hydrodynamical equations; it combines ideas from fluid dynamics and turbulence, on the one hand, and equilibrium and nonequilibrium statistical mechanics on the other.

2.1 Introduction

The elucidation of the nature of superfluid turbulence, which began with the pioneering studies of Feynman [2] and of Vinen and Hall [3–7], has continued to engage the attention of experimentalists, theoreticians, and numerical simulators [8–14] and has experienced a renaissance over the past few years. Experimental

systems, in which such turbulence is studied, include the bosonic superfluid ^{4}He, its fermionic counterpart ^{3}He, and Bose-Einstein condensates (BECs) of cold atoms in traps and their optical analogues; for representative studies we refer the reader to [15–24]. Theoretical and numerical studies have used a variety of models to study superfluid turbulence; these include the two-fluid model [25,26], Biot-Savart-type models with [27,28] or without [29,30] the local-induction approximation, and the Gross-Pitaevskii (GP) or nonlinear Schrödinger (NLS) equations [31,32]. These models have been studied by a combination of theoretical methods, such as wave-turbulence theory [31–34], and numerical simulations [35–41]. Most of these studies have been carried out in three dimensions (3D); numerical simulations of two-dimensional (2D) models for superfluid turbulence have been increasing steadily over the past few years [42–45]. Here we undertake a systematic direct numerical simulation (DNS) of the dissipationless, unforced, Fourier-truncated, 2D, GP equation with a view to identifying what, if any, features of the turbulent evolution of the solutions of this equation are universal, i.e., they do not depend on initial conditions. Some, though not all, parts of our results are contained in earlier simulations [42–49]. The perspective of our study is different from earlier studies of the 2D GP equation; in particular, we elucidate in detail the dynamical evolution of this system and examine the various stages of its thermalization; in this sense our work is akin to recent studies of thermalization in Euler and other hydrodynamical equations [50–52], which combine ideas from fluid dynamics and turbulence, on the one hand, and equilibrium and nonequilibrium statistical mechanics on the other. Recent studies [50–52] of the dynamics of spectrally truncated, 3D, incompressible Euler flows and related systems have shown that the inviscid and conservative Euler equation, with a high-wave-number spectral truncation, has long-lasting transients that behave just as those of the 3D dissipative Navier-Stokes equation, with generalized dissipation. This is so because the thermalized modes, between some transition wave number and the maximum wave number, act as an effective microworld that provides a viscosity to the modes, with wave numbers below the transition wave number; a similar study for the 3D GP equation has been carried out by Krstulovic and Brachet [39, 53].

In a recent review on Quantum Turbulence, Paoletti and Lathrop [13] write, “Despite the abundant examples of turbulence, there is no consensus definition of the term. Here, we define turbulence as a dynamic field that is spatially complex, aperiodic in time, and involves processes spanning several orders of magnitude in spatial extent and temporal frequency.” It is in this sense that we use the term

turbulence in our study of the dynamical evolution of solutions of the 2D, Fourier-truncated Gross-Pitaevskii equation.

It is useful to begin with a qualitative overview of our principal results. We find that the dynamical evolution of the dissipationless, unforced, 2D, Fourier-truncated GP equation can be classified, roughly, into the following four regimes, which have qualitatively different statistical properties: (1) The first is the region of initial transients; this depends on the initial conditions. (2) This is followed by the second regime, in which we see the onset of thermalization; here the energy and occupation-number spectra begin to show power-law-scaling behaviours, but the power-law exponent and the extents of the scaling regions change with time and depend on the initial conditions. (3) In the third regime, which we call the region of partial thermalization, these spectra show clear, power-law, scaling behaviours, with a power that is independent of the initial conditions, and, at large wave vectors, an initial-condition-dependent, self-truncation regime, where spectra drop rapidly; (4) finally, in the fourth regime, the system thermalizes completely and exhibits correlation functions that are consistent with the predictions of the Berezinskii-Kosterlitz-Thouless (BKT) theory [48,54–56], if the simulation domain and simulation time are large enough. Although some of these regimes have been seen in some earlier numerical studies of the 2D GP equation, we are not aware of any study that has systematized the study of these four dynamical regimes. In particular, regime 3, which shows partial thermalization and self-truncation in spectra, has not been identified in the 2D, Fourier-truncated, GP equation, even though its analogue has been investigated in the 3D case [33,39,53].

The remaining part of this chapter is organised as follows. In Sec. 2.2, we describe the 2D, GP equation and the different statistical measures we use to characterize turbulence in the Fourier-truncated, 2D, GP equation (Sec. 2.2.1); the details of our numerical methods and initial conditions are given in Sec. 2.2.2. In Sec. 2.3, we present our results; these are described in the four Sec. 2.3.1-2.3.4 that are devoted, respectively, to the following: (a) the temporal evolution of the energy components, velocity-component probability distribution functions (PDFs), and the population N_0 in the zero-wave-number mode; (b) the statistical characterization of the first two regimes of the dynamical evolution (by using various energy and the occupation-number spectra for different initial conditions); (c) a similar statistical characterization, as in Sec. 2.3.2, but for the regime with partial thermalization, and the study of the nature of the growth of the self-truncation region; (d) the final, completely thermalized state of the Fourier-truncated, 2D, GP equation. Section 2.4 contains our conclusions. A note on the units used for the GP equation and

the details of some analytical calculations are presented in Appendix A.1 and A.2, respectively.

2.2 Model, Initial Conditions, and Numerical Methods

In this Section, we describe the 2D, GP equation. We define all the statistical measures that we use to characterize the time evolution of this equation, given the three types of initial conditions that we describe below. We also describe the numerical methods, and computational procedures that we use to solve this equation.

2.2.1 The Gross-Pitaevskii Equation

The GP equation, which describes the dynamical evolution of the wave function ψ of a weakly interacting 2D Bose gas at low temperatures, is

$$i\frac{\partial\psi(\mathbf{x},t)}{\partial t} = -\nabla^2\psi(\mathbf{x},t) + g|\psi|^2\psi(\mathbf{x},t); \tag{2.1}$$

$\psi(\mathbf{x},t)$ is a complex, classical field and g is the effective interaction strength [57,58]. This equation conserves the total energy

$$E = \int_{\mathcal{A}} \left[|\nabla\psi|^2 + \frac{1}{2}g|\psi|^4 \right] d^2x \tag{2.2}$$

and the total number of particles

$$N = \int_{\mathcal{A}} |\psi|^2 d^2x, \tag{2.3}$$

where $\mathcal{A} = L^2$ is the area of our 2D, periodic, computational domain of side L. From Eq. (2.1) we obtain the continuity equation

$$\frac{\partial\rho}{\partial t} + \nabla\cdot(\rho\mathbf{v}) = 0, \tag{2.4}$$

where $\rho = |\psi|^2$ is interpreted as the particle density and the velocity is

$$\mathbf{v}(\mathbf{x},t) = \frac{\psi^*\nabla\psi - \psi\nabla\psi^*}{i|\psi|^2}. \tag{2.5}$$

We can use the Madelung transformation $\psi(\mathbf{x},t) = \sqrt{\rho}e^{i\theta(\mathbf{x},t)}$, where $\theta(\mathbf{x},t)$ is the phase of $\psi(\mathbf{x},t)$, to write $\mathbf{v}(\mathbf{x},t) = 2\nabla\theta(\mathbf{x},t)$, whence we get [36]

$$E = \int_{\mathcal{A}} \left[\frac{1}{4}\rho v^2 + \frac{1}{2}g|\psi|^4 + [\nabla\rho^{1/2}]^2 \right] d^2x = E_{kin} + E_{int} + E_q, \tag{2.6}$$

where the kinetic, interaction, and quantum-pressure energies are defined, respectively, as

$$E_{kin} = \frac{1}{4}\int_{\mathcal{A}} |\sqrt{\rho}v|^2 d^2x, \tag{2.7a}$$

$$E_{int} = \frac{1}{2}\int_{\mathcal{A}} g|\psi|^4 d^2x, \tag{2.7b}$$

$$E_q = \int_{\mathcal{A}} |\nabla\rho^{1/2}|^2 d^2x. \tag{2.7c}$$

We separate the compressible (superscript c) and the incompressible (superscript i) parts of the kinetic energy by making use of the decomposition

$$\rho^{1/2}\mathbf{v} = (\rho^{1/2}\mathbf{v})^i + (\rho^{1/2}\mathbf{v})^c, \tag{2.8}$$

where $\nabla\cdot(\rho^{1/2}\mathbf{v})^i = 0$ and $\nabla\times(\rho^{1/2}\mathbf{v})^c = 0$, whence we obtain the following:

$$E^i_{kin} = \frac{1}{4}\int_{\mathcal{A}} |(\sqrt{\rho}v)^i|^2 d^2x; \tag{2.9a}$$

$$E^c_{kin} = \frac{1}{4}\int_{\mathcal{A}} |(\sqrt{\rho}v)^c|^2 d^2x. \tag{2.9b}$$

The spectra for these energies are defined as follows:

$$E^i_{kin} = \frac{1}{4}\int |\widehat{(\rho^{1/2}\mathbf{v})^i}|^2 d^2k \equiv \int E^i_{kin}(k)dk; \tag{2.10}$$

$$E^c_{kin} = \frac{1}{4}\int |\widehat{(\rho^{1/2}\mathbf{v})^c}|^2 d^2k \equiv \int E^c_{kin}(k)dk; \tag{2.11}$$

$$E_{int} = \int |\widehat{\sqrt{g/2}|\psi|^2}|^2 d^2k \equiv \int E_{int}(k)dk; \tag{2.12}$$

and

$$E_q = \int |\widehat{\nabla\rho^{1/2}}|^2 d^2k \equiv \int E_q(k)dk; \tag{2.13}$$

furthermore, we define an occupation-number spectrum $n(k)$ via

$$N = \int |\widehat{\psi}|^2 d^2k \equiv \int n(k)dk; \tag{2.14}$$

here we denote the Fourier transform of $A(\mathbf{x})$ by $\widehat{A}$; and, for notational convenience, we do not show explicitly the dependence of these spectra on time t. In any computational study, we must limit the number of Fourier modes that we use in our study of the GP equation; we refer to such a GP equation as a Fourier-truncated GP equation (cf. [50, 51] for studies of the Fourier- or Galerkin-truncated Euler equation).

The Bogoluibov dispersion relation $\omega_{\rm B}(k)$ is obtained by linearizing Eq. (2.1) around a constant ψ. For a total number of particles Eq. (2.3) $N = 1$, it is

$$\omega_{\rm B}(k) = kc\sqrt{1 + \frac{\xi^2 k^2}{2}}, \tag{2.15}$$

where the sound velocity is $c = \frac{\sqrt{2g}}{L}$ and the coherence length is

$$\xi = \frac{L}{\sqrt{g}}. \tag{2.16}$$

We investigate thermalization in the 2D GP equation, so it is useful to recall that a uniform, interacting, 2D Bose gas has a high-temperature disordered phase and a low-temperature, Berezenskii-Kosterlitz-Thouless (BKT) phase [59–62], which shows quasi-long-range order with an algebraic decay of the spatial correlation function [54]

$$c(r) = \langle \left[e^{-i\theta(\mathbf{x})} - \langle e^{-i\theta(\mathbf{x})}\rangle\right]\left[e^{i\theta(\mathbf{x}+\mathbf{r})} - \langle e^{i\theta(\mathbf{x}+\mathbf{r})}\rangle\right)]\rangle; \tag{2.17}$$

for temperatures T below the transition temperature T_{BKT} (or energy E_{BKT} in the microcanonical ensemble),

$$c(r) \sim r^{-\eta}, \tag{2.18}$$

where $r \equiv |\mathbf{r}|$ and the critical exponent $\eta < 0.25$ for $T < T_{BKT}$; and $\eta = 0.25$ at $T = T_{BKT}$ [55]. The BKT phase shows bound vortex-antivortex pairs; these unbind above T_{BKT}, so

$$c(r) \sim e^{-r/\ell}, \tag{2.19}$$

in the disordered phase, with ℓ the correlation length.

2.2.2 Numerical Methods and Initial Conditions

To perform a systematic, pseudospectral, direct numerical simulation (DNS) of the spatiotemporal evolution of the 2D, Fourier-truncated, GP equation, we have developed a parallel, MPI code in which we discretize $\psi(\mathbf{x}, t)$ on a square simulation domain of side $L = 32$ with N_c^2 collocation points. We use periodic boundary conditions in both spatial directions, because we study homogeneous, isotropic turbulence in this 2D system, and a fourth-order, Runge-Kutta scheme, with time step Δt, for time marching. We evaluate the linear term in Eq. (2.1) in Fourier space and the nonlinear term in physical space; for the Fourier-transform operations we use the FFTW library [63]. Thus, the maximum wave number $k_{max} = (N_c/2)\Delta k$, where $\Delta k = 2\pi/L$, and

$$\xi k_{max} = \frac{\pi N_c}{\sqrt{g}}. \tag{2.20}$$

We have checked that, for the quantities we calculate, dealiasing of our pseudospectral code does not change our results substantially; here we present the results from our pseudospectral simulations that do not use dealiasing. For a general reference on numerical methods for quantum fluids, see [64].

To initiate turbulence in the 2D GP equation we use three types of initial conditions `IC1` [42], `IC2`, and `IC3` [53], always normalized to correspond to a total number of particles Eq. (2.3) $N = 1$. The first of these is best represented in Fourier space as follows:

$$\widehat{\psi}(\mathbf{k}, t = 0) = \frac{1}{\sqrt{\pi^{1/2}\sigma}} \exp\left(-\frac{(k - k_0)^2}{2\sigma^2}\right) \exp\left(i\Theta(k_x, k_y)\right), \tag{2.21}$$

where $k = \sqrt{k_x^2 + k_y^2}$, $\Theta(k_x, k_y)$ are random numbers distributed uniformly on the interval $\left[0, 2\pi\right]$; $k_0 = \mathcal{N}_0 \Delta k$ and $\sigma = \mathcal{B}\Delta k$, where the integer $\mathcal{N}_0$ controls the spatial scale at which energy is injected into the system, and the real number $\mathcal{B}$ specifies the Fourier-space width of $\widehat{\psi}$ at time $t = 0$. The initial condition `IC2` is like `IC1` but, in addition, it has a finite initial condensate population $N_0^i = \mid \widehat{\psi}(\mathbf{k} = 0, t) \mid^2 (\Delta k)^2$ at time $t = 0$. Note the study of [42] uses a hyper-viscosity term $\nu(-\nabla^2)^n\psi$, which is absent in our study; such hyperviscosity terms can modify energy spectra in important ways, as has been discussed in the context of turbulence in the Navier-Stokes equation in [51, 65].

We obtain the initial condition `IC3` by solving the 2D, stochastic, Ginzburg-Landau equation (SGLE), which follows from the free-energy functional

$$\mathcal{F} = \int_{\mathcal{A}} d^2x \left(|\nabla\psi|^2 - \mu|\psi|^2 + \frac{1}{2}g|\psi|^4\right), \tag{2.22}$$

where μ is the chemical potential[1]. The SGLE is

$$\frac{\partial\psi}{\partial t} = -\frac{\delta\mathcal{F}}{\delta\psi^*} + \zeta(\mathbf{x}, t), \tag{2.23}$$

where ζ is a zero-mean, Gaussian white noise with

$$\langle\zeta(\mathbf{x}, t)\zeta^*(\mathbf{x}', t')\rangle = D\delta(\mathbf{x} - \mathbf{x}')\delta(t - t'), \tag{2.24}$$

where $D = 2T$, in accordance with the fluctuation-dissipation theorem [66], T is the temperature, and δ the Dirac delta function. Finally, the SGLE Eq. (2.23) becomes

$$\frac{\partial\psi}{\partial t} = \nabla^2\psi - \mu\psi + g|\psi|^2\psi + \zeta, \tag{2.25}$$

which we solve along with the following, ad-hoc equation

$$\frac{d\mu}{dt} = -\frac{\nu_N}{\mathcal{A}}\left(N - N_{\rm av}\right), \tag{2.26}$$

[1]Recall that the SGLE can be thought of as an imaginary-time GP equation with external, additive noise (see, *e.g.* Ref. [39])

to control the number of particles N; the parameter $N_{\rm av}$ controls the mean value of N; and ν_N governs the rate at which the SGLE equilibrates. We solve the SGLE by using a pseudospectral method, similar to the one described above for the 2D, GP equation, with periodic boundary conditions in space, an implicit-Euler scheme, with time step Δt, for time marching and the method of Ref. [67] (see page 25 of this reference).

The motivation for choosing the parameters for our runs is to explore the initial-condition dependence of our results by varying the energy, the value k_0 of the wave number at which the initial energy is concentrated, the spread σ of the energy about k_0 at time $t = 0$, the interaction strength g, and the presence of the initial condensate density N_0^i. For our systematic study, we have performed numerous runs; these are listed in Table 2.1; the parameters for these runs have been chosen to highlight one type of behaviour or another; e.g., the time dependence of the self-truncation wave number k_c (see below) changes dramatically as we change the parameters of our runs (see Table 2.2); this exploration of parameter space is necessary in order to gain a comprehensive understanding of the dynamics of the 2D, Fourier-truncated, Gross-Pitaevskii equation.

Note that we introduce the initial conditions `IC2` and `IC3` to obtain the relevant behaviour in a shorter time span than is possible with `IC1`. The initial condition `IC1` has zero initial condensate population N_0^i and, therefore, several vortices; its dynamics involves a build up of the condensate population; this takes a long time. The initial condition `IC2` is similar to `IC1` but with an initial condensate population $N_0^i > 0$; thus, condensate build up is bypassed. In the same manner, `IC3` allows us to study the late stages of the self-truncation regime.

2.3 Results

We first present the time evolution of the different energies, the probability distribution functions (PDFs) of the velocity components, and the population N_0 in the zero-wave-number mode. We then give a detailed statistical characterization of the temporal evolution of the Fourier-truncated, 2D, GP equation in the four regimes mentioned in the Introduction (Sec. 2.1).

2.3.1 Evolution of energies, velocity PDFs, and the zero-wave-number population

We show the early stages of the time evolution of the energies E_{kin}^i, E_{kin}^c, E_{int}, and E_q, from our DNS runs `A1-A4`, `B1`, and `C6` in Fig. 2.1. The runs `A1-A4` use initial con-

	N_c	$k_0(\times\Delta k)$	$\sigma(\times\Delta k)$	g	N_0^i	$\sqrt{D}(\times 10^{-3})$	k_c^{in}	E
A1	1024	5	2	1000	–	–	–	2.120
A2	1024	5	2	2000	–	–	–	3.045
A3	1024	5	2	5000	–	–	–	5.82
A4	1024	35	5	1000	–	–	–	49.69
A5	512	5	2	1000	–	–	–	2.15
A6	256	5	2	1000	–	–	–	2.07
A7	128	5	2	1000	–	–	–	2.1
A8	64	5	2	1000	–	–	–	2.2
A9	256	5	2	2000	–	–	–	2.94
A10	256	5	2	5000	–	–	–	5.57
A11	256	15	2	1000	–	–	–	9.86
A12	256	15	2	2000	–	–	–	10.82
A13	256	15	2	5000	–	–	–	13.68
B1	128	5	1	10000	0.95	–	–	5.44
B2	128	5	1	1000	0.95	–	–	0.59
C1	256	–	–	5000	–	8	6	2.536
C2	256	–	–	1000	–	8	6	0.583
C3	256	–	–	1000	–	10	6	0.637
C4	256	–	–	1000	–	8	9	0.7
C5	256	–	–	1000	–	8	15	1.085
C6	256	–	–	1000	–	8	20	1.557

Table 2.1: Parameters for our DNS runs A1-A13, B1-B2, and C1-C6: N_c^2 is the number of collocation points, k_0 is the energy-injection scale, σ is the Fourier-space width of $\widehat{\psi}$ at $t = 0$; g is the effective interaction strength; N_0^i is the initial condensate population; D and k_c^{in} are respectively, the variance of the white-noise and the initial value of the truncation wave number, which we use in the initial conditions of type IC3; E is the total energy; we use a square simulation domain of area $\mathcal{A} = L^2$; we choose $L = 32$.

ditions of type IC1, in which E^i_{kin} is a significant fraction of the total initial energy; the runs B1 and C6 start with initial configurations of type IC2 and IC3, respectively, in which E^i_{kin} is negligibly small at $t = 0$. The transient nature of the early stages of the dynamical evolution of the dissipationless, unforced, 2D, GP equation is evident from Fig. 2.1, in which we observe a rapid conversion of E^i_{kin} into the other three components, with a significant fraction being transferred to E^c_{kin}; moreover, the transient stage depends on the initial conditions, as we describe below. Figures 2.1 (a)-(c), show comparisons of the temporal evolution of the energies, from the runs A1-A3; we observe, in particular, that the conversion of E^i_{kin} into the other energy components is accelerated as g increases from 1000 to 5000 (cf. [43]); and there is a corresponding acceleration in the approach to thermalization. The time evolution of the incompressible kinetic energy follows that of the total number of vortices N_v; see, e.g., [68], and the figure F1, which we have included in the supplementary material. Moreover, the larger the value of E^i_{kin} the larger is the time required for thermalization, as we can see by comparing Figs. 2.1 (a) and (d), for the runs A1 and A4, respectively; the run A4 starts with a high value of $E^i_{kin}(t = 0)$ because of a large number of vortices and anti-vortices, so it takes a long time to thermalize; indeed, if the spatial resolution of our DNS is very high, the computational cost of achieving a statistically steady state is prohibitively high for initial conditions A1-A4. In contrast, the runs B1 and C6 have negligibly small values of $E^i_{kin}(t = 0)$ to begin with (Figs. 2.1 (e) and (f), respectively); and $E^i_{kin}(t)$ remains close to zero throughout the dynamical evolution here. For run B1, both E^c_{kin} and E_q start from values close to zero, grow at the cost of E_{int}, and finally saturate to small, statistically steady values. For run C6, there are hardly any vortices in the initial configuration, so the energies start fluctuating about their statistically steady values very rapidly.

In Fig. 2.2 we plot, at three instants of time, the PDFs of v_x and v_y, the Cartesian components of the velocity, for our DNS runs A1, B1, and C6, which correspond, respectively, to initial conditions of types IC1, IC2, and IC3. For the run A1, these PDFs, in Figs. 2.2 (a)-(c), show a crossover from a distribution with power-law tails to one that is Gaussian; the right and left tails of the PDFs in Fig. 2.2 (a) can be fit to the form $\sim v_i^{-\gamma}$, with $\gamma \simeq 3.2$, and $i = x$ or y (we show fits only for $i = x$). Such power-law tails in velocity-component PDFs have been seen in experiments [69] and some numerical studies [40,46,70,71]. However, it has not been noted hitherto that, for turbulence in the Fourier-truncated, 2D, GP equation with low-energy initial conditions, such PDFs evolve, as t increases, from PDFs with power-law tails (Fig. 2.2 (a) for run A1), to ones with a Gaussian form near the mean, followed

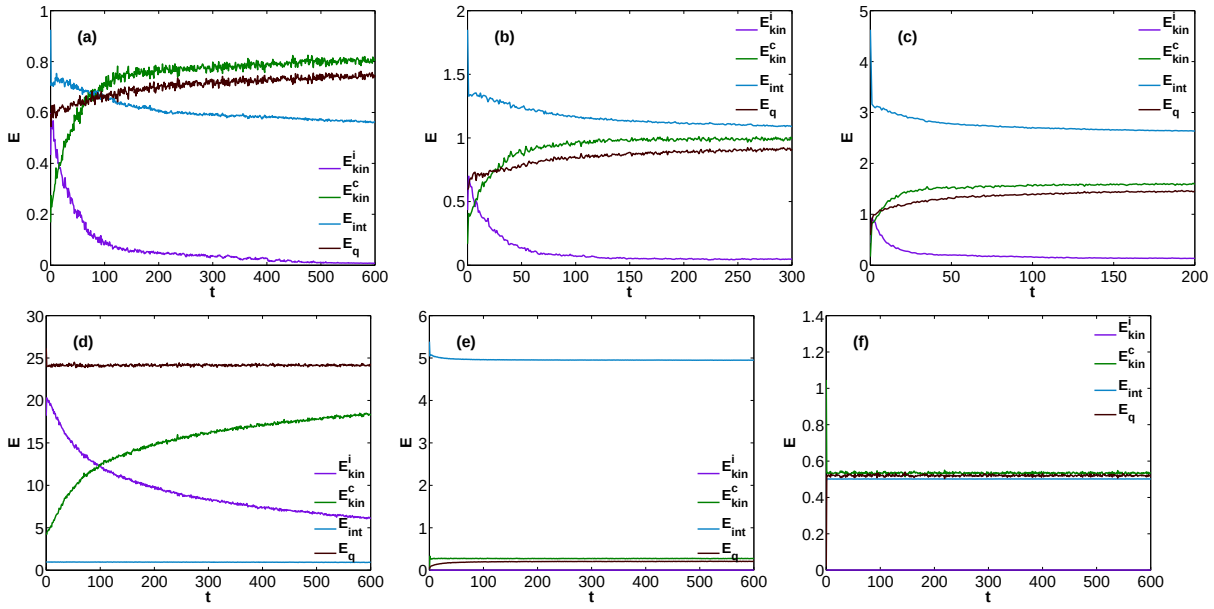

Figure 2.1: Plots versus time t of the four components of the total energy E^i_{kin}, E^c_{kin}, E_{int}, and E_q, during the initial stages of evolution, from our DNS runs (a) `A1`, (b) `A2` (c) `A3`, (d) `A4`, (e) `B1`, and (f) `C6` (see Table 2.1).

by broad tails (Fig. 2.2 (b) for run `A1`), and then to more-or-less Gaussian PDFs (Fig. 2.2 (c) for run `A1`), but with tails that can be fit to an exponential form. This evolution towards Gaussian PDFs is associated with the annihilation of vortices and anti-vortices. The Video M1 in the Supplementary Material shows the temporal evolution of this PDF in the left panel and the spatiotemporal evolution of the pseudocolor plot of the vorticity in the right panel. The analogues of Figs. 2.2(a)-(c) for runs `B1` and `C1`, both of which have a negligibly small value of E^i_{kin} at $t = 0$, are given, respectively, in Figs. 2.2(d)-(f) and Figs. 2.2(g)-(i).

To calculate the velocity PDFs, during the various stages of the evolution of the system, we obtain the velocity at every grid point in our simulation domain; thus, we make these numerical measurements at a length scale that is always less than the inter-vortex separation. The power-law tails, which we observe in the velocity PDFs for our DNS run `A1`, arise because of the singular nature of quantum vortices [13]; and the cross-over from such power-law tails, in the initial stages of evolution, to the more-or-less Gaussian PDFs, in the partially thermalized state, arises because of the depletion of the vortex density with time. Thus, our results complement those in [72] insofar as the cross-over from power-law to Gaussian tails occurs as our system evolves in time and not as we change the length scale of our measurement as in [72].

We turn now to the time evolution of the population $N_0(t)$, in the $k = 0$ mode [37, 41, 73], and its dependence on the initial conditions. In Fig. 2.3 (a) we plot N_0

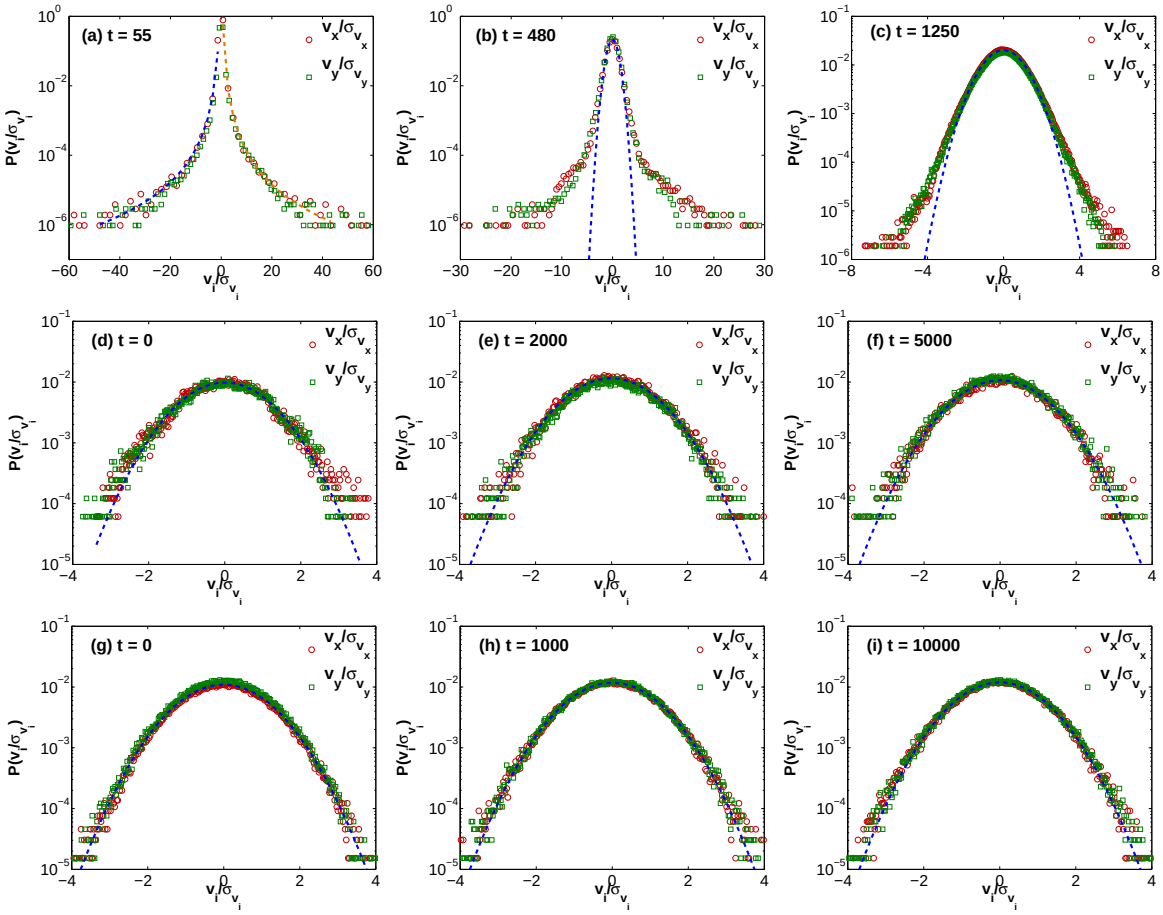

Figure 2.2: Semilog (base 10) plots of the PDFs of the x (red circles) and y (green squares) components of the velocity from our DNS runs: (a)-(c) `A1`, (d)-(f) `B1`, and (g)-(i) `C6`, corresponding to each of the three types of initial conditions `IC1`, `IC2`, and `IC3`, respectively. The complete time evolution of the PDFs (a)-(c) for the run `A1` is illustrated in the top-left panel of the Video M1 (supplementary material). The blue-dashed lines in (b)-(i) indicate fits to Gaussian PDFs; the dashed lines in (a) indicate power-law fits to the left (blue-dashed line) and right (orange-dashed line) tails of the PDFs (see text).

versus t for the runs A1-A4 (red, blue, green, and brown curves, respectively), which use initial configurations of type IC1; these figures show that $N_0(t)$ increases with t, on average, and depends on E, g, k_0, and σ. For the runs A1 and A2 (red and blue curves in Fig. 2.3 (a)), $N_0(t)$ approaches a saturation value for the time scales probed by our simulations; Fig. 2.3 (a) also shows that, as we increase g (red, blue, and green lines in Fig. 2.3 (a)), the fluctuations in N_0 are enhanced and its large-t value, which it seems to approach asymptotically, diminishes. By comparing the runs A1 and A4 (red and brown lines in Fig. 2.3 (a)), we see that the latter has a higher value of E than the former, because both k_0 and σ are smaller for A1 than for A4; thus, $N_0(t)$ grows more slowly in A4 than in A1; and, after an equal amount of simulation time, its value in A4 is nearly an order of magnitude lower than in A1; the former shows large fluctuations in $N_0(t)$ and no sign of saturation. The run B1 (Fig. 2.3 (e)) uses an initial configuration of type IC2, with a large value of $N_0(t=0) = 0.95$; in this case, after a period of initial transients, $N_0(t) \to 0.98$ over our simulation time. The run C6 (Fig. 2.3 (f)) uses an initial condition of type IC3; here $N_0(t)$ fluctuates slightly but remains close to its initial value (cf. [41, 73]).

To study the dependence of $N_0(t)$ on the number of collocation points N_c^2, we evolve the initial configuration of A1 for $N_c = 512$ (run A5), $N_c = 256$ (run A6), $N_c = 128$ (run A7), and $N_c = 64$ (run A8). Figure 2.3 (g) shows plots of $N_0(t)$ versus t for these five runs; clearly, the initial evolution of $N_0(t)$ depends significantly on N_c; however, the large-t values of $N_0(t)$, on the time scales of our runs, are comparable ($\simeq 0.9$) for the runs with $N_c = 128$ (run A7), $N_c = 256$ (run A6), and $N_c = 1024$ (run A1). In contrast, the saturation value for the run with $N_c = 64$ (run A8) is $\simeq 0.8$. For the run A5 ($N_c = 512$), $N_0(t)$ shows large fluctuations and no sign of saturation over the time scale that we have covered; this suggests that $N_0(t)$ also depends on the realisation of the random phases $\Theta(k_x, k_y)$ in Eq. (2.21). These plots of $N_0(t)$ illustrate that complete thermalization proceeds very slowly for N_0; in the completely thermalized state of the Fourier-truncated, 2D, GP system, N_0 must vanish in the thermodynamic limit by virtue of the Hohenberg-Mermin-Wagner theorem [59, 60]; however, it is not easy to realize this limit in finite-size systems and with the limited run times that are dictated by computational resources. We discuss these issues again in Sec. 2.3.4 and also refer the reader to [73, 74].

2.3.2 Initial transients and the onset of thermalization

The initial stages of the evolution of energy spectra for the Fourier-truncated, 2D, GP equations are qualitatively different for initial conditions of types IC1, IC2, and IC3. The first type begins with a sizeable incompressible kinetic energy spectrum

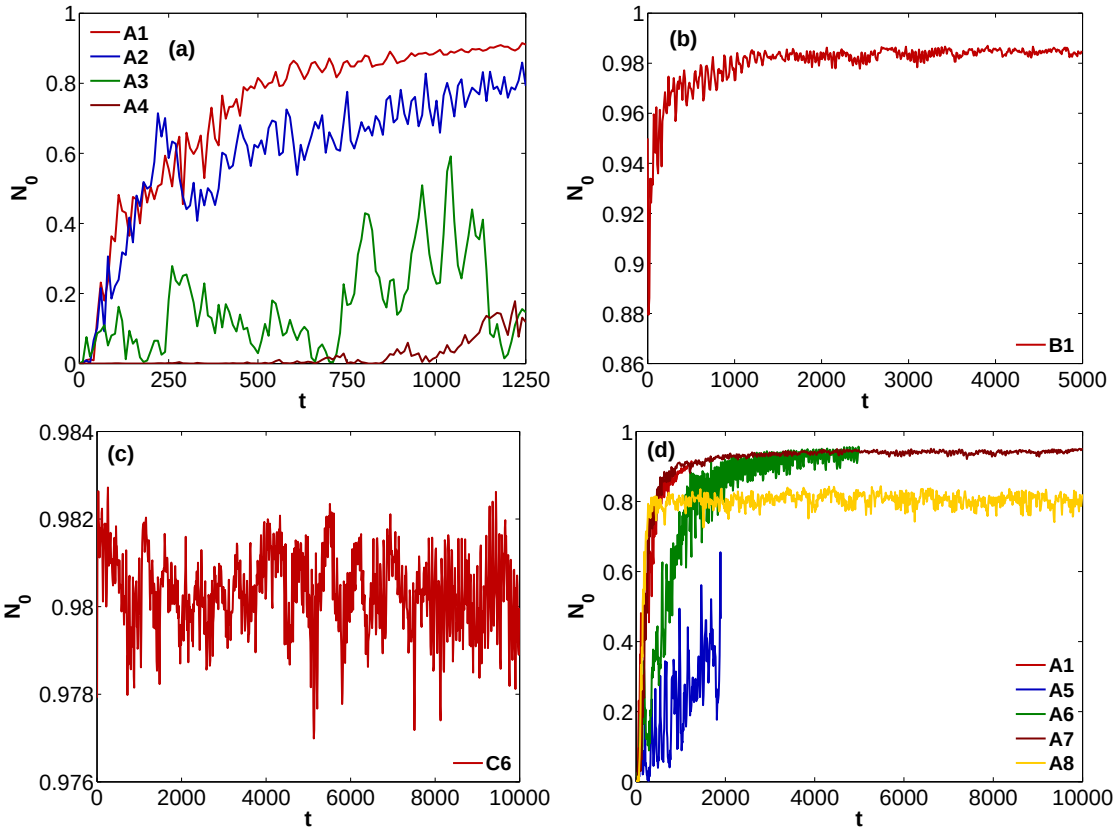

Figure 2.3: Plots versus time t of the population N_0, in the zero-wave-number mode, from our DNS runs (a) `A1`-`A4` (initial condition of type `IC1`), (b) `B1` (initial condition of type `IC2`), (c) `C6` (initial condition of type `IC3`), and (d) `A1` and `A5`-`A8`, for five values for the number of collocation points N_c^2, namely, 1024^2, 512^2, 256^2, 128^2, and 64^2.

$E^i_{kin}(k)$; and the initial transients are associated with the annihilation and creation of vortex-antivortex pairs, the associated depletion of $E^i_{kin}(k)$, and the growth of the other energy components [42]. In contrast, runs with initial conditions of types `IC2` and `IC3` start with a very small incompressible-energy component, therefore, even the early stages of their dynamical evolution are akin to the late stages of the dynamical evolution with initial conditions of type `IC1`. In Figs. 2.4 (a)-(d) we show the time evolution of the spectra $E^i_{kin}(k)$, for the runs `A1`, `A2`, `A3`, and `A4`, to ascertain the presence of scaling behaviour, if any. We find that, in the low-k region, $E^i_{kin}(k)$ lacks a well-defined scaling region (unlike in [43]); indeed, this region depends on the initial configuration, changes continuously with time, and, in particular, a $k^{-5/3}$ scaling region is tenable (a) over a range of wave numbers that is very tiny and (b) over a fleetingly short interval of time (around $t = 50$ for the run `A1`). At large wave numbers, $E^i_{kin}(k) \sim k^{-3}$, during the initial stages of evolution, because of the presence of the vortices [45]; this power-law form holds over the same time scales for which the PDF $P(v_x/\sigma_{v_x}) \sim v_x^{-\gamma}$ (Figs. 2.2 (a)-(b)).

It is useful to define a wave number $k_{hd} = 2\pi/\delta$ based on the average vortex separation $\delta = \lambda^{-1/2}$, where $\lambda = N_v/\mathcal{A}$ is the vortex density. We calculate k_{hd} and plot it versus time t, for the DNS runs `A1`-`A3`, in figure F2 in the supplementary material. In our simulations, only a small number of modes have $k \leq k_{hd}$, especially for our DNS runs `A1`-`A3` (see Fig. 2.4 in which we have plotted the $E^i_{kin}(k)$). In our study, given the systems sizes and initial conditions we use, the system evolves towards states in which the vortex density is low.

The initial transients described above are followed by a regime in which the energy and occupation-number spectra begin to show power-law-scaling behaviours, but the power-law exponent and the extent of the scaling region change with time and depend on the initial conditions; we regard this as the onset of thermalization, which is shown in Figs. 2.5 and 2.6, where we illustrate the time evolution of E^c_{kin}. Figure 2.5 (a) shows $E^c_{kin}(k)$ for the run `A1`; we begin to see a power-law region here with $E^c_{kin}(k) \sim k$, on the low-k side of the peak after which the spectrum falls steeply. A similar $E^c_{kin}(k) \sim k$ behaviour starts to emerge in the region $k \lesssim k_{max}$ for the run `B1` (Fig. 2.5 (g)). In this onset-of-thermalization regime, we also see the development of the following power laws: $E_{int}(k) + E_q(k) \sim k$ (Fig. 2.7) and $n(k) \sim 1/k$ (Fig. 2.8).

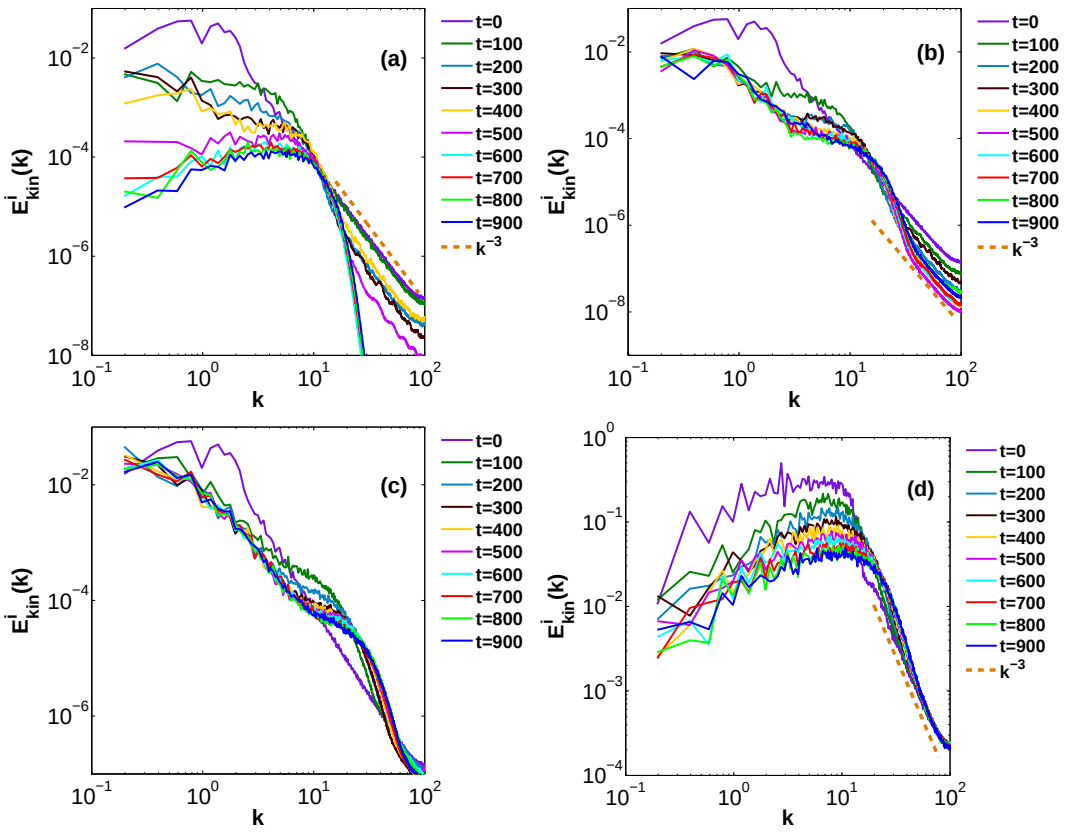

Figure 2.4: Log-log (base 10) plots of the spectra $E^i_{kin}(k)$ from our DNS runs (a) `A1`, (b) `A2`, (c) `A3`, and (d) `A4` at different times t (indicated by curves of different colours); a k^{-3} power law is shown by orange-dashed lines. The complete time evolution of the spectra in (a), (b), (c), and (d) is illustrated in the Video M2 (supplementary material).

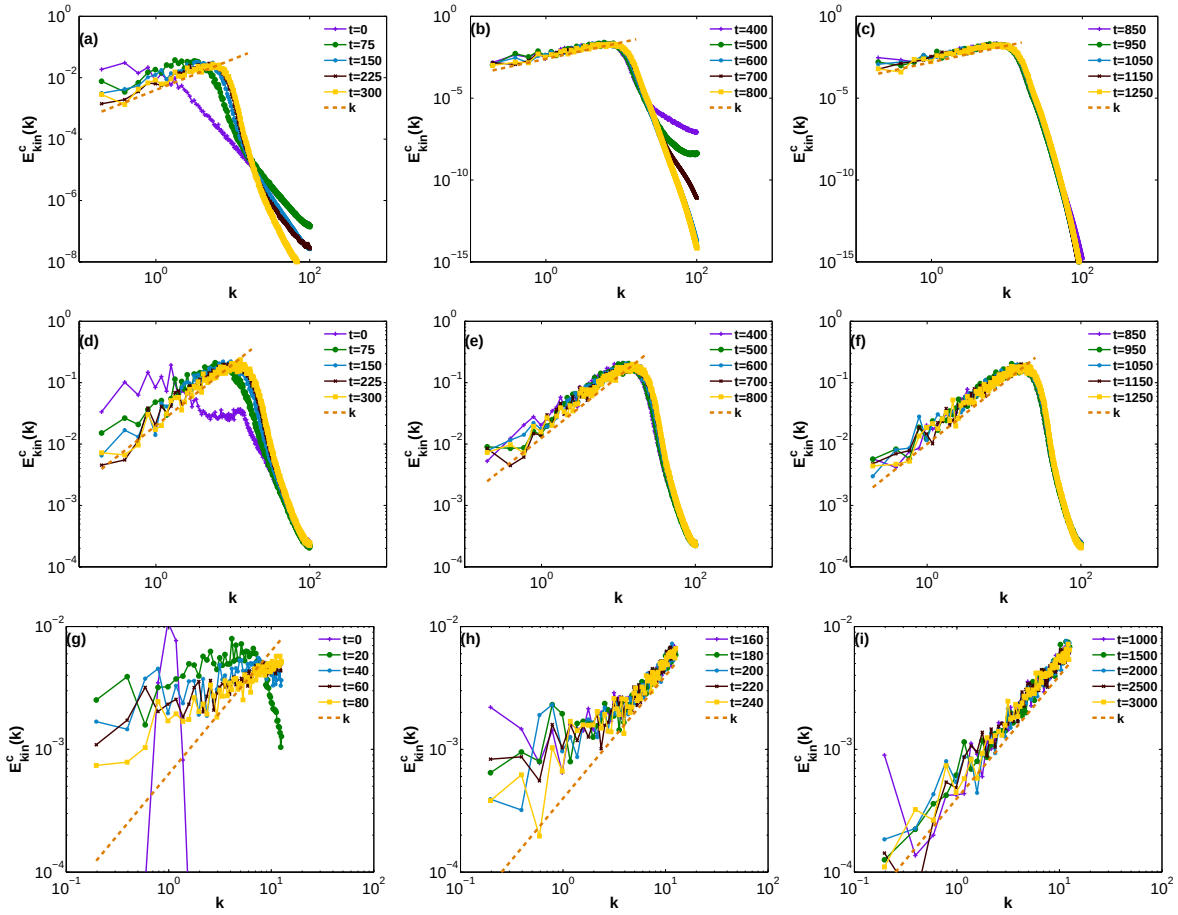

Figure 2.5: Log-log (base 10) plots of the spectra $E^c_{kin}(k)$ from our DNS runs (a)-(c) `A1`, (d)-(f) `A4`, and (g)-(i) `B1` at different times t (indicated by curves of different colours); a k power law is shown by orange-dashed lines.

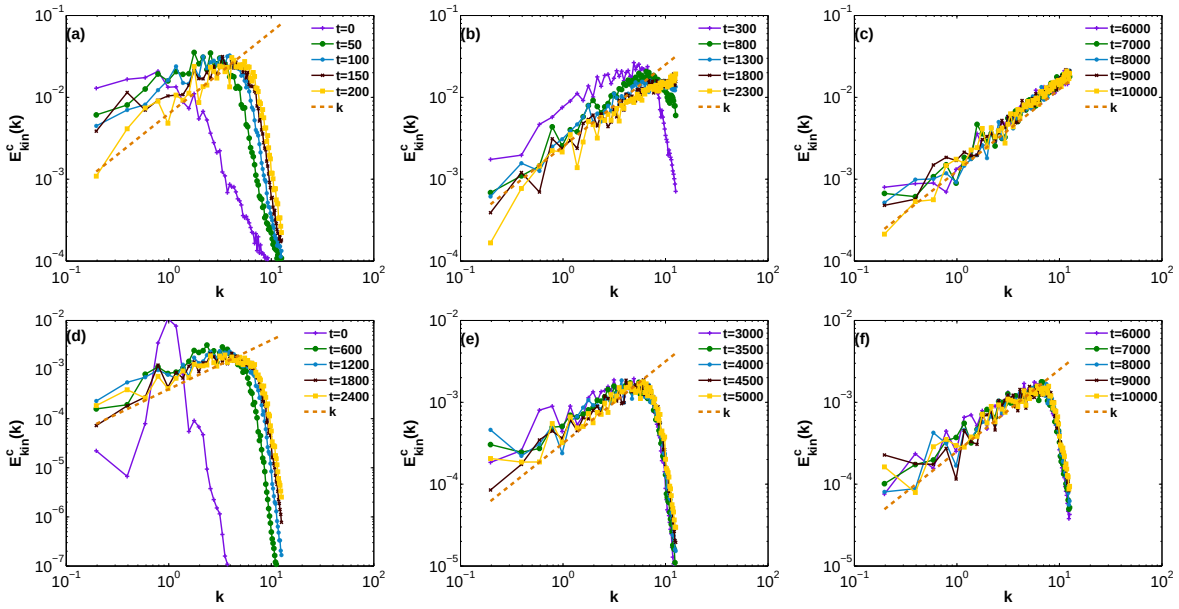

Figure 2.6: Log-log (base 10) plots of the spectra $E^c_{kin}(k)$ from our DNS runs (a)-(c) A7 and (d)-(f) B2 at different times t (indicated by curves of different colours); a k power law is shown by orange-dashed lines.

2.3.3 Partial thermalization and self-truncation

Partial thermalization

In the third stage of the dynamical evolution of the 2D, Fourier-truncated, GP equation, which we refer to as the partial-thermalization stage, well-defined, power-law-scaling behaviours appear in energy and occupation-number spectra, with exponents that are independent of the initial conditions as illustrated by the compressible-kinetic-energy spectra in Figs. 2.5 (b), (c) (e), (f), and 2.6 (b) for initial conditions of type IC1, and Figs. 2.5 (h) and 2.6 (e), and (f), for initial conditions of type IC2. It is important to distinguish between (I) spectra that fall steeply at large values of k, e.g., the spectra in Figs. 2.5 (b), (c) (e), (f), and 2.6 (e) and (f), and (II) spectra that increase all the way to k_{max}, e.g., the spectra in Figs. 2.5 (h) and 2.6 (b) and (c). In case (I), we have spectral convergence to the 2D GP partial differential equation (PDE); in case (II), the effects of Fourier truncation are so pronounced that our truncated 2D, GP system does not provide a good representation of the 2D, GP PDE. As we show below, case (I) can be further subdivided into (A) a subclass in which the maximum, at $k = k_c$ in $E_{kin}(k) = (E^c_{kin}(k) + E^i_{kin}(k))$, referred to as the self-truncation wave number [53], moves out to k_{max} as a power of t and (B) a subclass in which k_c moves out to k_{max} at a rate that is slower than a power of t.

Figures 2.5 (g)-(i), from the run B1, show how $E^c_{kin}(k)$ evolves as the spectral convergence to the GP PDE is lost in case (II); note that the scaling region with

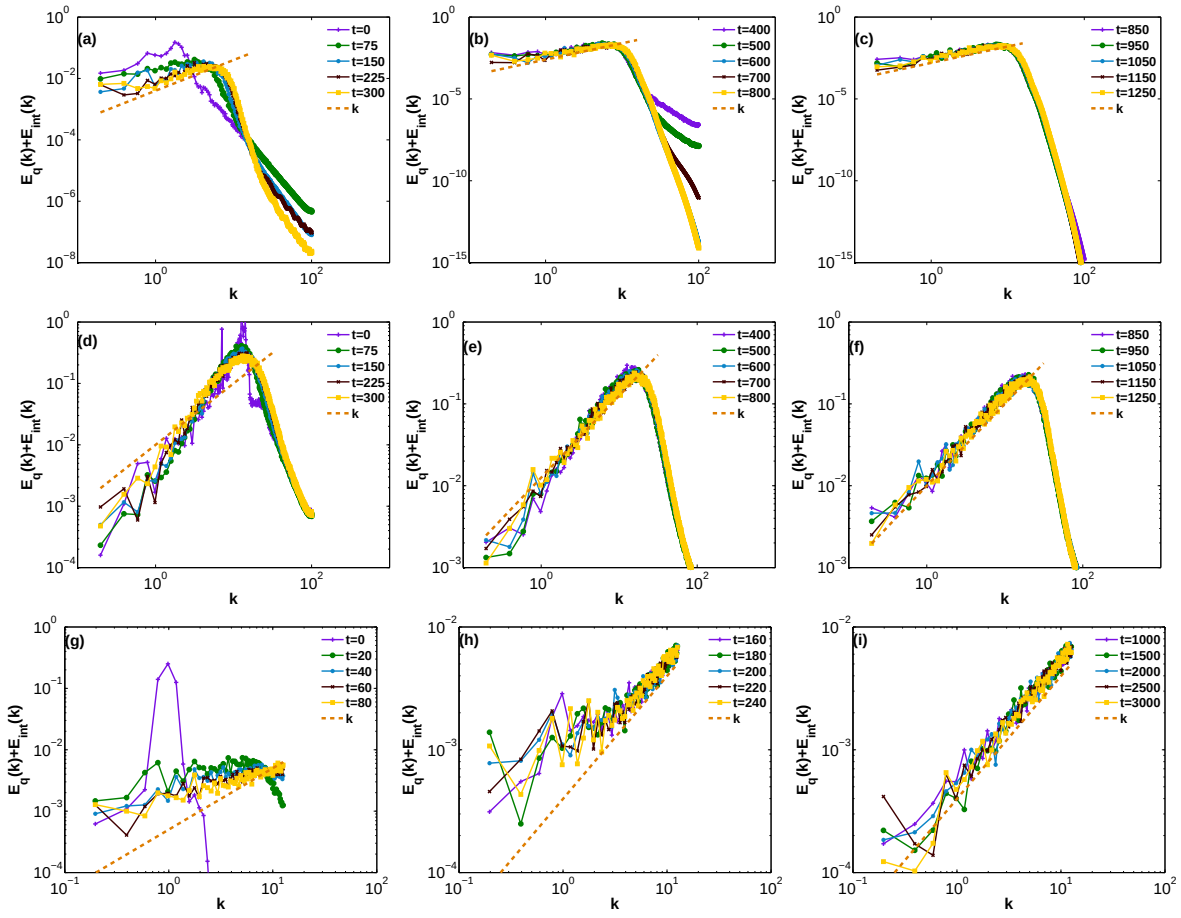

Figure 2.7: Log-log (base 10) plots of the spectra $E_{int}(k) + E_q(k)$ from our DNS runs (a)-(c) `A1`, (d)-(f) `A4`, and (g)-(i) `B1` at different times t (indicated by curves of different colours); a k power law is shown by orange-dashed lines.

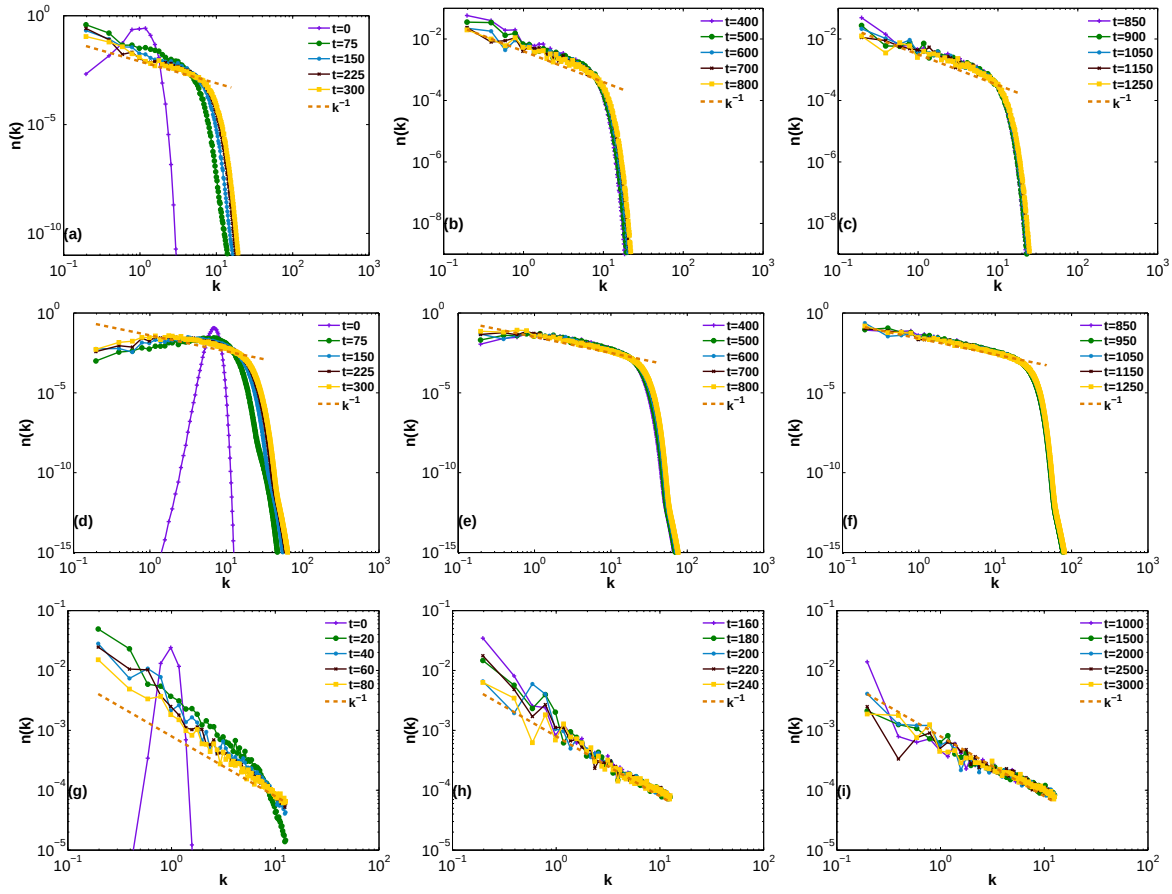

Figure 2.8: Log-log (base 10) plots of the spectra $n(k)$ from our DNS runs (a)-(c) `A1`, (d)-(f) `A4`, and (g)-(i) `B1` at different times t (indicated by curves of different colours); a k^{-1} power law is shown by orange-dashed lines. The total number of particles $N = 1$ (see Eq. (2.14)) and the area $\mathcal{A} = 32^2$ of the simulation domain is the same for the DNS runs `A1`, `A4` and `B1`; and N is conserved during the time evolution of the system.

$E^c_{kin} \sim k$ sets in at high wave numbers close to k_{max} and then extends to the low-wave-number regime. For case (IA) analogous plots of $E^c_{kin}(k)$ are given in, e.g., Figs. 2.6 (a)-(c). We give plots for case (IB) in the next subsection, where we study in detail the time dependence of k_c. Illustrative plots of the spectra $(E_i(k) + E_q(k))$ and $n(k)$ in this regime of partial thermalization are given in Figs. 2.7 and 2.8, respectively.

Self-truncation

We now present a detailed characterization of the partial-thermalization regime, when energy spectra display self-truncation at wave-numbers beyond $k_c(t)$, which can be defined as follows:

$$k_c = \sqrt{\frac{2\int_0^{k_{max}} k^2 E_{kin}(k)dk}{\int_0^{k_{max}} E_{kin}(k)dk}}; \tag{2.27}$$

as the system approaches complete thermalization, $k_c(t) \to k_{max}$. In particular, we explore how the scaling ranges in energy spectra grow with t for different values of g, with the initial configuration and number of collocation points N_c held fixed. For an initial condition of type IC1, with $k_0 = 5\Delta k$, $\sigma = 2\Delta k$, and $N_c = 256$, we obtain the time evolution of energy spectra for $g = 1000$ (run A6), $g = 2000$ (run A9), and $g = 5000$ (run A10) in Figs. 2.9 (a), (b), and (c), respectively, and their video analogues (Videos M3 (panel V2) in the Supplementary Material). The larger the value of g, the more rapid is the thermalization, and the consequent loss of spectral convergence, as we can see by comparing the sky-blue (run A10), green (run A9), and purple (run A6) spectra in Figs. 2.9 (a)-(c); run A6 loses spectral convergence around $t = 2500$. We obtain the same qualitative g dependence, with $k_0 = 15\Delta k$, $\sigma = 2\Delta k$, and $N_c = 256$, for $g = 1000$, 2000, and 5000, i.e., runs A11, A12, and A13, respectively, for which energy spectra are portrayed in Figs. 2.9 (d)-(f) and Video M3 (panel V3) in the Supplementary Material.

In Figs. 2.9 (g)-(i) we explore the N_c dependence of the self-truncation of energy spectra, for initial conditions, with $k_0 = 5\Delta k$, $\sigma = 2\Delta k$, and $g = 1000$, and five different values of N_c, namely, $N_c = 1024$ (run A1), 512(run A5), 256 (run A6), 128 (run A7), and 64 (run A8). We find, not surprisingly, that the lower the value of N_c the more rapidly does the system lose spectral convergence.

Note the dual nature of solutions to the truncated GPE: in the early part of the dynamical evolution of this system, which lasts only as long as spectral convergence is ensured, the solutions approximate numerically genuine solutions of the original PDE (i.e., the untruncated GPE). In subsequent evolution, when spec-

tral convergence is lost, the truncated system evolves to a truncation-dependent thermodynamic equilibrium, which we call "complete thermalisation". These two distinct aspects might appear, at first sight, to be mutually exclusive. Indeed, in the first part of the evolution, the truncation wavenumber $k_{\rm max}$ has no effect (or a vanishingly small one) on the solution, whereas, in the next part, the very existence of the equilibrium needs the influence of $k_{\rm max}$. However, Fig. 2.9 shows that, in a regime, which we call "partial thermalization", the system "self truncates" with a physical cutoff at momentum $k_c < k_{\rm max}$. In this new regime the system is in a state that both approximates a solution to the original PDE and can also be thought of as a thermalized state with a slowly growing "self truncation" at wave number k_c. We show below that the self-truncation regime can last a long time when ξk_c is large.

Initial conditions of type `IC2` lead to energy spectra whose time evolution, and their dependence on g and N_c, is similar to those that are obtained from initial conditions of type `IC1`.

With initial conditions of types `IC1` and `IC2`, we cannot control the initial value $k_c(t = 0) \equiv k_c^{in}$ easily. However, initial conditions of type `IC3`, which we obtain from the SGLE, allow us to control k_c^{in} and start, therefore, with initial spectra that display partial thermalization for $k < k_c^{in}$ [53] and a sharp fall thereafter. In Fig. 2.10 we show the time evolution of $E^c_{kin}(k)$ for such initial conditions from runs `C1`-`C6`. For different representative values of k_c^{in}, g, and D, we now study the time evolution of $k_c(t)$, which characterizes the growth of the partially thermalized scaling region. Here too, as with initial conditions of types `IC1` and `IC2`, if all other parameters like $k_c^{in} = 6.0$ and D are held fixed, the speed of thermalization increases with g (cf. Fig. 2.10 (a) for the run `C1`, with $g = 5000$, and Fig. 2.10 (b) for the run `C2`, with $g = 1000$). For these runs `C1`-`C6`, the growth of the energy spectra, in the region $k > k_c^{in}$, starts with the smoothening of the sharp cut-off at k_c^{in}; the higher the value of k_c^{in}, the slower is this growth (cf. Figs. 2.10 (b), (d), (e), and (f) for runs `C2`, `C4`, `C5`, and `C6`, respectively). By contrast, an increase in D (or T) in the SGLE, accelerates this growth (cf. Figs. 2.10 (b) and (c) for runs `C2` and `C3`, respectively).

The growth of $k_c(t)$ with t, illustrated in Fig. 2.11 (a), can be fit to the form $k_c(t) \sim t^{\alpha}$; however, as we show below, α depends on the initial condition. We obtain the exponent α either from slopes of log-log plots of (i) $k_c(t)$ versus t or (ii) dk_c/dt versus k_c/k_{max}; we denote the values from procedures (i) and (ii) as α_1 and α_2, respectively. Note that in (ii) we have a parametric plot [39,53], shown in Fig. 2.11 (b); this yields a straight-line scaling regime with slope χ and $\alpha_2 = 1/(1 - \chi)$. The values of α_1 and α_2, listed in Table 2.2, show that $\alpha_1 \simeq \alpha_2$; the discrepancy between

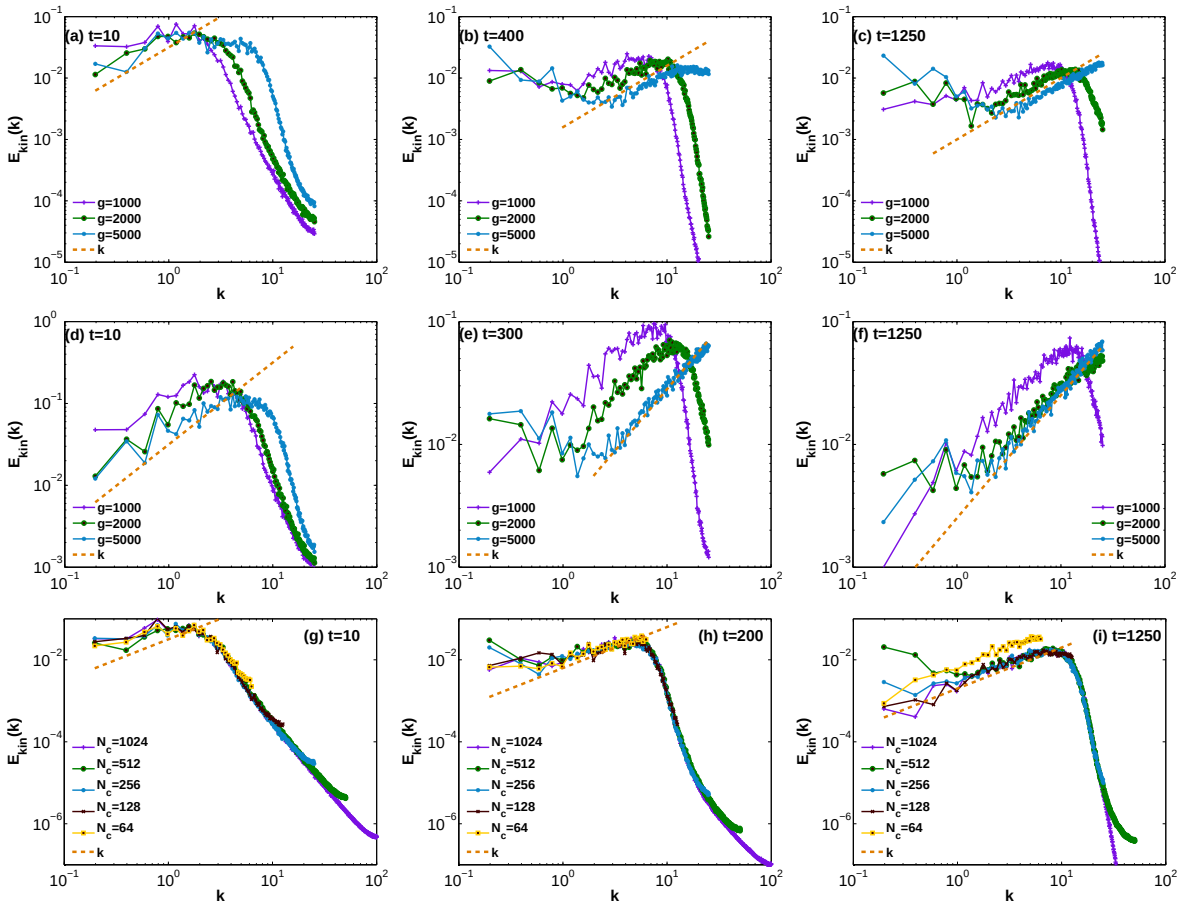

Figure 2.9: Log-log (base 10) plots of the spectra $E_{kin}(k)$ from our DNS runs (a)-(c) A6, A9, and A10 ($k_0 = 5\Delta k$ and $\sigma = 2\Delta k$), (d)-(f) A11, A12 and A13 ($k_0 = 15\Delta k$ and $\sigma = 2\Delta$), and (g)-(i) A1, A5-A8 ($N_c^2 = 1024^2$, 512^2, 256^2, 128^2, and 64^2). The complete time evolutions of the spectra in (a)-(c), (d)-(f), and, (g)-(i) are illustrated in the panels V2, V3, and V4 of Video M3.

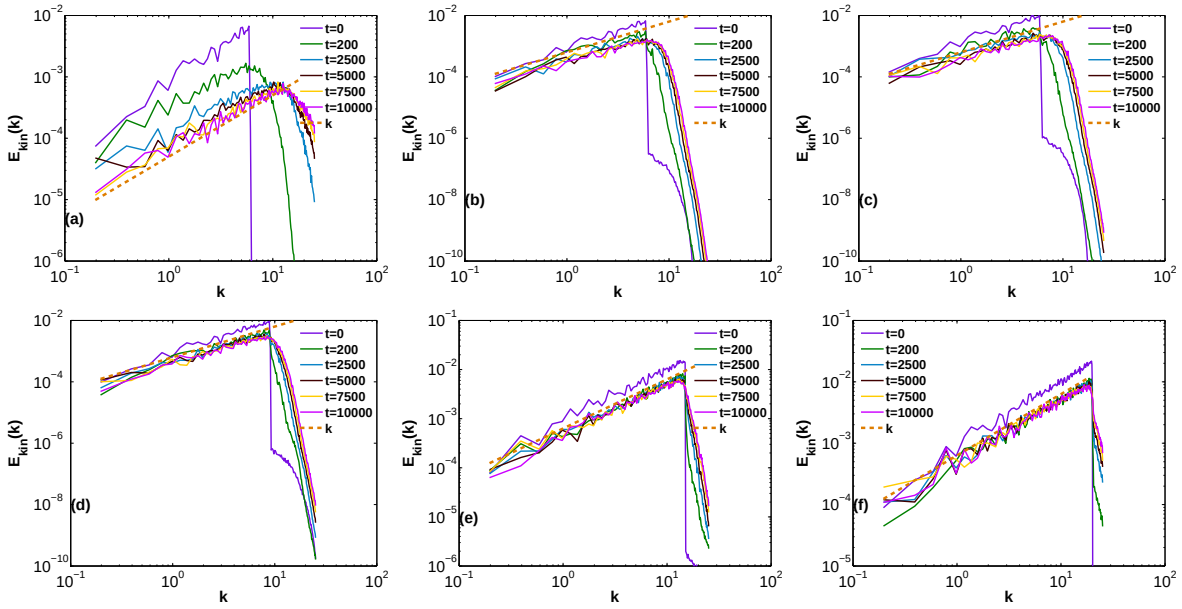

Figure 2.10: Log-log (base 10) plots of the spectra $E_{kin}(k)$ from our DNS runs (initial conditions of type `IC3` (a) `C1`, (b) `C2`, (c) `C3`, (d) `C4`, (e) `C5`, and (f) `C6`.

these two values for α is a convenient measure of the errors of our estimates. For runs `C4`, `C5`, and `C6`, we cannot obtain α_2 reliably; the small values of α_1 for these runs indicate very slow growth of $k_c(t)$; indeed, in runs `C5` and `C6`, a case can be made for a logarithmic growth of $k_c(t)$ with t.

2.3.4 Complete thermalization

The partially thermalized stage of the dynamical evolution of the 2D, Fourier-truncated, GP equation may either gradually become completely thermalized, in

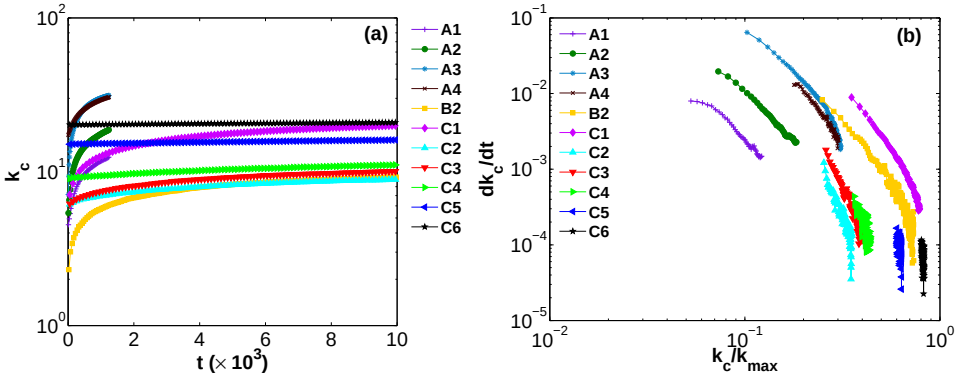

Figure 2.11: Plots of (a) the self-truncation wave-number $k_c(t)$ versus time t and (b) dk_c/dt versus k_c/k_{max} from our DNS runs `A1`-`A4`, `B2`, and `C1`-`C6`.

	E	k_{max}	ξ	ξk_{max}	k_c^i	k_c^f	α_1	α_2
A1	2.120	100.53	1.01	101.73	4.52	12.42	0.28	0.26
A2	3.045	100.53	0.72	71.9	5.39	18.72	0.28	0.28
A3	5.82	100.53	0.45	45.49	7.11	31.3	0.29	0.27
A4	49.69	100.53	1.01	101.73	17.31	30.53	0.2	0.21
B2	0.589	12.57	1.01	12.72	2.23	9.23	0.24	0.25
C1	2.536	25.13	0.45	11.37	7.08	19.91	0.22	0.22
C2	0.583	25.13	1.01	25.43	6.15	8.90	0.12	0.14
C3	0.637	25.13	1.01	25.43	6.18	10.05	0.14	0.15
C4	0.6999	25.13	1.01	25.43	9.05	11.07	0.09	–
C5	1.085	25.13	1.01	25.43	15.09	16.08	0.04	–
C6	1.557	25.13	1.01	25.43	20.17	20.87	0.02	–

Table 2.2: Summary of the self-truncation results from our DNS runs A1-A4, B2, and C1-C6: E is the total energy; $k_{max} = 2\pi N_c/2L$; $\xi = L/\sqrt{g}$ is the healing length; k_c^i and k_c^f are the initial and final values of k_c (averaged over a few time steps); α_1 is the slope obtained from the log-log (base 10) plot of k_c versus t and $\alpha_2 = 1/(1-\chi)$, where χ is the slope obtained from the log-log (base 10) plot of dk_c/dt versus k_c/k_{max}.

which state a power-law scaling region is present in the entire energy and the occupation number spectra, or remain self-truncated with logarithmic growth. In Figs. 2.5 (g)-(i) and 2.6 (a)-(c), we show the compressible kinetic energy spectra E^c_{kin} for the runs B1 and A7, where E^c_{kin} shows power-law scaling over the entire wave number range, from $k = 2\pi/L$ up to k_{max}, towards the end of the respective simulations; a naïve fit is consistent with $E^c_{kin}(k) \sim k$ (but see below).

Correlation functions and the BKT transition

A uniform, 2D, interacting Bose gas exhibits a BKT phase at low energies (temperatures in the canonical ensemble). Thus, the completely thermalized state of the 2D, Fourier-truncated, GP equation should yield a BKT phase [54, 56], with the correlation function $c(r) \sim r^{-\eta}$, at energies $E < E_{BKT}$; and $c(r)$ should decay exponentially with r if $E > E_{BKT}$. We show this explicitly now by using initial conditions of type IC1 with $N_c = 64$ and $N_c = 128$ and $g = 1000$; we obtain different energies by changing k_0 and σ (runs D1-D13 and E1-E12 in Table 2.3).

In Fig. 2.12, we present plots of the correlation functions $c(r)$. To illustrate the BKT transition clearly, we present log-log plots of $c(r)$ versus r, for $E < E_{\rm BKT}$, in Figs. 2.12 (a) and (d), where the straight lines indicate power-law regimes; and, for $E > E_{\rm BKT}$, we use semi-log plots, as in Figs. 2.12 (b) and (e), where the straight lines signify an exponential decay of $c(r)$ with r. Given the resolution of our DNS runs, we find that, in a small energy range in the vicinity of $E_{\rm BKT}$, we cannot fit power-law or exponential forms satisfactorily; this leads to an uncertainty in our estimate for $E_{\rm BKT}$. Aside from this uncertainty, the behavior of $c(r)$, in the regime

$N_c = 128$	k_0 ($\times\Delta k$)	σ ($\times\Delta k$)	E	η	$N_c = 64$	k_0 ($\times\Delta k$)	σ ($\times\Delta k$)	E	η
D1	5	2	2.1	0.008	E1	0	2	1.12	0.012
D2	10	2	5.05	0.024	E2	3	2	1.64	0.025
D3	12	2	6.74	0.034	E3	5	2	2.2	0.040
D4	14	2	8.74	0.047	E4	8	2	3.68	0.083
D5	16	2	11.05	0.080	E5	10	2	5.04	0.164
D6	18	2	13.68	0.111	E6	11	2	5.84	0.255
D7	20	2	16.62	0.181	E7	12	2	6.75	
D8	21	2.5	18.34	0.239	E8	13	2	7.74	
D9	24	3	23.75		E9	14	2	8.78	
D10	25	2	25.3		E10	15	2	9.88	
D11	26	2	27.27		E11	16	2	11.05	
D12	28	2	31.44		E12	17	2	12.32	
D13	30	2	35.9						

Table 2.3: List of parameters for our complete-thermalization DNS runs D1-D13 ($N_c^2 = 128^2$) and E1-E12 ($N_c^2 = 64^2$): N_c^2 is the number of collocation points; k_0 is the energy-injection scale; σ is Fourier-space width of ψ at $t = 0$; E is the total energy; and η is the exponent of the correlation function $c(r) \sim r^{-\eta}$ for $E < E_{BKT}$. $g = 1000$ for all the DNS runs and they have been performed on a square simulation domain of area $\mathcal{A} = L^2$, with $L = 32$.

of complete thermalization, is in accord with our expectations for the BKT phase; in particular, the exponent η (see Eq. (2.18)) depends on E for $E < E_{\rm BKT}$ as shown in Figs. 2.12 (c) and (f). Our values for η, for the runs with $E < E_{\rm BKT}$ and with $N_c = 64$ and $N_c = 128$, are listed in Table 2.3. Note that $E_{\rm BKT} \simeq 6(N_c = 64)$ and $E_{\rm BKT} \simeq 19(N_c = 128)$, i.e., $E_{\rm BKT}$ depends on N_c, the number of collocation points; we show analytically below how a low-temperature analysis can be used to understand this dependence of $E_{\rm BKT}$ on N_c. In the completely thermalized state of the Fourier-truncated, 2D, GP system, N_0 must vanish in the thermodynamic limit by virtue of the Hohenberg-Mermin-Wagner theorem [59, 60] and $n(k) \sim k^{-1+\eta}$; it is not easy to realize this limit in finite-size systems and with the limited run times that are dictated by computational resources (see the plots of N_0 in Fig. 2.3); however, finite-size scaling can be used to extract the exponent η from the $k = 0$ part of $n(k)$ as shown in Ref. [74]; similarly, $E^c_{kin}(k)$ should also show a power-law form with an exponent that depends on η, but this is difficult to realize in numerical calculations with limited spatial resolutions and run lengths.

Analytical estimation of the energy of the BKT transition

The energy of a pure condensate of a uniform, weakly interacting, 2D Bose gas, which is described by the GP equation Eq. (2.1), is $E_0 = g/(2\mathcal{A})$. We define the

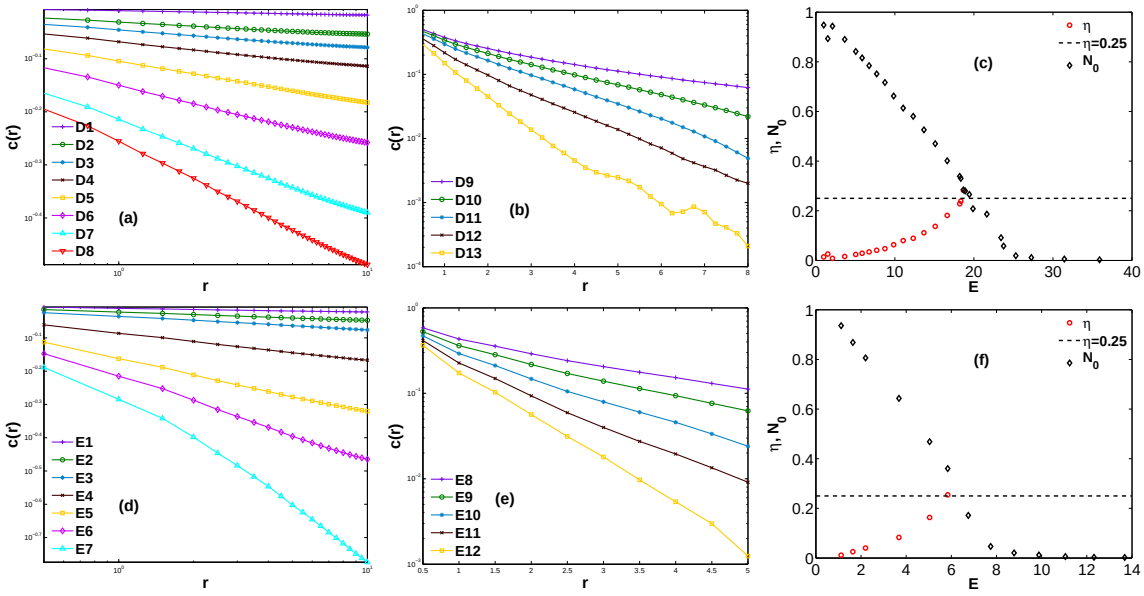

Figure 2.12: Plots of $c(r)$ versus r for different energies in the complete-thermalization regime, for $N_c^2 = 128^2$ ((a) and (b)) and $N_c^2 = 64^2$ ((d) and (e)). (a) and (d) Log-log (base 10) plots of $c(r)$ versus r for different energies $E < E_{KT}$; the slopes of the linear parts of these plots yield the exponent η (Table 2.3); (b) and (e) semilog (base(10) plots of $c(r)$ versus r for different energies $E > E_{KT}$; (c) ($N_c^2 = 128^2$) and (f) ($N_c^2 = 64^2$) show plots of η and N_0 versus E (on the time scales of our runs N_0 is nonzero; see the text for a detailed discussion).

energy of our system to be $E = E_0(1 + \delta\mathcal{E})$; this energy E is fixed by the initial condition; and $\delta\mathcal{E}$ measures the relative amount by which E exceeds E_0. As we show in the Appendix A.2, the N_c dependence of the energy $E_{\rm BKT}$, at which the BKT transition occurs, can be obtained approximately as follows. We begin with

$$\delta\mathcal{E}_{\rm BKT} = \delta\tilde{\mathcal{E}}_{\rm BKT}\frac{8}{\log(\pi^2\,{N_c}^2\,\left(1+\frac{\pi^2\,{N_c}^2}{2\,g}\right))}, \tag{2.28}$$

where $\delta\tilde{\mathcal{E}}_{\rm BKT}$, the estimate for the BKT transition energy that follows from an energy-entropy argument (see Eq. (2.20) in the Appendix and [54]), is

$$\delta\tilde{\mathcal{E}}_{\rm BKT} = \frac{\pi^2\,{N_c}^2}{2\,g} = \frac{\xi^2 k_{\rm max}^2}{2}, \tag{2.29}$$

whence we obtain

$$\delta\mathcal{E}_{\rm BKT} = \frac{4\,k_{\rm max}^2\,\xi^2}{\log(k_{\rm max}^2\,\mathcal{A}\,\left(1+\frac{k_{\rm max}^2\,\xi^2}{2}\right))}. \tag{2.30}$$

We can now write

$$E_{\rm BKT} = E_0\left(1+\frac{4\pi^2 N_c^2}{g\log(\pi^2 N_c^2(1+\frac{\pi^2 N_c^2}{2g}))}\right); \tag{2.31}$$

N_c	E_0	$\delta\tilde{\mathcal{E}}_{\rm BKT}$	$\delta\mathcal{E}_{\rm BKT}$	$E^{\rm A}_{\rm BKT}$	$E^{\rm DNS}_{\rm BKT}$
64	0.488	20.21	11.84	6.27	5.84
128	0.488	80.85	39.44	19.75	18.34

Table 2.4: The values of E_0, $\delta\tilde{\mathcal{E}}_{\rm BKT}$ (see Eq. (2.29)), $\delta\mathcal{E}$ (see Eq. (2.30)), $E^{\rm A}_{\rm BKT}$ (see Eq. (2.31)), and $E^{\rm DNS}_{\rm BKT}$ from our DNS runs D1-D13 ($N_c = 64$) and E1-E12 ($N_c = 64$). E_0 is the ground state energy of a pure condensate of a uniform, interacting, 2D Bose gas and $E^{\rm DNS}_{\rm BKT}$ is BKT-transition energy determined using our DNS runs.

by using this expression we can determine the ratio $E_{\rm BKT}(N_c^a)/E_{\rm BKT}(N_c^b)$ for runs with two different values, N_c^a and N_c^b, for the number of collocation points; we can also obtain this ratio from our DNS, by determining the value of E at which the exponent η becomes $1/4$. In Table 2.4 we compare $E_{\rm BKT}(N_c)$ for $N_c = 64$ and $N_c = 128$; our analytical approximation Eq. (2.31) yields $E^{128}_{\rm BKT}/E^{64}_{\rm BKT} \simeq 3.15$; this is in excellent agreement with the value $\simeq 3.14$ that we obtain for this ratio from our DNS results.

The thermalized state in the run A1 is in the BKT phase, because its total energy $E < E^{1024}_{BKT} = 818.7$ Eq. (2.31); thus, the system should be devoid of any free vortices, so the power-law tails in the velocity PDFs should disappear; this is indeed what we find. By contrast, for the thermalized states with energy $E > E_{BKT}$, free vortices and antivortices are present so the velocity PDFs should show power-law tails, in such states, as we show explicitly in figure F3 in the supplementary material for the run D10, which has $E > E_{BKT}$ in the thermalized state.

2.4 Conclusions

We have carried out an extensive study of the statistical properties of the dissipationless, unforced, 2D, Fourier-truncated, GP equation. Our study has been designed specifically to study and identify the universal features, if any, of the turbulent evolution of the solutions of this equation, by undertaking a systematic DNS. In our study, we have used statistical measures such as velocity-component PDFs and energy and occupation-number spectra, for a large number of initial conditions. To the best of our knowledge, such a comprehensive study of the Fourier-truncated, 2D, GP equation has not been attempted hitherto.

Our comprehensive study of the Fourier-truncated, 2D, GP equation, which makes use of the three types of initial conditions (Sec. 2.2.2) and a wide range of parameters (Tables 2.1 and 2.3), allows us to systematize the dynamical evolution of this system into four different regimes, with qualitatively different statistical properties. This demarkation of the evolution into different regimes has not been systematized in earlier studies, which have concentrated only on one or

two of these regimes. For example, the study of Ref. [40] has investigated states with a significant number of vortex-anitvortex pairs and obtained for them PDFs of velocity components that have power-law tails of the type shown in Fig. 2.2. References [48, 56, 74] have investigated the BKT nature of the thermalized state. Wave-turbulence studies [33, 42, 75] have focussed on power-law regions in energy and occupation-number spectra of the type we find in our third regime. The DNS studies in [42–46, 49, 76] have considered the time evolution of spectra and PDFs for the Fourier-truncated, 2D, GP equation; in some cases, these studies introduce dissipation or hyperviscosity and forcing; they have also reported different power laws in spectra [43, 44, 46]. A recent theoretical and numerical study [49] has studied power-law regimes, associated with metastable transient states in the 2D Gross-Pitaevskii system; it suggests that these power-law regimes occur because of non-thermal fixed points. Our work suggests that, *for the class of initial conditions which we have considered, at least in the dissipationless, unforced, Fourier-truncated, 2D, GP equation*, the only robust power laws in spectra are the the ones we have reported above; all other apparent power laws occur either (a) for very special initial conditions [45] or (b) last for fleetingly small intervals of time and extend over very small ranges of k.

To recapitulate, we find that, in the first dynamical-evolution regime of the Fourier-truncated, 2D, GP equation, there are initial-condition-dependent transients. In the second regime the energy and the occupation-number spectra start to develop power-law scaling regions, but the power-law exponent and the extent of the scaling region change with time and are influenced by the initial conditions. In the third regime, of partial thermalization, we find $E^c_{kin}(k)$ and $E_{int}(k) + E_q(k) \sim k$, and $n(k) \sim 1/k$, for $k < k_c(t)$ and, for $k > k_c$, we find an initial-condition-dependent self-truncation regime, in which the spectra drop rapidly; the self-truncation wave number $k_c(t)$ grows either as t^α or logarithmically for different initial conditions (Table 2.2). In the fourth, complete-thermalization regime, power-law forms of correlation functions and spectra, for $E < E_{\rm BKT}$, are consistent with their nontrivial BKT forms; however, considerable care must be exercised, as explained in Sec. 2.3.4 and [48, 56, 74], to distinguish these nontrivial power laws from their wave-turbulence analogs [33, 42, 75].

We have calculated a variety of order-p structure functions in our study; a full analysis of these structure functions lies outside the scope of this chapter. However, we comment briefly on the use of the extended-self-similarity (ESS) procedure [77–79] here. Recall that, in the ESS procedure, log-log plots of the order-p structure functions $S_p(r)$ versus the third-order structure function $S_3(r)$ extend the

scaling region, and their slopes yield estimates for the multiscaling exponent ratios ζ_p/ζ_3 that are better than the estimates of ζ_p obtained from slopes of log-log plots of $S_p(r)$ versus r; this procedure is especially valuable if $\zeta_3 = 1$, as it is in 3D fluid turbulence, by virtue of the von Kármán-Howarth relation. We have calculated structure functions [80] of the ψ [81], velocity, and vorticity fields in the 2D, Fourier-truncated, Gross-Pitaevskii equation. The ESS procedure works here insofar as it extends the range over which scaling occurs; however, the exponents that follow from such plots evolve in time in a manner that mirrors the evolution of the spectral exponents that we have described above. A full elucidation of ESS and multiscaling in the 2D, Fourier-truncated, Gross-Pitaevskii system will be presented elsewhere [82].

1 Supplementary Material

In Fig. F1, we have plotted the time evolution of the total number of vortices N_v for our DNS runs `A1`-`A3`.

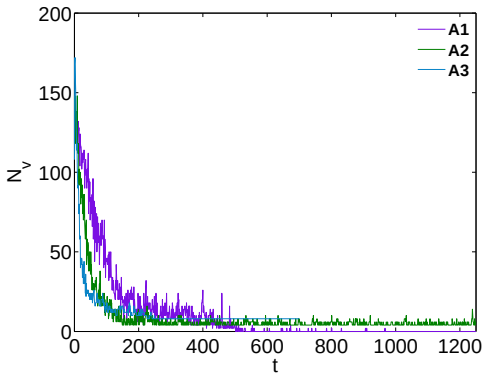

Figure F1: Plots showing the time evolution of the total number of vortices N_v (both vortices and antivortices) from our DNS runs `A1` (purple curve), `A2` (green curve) and `A3` (sky-blue curve).

Figure F2 shows the time evolution of $k_{hd}(t)$ for the DNS runs `A1`-`A3`.

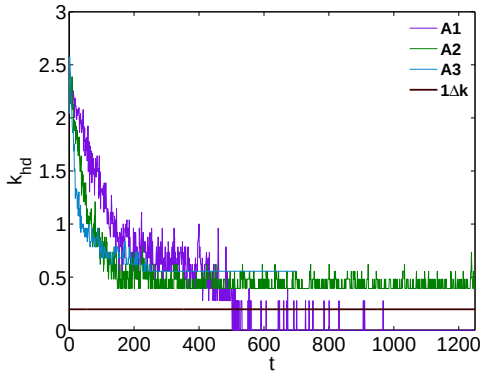

Figure F2: Plot showing the time evolution of the wave number k_{hd} from our DNS runs `A1` (purple curve), `A2` (green curve) and `A3` (sky-blue curve); here, $k_{hd} = 2\pi\lambda^{1/2} = N_v^{1/2}\Delta k$. A brown horizontal line represents the wave number $k = 1\Delta k$, which is related to the inverse of the system-size length scale.

Figure F3 shows the PDFs of v_x and v_y, the Cartesian components of the velocity, for our DNS runs `D10` ($E^{\texttt{D10}} > E^{128^2}_{BKT}$, see table 4 in the main text) at $t = 9500$.

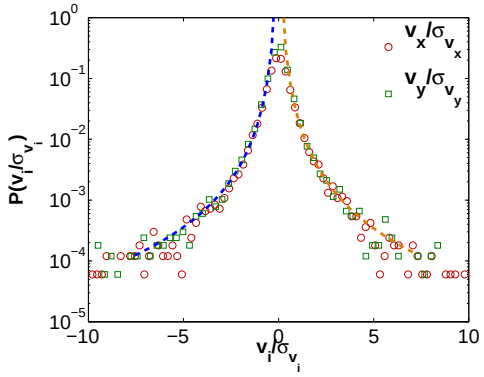

Figure F3: Semilog (base 10) plots of the PDFs of the x (red circles) and y (green squares) components of the velocity from our DNS run `D10` ($N_c = 128$) at $t = 9500$, corresponding to the initial condition of type `IC1` (see table 4 in the main text). The dashed lines indicate power-law fits ($\sim v_i^{-\gamma}$) to the left (blue-dashed line, $\gamma = 2.6$) and right (orange-dashed line, $\gamma = 2.6$) tails of the PDFs, we show fits only for $i = x$.

Video M1 This video illustrates the time evolutions, from our DNS run `A1`, of the following: [top left panel] semilog (base 10) plots of the PDFs of the x (red circles) and y (green squares) components of the velocity (cf. Fig. 2.2(a)-(c)); [top right panel] pseudocolor plots of the vorticity $\omega = \nabla \times \mathbf{v}$ (with high-k modes filtered out); [bottom left panel] log-log (base 10) plots of the spectra $E^i_{kin}(k)$, $E^c_{kin}(k)$, and $E_q(k) + E_{int}(k)$ (cf. Figs. 2.4(a), 2.5(a)-(c), and 2.7 (a)-(c); the orange-dashed line shows a k power-law behaviour); [bottom right panel] log-log (base 10) plots of the spectra $n(k)$ (cf. Figs. 2.8 (a)-(c); a k^{-1} power law is shown by the orange-dashed line).

Video M2 This video illustrates the time evolution of log-log (base 10) plots of the compensated, incompressible kinetic energy spectra $k^{5/3}E^i_{kin}(k)$ from our DNS runs `A1` (purple curve), `A2` (green curve), `A3` (sky-blue curve), and `A4` (brown curve); a $k^{-5/3}$ power law in $E^i_{kin}(k)$ is shown by the orange-dashed line to guide the eye (for uncompensated versions of these spectra see Figs. 2.4 (a)-(d)).

Video M3 This video illustrates the time evolution of log-log (base 10) plots of the spectrum $E_{kin}(k)$ from the following DNS runs: [`panel V1`] - `A1` (purple curve), `A2` (green curve), and `A3` (sky-blue curve); [`panel V2`] `A6` (purple curve), `A9` (green curve), and `A10` (sky-blue curve); [`panel V3`] `A11` (purple curve), `A12` (green curve), and `A13` (sky-blue curve); [`panel V4`] `A1` and `A5`-`A8` (with $N_c^2 = 1024^2$, 512^2, 256^2, 128^2, and 64^2).

Appendix A

A.1 Note on units

The GP equation, which describes the dynamical evolution of the wave function $\psi(\mathbf{x}, t)$ of a weakly interacting, 2D Bose gas at low temperatures, is

$$i\hbar\frac{\partial\psi(\mathbf{x},t)}{\partial t} = -\frac{\hbar^2}{2m}\nabla^2\psi(\mathbf{x},t) + g_{2\mathrm{D}}|\psi|^2\psi(\mathbf{x},t), \tag{A.1}$$

where g_{2D} is the effective interaction strength. As we have mentioned earlier (see Eqs. (2.2) and 2.3), the GP equation conserves the energy, given by the Hamiltonian

$$H = \int_{\mathcal{A}} d^2x \left(\frac{\hbar^2}{2m}|\nabla\psi|^2 + \frac{g_{2\mathrm{d}}}{2}|\psi|^4\right), \tag{A.2}$$

and the total number of particles $n = \int_{\mathcal{A}} |\psi|^2 d^2x$. To obtain Eq. (2.1), we first divide Eq. (A.1) by $\hbar$ and define $g = g_{2\mathrm{D}}/\hbar$; we then set $\hbar/2m = 1$, with $m = 1$, so that $|\psi|^2$ is the same as ρ; this is tantamount to using units with $\hbar = 2$. The energy of the system, as expressed in Eq. (2.2), is obtained by dividing the Eq. (A.2) by $\hbar = 2$. A comparison with the experimental values can be made by noting that the healing energy $E_h = \hbar^2/(2m\xi^2)$; in our units this is simply $E_h = 1/\xi^2$; ξ depends on g through equation (16); and g is related to $g_{2\mathrm{D}}$ as mentioned above. The interaction strength $g_{2\mathrm{D}}$ depends, *inter alia*, on the scattering length of the 2D interaction potential and the size of the BEC-cloud; for more details about the actual form of $g_{2\mathrm{D}}$ in two dimensions see [58]. The wave number $k = n_i\Delta k$, where $\Delta k = 2\pi/L$ and $n_i = 0, 1, 2, ...$; L is the length of the side of a square simulation domain.

A.2 Standard results on the BKT transition

The Berezinskii-Kosterlitz-Thouless (BKT) transition is best studied by using the renormalization group [54]; here, we restrict ourselves to the heuristic, energy-entropy argument to obtain a rough estimate of the BKT transition temperature

$T_{\rm BKT}$. In the XY model, this transition is studied by using the Hamiltonian

$$H_{\rm XY} = -J \sum_{<i,j>} \cos(\theta_i - \theta_j), \tag{A.3}$$

where $< i, j >$ denotes nearest-neighbour pairs of sites, on a 2D square lattice, J is the nearest-neighbour exchange coupling, and $(\theta_i - \theta_j)$ is the angle between the nearest-neighbour, XY spins on sites i and j. In the continuum limit, the above Hamiltonian becomes, to lowest order in spatial gradients,

$$H_{\rm XY} = \frac{J}{2} \int d^2x (\nabla\theta(x))^2. \tag{A.4}$$

By comparing Eq. (A.4) with the kinetic-energy term in Eq. (A.1), we find that

$$J = \frac{|\langle\psi\rangle|^2\hbar^2}{m} = \frac{\rho\Gamma^2}{(2\pi)^2}, \tag{A.5}$$

where Γ denotes the Onsager-Feynman quantum of velocity circulation $\Gamma = 4\pi\hbar/2m = h/m$. A rough estimate for the BKT transition temperature $T_{\rm BKT}$ is given below:

$$\tilde{T}_{\rm BKT} = \frac{\pi J}{2k_B} = \frac{\pi \mid \langle\psi\rangle \mid^2 \hbar^2}{2mk_B} = \frac{\rho\Gamma^2}{8\pi k_B}, \tag{A.6}$$

here $\tilde{T}_{\rm BKT}$ denotes the estimate for $T_{\rm BKT}$ that follows from an energy-entropy argument [54]. For $T < T_{\rm BKT}$, the phase correlation function $c(r)$ (see Eq. (2.17)) and the angle-integrated spectrum $\hat{c}(k)$, which follows from a Fourier transform of $c(r)$, scale as

$$c(r) \sim (a/r)^{\frac{T}{4T_{\rm BKT}}} \tag{A.7}$$

and

$$\hat{c}(k) \sim k^{-1+\frac{T}{4T_{\rm BKT}}}, \tag{A.8}$$

respectively. Above $T_{\rm BKT}$ the correlation length

$$\ell = \frac{\int k^{-1}E(k)dk}{\int E(k)dk} \tag{A.9}$$

is finite; and, as $T \to T_{\rm BKT}$, it displays the essential singularity

$$\ell \sim \exp(b(T_{\rm BKT}/(T - T_{\rm BKT}))^{1/2}). \tag{A.10}$$

A.2.1 Low-temperature thermodynamical computations

We now develop an analytical framework, which is valid at low-temperatures $T \ll T_{\rm BKT}$, that can be used to test some of the results of our DNS runs in the region of complete thermalization. We first calculate equilibrium thermodynamic functions

for a weakly-interacting, 2D Bose gas, in the grand-canonical ensemble; we then obtain their analogues in the microcanonical ensemble. In the grand-canonical ensemble the probability of a given state is

$$\mathbb{P} = \frac{1}{\Xi} e^{-\beta(H-\mu N)}, \tag{A.11}$$

where Ξ is the grand partition function, β the inverse temperature, μ the chemical potential, and N the number of bosons. The grand-canonical potential is

$$\Omega = -\beta^{-1} \log(\Xi); \tag{A.12}$$

and the mean energy E, entropy S, and N are

$$N = -\frac{\partial \Omega}{\partial \mu}, \tag{A.13a}$$

$$S = \beta^2 \partial \Omega / \partial \beta, \tag{A.13b}$$

$$E = \frac{\partial \Omega}{\partial \beta} + \mu N = \frac{S}{\beta} + \mu N. \tag{A.13c}$$

We adapt to 2D the 3D study of Ref. [53], expand ψ in terms of Fourier modes $A_{\mathbf{k}}$, and obtain Ω as the sum of the saddle-point part Ω_{sp} and Ω_Q, the deviations from the saddle point that are quadratic in $A_{\mathbf{k}}$. We write $\Omega = \Omega_{sp} + \Omega_Q$, where $\Omega_{sp} = -\mathcal{A}\mu^2/2g$ and

$$\Omega_Q = -\int_0^{p_{\max}} \frac{\left(p\mathcal{A} \log(\frac{2m}{\beta\sqrt{p^4+4mp^2\mu}}) \right)}{2\pi\beta\hbar^2}. \tag{A.14}$$

We can also calculate the condensate depletion δN, where the particle number $N = N_0 + \delta N$ and N_0 is the number of particles in the $k = 0$ mode, as follows:

$$\delta N = \int_0^{p_{\max}} \frac{mp\mathcal{A} \left(p^{-2} + \frac{1}{p^2+4m\mu} \right)}{2\pi\beta\hbar^2}. \tag{A.15}$$

The integrals in the Eqs. (A.14) and (A.15) can be performed analytically, but, in contrast to the 3D case where the primitives are zero at $p = 0$, the $2D$ primitive for $\Omega_{\rm ph}$ is finite at $p = 0$ and for δN it is infra-red (I.R.) divergent. By subtracting the I.R. finite and divergent terms from Ω_Q and δN, respectively, we get the following expressions, in $2D$, in the thermodynamic limit $\mathcal{A} \to \infty$:

$$\begin{aligned} \Omega = &-\frac{\mu^2\mathcal{A}}{2g} - \frac{p_{\max}^2\mathcal{A}}{4\pi\beta\hbar^2} + \frac{m\mu\mathcal{A}\log(1+\frac{p_{\max}^2}{4m\mu})}{2\pi\beta\hbar^2} \\ &- \frac{p_{\max}^2\mathcal{A}\log(\frac{2m}{\beta\sqrt{p_{\max}^4+4m\mu p_{\max}^2}})}{4\pi\beta\hbar^2} \end{aligned} \tag{A.16}$$

and

$$\delta N = \frac{m\mathcal{A}\left(\log(1+\frac{p_{\max}^2}{4m\mu})+\log(\frac{p_{\max}^2\mathcal{A}}{\hbar^2})\right)}{4\pi\beta\hbar^2}. \tag{A.17}$$

By using the thermodynamic relations Eq. (A.13), we get

$$N = \frac{\mu\mathcal{A}}{g} - \frac{m\mathcal{A}\log(1+\frac{p_{\max}^2}{4m\mu})}{2\pi\beta\hbar^2} \tag{A.18}$$

and

$$E = \frac{\mu^2\mathcal{A}}{2g} + \frac{p_{\max}^2\mathcal{A}}{4\pi\beta\hbar^2} - \frac{m\mu\mathcal{A}\log(1+\frac{p_{\max}^2}{4m\mu})}{2\pi\beta\hbar^2}. \tag{A.19}$$

A.2.2 Low-temperature results at given density

We next determine the chemical potential μ, which fixes the total density $\rho = mN/\mathcal{A}$ at a given value, by solving the equation

$$\rho - \frac{m\mu}{g} + \frac{m^2\log(1+\frac{p_{\max}^2}{4m\mu})}{2\pi\beta\hbar^2} = 0; \tag{A.20}$$

at $\beta = \infty$, i.e., zero temperature (subscript 0) we obtain

$$\mu_0 = \frac{g\,\rho}{m}; \tag{A.21}$$

to order β^{-1} we get

$$\mu = \mu_0 + \delta\mu, \tag{A.22}$$

where

$$\delta\mu = \frac{mg\,(4g\rho^2+\rho p_{\max}^2)\log(1+\frac{p_{\max}^2}{4g\rho})}{m^2p_{\max}^2+2\pi\beta\hbar^2\rho p_{\max}^2+8\pi\beta\hbar^2g\rho^2}. \tag{A.23}$$

We insert μ from Eq. (A.22) into Eq. (A.17), define the change in density $\delta\rho = m\delta N/\mathcal{A}$, use the energy E from Eq. (A.19), and then expand to order β^{-1} to obtain

$$\delta\rho = \frac{m^2\left(\log(1+\frac{p_{\max}^2}{4g\rho})+\log(\frac{p_{\max}^2\mathcal{A}}{\hbar^2})\right)}{4\pi\beta\hbar^2} \tag{A.24}$$

and

$$E = \frac{g\rho^2\mathcal{A}}{2m^2} + \frac{p_{\max}^2\mathcal{A}}{4\pi\beta\hbar^2}. \tag{A.25}$$

By using Eq. (A.6) and $\rho = m \mid \langle\psi\rangle \mid^2$, we obtain

$$\tilde{\beta}_{\rm BKT} = \frac{1}{k_{\rm B}\tilde{T}_{\rm BKT}} = \frac{2m^2}{\pi\rho\hbar^2}, \tag{A.26}$$

which we can use along with Eq. (A.24) to relate the condensate relative depletion $\delta\rho/\rho$ to $\beta/\tilde{\beta}_{\rm BKT}$, where $\beta = 1/(k_{\rm B}T)$ and $k_{\rm B}$ is the Boltzmann constant, as given below:

$$\frac{\delta\rho}{\rho} = \frac{\tilde{\beta}_{\rm BKT}}{8\beta} \log\left(\frac{p_{\rm max}^2\left(1+\frac{p_{\rm max}^2}{4g\rho}\right)\mathcal{A}}{\hbar^2}\right). \tag{A.27}$$

We use this low-temperature result Eq. (A.27) to estimate the inverse-temperature scale $\beta_{\rm BKT}$, at which the depletion of the $k = 0$ condensate mode becomes significant for a finite-size system with N_c^2 collocation points (which fixes the maximum momentum $p_{\rm max}$); in particular, we can solve Eq. (A.27), for $\delta\rho/\rho = 1$, to obtain

$$\frac{\beta_{\rm BKT}}{\tilde{\beta}_{\rm BKT}} = \frac{1}{8} \log\left(\frac{p_{\rm max}^2\left(1+\frac{p_{\rm max}^2}{4g\rho}\right)\mathcal{A}}{\hbar^2}\right). \tag{A.28}$$

By making the replacements that correspond do defining $\hbar$, m, and g in terms of c and ξ, as in [53], $p_{\rm max} \to \hbar k_{\rm max}$, $\hbar \to \sqrt{2}cm\xi$, and $g \to c^2m^2/\rho$, we can rewrite Eq. (A.28) as

$$\frac{\beta_{\rm BKT}}{\tilde{\beta}_{\rm BKT}} = \frac{1}{8} \log\left(k_{\rm max}^2\mathcal{A}\,(1+\frac{{k_{\rm max}}^2\,\xi^2}{2})\right). \tag{A.29}$$

A.2.3 Results expressed in terms of energy increase

Our DNS runs, which use initial conditions of type `IC1` and `IC2`, give the dynamical evolutions of the Fourier-truncated, 2D GP equation, which is a Hamiltonian system. The energy E, particle number N, and area $\mathcal{A}$ are conserved in this evolution, so our calculation can be viewed as a simulation of this Hamiltonian system in the microcanonical ensemble, which yields, eventually, the fully thermalized state that we have described above. Therefore, we now transform the results, which we have obtained in the previous subsection, into their counterparts in the microcanonical ensemble. In the low-temperature limit, Eq. (A.25) yields

$$\beta = \frac{m^2\,p_{\rm max}^2\,\mathcal{A}}{2\pi\hbar^2\,(2m^2E - g\rho^2\mathcal{A})}. \tag{A.30}$$

The energy of a pure condensate is

$$E_0 = \lim_{\beta\to\infty} E = \frac{g\,\rho^2\,\mathcal{A}}{2\,m^2}; \tag{A.31}$$

and the energy and the inverse temperature β Eq. (A.30) can be related as follows:

$$E = E_0(1+\delta\mathcal{E}), \tag{A.32}$$

where $\delta\mathcal{E}$ is the relative increase of energy above E_0, and

$$\beta = \frac{m^2\, p_{\rm max}^2}{2\pi\hbar^2 g\rho^2\delta\mathcal{E}}. \tag{A.33}$$

If we now substitute $\beta = \beta_{\rm BKT}$ by using Eq. (A.28), we obtain, in terms of c, ξ and ρ (see text just below Eq. (A.28))

$$E_0 = \frac{c^2\,\rho\,\mathcal{A}}{2}, \tag{A.34}$$

$$\delta\tilde{\mathcal{E}}_{\rm BKT} = \frac{k_{\rm max}^2\xi^2}{2}, \tag{A.35}$$

and

$$\delta\mathcal{E}_{\rm BKT} = \frac{4k_{\rm max}^2\xi^2}{\log\left(k_{\rm max}^2\mathcal{A}(1+\frac{k_{\rm max}^2\xi^2}{2})\right)}. \tag{A.36}$$

All the energies mentioned in the main chapter are dimensionless; thus, to convert the energies given in this Appendix to dimensionless forms, we divide them by $\hbar$. Hence, the energy of a pure condensate is obtained, in the dimensionless form, by dividing Eq. (A.31) by $\hbar$, which gives

$$E_0 = \frac{g}{2\mathcal{A}} = \frac{1}{2}\frac{g}{L^2}. \tag{A.37}$$

Bibliography

[1] V. Shukla, M. Brachet, and R. Pandit. Turbulence in the two-dimensional Fourier-truncated Gross-Pitaevskii equation. *New J. Phys.*, 15(11):113025, 2013.

[2] R. P. Feynman. Application of quantum mechanics to liquid helium. In C. J. Gorter, editor, *Progress in Low Temperature Physics*, volume I, page 17. North-Holland, Amsterdam, 1955.

[3] W. F. Vinen. Mutual Friction in a Heat Current in Liquid Helium II. I. Experiments on Steady Heat Currents. *Proc. Roy. Soc. A*, 240(1220):114–127, April 1957.

[4] W. F. Vinen. Mutual Friction in a Heat Current in Liquid Helium II. II. Experiments on Transient Effects. *Proc. Roy. Soc. A*, 240(1220):128–143, April 1957.

[5] W. F. Vinen. Mutual Friction in a Heat Current in Liquid Helium II. III. Theory of the Mutual Friction. *Proc. Roy. Soc. A*, 242(1231):493–515, November 1957.

[6] D. R. Tilley and J. Tilley. *Superfluidity and Superconductivity*. IOP Publishing, Bristol, 3 edition, 1990.

[7] R.J. Donnelly. *Quantized vortices in helium II*, volume 3. Cambridge University Press, 1991.

[8] C. F. Barenghi, R. J. Donnelly, and W. F. Vinen, editors. *Quantized Vortex Dynamics and Superfluid Turbulence*, volume 571 of *Lecture Notes in Physics, Berlin Springer Verlag*, 2001.

[9] W. F. Vinen and J. J. Niemela. Quantum turbulence. *J. Low Temp. Phys.*, 128(5):167–231, 2002.

[10] J. J. Niemela. Reconnecting to superfluid turbulence. *Physics*, 1:26, Oct 2008.

[11] I. Procaccia and K. R. Sreenivasan. The state of the art in hydrodynamic turbulence: Past successes and future challenges. *Physica D*, 237(1417):2167 – 2183, 2008. Euler Equations: 250 Years On – Proceedings of an international conference.

[12] M. Tsubota. Quantum Turbulence. *J. Phys. Soc. Jpn.*, 77(11):111006, 2008.

[13] M. S. Paoletti and D. P. Lathrop. Quantum turbulence. *Annu. Rev. Condens. Matter Phys.*, 2:213–234, March 2011.

[14] L. Skrbek and K. R. Sreenivasan. Developed quantum turbulence and its decay. *Phys. Fluids*, 24:011301, 2012.

[15] J. Maurer and P. Tabeling. Local investigation of superfluid turbulence. *Europhys. Lett.*, 43(1):29, 1998.

[16] M. R. Smith, R. J. Donnelly, N. Goldenfeld, and W. F. Vinen. Decay of vorticity in homogeneous turbulence. *Phys. Rev. Lett.*, 71:2583–2586, Oct 1993.

[17] S. R. Stalp, L. Skrbek, and R. J. Donnelly. Decay of Grid Turbulence in a Finite Channel. *Phys. Rev. Lett.*, 82:4831–4834, Jun 1999.

[18] L. Skrbek, J. J. Niemela, and R. J. Donnelly. Four Regimes of Decaying Grid Turbulence in a Finite Channel. *Phys. Rev. Lett.*, 85:2973–2976, Oct 2000.

[19] L. Skrbek and S. R. Stalp. On the decay of homogeneous isotropic turbulence. *Phys. Fluids*, 12(8):1997–2019, 2000.

[20] S. R. Stalp, J. J. Niemela1, W. F. Vinen, and R. J. Donnelly. Dissipation of grid turbulence in helium II. *Phys. Fluids*, 14(4):1377–1379, 2002.

[21] S. N. Fisher, A. J. Hale, A. M. Guénault, and G. R. Pickett. Generation and Detection of Quantum Turbulence in Superfluid $^3He - B$. *Phys. Rev. Lett.*, 86:244–247, Jan 2001.

[22] E. A. L. Henn, J. A. Seman, G. Roati, K. M. F. Magalhães, and V. S. Bagnato. Emergence of Turbulence in an Oscillating Bose-Einstein Condensate. *Phys. Rev. Lett.*, 103:045301, Jul 2009.

[23] T. W. Neely, A. S. Bradley, E. C. Samson, S. J. Rooney, E. M. Wright, K. J. H. Law, R. Carretero-González, P. G. Kevrekidis, M. J. Davis, and B. P. Anderson. Characteristics of Two-Dimensional Quantum Turbulence in a Compressible Superfluid. *Phys. Rev. Lett.*, 111:235301, Dec 2013.

[24] C. Sun, S. Jia, C. Barsi, S. Rica, A. Picozzi, and J. W. Fleischer. Observation of the kinetic condensation of classical waves. *Nat. Phys.*, 8:470474, 2012.

[25] P.-E. Roche, C. F. Barenghi, and E. Leveque. Quantum turbulence at finite temperature: The two-fluids cascade. *Europhys. Lett.*, 87(5):54006, 2009.

[26] J. Salort, P.-E. Roche, and E. Lévêque. Mesoscale equipartition of kinetic energy in quantum turbulence. *Europhys. Lett.*, 94(2):24001, 2011.

[27] K. W. Schwarz. Three-dimensional vortex dynamics in superfluid ^{4}He: Line-line and line-boundary interactions. *Phys. Rev. B*, 31:5782–5804, May 1985.

[28] K. W. Schwarz. Three-dimensional vortex dynamics in superfluid ^{4}He: Homogeneous superfluid turbulence. *Phys. Rev. B*, 38:2398–2417, Aug 1988.

[29] C. F. Barenghi and D. C. Samuels. Self-consistent decay of superfluid turbulence. *Phys. Rev. B*, 60:1252–1260, Jul 1999.

[30] H. Adachi, S. Fujiyama, and M. Tsubota. Steady-state counterflow quantum turbulence: Simulation of vortex filaments using the full Biot-Savart law. *Phys. Rev. B*, 81:104511, Mar 2010.

[31] Yu. M. Kagan, B. V. Svistunov, and G. V. Shlyapnikov. Kinetics of Bose condensation in an interacting Bose gas. *Sov. Phys. JETP*, 75(2):387, August 1992.

[32] V. E. Zakharov and S. V. Nazarenko. Dynamics of the Bose-Einstein condensation. *Physica D*, 201:203–211, 2005.

[33] B. V. Svistunov. Highly nonequilibrium Bose condensation in a weakly interacting gas. *J. Moscow Phys. Soc.*, 1:373, 1991.

[34] Yu. Lvov, S. V. Nazarenko, and R. J. West. Wave turbulence in Bose-Einstein condensates. *Physica D*, 184:333 – 351, 2003.

[35] J. Koplik and H. Levine. Vortex reconnection in superfluid helium. *Phys. Rev. Lett.*, 71:1375–1378, Aug 1993.

[36] C. Nore, M. Abid, and M. E. Brachet. Kolmogorov Turbulence in Low-Temperature Superflows. *Phys. Rev. Lett.*, 78:3896–3899, May 1997.

[37] N. G. Berloff and B. V. Svistunov. Scenario of strongly nonequilibrated Bose-Einstein condensation. *Phys. Rev. A*, 66:013603, Jul 2002.

[38] M. Kobayashi and M. Tsubota. Kolmogorov Spectrum of Superfluid Turbulence: Numerical Analysis of the Gross-Pitaevskii Equation with a Small-Scale Dissipation. *Phys. Rev. Lett.*, 94:065302, Feb 2005.

[39] G. Krstulovic and M. Brachet. Dispersive Bottleneck Delaying Thermalization of Turbulent Bose-Einstein Condensates. *Phys. Rev. Lett.*, 106:115303, Mar 2011.

[40] A. C. White, C. F. Barenghi, N. P. Proukakis, A. J. Youd, and D. H. Wacks. Nonclassical Velocity Statistics in a Turbulent Atomic Bose-Einstein Condensate. *Phys. Rev. Lett.*, 104:075301, Feb 2010.

[41] C. Connaughton, C. Josserand, A. Picozzi, Y. Pomeau, and S. Rica. Condensation of Classical Nonlinear Waves. *Phys. Rev. Lett.*, 95:263901, Dec 2005.

[42] S. Nazarenko and M. Onorato. Freely decaying turbulence and Bose-Einstein condensation in Gross-Pitaevski model. *J. Low Temp Phys.*, 146:31–46, Jan 2007.

[43] R. Numasato, M. Tsubota, and V. S. L'vov. Direct energy cascade in two-dimensional compressible quantum turbulence. *Phys. Rev. A*, 81:063630, Jun 2010.

[44] B. Nowak, D. Sexty, and T. Gasenzer. Superfluid turbulence: Nonthermal fixed point in an ultracold Bose gas. *Phys. Rev. B*, 84:020506, Jul 2011.

[45] A. S. Bradley and B. P. Anderson. Energy Spectra of Vortex Distributions in Two-Dimensional Quantum Turbulence. *Phys. Rev. X*, 2:041001, Oct 2012.

[46] B. Nowak, J. Schole, D. Sexty, and T. Gasenzer. Nonthermal fixed points, vortex statistics, and superfluid turbulence in an ultracold Bose gas. *Phys. Rev. A*, 85:043627, Apr 2012.

[47] M. T. Reeves, B. P. Anderson, and A. S. Bradley. Classical and quantum regimes of two-dimensional turbulence in trapped Bose-Einstein condensates. *Phys. Rev. A*, 86:053621, Nov 2012.

[48] E. Small, R. Pugatch, and Y. Silberberg. Berezinskii-Kosterlitz-Thouless crossover in a photonic lattice. *Phys. Rev. A*, 83:013806, Jan 2011.

[49] Jan Schole, Boris Nowak, and Thomas Gasenzer. Critical dynamics of a two-dimensional superfluid near a nonthermal fixed point. *Phys. Rev. A*, 86:013624, Jul 2012.

[50] C. Cichowlas, P. Bonaïti, F. Debbasch, and M. Brachet. Effective Dissipation and Turbulence in Spectrally Truncated Euler Flows. *Phys. Rev. Lett.*, 95:264502, Dec 2005.

[51] U. Frisch, S. Kurien, R. Pandit, W. Pauls, S. S. Ray, A. Wirth, and J.-Z. Zhu. Hyperviscosity, Galerkin Truncation, and Bottlenecks in Turbulence. *Phys. Rev. Lett.*, 101:144501, Sep 2008.

[52] S. S. Ray, U. Frisch, S. Nazarenko, and T. Matsumoto. Resonance phenomenon for the Galerkin-truncated Burgers and Euler equations. *Phys. Rev. E*, 84:016301, Jul 2011.

[53] G. Krstulovic and M. Brachet. Energy cascade with small-scale thermalization, counterflow metastability, and anomalous velocity of vortex rings in Fourier-truncated Gross-Pitaevskii equation. *Phys. Rev. E*, 83:066311, Jun 2011.

[54] J. B. Kogut. An introduction to lattice gauge theory and spin systems. *Rev. Mod. Phys.*, 51:659–713, Oct 1979.

[55] P. M. Chaikin and T. C. Lubensky. *Principles of Condensed Matter Physics*. Cambridge University Press, Cambridge, 1995.

[56] C. J. Foster, P. B. Blakie, and M. J. Davis. Vortex pairing in two-dimensional Bose gases. *Phys. Rev. A*, 81:023623, Feb 2010.

[57] C. J. Pethick and H. Smith. *Bose-Einstein condensation in dilute gases*. Cambridge university press, 2001.

[58] A. Posazhennikova. Colloquium: Weakly interacting, dilute Bose gases in 2D. *Rev. Mod. Phys.*, 78:1111–1134, Oct 2006.

[59] N. D. Mermin and H. Wagner. Absence of Ferromagnetism or Antiferromagnetism in One- or Two-Dimensional Isotropic Heisenberg Models. *Phys. Rev. Lett.*, 17:1133–1136, Nov 1966.

[60] P. C. Hohenberg. Existence of Long-Range Order in One and Two Dimensions. *Phys. Rev.*, 158:383–386, June 1967.

[61] V. L. Berezinskii. Destruction of Long-range Order in One-dimensional and Two-dimensional Systems having a Continuous Symmetry Group I. Classical Systems. *Sov. Phys. JETP*, 32(3):493, March 1971.

[62] J. M. Kosterlitz and D. J. Thouless. Ordering, metastability and phase transitions in two-dimensional systems. *J. Phys. C*, 6(7):1181, 1973.

[63] `http://www.fftw.org`.

[64] A. Minguzzi, S. Succi, F. Toschi, M.P. Tosi, and P. Vignolo. Numerical methods for atomic quantum gases with applications to Bose-Einstein condensates and to ultracold fermions. *Phys. Rep.*, 395(45):223 – 355, 2004.

[65] U. Frisch, S. S. Ray, G. Sahoo, D. Banerjee, and R. Pandit. Real-Space Manifestations of Bottlenecks in Turbulence Spectra. *Phys. Rev. Lett.*, 110:064501, Feb 2013.

[66] R. Kubo. The fluctuation-dissipation theorem. *Rep. Prog. Phys.*, 29(1):255, 1966.

[67] M. Miguel and R. Toral. Stochastic Effects in Physical Systems. In Enrique Tirapegui, Javier Martnez, and Rolando Tiemann, editors, *Instabilities and Nonequilibrium Structures VI*, volume 5 of *Nonlinear Phenomena and Complex Systems*, pages 35–127. Springer Netherlands, 2000.

[68] M. Abid, C. Huepe, S. Metens, C. Nore, C. T. Pham, L. S. Tuckerman, and M. E. Brachet. Gross-Pitaevskii dynamics of Bose-Einstein condensates and superfluid turbulence. *Fluid Dyn. Res.*, 33(5-6):509, 2003.

[69] M. S. Paoletti, M. E. Fisher, K. R. Sreenivasan, and D. P. Lathrop. Velocity Statistics Distinguish Quantum Turbulence from Classical Turbulence. *Phys. Rev. Lett.*, 101:154501, Oct 2008.

[70] H. Adachi and M. Tsubota. Numerical study of velocity statistics in steady counterflow quantum turbulence. *Phys. Rev. B*, 83:132503, Apr 2011.

[71] P. Davide, S. Nazarenko, and M. Onorato. Sustained turbulence in the three-dimensional Gross-Pitaevskii model. *Physica D*, 241(3):304 – 314, 2012. Special Issue on Small Scale Turbulence.

[72] A. W. Baggaley and C. F. Barenghi. Quantum turbulent velocity statistics and quasiclassical limit. *Phys. Rev. E*, 84:067301, Dec 2011.

[73] G. Düring, A. Picozzi, and S. Rica. Breakdown of weak-turbulence and nonlinear wave condensation. *Physica D*, 238(16):1524 – 1549, 2009.

[74] K. Damle, S. N. Majumdar, and S. Sachdev. Phase ordering kinetics of the Bose gas. *Phys. Rev. A*, 54:5037–5041, Dec 1996.

[75] S. Nazarenko and M. Onorato. Wave turbulence and vortices in Bose-Einstein condensation. *Physica D*, 219(1):1 – 12, 2006.

[76] T. R. Matthew, T. P. Billam, B. P. Anderson, and A. S. Bradley. Inverse Energy Cascade in Forced 2D Quantum Turbulence. *arXiv*, arXiv:1209.5824v1, September 2012.

[77] M. Briscolini, P. Santangelo, S. Succi, and R. Benzi. Extended self-similarity in the numerical simulation of three-dimensional homogeneous flows. *Phys. Rev. E*, 50:R1745–R1747, Sep 1994.

[78] R. Pandit, P. Perlekar, and S. S. Ray. Statistical properties of turbulence: An overview. *Pramana*, 73(1):157–191, 2009.

[79] S. Chakraborty, U. Frisch, and S. S. Ray. Extended self-similarity works for the Burgers equation and why. *J. Fluid Mech.*, 649:275, 2010.

[80] U. Frisch. *Turbulence*. Cambridge University Press, Cambridge, UK., 1996.

[81] A. Dyachenko and G. Falkovich. Condensate turbulence in two dimensions. *Phys. Rev. E*, 54:5095–5099, Nov 1996.

[82] V. Shukla, M. Brachet, and R. Pandit, to be published.

Chapter 3

Superfluid Mutual-friction Coefficients from Vortex Dynamics in the Two-dimensional Galerkin-truncated Gross-Pitaevskii Equation

In the previous Chapter we had discussed the equilibration of generic initial conditions, under the two-dimensional Fourier-truncated Gross-Pitaevskii equation dynamics. In this Chapter we present the first calculation of the mutual friction coefficients as a function of temperature in a homogeneous, two-dimensional Bose gas by using the Galerkin-truncated Gross-Pitaevskii equation; for this calculation it is best to use special initial conditions that we describe here.

3.1 Introduction

The elucidation of the statistical properties of superfluid turbulence and the comparison of these with their fluid-turbulence analogs is a problem of central importance that lies at the interface between fluid dynamics and statistical mechanics. Theoretical treatments of superfluid turbulence use a variety of models [1–3], which are applicable at different length scales and for different interaction strengths. At low temperatures T and for weakly interacting bosons, the Gross-Pitaevskii (GP) equation provides a good hydrodynamical description of a superfluid in which quantum vortices can be resolved. If we consider length scales that are larger than the mean separation between quantum vortices, and if we concentrate on low-Mach-number flows, then the two-fluid model [4, 5] of Hall, Vinen, Bekarevich, and Khalatnikov (HVBK) provides a good description of superfluid turbulence. In the HVBK equations (see below and Chapter 1 Eqs. (1.65), (1.66), and (1.67)) the normal and superfluid components are coupled by two mutual-friction coefficients, α and α', which can be determined, along with the normal-fluid density $\rho_{\rm n}$, as functions of T, from (a) experiments [4, 6, 7], (b) kinetic models [1, 3, 8], or

(c) the Galerkin-truncated GP equation [9, 10]. Such studies have been carried out only in three dimensions (3D) so far. Given that (a) two-dimensional (2D) and 3D fluid turbulence are qualitatively different [11, 12] and (b) 2D and 3D superfluids are also qualitatively different (see, e.g., Refs. [13, 14]), it behooves us to carry out GP-based investigations of α and α' for a 2D superfluid.

We present the first calculation of $\alpha(T), \alpha'(T)$, and $\rho_{\rm n}(T)$ in two dimensions (2D) by using the Galerkin-truncated GP system, with very special initial conditions, which we obtain by using the advective, real, Ginzburg-Landau equation (ARGLE) and an equilibration procedure that uses a stochastic Ginzburg-Landau equation (SGLE). We obtain the following interesting and unanticipated results: The determination of $\alpha(T), \alpha'(T)$, and $\rho_{\rm n}(T)$ turns out to be considerably more challenging in 2D than in three dimensions (3D) [9] because of large fluctuations. We extract the dependence of $\alpha(T), \alpha'(T)$, and $\rho_{\rm n}(T)$ on T by using a sophisticated, vortex-tracking algorithm, which allows us to examine the evolution of vortical configurations, such as, a pair of vortices and a quadruplet of vortices, placed initially at the corners of a square.

The remaining part of this chapter is organised as follows. In Sec. 3.2, we describe the models, initial conditions, and numerical methods we use. Section 3.3 is devoted to our results. We end with conclusions in Sec. 3.4

3.2 Model, Initial Conditions, and Numerical Methods

The Galerkin-truncated GP equation, which describes the spatiotemporal evolution of the complex, classical, wave function $\psi(\mathbf{x}, t)$ of a weakly interacting 2D Bose gas at low temperatures, is

$$i\frac{\partial\psi(\mathbf{x},t)}{\partial t} = \mathcal{P}_G\Big[-\alpha_0\nabla^2\psi(\mathbf{x},t) + g\mathcal{P}_G[|\psi|^2]\psi(\mathbf{x},t)\Big], \tag{3.1}$$

where g is the effective interaction strength, the Galerkin projector $\mathcal{P}_G[\hat{\psi}(k)] = \theta(k_{\rm max}-k)\hat{\psi}(k)$, with $\hat{\psi}$ as the Fourier transform of ψ and $\theta(\cdot)$ the Heaviside function. We can use the Madelung transformation $\psi = \sqrt{\rho(\mathbf{x},t)}\exp(i\phi)$, where ρ and ϕ are the density and the phase field, respectively, to write the velocity $\mathbf{v} = 2\alpha_0\nabla\phi$. In our units (Appendix C.1), the quantum of circulation is $4\pi\alpha_0$, the sound velocity $c = \sqrt{g\rho^*}$, the healing length $\xi = \sqrt{2\alpha_0^2/(g\rho^*)}$, the total density $\rho^* = N/\mathcal{A}$, and $\mathcal{A} = L^2$ is the area of our 2D, periodic, computational domain of side L. This truncated GP equation (TGPE) conserves the total energy $H = 2\alpha_0\int_{\mathcal{A}} d^2x(\alpha|\nabla\psi|^2 + \frac{g}{2}[\mathcal{P}_G|\psi|^2]^2)$, the total number of particles $N = \int_{\mathcal{A}} d^2x|\psi|^2$, and the momentum $\mathbf{P} = \alpha_0\int_{\mathcal{A}} d^2x(\psi\nabla\psi^* - \psi^*\nabla\psi)$. We use the $2/3$ dealiasing rule in our pseudospectral direct

numerical simulation (DNS) of the TGPE, with the maximum wave number $k_{max} = 2/3 \times N_c/2$, where N_c^2 is the number of collocation points [9]. Global momentum conservation in this DNS is essential for capturing accurately the interactions of the normal fluid with the superfluid vortices [9].

Generic initial conditions evolve, under the 2D TGPE dynamics, towards equilibrium in the microcanonical ensemble; this process of equilibration is slow [10]: the system goes through initial transients, then displays the onset of thermalization, which is followed by a regime of partial thermalization, and then complete thermalization with a low-T Berezinskii-Kosterlitz-Thouless (BKT) phase, a high-T phase with unbound vortices, and a transition between these phases at $T_{\rm BKT}$. To accelerate equilibration and to have direct control over (a) T, for the desired equilibrium state, and (b) states with counterflows, we use the generalized grand canonical ensemble with the equilibrium probability distribution $\mathbb{P}[\psi] = \Xi^{-1} \exp[-\beta(H - \mu N - \mathbf{w}\cdot\mathbf{P})]$, where Ξ is the grand partition function, $\beta = T^{-1}$ (we set the Boltzmann constant $k_B = 1$), μ the chemical potential, and $\mathbf{w} = \mathbf{v}_n - \mathbf{v}_s$ the counterflow velocity, and $\mathbf{v}_n$ and $\mathbf{v}_s$ the normal and superfluid velocities, respectively. We construct a stochastic process, which leads to this $\mathbb{P}[\psi]$, via the 2D SGLE Langevin equation

$$\frac{\partial\psi}{\partial t} = \mathcal{P}_G\Big[\alpha\nabla^2\psi - g\mathcal{P}_G[|\psi|^2]\psi + \mu\psi - i\mathbf{w}\cdot\nabla\psi + \zeta(\mathbf{x},t)\Big], \tag{3.2}$$

where ζ is a zero-mean, Guassian white noise with $\langle\zeta(\mathbf{x},t)\zeta^*(\mathbf{x}',t')\rangle = D\delta(\mathbf{x}-\mathbf{x}')\delta(t-t')$, δ the Dirac delta function and $D = 1/(2\alpha\beta)$, in accordance with the fluctuation-dissipation theorem. We solve this SGLE along with $d\mu/dt = -\frac{\nu_N}{\mathcal{A}}(N - N_{av})$, so that N_{av} controls the mean value of N and ν_N governs the rate at which the SGLE equilibrates. If we include the counterflow term $i\mathbf{w}\cdot\nabla\psi$, we obtain equilibrium states with a non-vanishing w, by inducing an asymmetry in the repartitioning of the sound waves in the system.

In the HVBK, two-fluid model [4, 6], the mutual friction leads to an interaction between the normal fluid and the superfluid. Here, a superfluid vortex does not move with the superfluid velocity $\mathbf{v}_{\rm s}$ but with velocity

$$\mathbf{v} = \mathbf{v}_{\rm sl} + \alpha\mathbf{s}'\times(\mathbf{v}_{\rm n} - \mathbf{v}_{\rm sl}) - \alpha'\mathbf{s}'\times[\mathbf{s}'\times(\mathbf{v}_{\rm n} - \mathbf{v}_{\rm sl})], \tag{3.3}$$

where $\mathbf{v}_{\rm sl} = \mathbf{v}_{\rm s} + \mathbf{v}_{\rm si}$ is the local superfluid velocity, with $\mathbf{v}_{\rm s}$ and $\mathbf{v}_{\rm si}$ the imposed superfluid velocity and the self-induced velocity because of the vortices, respectively, $\mathbf{v}_{\rm n}$ is the normal fluid velocity and $\mathbf{s}'$ is the unit tangent at a point on the vortex, with position vector s. (Equation (3.3) is normally written in three dimensions (3D). To use it in 2D, it is simplest to use a 2D projection of an infinitely long and straight vortical filaments in 3D.) We compute the normal-fluid density $\rho_{\rm n}$ and the

mutual-friction coefficients α and α' for some representative temperatures T below $T_{\rm BKT}$, from the dynamical evolution of the following two initial configurations in the 2D TGPE: (1) $\psi_{\tt IC1} = \psi_{\rm pair}\psi_{\rm eq}$; and (2) $\psi_{\tt IC2} = \psi_{\rm lattice}\psi_{\rm eq}^{\rm cf}$. We obtain the initial configuration $\psi_{\tt IC1}$ by (a) first preparing a state $\psi_{\rm pair}$, which corresponds to a small, vortex-antivortex pair translating with a constant velocity along the x direction (Appendix C.2) and (b) then combining it with an equilibrium state $\psi_{\rm eq}$ to include finite-temperature effects (Appendix C.3). To obtain the second initial configuration $\psi_{\tt IC2}$, we first prepare $\psi_{\rm lattice}$, in which we place vortices of alternating signs on the corners of a square (a crystal-like vortex lattice by virtue of the periodic boundary conditions we use) (Appendix C.2); and then we include finite-temperature and counterflow effects by combining it with the state $\psi_{\rm eq}^{\rm cf}$ (Appendix C.3). We obtain $\psi_{\rm eq}$ and $\psi_{\rm eq}^{\rm cf}$ by solving the SGLE Eq. (3.2); and then we use $\psi_{\tt IC1}$ to determine α and $\psi_{\tt IC2}$ to calculate both, α and α'.

We perform a pseudospectral, direct numerical simulations (DNS) of the TGPE Eq. (3.1), to study the spatiotemporal evolution of the initial configurations $\psi_{\tt IC1}$ and $\psi_{\tt IC2}$. We discretize $\psi(\mathbf{x}, t)$ on a square simulation domain of side $L = 2\pi$ with $N_c^2 = 128^2$ collocation points. We use periodic boundary conditions in both spatial directions, because we study the homogeneous flows in the 2D TGPE; and we use a fourth-order, Runge-Kutta scheme, with time step Δt, for time marching. In all our DNSs, we use $c = 1$ and $\xi = 1.44dx$, with $dx = L/N_c$; moreover, we set the total average density $\rho^* = N/\mathcal{A} = 1$. We take $\mathrm{w} = v_n\hat{x}$ for all our SGLE DNSs with counterflows.

3.3 Results

In this Section we present the results from our DNS studies of the 2D TGPE and SGLE. We begin with our results for $\rho_{\rm n}$ and then show how to obtain $\alpha(T)$ and $\alpha'(T)$ by analysing the time evolutions of the special vortical configurations.

We calculate $\rho_{\rm n}$ at a temperature T as follows: We first plot the x component of the momentum P_x versus v_n, the modulus of the counterflow velocity $\mathrm{w} = v_n\hat{x}$, by using our SGLE DNS for five representative values of $T/\tilde{T}_{\rm BKT}$ (Fig. 3.1(a)); we then obtain

$$\rho_{\rm n} = \frac{1}{\mathcal{A}}\frac{\partial P_{\rm x}}{\partial v_{\rm n}}|_{v_{\rm n}=0}. \tag{3.4}$$

The values of $\rho_{\rm n}$, at different values of $T/\tilde{T}_{\rm BKT}$, are listed in column 3 of Table 3.1. In Fig. 3.1(b), we plot versus the scaled temperature $T/\tilde{T}_{\rm BKT}$, where $\tilde{T}_{\rm BKT}$ is a rough, energy-entropy-argument estimate of the BKT transition temperature [13, 14], $\rho_{\rm n}$

	$T/\tilde{T}_{\rm BKT}$	$\rho_{\rm n}$	$\alpha_{\rm IC1}$	w	$\alpha_{\rm IC2}$	$\alpha'_{\rm IC2}$
R1	6.37×10^{-4}	2.7×10^{-4}	$(2 \pm 1) \times 10^{-6}$	0.8	2.5×10^{-5}	-2.2×10^{-5}
R2	3.19×10^{-3}	1.37×10^{-3}	$(1.0 \pm .3) \times 10^{-4}$	0.8	1.8×10^{-4}	-1.5×10^{-4}
R3	6.37×10^{-3}	2.7×10^{-3}	$(2.2 \pm .6) \times 10^{-4}$	0.6	3.6×10^{-4}	-1.8×10^{-4}
R4	3.19×10^{-2}	1.39×10^{-2}	$(1.6 \pm .5) \times 10^{-3}$	0.4	2.3×10^{-3}	-4.5×10^{-4}
R5	6.37×10^{-2}	2.85×10^{-2}	$(4 \pm 1) \times 10^{-3}$	0.2	6.9×10^{-3}	4.0×10^{-4}
R6	9.56×10^{-2}	4.37×10^{-2}	–	0.1	1.2×10^{-2}	-1.2×10^{-3}
R7	1.20×10^{-1}	5.97×10^{-2}	$(1.2 \pm .6) \times 10^{-2}$	0.1	1.6×10^{-2}	2.9×10^{-3}
R8	1.59×10^{-1}	7.66×10^{-2}	–	0.1	1.4×10^{-2}	4.2×10^{-3}
R9	1.78×10^{-1}	8.71×10^{-2}	–	0.1	2.2×10^{-2}	-3.5×10^{-3}

Table 3.1: Mutual-friction results from our DNS runs R1-R9: $T/\tilde{T}_{\rm BKT}$ is the scaled temperature; $\tilde{T}_{\rm BKT} = 1.57 \times 10^{-2}$ is the energy-entropy-argument based estimate of the BKT transition temperature; $\rho_{\rm n}$ is the normal-fluid density; $\mathbf{w} = v_n \hat{x}$ is the counterflow velocity; α and α' are the mutual friction coefficients, where the subscripts IC1 and IC2 denote the initial configurations. In all our DNS runs, the total average density $\rho^* = 1$, the total number of collocation points $N_c^2 = 128^2$, the healing length $\xi = 1.44\Delta x$, $\Delta x = 2\pi/N_c$, the speed of sound $c = 1$, and the quantum of circulation $\alpha_0 \simeq 0.05$ are kept fixed.

(green curve), $(1 - \rho_{\rm n})$ (sky-blue curve), and the condensate fraction N_0/N (purple line), where N_0 is the population of the zero-wave-number mode.

We begin with our results for the time evolution of $\psi_{\rm IC1} = \psi_{\rm pair}\psi_{\rm eq}$ as dictated by the TGPE (3.1); the state $\psi_{\rm pair}$ represents a vortex-anitvortex pair, whose centers are separated, initially, by the small distance $d \simeq 5.4\xi$ and which moves at a constant velocity $v_{\rm pair} = 0.2775\hat{x}$. The state $\psi_{\rm eq}$, which is an absolute-equilibrium state at a temperature $T < T_{\rm BKT}$, provides the normal fluid that interacts with the vortex-antivortex pair. This interaction, during the TGPE evolution of $\psi_{\rm IC1} = \psi_{\rm pair}\psi_{\rm eq}$, leads to a decrease in d as time increases. We determine this time dependence by tracking the positions of the vortices and thus obtain the plots of d^2 versus time t, shown in Fig. 3.2, for six representative values of $T/\tilde{T}_{\rm BKT}$, by using equilibrium states $\psi_{\rm eq}$ at different temperatures (DNS runs R1-R5, R7 in Table 3.1). To average our data for d^2, we use 10 different realizations of $\psi_{\rm eq}$, which we obtain from the SGLE at every value of $T/\tilde{T}_{\rm BKT}$ that we consider. The Video M1, for the DNS run R2, shows, via pseudocolor plots, the spatiotemporal evolution of the field $|\psi(\mathbf{x}, t)|^2$; we observe here that the vortex-antivortex pair moves under the combined influence of its initial momentum and the finite-temperature fluctuations; and the mean distance between the vortex and antivortex decreases with time; finally, this pair disappears from the system (on time scales that are much longer than those shown in the video). From the plots in Fig. 3.2, which show data for

all the 10 realizations mentioned above, we see that (a) d^2 fluctuates significantly in time and (b) these fluctuations increase with $T/\tilde{T}_{\rm BKT}$ (compare Figs. 3.2(a) -(f)). Thus, the higher the temperature, the more these fluctuations limit our ability to determine d^2 reliably, with averages over a fixed number (10 in our calculations) of realizations of $\psi_{\rm eq}$, which we must limit, perforce, because of the computational cost of these calculations. In Appendix B.1.1 we show that

$$\mathrm{d}d^2/\mathrm{d}t = -8\alpha_0(1-\alpha')\alpha, \tag{3.5}$$

in which we can neglect α', because $\alpha' \ll 1$ (as we show below). For details see appendix B.1.1. Thus, for a given realization of $\psi_{\rm eq}$ at temperature T, we can obtain $\alpha(T)$ from the slope of a straight-line fit to a plot of d^2 versus t. At each value of T, we obtain 10 values of $\alpha(T)$, because we have 10 realizations of $\psi_{\rm eq}$. The mean of these values yield the values of α that we have listed in column 4 of Table 3.1; the standard deviations yield the error bars. Note that α increases with the temperature (over the range we consider).

We consider next the time evolution of $\psi_{\texttt{IC2}} = \psi_{\rm lattice}\psi_{\rm eq}^{\rm cf}$ under 2D TGPE dynamics. The state $\psi_{\rm lattice}$ consists of a quadruplet of alternating vortices and antivortices on the vertices of a square with sides of length π; for this state, the self-induced velocity $\mathbf{u}_{\rm i}$, because of these vortices and antivortices, is zero at $T = 0$. We combine $\psi_{\rm lattice}$ with the thermalized state $\psi_{\rm eq}^{\rm cf}$, which we obtain from the 2D SGLE, at different values of $T/\tilde{T}_{BKT}$ and counterflow velocity $\mathbf{w} = w\hat{x}$, with $w = v_n$. Figures 3.3(a)-(c) show pseudocolor plots of the density field, for our DNS run `R2` at $T/\tilde{T}_{\rm BKT} = 3.19 \times 10^{-3}$ and $w = 0.8$, at three different times $t = 0$, $t = 500$, and $t = 1000$, respectively. Figures. 3.3(a)-(c) and the corresponding Video M2 show that the vortex-lattice drifts under the influence of the imposed counterflow. In the initial phase of this drift, the vortex-lattice has an adaptation time period, during which a perpendicular motion with a negligible velocity and a drift parallel to the applied counterflow are generated. This adaptation makes the vortex-lattice imperfect, which we quantify by $\delta = \frac{1}{4}[(\delta y_2 + \delta y_4) - (\delta y_1 + \delta y_3)]$, where δy_i is the y-displacement of the vortex i (see Fig. 3.4(a)); the drift parallel to the applied counterflow is given by $\delta x = \frac{1}{4}(\delta x_1 + \delta x_2 + \delta x_3 + \delta x_4)$, with δx_i being the x-displacement of the vortex i. The appearance of the imperfection $\delta(t)$ and its increase with t results in a self-induced velocity $\mathbf{v}_{\rm si}$, which leads to a decrease in the effective counterflow $w(t)$ because of the conservation of the total momentum. A phenomenological model, which accounts for this effect (Appendix B.1.2 of this Chapter) yields

$$\delta(t) = \frac{\rho_n w_0}{\alpha_0(\chi_v\rho_n + \chi_p\rho)}\left(1 - \exp\Big[-\frac{\alpha\alpha_0(\chi_v\rho_n + \chi_p\rho)}{\rho_n}t\Big]\right) \tag{3.6}$$

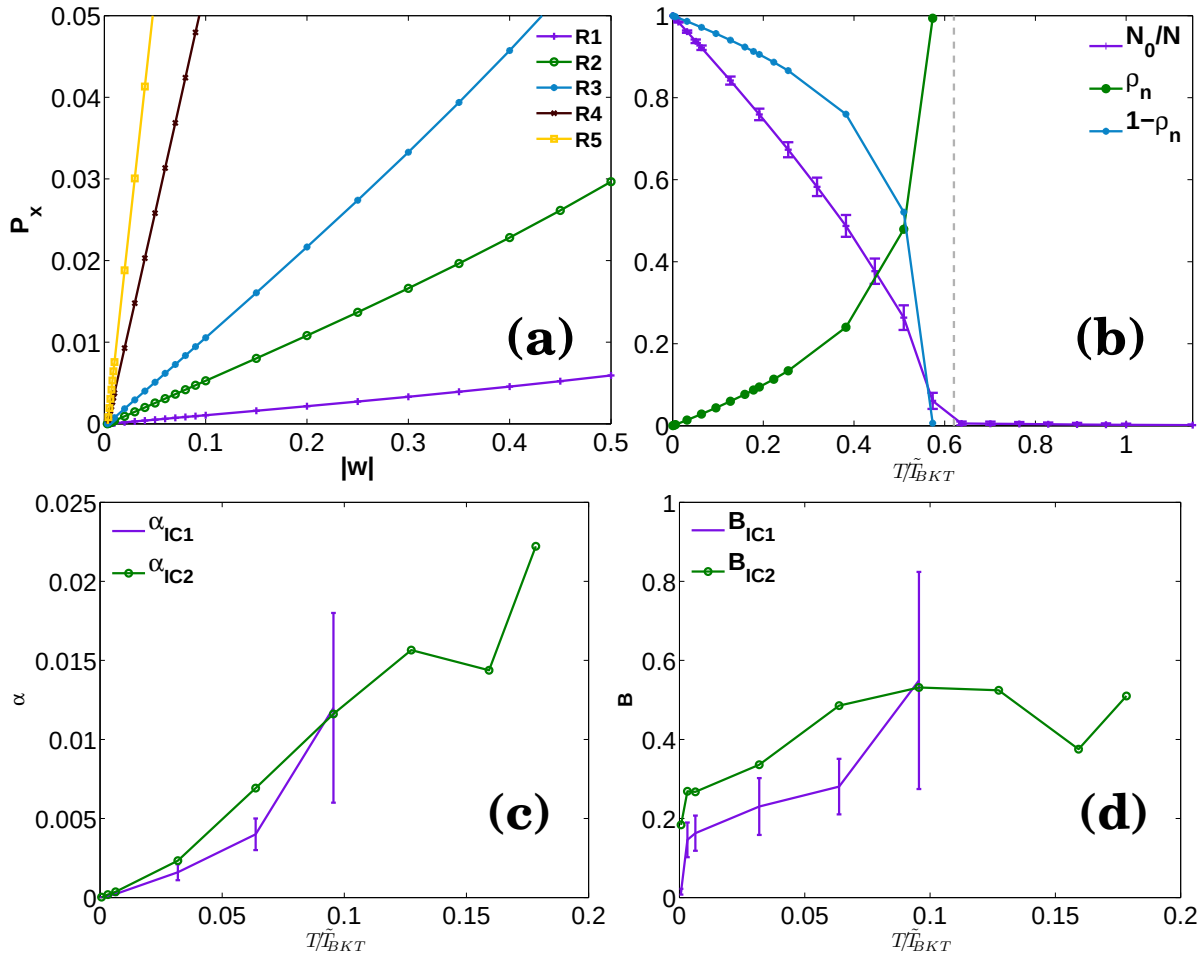

Figure 3.1: Plots of (a) the momentum $P_{\rm x}$ versus the applied counterflow velocity w for the DNS runs `R1`-`R5`; (b) the condensate fraction N_0/N (purple line), the normal fluid density $\rho_{\rm n}$ (green line), and $1-\rho_{\rm n}$ (sky-blue line) versus $T/\tilde{T}_{BKT}$; (c) the mutual friction coefficients $\alpha_{\texttt{IC1}}$ (purple line) and $\alpha_{\texttt{IC2}}$ (green line) versus $T/\tilde{T}_{BKT}$; (d) $B=2\alpha/\frac{\rho_n}{\rho}$ versus $T/\tilde{T}_{BKT}$. Here the subscripts on α refer to the initial conditions `IC1` and `IC2`.

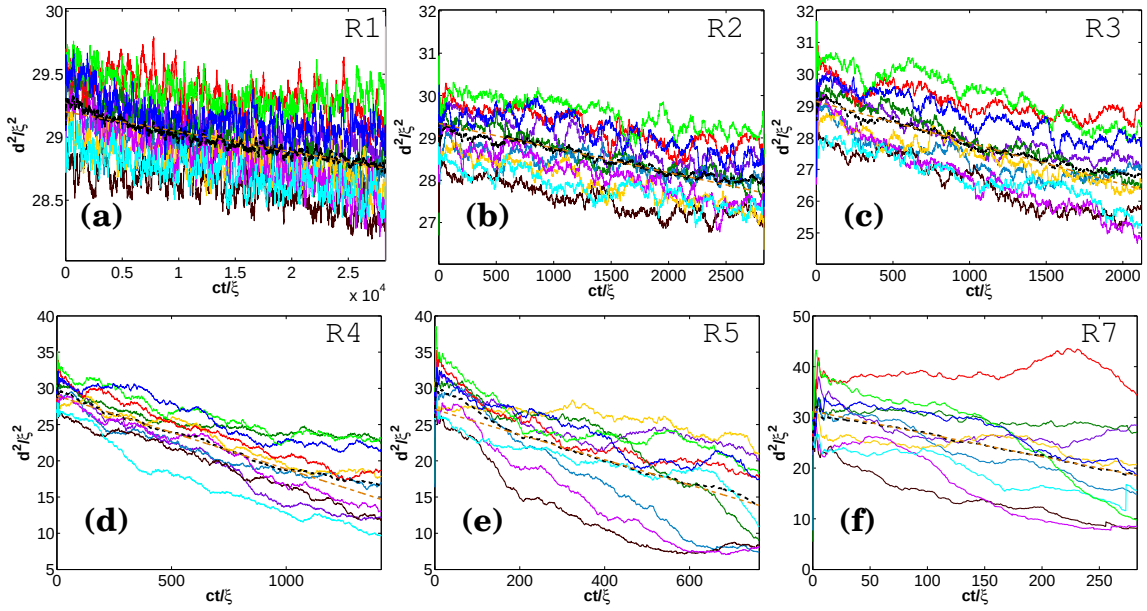

Figure 3.2: Plots of the square of the vortex-pair length d^2/ξ^2 versus time ct/ξ from our DNS runs: (a) R1 at $T/\tilde{T}_{\rm BKT} = 6.37 \times 10^{-4}$; (b) R2 at $T/\tilde{T}_{\rm BKT} = 3.19 \times 10^{-3}$; (c) R3 at $T/\tilde{T}_{\rm BKT} = 6.37 \times 10^{-3}$; (d) R4 at $T/\tilde{T}_{\rm BKT} = 3.19 \times 10^{-2}$; (e) R5 at $T/\tilde{T}_{\rm BKT} = 6.37 \times 10^{-2}$; (f) R7 at $T/\tilde{T}_{\rm BKT} = 1.20 \times 10^{-1}$. For each plot, the different solid lines indicate the time evolution of d^2/ξ^2 for the different realizations of $\psi_{\rm eq}$, which we obtain from the steady state of the SGLE. To reduce the noise in the plots of d^2, for these different realizations we have a moving-average-based smoothening procedure (the function *smooth* in Matlab®); this procedure introduces slight artifacts (high or low values of d^2) near the lowest and highest values of t in these plots. The average of the plots of d^2 versus t is shown by a black dashed curve, at given value of T. The orange dashed line, a linear fit to this curve, is shown to guide the eye.

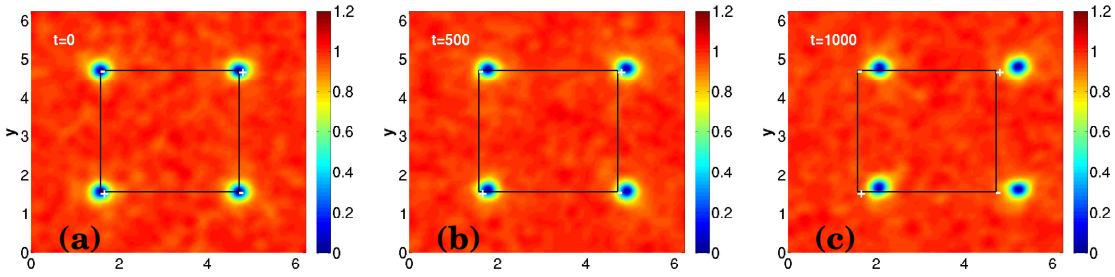

Figure 3.3: Pseudocolor plots of the density field $|\psi(\mathbf{x},t)|^2$ from our DNS run `R2` at three different instants of time: (a) $t=0$, (b) $t=500$, and (c) $t=1000$; showing the drift of the vortex-crystal under the imposed counterflow $w=0.8\hat{x}$ at $T/\tilde{T}_{\rm BKT}=3.19\times10^{-3}$. The $+$ and $-$ symbols in white color show the sign of the vortices and the black-frame box is an aid-to-eye to show the displacement from the initial location. The Video `M2` shows, via pseudocolor plots, the spatiotemporal evolution of the field $|\psi(\mathbf{x},t)|^2$.

and

$$\delta x(t) = \Bigg(\big[\chi_v\rho_n - \alpha'(\chi_v\rho_n+\chi_p\rho)\big]\exp\big[-\frac{\alpha\alpha_0(\chi_v\rho_n+\chi_p\rho)}{\rho_n}t\big] - \chi_v\rho_n \\ + (\chi_v\rho_n+\chi_p\rho)(\alpha'+\alpha\alpha_0 t)\Bigg)\frac{\rho_n w_0}{\alpha\alpha_0(\chi_v\rho_n+\chi_p\rho)^2}, \tag{3.7}$$

where w_0 is the counterflow velocity at $t=0$; χ_v and χ_p are the proportionality constants given by $v_{\rm si}(\delta)=\chi_v\alpha_0\delta$ and $P_{\rm si}(\delta)=4\pi^2\chi_P\alpha_0\rho\delta$, where $P_{\rm si}$ the self-induced momentum arising from the vortex-lattice imperfection, respectively. We determine $\alpha(T)$ and $\alpha'(T)$ from the fits, suggested by the forms in Eqs. (3.6) and (3.7), to the plots of δ and δx, which we obtain from our DNS runs `R1`-`R9` at different temperatures; we give the details in Appendix B.1.2. Figures 3.4(b) and (c) contain plots versus t of $\delta(t)$ and $\delta x(t)$, respectively; Fig. 3.4(b) shows the saturation of the vortex-lattice imperfection. The values of $\alpha(T)$ and $\alpha'(T)$ that we obtain are listed in columns 6 and 7 of Table 3.1 for different values of $T/\tilde{T}_{BKT}$.

We note that the measurement of $\alpha'(T)$ in 2D is difficult because of the following reasons: (1) at low-temperatures the effect is small; (2) at high-temperatures there are large thermal fluctuations that lead to large and noisy oscillations of the vortex-lattice. Even though an accurate determination of $\alpha'(T)$ is difficult, we find that $\alpha'(T)$ is always smaller in magnitude than $\alpha(T)$. For similar studies in the 3D GPE we refer the readers to Refs. [9, 15–17].

The existence of the transverse force, which is related to the third term on the right-hand side of Eq.(3.3), has been the subject of a debate in the latter half of the 1990s [18–24]. There is agreement on the longitudinal force; but the existence of a transverse (or Iordanskii) force is often debated. This transverse force is linked to

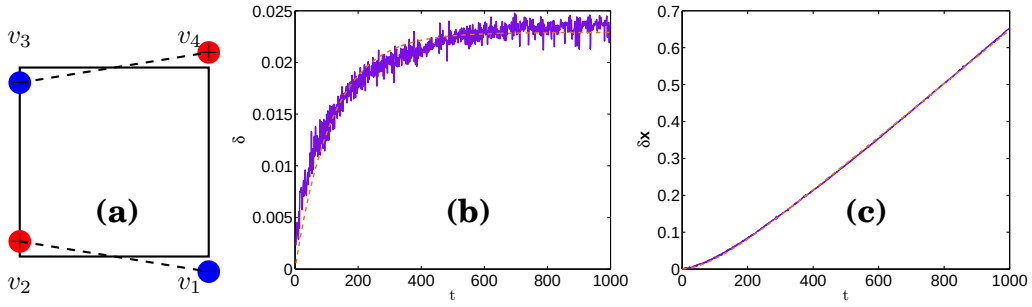

Figure 3.4: (a) Schematic diagram of the vortex-lattice imperfection; the square shows the shape of the vortex lattice at $t = 0$. Plots versus time t of (b) imperfection $\delta = \frac{1}{4}[(\delta y_2 + \delta y_4) - (\delta y_1 + \delta y_3)]$; (c) drift $\delta x = \frac{1}{4}(\delta x_1 + \delta x_2 + \delta x_3 + \delta x_4)$; from our DNS run R2. The orange-dashed lines indicate the fits obtained by the use of Eqs. (3.6) and (3.7).

the asymmetry of the scattering of quasiparticles by a vortex [25, 26]; and, if it is present, it implies that the second mutual-friction coefficient α' (or B') is nonzero. Thus, given that we find that $\alpha' \neq 0$, our calculations imply that there is a nonvanishing Iordanskii force. However, we emphasize that the numerical determination of α' is a difficult tasks. We hope that our work will lead to more accurate determination of α and α' than those we have given here.

3.4 Conclusion

We have shown how to obtain $\alpha(T), \alpha'(T)$, and $\rho_{\rm n}(T)$, which are required as inputs for the 2D HVBK two-fluid model for superfluids, by using the Galerkin-truncated GP system, with very special initial conditions, which we obtain by using the advective, real, Ginzburg-Landau equation (ARGLE) and an equilibration procedure that uses the SGLE. The determination of $\alpha(T), \alpha'(T)$, and $\rho_{\rm n}(T)$ turns out to be considerably more challenging in 2D than in three dimensions (3D) [9] because of large fluctuations. Nevertheless, we succeed in obtaining $\alpha(T), \alpha'(T)$, and $\rho_{\rm n}(T)$ for temperatures such that $T/\tilde{T}_{\rm BKT} \lesssim 10^{-1}$, by using a sophisticated, vortex-tracking algorithm, which allows us to examine the evolution of special vortical configurations. At such low temperatures, the difference between the superfluid density ρ_s, which should be obtained strictly by using a helicity modulus [13, 14, 27], and $(1-\rho_n)$ should not be significant in typical, laboratory-scale systems; and the HVBK model, with the values of $\alpha(T), \alpha'(T)$, and $\rho_{\rm n}(T)$ that we have listed in Table 3.1, should provide a good description of the dynamics of 2D superfluids so long as we probe scales that are larger than the mean separation between quantum vortices. We hope our study will lead to experimental measurements of $\alpha(T), \alpha'(T)$,

and $\rho_{\mathrm{n}}(T)$ in 2D superfluids, whose analogs for 3D superfluids [6] have been known for several decades.

3.5 Video Captions

Video M1 This video illustrates the spatiotemporal evolution of the field $|\psi(\mathbf{x}, t)|^2$ for the initial configuration $\psi_{\texttt{IC1}} = \psi_{\text{pair}}\psi_{\text{eq}}$ from our DNS run `R2`.

Video M2 This video illustrates the spatiotemporal evolution of the field $|\psi(\mathbf{x}, t)|^2$ for the initial configuration $\psi_{\texttt{IC2}} = \psi_{\text{lattice}}\psi_{\text{eq}}^{\text{cf}}$ from our DNS run `R2`.

Appendix B

Determination of the mutual-friction coefficients

B.1 Mutual friction coefficients α and α'

B.1.1 Determination of α by using the initial configuration `IC1`

We can use Eq. (3.3) to write the distance $L_{\rm pair}(t)$ travelled in the x direction by a vortex-antivortex pair of size d (in the y direction) as

$$\frac{dL_{\rm pair}}{dt} = (1-\alpha')v_{\rm si} = (1-\alpha')\frac{\kappa}{2\pi d}, \tag{B.1}$$

where $\kappa = 4\pi\alpha_0$. The time variation of the pair-size d is governed by

$$\frac{dd}{dt} = -2\alpha\frac{dL_{\rm pair}}{dt}, \tag{B.2}$$

where α and α' are the coefficients of mutual friction. Equations (B.1) and (B.2) yield

$$\frac{dd}{dt} = -4\alpha_0(1-\alpha')\alpha\frac{1}{d}; \tag{B.3a}$$

$$\frac{dd^2}{dt} = -8\alpha_0(1-\alpha')\alpha. \tag{B.3b}$$

Therefore, α is given by

$$\alpha = \frac{dd^2/dt}{8\alpha_0(1-\alpha')}. \tag{B.4}$$

If $\alpha' \ll 1$, then

$$\alpha = \frac{dd^2/dt}{8\alpha_0}. \tag{B.5}$$

B.1.2 Determination of α and α' by using the initial configuration `IC2`

To a first approximation, the self-induced velocity $v_{\rm si}$ and momentum $P_{\rm si}$ are linear functions of the vortex-lattice imperfection δ:

$$v_{si}(\delta) = \chi_v \alpha_0 \delta; \tag{B.6}$$

and

$$P_{si}(\delta) = 4\pi^2 \chi_P \alpha_0 \rho \delta; \tag{B.7}$$

here ρ is the total density. The coefficients χ_v and χ_P depend on the properties of the system. We determine these by imposing a flow with velocity $v_{\rm si}$ on the perfect vortex lattice and then obtaining the ground state of this system by using the ARGLE (Appendix C.2) coupled with a Newton's method (Appendix C.2); the vortex lattice adapts to the applied flow. We repeat the above procedure for different flow velocities and measure the imperfection δ and the momentum $P_{\rm si}$; the coefficients χ_v and χ_P are then extracted from the slopes of the linear fits to the plots of $v_{\rm si}$ versus δ and $P_{\rm si}$ versus δ, respectively (Eqs.(B.6) and (B.7)).

The counterflow momentum $P_{cf}(w)$, from Eq. (3.4), is linear in the counterflow w

$$P_{cf}(w) = \rho_n w \mathcal{A}, \tag{B.8}$$

where $\mathcal{A} = 4\pi^2$. The total momentum conservation implies that an increase in the vortex-lattice imperfection leads to a decrease in the effective counterflow velocity w. We have

$$P_0 = 4\pi^2 \rho_n w_0 = P_{si} + P_{cf}, \tag{B.9}$$

where ρ_n is the normal-fluid density and P_0 and w_0 are the $t = 0$ values of the counterflow momentum and velocity, respectively. Therefore, the counterflow velocity as a function of δ is

$$w(\delta) = w_0 - \frac{\chi_P \alpha_0 \rho}{\rho_n}\delta. \tag{B.10}$$

From Eq. (3.3) the components of the velocity (for any vortex or antivortex in our system) parallel and perpendicular to the counterflow velocity are, respectively,

$$\begin{aligned} v^{\shortparallel} &= v_{\rm si}(\delta) + \alpha'[w(\delta) - v_{si}(\delta)] \\ &= \alpha_0 \left(\chi_v - \alpha' \chi_v - \frac{\alpha' \chi_p \rho}{\rho_n} \right) \delta + \alpha' w_0 \end{aligned} \tag{B.11}$$

and

$$\begin{aligned} v^{\perp} &= \alpha[w(\delta) - v_{\rm sl}(\delta)] \\ &= \alpha w_0 - \frac{\alpha(\chi_v \rho_n + \chi_p \rho)\alpha_0}{\rho_n}\delta. \end{aligned} \tag{B.12}$$

The imperfection in the vortex lattice saturates when $v^{\perp}$ is zero, which gives the following values for the imperfection and the drift velocity, respectively, at saturation (subscript ∞):

$$\delta_{\infty} = \frac{\rho_n w_0}{\alpha_0(\chi_v \rho_n + \chi_p \rho)}; \tag{B.13}$$

and

$$v^{\shortparallel}_{\infty} = \frac{\chi_v \rho_n w_0}{\chi_v \rho_n + \chi_p \rho}. \tag{B.14}$$

The Eqs. (B.13) and (B.14) show that the large-time behavior of δ and $v^{\shortparallel}$ are independent of α'. The equation of motion for δ is

$$\frac{d\delta(t)}{dt} = \alpha w_0 - \frac{\alpha\alpha_0(\chi_v \rho_n + \chi_p \rho)}{\rho_n}\delta, \tag{B.15}$$

whose solution, with the initial condition $\delta(0) = 0$, is

$$\delta(t) = \frac{\rho_n w_0}{\alpha_0(\chi_v \rho_n + \chi_p \rho)}\left(1 - \exp\big[-\frac{\alpha\alpha_0(\chi_v \rho_n + \chi_p \rho)}{\rho_n}t\big]\right). \tag{B.16}$$

We use Eq. (B.16) to rewrite Eq. (B.11) as

$$v^{\shortparallel}(t) = \frac{\chi_v \rho_n w_0}{\chi_v \rho_n + \chi_p \rho} + \left(\alpha' w_0 - \frac{\chi_v \rho_n w_0}{\chi_v \rho_n + \chi_p \rho}\right)\exp\big[-\frac{\alpha\alpha_0(\chi_v \rho_n + \chi_p \rho)}{\rho_n}t\big]; \tag{B.17}$$

the equation of motion for the drift δx is

$$\frac{d\delta x}{dt} = v^{\shortparallel}(t); \tag{B.18}$$

the solution of the Eq. (B.18), with the initial condition $\delta x(0) = 0$, is

$$\begin{aligned}\delta x(t) = \Bigg(&\big[\chi_v \rho_n - \alpha'(\chi_v \rho_n + \chi_p \rho)\big]\exp\big[-\frac{\alpha\alpha_0(\chi_v \rho_n + \chi_p \rho)}{\rho_n}t\big] - \chi_v \rho_n \\ &+ (\chi_v \rho_n + \chi_p \rho)(\alpha' + \alpha\alpha_0 t)\Bigg)\frac{\rho_n w_0}{\alpha\alpha_0(\chi_v \rho_n + \chi_p \rho)^2}.\end{aligned} \tag{B.19}$$

To extract α and α' from our data, from the DNS runs `R1-R9` with the initial configuration `IC2`, we rewrite Eqs. (B.16) and (B.19), respectively, in the following simplified form:

$$\delta(t) = D(1 - \exp(-Bt)) \tag{B.20}$$

and

$$\delta x(t) = A(1 - \exp(-Bt)) + Ct. \tag{B.21}$$

The coefficients are

$$A = \frac{\alpha' \rho_n w_0}{\alpha\alpha_0(\chi_p \rho + \chi_v)} - \frac{\chi_v \rho_n^2 w_0}{\alpha\alpha_0(\chi_p \rho + \chi_v)^2}, \tag{B.22}$$

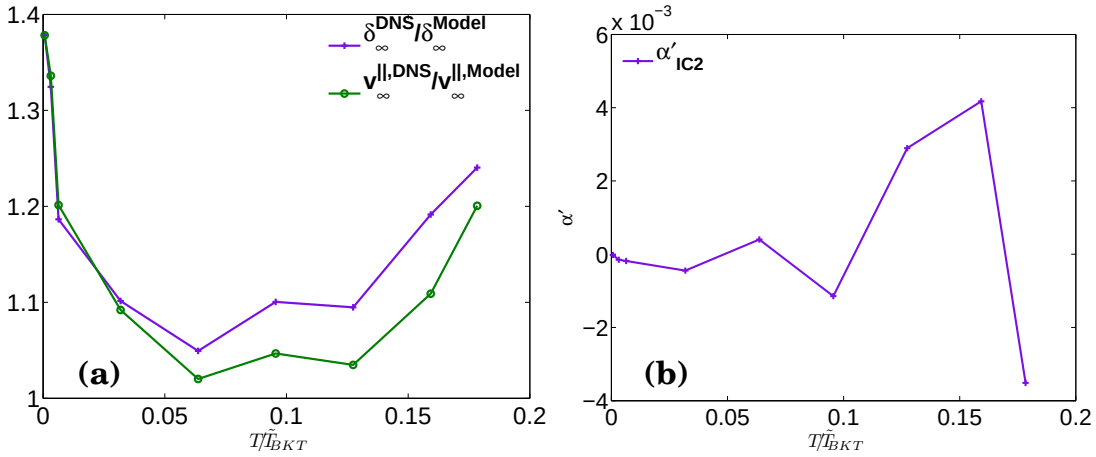

Figure B.1: Plots of the (a) $\delta_\infty^{\rm DNS}/\delta_\infty^{\rm Model}$ and $v_\infty^{\rm ll,DNS}/v_\infty^{\rm ll,Model}$ versus $T/\tilde{T}_{BKT}$; (b) mutual friction coefficient α' versus $T/\tilde{T}_{BKT}$, obtained from the DNS runs `R1`-`R9` using the initial configuration `IC2`.

$$B = \frac{\alpha\alpha_0(\chi_p\rho + \chi_v)}{\rho_n}, \tag{B.23}$$

$C = v_\infty^{\rm ll}$, and $D = \delta_\infty$. In Fig. B.1(a) we compare the values of δ_∞ and $v_\infty^{\rm ll}$, from fits to our DNS data, and the predictions of our phenomenological model (Eqs. (B.13) and (B.14)). Figure B.1(b) shows the temperature variation of α'. We cannot fit this reliably to any functional form; however, we can infer that α' is smaller than α in magnitude.

Appendix C

C.1 Note on Units

The GP equation, which describes the dynamical evolution of the wave function $\psi(\mathbf{x},t)$ of a weakly interacting, 2D Bose gas at low temperatures, is

$$i\hbar\frac{\partial\psi(\mathbf{x},t)}{\partial t} = -\frac{\hbar^2}{2m}\nabla^2\psi(\mathbf{x},t) - \mu\psi(\mathbf{x},t) + g_{2\mathrm{D}}|\psi|^2\psi(\mathbf{x},t), \tag{C.1}$$

where $g_{2\mathrm{D}}$ is the effective interaction strength. As we have mentioned earlier, the GP equation conserves the energy, given by the Hamiltonian

$$H = \int_{\mathcal{A}} d^2x\big(\frac{\hbar^2}{2m}|\nabla\psi|^2 + \frac{1}{2}g_{2\mathrm{D}}|\psi|^4\big), \tag{C.2}$$

and the total number of particles $N = \int_{\mathcal{A}} d^2x|\psi|^2$. We can use the Madelung transformation to write $\psi(\mathbf{x},t) = \sqrt{\rho(\mathbf{x},t)/m}e^{i\phi(\mathbf{x},t)}$ and the total density is $\rho^* = N/\mathcal{A}$. To obtain Eq. (3.1), we first divide Eq. (C.1) by $\hbar$ and define $\mu = \mu/\hbar$, $g = g_{2\mathrm{D}}/\hbar$; we then set $\hbar/2m = \alpha_0$, with $m = 1$. In these units, the quantum of circulation is $h/m = 4\pi\alpha_0$, the sound velocity is $c = \sqrt{g|\psi_0|^2/m} = \sqrt{g\rho_0}$, and the healing length is $\xi = \sqrt{\hbar^2/2m|\psi_0|^2 g} = \sqrt{2\alpha_0^2/\rho_0 g}$, where $\rho_0 = m|\psi_0|^2$ is the condensate density. This choice of units is slightly different from the choice we have made in Chapter 2 (see AppendixA.1). We use these units in our numerical studies.

C.2 Advective real Ginzburg-Landau equation (ARGLE)

Compressible superfluid hydrodynamics, described by the GP equation, can lead, in the presence of vortices, to regimes dominated by acoustic emission. To minimize this acoustic emissions, we prepare our initial states by using a specialized scheme, which we refer to as the advective-real-Ginzburg-Landau equation (ARGLE) [28]. The desired initial states are the large-time-asymptotic solutions of the ARGLE

$$\frac{\partial\psi}{\partial t} = \alpha_0\nabla^2\psi - g|\psi|^2\psi + \mu\psi - i\mathbf{u}_{\mathrm{adv}}\cdot\nabla\psi - \frac{\mathbf{u}_{\mathrm{adv}}^2}{4\alpha_0}\psi; \tag{C.3}$$

and these states minimize the free-energy functional

$$\mathcal{F}_{\rm ARGLE}(\psi,\psi^*)=\int d^3x\left(\alpha_0\left|\nabla\psi-i\frac{\mathbf{u}_{\rm adv}}{2\alpha_0}\psi\right|^2+\frac{1}{2}g|\psi|^4-\mu|\psi|^2\right); \tag{C.4}$$

$\mathbf{u}_{\rm adv}$ is the imposed flow velocity.

Numerical implementation

We use the implicit-Euler method for time stepping in the ARGLE, i.e.,

$$\psi(t+\Delta t)=\frac{\psi(t)+NL(t)\Delta t}{1-L\Delta t}, \tag{C.5}$$

where we suppress the spatial argument of ψ, $L=\alpha_0\nabla^2$, and $NL=(\mu-g|\psi|^2)\psi-i\mathbf{u}_{\rm adv}\cdot\nabla\psi-\frac{\mathbf{u}_{\rm adv}^2}{4\alpha_0}\psi$. The field ψ at the $(n+1)$ time step is given by

$$\hat{\psi}_{n+1}=\frac{\hat{\psi}_n+\Delta t(\mu-g\widehat{|\psi_n|^2\psi_n}-i\widehat{\mathbf{u}_{\rm adv}\cdot\nabla}\psi_n-\widehat{\frac{\mathbf{u}_{\rm adv}^2}{4\alpha_0}\psi_n})}{1-(-\alpha_0k^2)\Delta t}. \tag{C.6}$$

We also use the Newton's method to find both the stable and the unstable fixed points of the above equation, which is equivalent to finding ψ_*, such that

$$F(\psi_*)\equiv\psi_*(t)-\psi_*(t+\Delta t)=0. \tag{C.7}$$

Every Newton step requires the solution, for $\delta\psi$, of

$$\frac{\delta F}{\delta\psi}\delta\psi=-F(\psi), \tag{C.8}$$

which we obtain by an iterative bi-conjugate-gradient-stabilized method (BiCGSTAB) [29]. This method uses the direct application of $[\delta F/\delta\psi]$ over an arbitrary field ϕ, given by

$$\frac{\delta F}{\delta\psi}\phi=\frac{-\Delta t}{1-L\Delta t}\Big[L\phi+g(2|\psi|^2\phi+\psi^2\phi^*)-i\mathbf{u}_{\rm adv}\cdot\nabla\phi-(\mathbf{u}_{\rm adv}^2/4\alpha_0)\phi\Big]. \tag{C.9}$$

Preparation of a translating vortex-antivortex pair: $\psi_{\rm pair}$

The steps involved in the preparation of $\psi_{\rm pair}$ are outlined below:

1. Initialize $\psi(x,y)=\exp(ix)$ for $l_{\rm min}<y<l_{\rm max}$ and $\psi(x,y)=1$ otherwise.
2. Evolve ψ using ARGLE, with $u_{\rm adv}=0$, and allow the vortex-antivortex pair generated to contract until it reaches the desired pair-length.
3. Evolve ψ obtained in step-2 by using ARGLE with $\mathbf{u}_{\rm adv}=u\hat{x}$, so that the contraction of the vortex-antivortex pair stops.

4. Use Newton's method, coupled with BiCGSTAB, to find the exact state of the vortex-antivortex pair for the $\mathbf{u}_{\rm adv}$ in step-3 above. This Newton method is used to speed up the convergence to the desired solution (because the ARGLE procedure converges slowly).

Preparation of a vortex-lattice: $\psi_{\rm lattice}$

The steps involved in the preparation of $\psi_{\rm lattice}$ are outlined below:

1. Initialize $\psi = \frac{(\lambda_1+\iota\lambda_2)}{A}\tanh\big(\frac{A}{\sqrt{2}\xi}\big)$, where $\lambda_1 = \frac{1}{\sqrt{\gamma_d}}\cos x$, $\lambda_2 = \frac{1}{\sqrt{\gamma_d}}\cos y$, $\gamma_d = 8/(4\pi\alpha_0)$, and $A = \sqrt{\lambda_1^2+\lambda_2^2}$.
2. Evolve ψ by using ARGLE with $u_{\rm adv,x} = \frac{1}{\gamma_d}\sin(x)\cos(y)$, $u_{\rm adv,y} = -\frac{1}{\gamma_d}\cos(x)\sin(y)$.
3. Evolve ψ obtained in step-2 by using ARGLE, followed by Newton-BCGSTAB, with $\mathbf{u}_{\rm adv} = 0$ to find the exact solution.

For more details on the preparation of an assembly of vortices, we refer the reader to Ref. [28].

C.3 Stochastic Ginzburg-Landau equation (SGLE)

The stochastic Ginzburg-Landau equation (SGLE) is

$$\frac{\partial\psi}{\partial t} = \mathcal{P}_G\Big[\alpha_0\nabla^2\psi - g\mathcal{P}_G[|\psi|^2]\psi + \mu\psi - i\mathbf{v}_n\cdot\nabla\psi + \zeta(\mathbf{x},t)\Big], \tag{C.10}$$

where ψ is the wave function, g the interaction strength, μ the chemical potential, and $\mathbf{v}_n$ the counterflow velocity. ζ is a Guassian white noise satisfying

$$\langle\zeta(\mathbf{x},t)\rangle = 0 \tag{C.11}$$

and

$$\langle\zeta(\mathbf{x},t)\zeta^*(\mathbf{x}',t')\rangle = D\delta(\mathbf{x}-\mathbf{x}')\delta(t-t') \tag{C.12}$$

with $D = 1/(2\alpha_0\beta)$, where $\beta = 1/(k_{\rm B}T)$ (we set the Boltzmann constant $k_{\rm B} = 1$).

Numerical implementation

We solve the SGLE Eq. (C.10) along with the following, ad-hoc equation

$$\frac{d\mu}{dt} = -\frac{\nu_N}{\mathcal{A}}(N - N_{av}), \tag{C.13}$$

to control the number of particles N; the parameter N_{av} controls the mean value of N; and ν_N governs the rate at which the SGLE equilibrates.

The spatial Fourier-transform of Eq. C.10 gives

$$\frac{d\hat{\psi}}{dt} = -\alpha_0 k^2 \hat{\psi} - g\widehat{|\psi|^2\psi} + \mu\hat{\psi} - i\widehat{\mathbf{v}_n \cdot \nabla\psi} + \hat{\zeta}, \tag{C.14}$$

where we have omitted the Galerkin projector $\mathcal{P}_G$ for the notational simplicity. We solve the SGLE by using a pseudospectral method with periodic boundary conditions in space, an implicit-Euler scheme with time step Δt, for time marching. The discrete versions are

$$\mu_{n+1} = \mu_n - \Delta t \frac{\mu_N}{\mathcal{A}}(N_n - N_{av}) \tag{C.15}$$

and

$$\hat{\psi}_{n+1} = \frac{\hat{\psi}_n + \Delta t(-g\widehat{|\psi_n|^2\psi_n} - i\widehat{\mathbf{v}_n \cdot \nabla\psi_n})}{1 + (\alpha_0 k^2 - \mu_n)\Delta t} + dW_\zeta \tag{C.16}$$

where $dW_\zeta = \sqrt{D}(d\mathcal{A})^{-1/2}\eta_i\sqrt{dt}$, with $d\mathcal{A} = \Delta x \Delta y$ and η_i are random variables that we obtain from a normal distribution with zero mean and unit variance.

Appendix D

Low-temperature phenomenological model

We present a phenomenological model to characterize the thermodynamic equilibrium properties of the low-temperature Bose gas. For the sake of completeness, we repeat some of the material already covered in Chapter 2.

D.1 Standard results on the BKT transition

We can use the heuristic, energy-entropy argument to obtain a rough estimate of the BKT transition temperature $T_{\rm BKT}$. In the XY model, this transition is studied by using the Hamiltonian

$$H_{\rm XY} = -J \sum_{<i,j>} \cos(\theta_i - \theta_j), \tag{D.1}$$

where $< i, j >$ denotes nearest-neighbour pairs of sites, on a 2D square lattice, J is the nearest-neighbour exchange coupling, and $(\theta_i - \theta_j)$ is the angle between the nearest-neighbour, XY spins on sites i and j. In the continuum limit, the above Hamiltonian becomes, to lowest order in spatial gradients,

$$H_{\rm XY} = \frac{J}{2} \int d^2x (\nabla\theta(x))^2. \tag{D.2}$$

By comparing Eq. (D.2) with the kinetic-energy term in the energy, we find that

$$J = \frac{|\langle\psi\rangle|^2\hbar^2}{m} = \frac{\rho\Gamma^2}{(2\pi)^2}, \tag{D.3}$$

where Γ denotes the Onsager-Feynman quantum of velocity circulation $\Gamma = 4\pi\hbar/2m = h/m = \kappa$. A rough estimate for the BKT transition temperature $T_{\rm BKT}$ is given below:

$$\tilde{T}_{\rm BKT} = \frac{\pi J}{2k_B} = \frac{\pi \mid \langle\psi\rangle \mid^2 \hbar^2}{2mk_B} = \frac{\rho\Gamma^2}{8\pi k_B}, \tag{D.4}$$

here $\tilde{T}_{\rm BKT}$ denotes the estimate for $T_{\rm BKT}$ that follows from an energy-entropy argument [10].

D.2 Low-temperature thermodynamical computations with counterflows

We now develop an analytical framework, which is valid at low-temperatures $T \ll T_{\rm BKT}$, that can be used to test some of the results of our DNS runs in the region of complete thermalization. We calculate the equilibrium thermodynamic functions for a weakly-interacting, 2D Bose gas, in the grand-canonical ensemble. In the grand-canonical ensemble the probability of a given state is

$$\mathbb{P} = \frac{1}{\Xi} e^{-\beta(H-\mu N-\mathbf{w}\cdot\mathbf{P})}, \tag{D.5}$$

where Ξ is the grand partition function, β the inverse temperature, μ the chemical potential,N the number of bosons, and $\mathbf{P}$ the momentum. The grand-canonical potential is

$$\Omega = -\beta^{-1}\log(\Xi); \tag{D.6}$$

and the mean energy E and number of particles N are

$$N = -\frac{\partial\Omega}{\partial\mu}, \tag{D.7a}$$

$$\mathbf{P} = -\frac{\partial\Omega}{\partial\mathbf{w}}, \tag{D.7b}$$

$$E = \frac{\partial\Omega}{\partial\beta} + \mu N + \mathbf{w}\cdot\mathbf{P}. \tag{D.7c}$$

We adapt to 2D the 3D study of Ref. [9], expand ψ in terms of Fourier modes $A_{\mathbf{k}}$, and obtain Ω as the sum of the saddle-point part Ω_{sp} and Ω_Q, the deviations from the saddle point that are quadratic in $A_{\mathbf{k}}$. We write $\Omega = \Omega_{sp} + \Omega_Q$, where $\Omega_{sp} = -\mathcal{A}\mu^2/2g$ and

$$\Omega_Q = -\frac{\mathcal{A}}{2\pi\beta\hbar^2}\int_0^{p_{\max}}\left(\log(\frac{2m}{\beta\sqrt{p^4+4mp^2\mu}}) + \frac{2m^2w^2(5p^2+6m^2w^2+20m\mu)}{15(p^2+4m\mu)^2}\right)pdp, \tag{D.8}$$

where $\mathbf{w} = w\hat{\mathbf{x}}$. We can also calculate the condensate depletion δN, where the particle number $N = N_0 + \delta N$ and N_0 is the number of particles in the $k = 0$ mode as follows:

$$\delta N = \int_0^{p_{\max}} \frac{mp\mathcal{A}\left(p^{-2} + \frac{1}{p^2+4m\mu}\right)}{2\pi\beta\hbar^2}dp + \mathcal{O}(w^2). \tag{D.9}$$

The integrals in Eqs. (D.8) and (D.9) can be performed analytically, but, in contrast to the 3D case where the primitives are zero at $p = 0$, the $2D$ primitive for $\Omega_{\rm ph}$ is finite at $p = 0$ and for δN it is infra-red (I.R.) divergent. By subtracting the I.R. finite and divergent terms from Ω_Q and δN, respectively, we get the following expressions, in $2D$, in the thermodynamic limit $\mathcal{A} \to \infty$:

$$\Omega = -\frac{\mu^2\mathcal{A}}{2g} - \frac{p_{\rm max}^2\mathcal{A}}{4\pi\beta\hbar^2} + \frac{m\mu\mathcal{A}\log(1+\frac{p_{\rm max}^2}{4m\mu})}{2\pi\beta\hbar^2} - \frac{p_{\rm max}^2\mathcal{A}\log(\frac{2m}{\beta\sqrt{p_{\rm max}^4+4m\mu p_{\rm max}^2}})}{4\pi\beta\hbar^2} - \frac{m^2w^2\mathcal{A}\log(1+\frac{p_{\rm max}^2}{4m\mu})}{6\pi\beta\hbar^2} + \frac{m^3w^4p_{\rm max}^2\mathcal{A}}{20\pi\mu\beta\hbar^2p_{\rm max}^2+80\pi m\mu^2\beta\hbar^2} \tag{D.10}$$

and

$$\delta N = m\mathcal{A}\frac{\log(1+\frac{p_{\rm max}^2}{4m\mu})+\log(\frac{p_{\rm max}^2\mathcal{A}}{\hbar^2})}{4\pi\beta\hbar^2} + \mathcal{O}(w^2). \tag{D.11}$$

By using the thermodynamic relations Eq. (D.7), we obtain

$$N = \frac{\mu\mathcal{A}}{g} - \frac{m\mathcal{A}\log(1+\frac{p_{\rm max}^2}{4m\mu})}{2\pi\beta\hbar^2} + \mathcal{O}(w^2), \tag{D.12}$$

$$E = \frac{\mu^2\mathcal{A}}{2g} + \frac{p_{\rm max}^2\mathcal{A}}{4\pi\beta\hbar^2} - \frac{m\mu\mathcal{A}\log(1+\frac{p_{\rm max}^2}{4m\mu})}{2\pi\beta\hbar^2} + \mathcal{O}(w^2), \tag{D.13}$$

and

$$P_x = m^2w\mathcal{A}\frac{\log(1+\frac{p_{\rm max}^2}{4m\mu})}{3\pi\beta\hbar^2} + \mathcal{O}(w^3). \tag{D.14}$$

The expression for P_x is different from the one that can be derived from the density corresponding to the condensate depletion $mw\delta N$; this allows us to define $\rho_n = P_x/(w\mathcal{A})$.

D.3 Low-temperature results at a given density

We next determine the chemical potential μ, which fixes the total density $\rho = mN/\mathcal{A}$ at a given value, by solving the equation

$$\rho - \frac{m\mu}{g} + \frac{m^2\log(1+\frac{p_{\rm max}^2}{4m\mu})}{2\pi\beta\hbar^2} = 0; \tag{D.15}$$

at $\beta = \infty$, i.e., zero temperature (subscript 0) we obtain

$$\mu_0 = \frac{g\,\rho}{m}; \tag{D.16}$$

to order β^{-1} we get

$$\mu = \mu_0 + \delta\mu, \tag{D.17}$$

where

$$\delta\mu = \frac{mg\left(4g\rho^2 + \rho p_{\max}^2\right)\log(1+\frac{p_{\max}^2}{4g\rho})}{m^2 p_{\max}^2 + 2\pi\beta\hbar^2\rho p_{\max}^2 + 8\pi\beta\hbar^2 g\rho^2}. \tag{D.18}$$

We insert μ from Eq. (D.17) into Eq. (D.11), define the change in density $\delta\rho = m\delta N/\mathcal{A}$, use the energy E from Eq. (D.13), and then expand to order β^{-1} to obtain

$$\delta\rho = \frac{m^2\left(\log(1+\frac{p_{\max}^2}{4g\rho}) + \log(\frac{p_{\max}^2\mathcal{A}}{\hbar^2})\right)}{4\pi\beta\hbar^2}, \tag{D.19}$$

and

$$E = \frac{g\rho^2\mathcal{A}}{2m^2} + \frac{p_{\max}^2\mathcal{A}}{4\pi\beta\hbar^2}. \tag{D.20}$$

We use Eq. (D.14) and the definition $\rho_n = P_x/(w\mathcal{A})$ to obtain

$$\rho_n = \frac{m^2\log(1+\frac{p_{\max}^2}{4g\rho})}{3\pi\beta\hbar^2}. \tag{D.21}$$

By using Eq. (D.4) and $\rho = m \mid \langle\psi\rangle \mid^2$, we obtain

$$\tilde{\beta}_{\mathrm{BKT}} = \frac{1}{k_{\mathrm{B}}\tilde{T}_{\mathrm{BKT}}} = \frac{2m^2}{\pi\rho\hbar^2}, \tag{D.22}$$

which we can use along with Eq. (D.19) to relate the condensate relative depletion $\delta\rho/\rho$ to $\beta/\tilde{\beta}_{\mathrm{BKT}}$, where $\beta = 1/(k_{\mathrm{B}}T)$ and k_{B} is the Boltzmann constant, as given below:

$$\frac{\delta\rho}{\rho} = \frac{\tilde{\beta}_{\mathrm{BKT}}}{8\beta}\log\left(\frac{p_{\max}^2\left(1+\frac{p_{\max}^2}{4g\rho}\right)\mathcal{A}}{\hbar^2}\right). \tag{D.23}$$

Similarly, the normal-fluid density fraction is

$$\frac{\rho_n}{\rho} = \frac{\tilde{\beta}_{\mathrm{BKT}}}{6\beta}\log\left(1+\frac{p_{\max}^2}{4g\rho}\right). \tag{D.24}$$

We use this low-temperature result Eq. (D.23) to estimate the inverse-temperature scale β_{BKT}, at which the depletion of the $k=0$ condensate mode becomes significant for a finite-size system with N_c^2 collocation points (which fixes the maximum momentum $p_{\max}$); in particular, we can solve Eq. (D.23), for $\delta\rho/\rho = 1$, to obtain

$$\frac{\beta_{\mathrm{BKT}}}{\tilde{\beta}_{\mathrm{BKT}}} = \frac{1}{8}\log\left(\frac{p_{\max}^2\left(1+\frac{p_{\max}^2}{4g\rho}\right)\mathcal{A}}{\hbar^2}\right). \tag{D.25}$$

By making the replacements that correspond to defining $\hbar$, m, and g in terms of c and ξ, $p_{\max} \to \hbar k_{\max}$, $\hbar \to \sqrt{2}cm\xi$, and $g \to c^2m^2/\rho$, we can rewrite Eq. (D.23), Eq. (D.24), and Eq. (D.25) as

$$\frac{\delta\rho}{\rho} = \frac{\tilde{\beta}_{\mathrm{BKT}}}{8\,\beta}\log\left(k_{\max}^2\mathcal{A}\,(1+\frac{{k_{\max}}^2\,\xi^2}{2})\right), \tag{D.26}$$

$$\frac{\rho_n}{\rho} = \frac{\tilde{\beta}_{\mathrm{BKT}}}{3\,\beta} \log\left(1 + \frac{{k_{\max}}^2\,\xi^2}{2}\right), \tag{D.27}$$

and

$$\frac{\beta_{\mathrm{BKT}}}{\tilde{\beta}_{\mathrm{BKT}}} = \frac{1}{8} \log\left(k_{\max}^2 \mathcal{A}\,(1 + \frac{{k_{\max}}^2\,\xi^2}{2})\right), \tag{D.28}$$

respectively.

Bibliography

[1] N. G. Berloff, M. Brachet, and N. P. Proukakis. Modeling quantum fluid dynamics at nonzero temperatures. *Proc. Natl. Acad. Sci. USA*, 111(Supplement 1):4675–4682, 2014.

[2] C. F. Barenghi, V. S. Lvov, and P.-E. Roche. Experimental, numerical, and analytical velocity spectra in turbulent quantum fluid. *Proc. Natl. Acad. Sci. USA*, 111(Supplement 1):4683–4690, 2014.

[3] N. P. Proukakis and B. Jackson. Finite-temperature models of Bose-Einstein condensation. *J. Phys. B: At. Mol. Opt. Phys.*, 41(20):203002, 2008.

[4] R. J. Donnelly. *Quantized vortices in helium II*, volume 2. Cambridge University Press, 1991.

[5] I. M. Khalatnikov. *An introduction to the theory of superfluidity*. WA Benjamin New York, 1965.

[6] C. F. Barenghi, R. J. Donnelly, and W. F. Vinen. Friction on quantized vortices in helium II. a review. *J. Low Temp. Phys.*, 52(3-4):189–247, 1983.

[7] R. J. Donnelly and C. F. Barenghi. The observed properties of liquid helium at the saturated vapor pressure. *J. Phys. Chem. Ref. Data*, 27(6):1217–1274, 1998.

[8] A. Griffin, T. Nikuni, and E. Zaremba. *Bose-condensed gases at finite temperatures*. Cambridge University Press, 2009.

[9] G. Krstulovic and M. Brachet. Energy cascade with small-scale thermalization, counterflow metastability, and anomalous velocity of vortex rings in Fourier-truncated Gross-Pitaevskii equation. *Phys. Rev. E*, 83:066311, Jun 2011.

[10] V. Shukla, M. Brachet, and R. Pandit. Turbulence in the two-dimensional Fourier-truncated Gross-Pitaevskii equation. *New J. Phys.*, 15(11):113025, 2013.

[11] G. Boffetta and R. E. Ecke. Two-dimensional turbulence. *Annu. Rev. Fluid Mech.*, 44:427–451, 2012.

[12] R. Pandit, P. Perlekar, and S. S. Ray. Statistical properties of turbulence: An overview. *Pramana*, 73(1):157–191, 2009.

[13] J. B. Kogut. An introduction to lattice gauge theory and spin systems. *Rev. Mod. Phys.*, 51:659–713, Oct 1979.

[14] P. Minnhagen. The two-dimensional coulomb gas, vortex unbinding, and superfluid-superconducting films. *Rev. Mod. Phys.*, 59:1001–1066, Oct 1987.

[15] N. G. Berloff and A. J. Youd. Dissipative Dynamics of Superfluid Vortices at Nonzero Temperatures. *Phys. Rev. Lett.*, 99:145301, Oct 2007.

[16] B. Jackson, N. P. Proukakis, C. F. Barenghi, and E. Zaremba. Finite-temperature vortex dynamics in Bose-Einstein condensates. *Phys. Rev. A*, 79:053615, May 2009.

[17] G. Krstulovic and M. Brachet. Anomalous vortex-ring velocities induced by thermally excited Kelvin waves and counterflow effects in superfluids. *Phys. Rev. B*, 83:132506, Apr 2011.

[18] D. J. Thouless, P. Ao, and Q. Niu. Transverse Force on a Quantized Vortex in a Superfluid. *Phys. Rev. Lett.*, 76:3758–3761, May 1996.

[19] G. E. Volovik. Comment on "Transverse Force on a Quantized Vortex in a Superfluid". *Phys. Rev. Lett.*, 77:4687–4687, Nov 1996.

[20] C. Wexler. Magnus and Iordanskii Forces in Superfluids. *Phys. Rev. Lett.*, 79:1321–1324, Aug 1997.

[21] H. E. Hall and J. R. Hook. Comment on "Magnus and Iordanskii Forces in Superfluids". *Phys. Rev. Lett.*, 80:4356–4356, May 1998.

[22] E. B. Sonin. Comment on "Berry's Phase and the Magnus Force for a Vortex Line in a Superconductor," "Transverse Force on a Quantized Vortex in a Superfluid," and "Magnus and Iordanskii Forces in Superfluids". *Phys. Rev. Lett.*, 81:4276–4276, Nov 1998.

[23] C. Wexler, D. J. Thouless, P. Ao, and Q. Niu. Wexler et al. Reply:. *Phys. Rev. Lett.*, 80:4357–4357, May 1998.

[24] J. Fuchs, G. Malka, J. C. Adam, F. Amiranoff, S. D. Baton, N. Blanchot, A. Héron, G. Laval, J. L. Miquel, P. Mora, H. Pépin, and C. Rousseaux. Fuchs et al. Reply:. *Phys. Rev. Lett.*, 81:4275–4275, Nov 1998.

[25] S. V. Iordanskii. *Sov. Phys.–JETP*, 22:160, 1966.

[26] S. V. Iordanskii. *Zh. Eksp. Teor. Fiz.*, 49:225, 1965.

[27] M. E. Fisher, M. N. Barber, and D. Jasnow. Helicity Modulus, Superfluidity, and Scaling in Isotropic Systems. *Phys. Rev. A*, 8:1111–1124, Aug 1973.

[28] C. Nore, M. Abid, and M. E. Brachet. Decaying Kolmogorov turbulence in a model of superflow. *Phys. Fluids*, 9(9):2644–2669, 1997.

[29] H. A. Van der Vorst. Bi-CGSTAB: A fast and smoothly converging variant of Bi-CG for the solution of nonsymmetric linear systems. *SIAM J. Sci. Stat. Comput.*, 13(2):631–644, 1992.

Chapter 4

Particles and Fields in Superfluids: Insights from the Two-dimensional Gross-Pitaevskii Equation

In this Chapter we study the dynamics of active particles in two-dimensional superfluids at $T = 0$, for a variety of initial configurations, by carrying out extensive direct-numerical-simulations of the two-dimensional, Galerkin-truncated Gross-Pitaevskii equation. Our study elucidates the interplay of particles and fields, in both simple and turbulent flows.

4.1 Introduction

The transport of particles by turbulent fluids is a problem of central importance in turbulence [1,2]. Not only is such transport of relevance for fundamental questions in turbulence [1, 2], but it also has implications for a geophysical, atmospheric, astrophysical, and industrial problems [3–9]. The superfluid counterpart of this problem, which has been studied occasionally over several decades [10–12], has received renewed attention recently in the wake of experiments [13–15] that have used particles to track quantum vortices in superfluid turbulence. We initiate a study of particles in superfluids by developing a new algorithm for particle motion in a superfluid, which is described by the Gross-Pitaevskii equation [16, 17]. The particles we use are active, i.e., they are not only advected by the flow, but they also act back on it; furthermore, they interact with each other, not only by virtue of superfluid-mediated, effective interactions, but also by repulsive interactions that rise rapidly as the particles approach each other.

Our study elucidates the interplay of particles and fields in superfluids, in both simple and turbulent flows. We carry out extensive direct numerical simulations (DNSs) of this interplay for the two-dimensional (2D) Gross-Pitaevskii (GP) equation. Our work yields several new and exciting results, which we summarize before we present the details of our study: At the one-particle level we explore, for light,

neutral, and heavy particles, the nature of its dynamics in the superfluid, when a constant external force acts on the particle; we find that the particle motion can become chaotic, even if the superfluid is not turbulent. We have also studied the interaction of the particle(s) with vortices, where we observe that the dynamics depends sensitively on the particle characteristics. We extend these studies to the case of two particles, where we show the existence of an effective, superfluid-mediated, attractive interaction between the particles. Moreover, we introduce a short-range repulsive interaction between particles and show how collisions of heavy, neutral, and light particles are different. Here, we find that, at low values of the range of the repulsive force, the collisions are completely inelastic, with coefficient of restitution equal to zero; as we increase the range of the repulsive force the coefficient of restitution becomes finite at a critical point, and finally attains values close to unity, when the collisions are elastic. Furthermore, we find that many-particle collision dynamics also depends on the range of the repulsive force, where its low value results in the formation of a many-particle bound state. At large values of the range of the repulsive force, we obtain chaotic many-particle collision dynamics. Our studies of the assemblies of particles and vortices demonstrates that their dynamics show rich, turbulent spatiotemporal evolution.

The remaining part of this chapter is organized as follows. In Sec. 4.2 we describe the model, initial conditions, and numerical methods we use. Section 4.3 is devoted to our results. We end with conclusions in Sec. 4.4.

4.2 Model, Initial Conditions, and Numerical Methods

To study particle dynamics in superfluids, we use the following Galerkin-truncated GP equation (henceforth TGPE) for the spatiotemporal evolution of the complex, classical, wave function $\psi(\mathbf{x},t)$ describing the superfluid:

$$i\frac{\partial\psi(\mathbf{x},t)}{\partial t} = \mathcal{P}_G\left[\left(-\alpha_0\nabla^2 + g\mathcal{P}_G[|\psi|^2] - \mu + \sum\nolimits_{\mathrm{i}=1}^{\mathcal{N}_\mathrm{o}} V_\mathcal{P}(\mathbf{x}-\mathbf{q}_i)\right)\psi(\mathbf{x},t)\right], \tag{4.1}$$

where $V_\mathcal{P}(\mathbf{x})$ is the potential used to represent the particles, g the effective interaction strength, $\mathcal{P}_G$ the Galerkin projector, i.e., $\mathcal{P}_G[\hat{\psi}(k)] = \theta(k_{\max}-k)\hat{\psi}(k)$, with $\hat{\psi}$ the spatial Fourier transform of ψ and $\theta(\cdot)$ the Heaviside function, μ the chemical potential, and $\mathcal{N}_\mathrm{o}$ the total number of particles included in the study. In our units the quantum of circulation is $4\pi\alpha_0$. We assume Newtonian dynamics for the particles and their equation of motion is

$$m_\mathrm{o}\ddot{\mathbf{q}}_i = \mathbf{f}_{\mathrm{o},i} + \mathbf{F}_{\mathrm{ext,i}}, \tag{4.2}$$

where $m_{\rm o}$ is the particle mass, $\mathbf{F}_{{\rm ext},i}$ the external force acting on the i-th particle, and $\mathbf{q}_{\rm i}$ the particle position vector (the overhead dot represents differentiation with respect to time). The force exerted by the superfluid on the particle, $\mathbf{f}_{{\rm o},i}$ is given by

$$\mathbf{f}_{{\rm o},i} = 2\alpha_0 \int_{\mathcal{A}} |\psi|^2 \nabla V_{\mathcal{P}}(\mathbf{x}-\mathbf{q}_i) d^2x, \tag{4.3}$$

which, in our Galerkin-truncation scheme, becomes

$$\mathbf{f}_{{\rm o},i} = -2\alpha_0 \int_{\mathcal{A}} \Big[\psi^* \mathcal{P}_G[V_{\mathcal{P}}(\mathbf{x}-\mathbf{q}_i)\nabla\psi] + \psi \mathcal{P}_G[V_{\mathcal{P}}(\mathbf{x}-\mathbf{q}_i)\nabla\psi^*] \Big] d^2x, \tag{4.4}$$

where $\mathcal{A} = L^2$ is the area of our 2D, periodic, computation domain of side L. We also study the dynamics of two or more inertial particles in the superfluid, so we introduce a short-range, repulsive two-particle potential $\mathcal{U}_{\rm SR}$, to prevent particles from passing through each other. The form of this repulsive potential is

$$\mathcal{U}_{\rm SR} = \frac{\Delta E r_{\rm SR}^{12}}{r^{12}}, \tag{4.5}$$

where r is the separation between two particles; we treat ΔE and $r_{\rm SR}$ as parameters in our study. We treat the superfluid and particles together as a single system; and, in the absence of any external applied force, the total energy E of this system is conserved. The total energy of the system is

$$E = E_{\rm field} + E_{\rm o} + E_{\rm SR}, \tag{4.6}$$

where the energy contained in the field $E_{\rm field}$, kinetic energy of the particles $E_{\rm o}$, and energy from the short-range repulsion E_{SR} are defined, respectively, as follows:

$$E_{\rm field} = 2\alpha_0 \int_{\mathcal{A}} \Big[\alpha_0 |\nabla\psi|^2 + \frac{1}{2} g|\psi|^4 - \mu|\psi|^2 + \sum\nolimits_{\rm i=1}^{\mathcal{N}_{\rm o}} V_{\mathcal{P}}(\mathbf{x}-\mathbf{q}_i)|\psi|^2 \Big] d^2x; \tag{4.7a}$$

$$E_{\rm o} = \sum\nolimits_{\rm i=1} \frac{1}{2} m_{\rm o} \dot{\mathbf{q}}_i^2; \tag{4.7b}$$

$$E_{\rm SR} = \frac{1}{2} \sum\nolimits_{\rm i,j,i\neq j}^{\mathcal{N}_{\rm o},\mathcal{N}_{\rm o}} \mathcal{U}_{{\rm SR},i,j}. \tag{4.7c}$$

The dynamical evolution of the coupled set of Eqs. (4.1) and (4.2) conserves the total momentum $\mathbf{P}$ of the system and the total number N of bosons, constituting the field. These are

$$\mathbf{P}(t) = \mathbf{P}(t=0) + \mathbf{F}_{\rm ext} t = 2\alpha_0 \int_{\mathcal{A}} \Im(\psi^* \nabla\psi) d^2x + \sum\nolimits_{\rm i=1}^{\mathcal{N}_{\rm o}} m_{\rm o} \dot{\mathbf{q}}_i; \tag{4.8a}$$

$$N = \int_{\mathcal{A}} |\psi|^2 d^2x. \tag{4.8b}$$

We use the Madelung transformation $\psi = \sqrt{\rho(\mathbf{x},t)}\exp(i\phi)$ to obtain a description of our system in terms of hydrodynamical variables, namely, the density ρ and the

velocity $\mathbf{v} = 2\alpha_0\nabla\phi$, where $\phi(\mathbf{x},t)$ is the phase of $\psi(\mathbf{x},t)$. In our units the sound velocity $c = \sqrt{g\rho^*}$, the healing length $\xi = \sqrt{2\alpha_0^2/(g\rho^*)}$, and the total density $\rho^* = N/\mathcal{A}$. In our study we represent a particle in the Eq. (4.1) by the Gaussian potential

$$V_{\mathcal{P}}(r) = V_{\rm o}\exp(-r^2/(2d_{\rm p}^2); \tag{4.9}$$

$V_{\rm o}$ is a measure of the strength of the potential and $d_{\rm p}$ its width. The inclusion of a particle in the superfluid results in the displacement of a superfluid with area equal to the particle area, whose mass we represent by $m_{\rm f}$. We use the ratio $\mathcal{M} \equiv m_{\rm o}/m_{\rm f}$ to define three types of particles: (1) heavy ($\mathcal{M} > 1$), (2) neutral ($\mathcal{M} = 1$), and (3) light ($\mathcal{M} < 1$).

We perform a systematic, pseudospectral, direct numerical simulation (DNS) of the spatiotemporal evolution of the 2D, Fourier-truncated, GP equation Eq. (4.1) coupled with the equations of motion of the particles Eq. (4.2). To achieve this, we have developed a parallel, MPI code in which we discretize $\psi(\mathbf{x},t)$ on a square simulation domain of side $L = 2\pi$ with N_c^2 collocation points. We use periodic boundary conditions in both spatial directions and a fourth-order, Runge-Kutta scheme, with time step Δt, to evolve equations Eq. (4.1) and Eq. (4.2) in time. We evaluate the linear terms in Eq. (4.1) in Fourier space and the nonlinear term in physical space; for the Fourier transform operations we use the FFTW library [18]. We use the dealiasing rule of Ref. [19] in our pseudospectral DNSs of this TGPE, where the maximum wave number $k_{max} = 2/3 \times N_c/2$.

In order to understand the interplay of particles and fields in superfluids, we have classified the initial configurations which we use into seven categories, with the aim of studying the following:

1. `ICP1`: Initial configurations with one particle on which a constant, external force acts for the duration of the DNS.

2. `ICP2`: Initial configurations with two particles and one of the following. (a) The particles are stationary and the repulsive interaction is absent; (b) the particles are stationary and the repulsive interactions are included; (c) a constant, external force acts on the particles, for a short duration, so as to accelerate them before a head-on collision.

3. `ICP3`: Initial configuration to study many-particle dynamics, for the case of five particles with (a) low $r_{\rm SR}$, (b) large $r_{\rm SR}$.

4. `ICP4`: Initial configuration to study the interaction of a single particle, placed in front of a translating vortex-antivortex pair.

5. `ICP5`: Initial configuration to study the interaction of two particles, placed in front of a translating vortex-antivortex pair;

6. `ICP6`: Initial configuration with a single particle moving in the presence of counter-rotating vortex clusters.

7. `ICP7`: Initial configuration with four particles in the presence of counter-rotating vortex clusters.

The compressible nature of the superfluid GP dynamics, in the presence of particles and vortices, can lead to regimes dominated by acoustic radiations; thus, to minimize the acoustic emission, we prepare our initial states for $\texttt{ICP1}-\texttt{ICP7}$ by using a specialized scheme, which uses the advective-Real-Ginzburg-Landau equation (ARGLE)

$$\frac{\partial\psi}{\partial t} = \alpha_0\nabla^2\psi - g|\psi|^2\psi + \mu\psi - \sum\nolimits_{\rm i=1}^{\mathcal{N}_{\rm o}} V_{\mathcal{P}}(\mathbf{x}-\mathbf{q}_i)\psi - i\mathbf{u}_{\rm adv}\cdot\nabla\psi - \frac{\mathbf{u}_{\rm adv}^2}{4\alpha_0}\psi, \qquad (4.10)$$

where $\mathbf{u}_{\rm adv}$ is the applied advective velocity field (for more details we refer to Ref. [20]).

In all our DNS runs, the average total density $\rho^* = 1$, the total number of collocation points $N_c^2 = 128^2$, the healing length $\xi = 1.44\Delta x$, $\Delta x = 2\pi/N_c$, and the quantum of circulation $\alpha_0 \simeq 0.05$ are kept fixed. In the DNS runs with initial configurations `ICP1-ICP2` we take the speed of sound $c = 1$, whereas, in the DNS run with `ICP7` $c = 2$. By varying values of c we can control the number of vortices in a cluster of vortices [20]. We take the strength of the particle potential $V_0 = 10g$ and its width $d_p = 1.5\xi$. In the short-range repulsive potential, $\Delta E = 0.062$, which we determine by using ARGLE, as the difference between the energies of the states in which (a) two particles are on top of each other and (b) they are far apart (the separation between the two particles $r = 4\pi/5$).

4.3 Results

We organize the presentation of our results as follows. In Sec. 4.3.1 we present the results from the dynamics of a single particle. Section 4.3.2 is devoted to two-particle dynamics and Sec. 4.3.3 to many-particle-collision dynamics. Sections 4.3.4 and 4.3.5 describe the interaction of a translating vortex-antivortex pair with a single particle and two particles, respectively. In Sec. 4.3.6 we present the results from the study of the motion of a single neutral particle in the presence of counter-rotating vortex clusters. Section 4.3.7 is devoted to the dynamics of four neutral particles in the presence of counter-rotating vortex clusters.

4.3.1 Single particle dynamics: Constant external force on the particle

We study the dynamics of a single particle in the superfluid by using the initial configuration `ICP1`, where an external force acts on the particle, for heavy, neutral, and light particles. We generate the initial configuration `ICP1` by (a) preparing an initial state with a single particle, represented by a potential $V_{\mathcal{P}}$ Eq. (4.9), at rest using the ARGLE Eq. (4.10); (b) we then use the initial state prepared in (a) in the TGPE Eq. (4.1). We use $\mathbf{F}_{\rm ext} = F_0\hat{\mathbf{x}}$ in the Eq. (4.2), where F_0 is constant in time. We now describe the dynamics of the heavy, neutral, and light particles for the initial configuration `ICP1`.

Heavy particle: We apply an external force $\mathbf{F}_{\rm ext} = 0.02\hat{\mathbf{x}}$ on the heavy particle. In Fig. 4.1 (a) we show the time evolution of the x- and the y-components of the particle velocity $u_{\rm o,x}$ (purple curve) and $u_{\rm o,y}$ (green curve), respectively; the particle starts to move from rest through the superfluid, without disturbing the latter until a critical velocity $u_c \simeq 0.47$ is reached at $t = 2344$. When the particle velocity $\simeq u_c$, a vortex-antivortex pair emerges, with a positive vortex at the top and a negative vortex at the bottom of the particle, but both still attached to, and co-moving with, the particle; the particle slows down slightly. Subsequently, the vortex-antivortex pair is detached from the particle; it is oriented perpendicular to and moves along the x-direction at a much reduced velocity compared to the particle. Given its large velocity, the particle moves ahead of the slowly moving vortex-antivortex pair; and, because of the periodic boundary conditions we use, it comes back and approaches the vortex-antivortex pair from behind. The particle passes through the vortex-antivortex pair, during which passage the positive and the negative vortices glide, repectively along the upper- and lower-half of the particle circumference; such an interaction is also associated with an initial increase that is followed by a decrease in the particle velocity because of the reinforcing nature of the velocity field in the region in between the vortex and the antivortex that constitute the pair. Moreover, this interaction of the particle and the vortex-antivortex pair leads to the generation of sound waves. The particle subsequently sheds another vortex-antivortex pair and now interacts with two vortex-antivortex pairs; this is accompanied by even greater emission of sound waves than in the case of one vortex-antivortex pair. Afterwards, the presence of sound waves during the interaction of the particles with the vortex-antivortex pairs, results in deflections of the latter from their trajectories; at the same time, small fluctuations are induced in the particle velocity (see Fig. 4.1 (a)). The subsequent motions of the particle and the vortex-antivortex pairs become complicated. Many more vortex-antivortex pairs are shed by the particle; and at several instances of the shedding

of vortex-antivortex pair one of the vortices is trapped on the particle for a short duration of time; now the vortex-antivortex pairs are emitted at $u_{\rm o,x} > u_c$. Moreover, the vortices and antivortices frequently annihilate and produce sound waves during this process. Figure 4.1 (d) shows that the force exerted by the superfluid on the particle (see Eq. (4.3)) exhibits large fluctuations, after the critical velocity is reached. In Fig. 4.1 (g) we plot the power spectra of the time series of the Cartesian components $f_{\rm o,x}$ (sky-blue curve) and $f_{\rm o,y}$ (brown curve); these show that many frequencies appear in these spectra. The Video M1 illustrates the spatiotemporal evolution of a forced heavy particle in a superfluid. This video, the time series of $u_{\rm o,x}$, $u_{\rm o,y}$, $f_{\rm o,x}$, and $f_{\rm o,y}$ and their power spectra (Figs. 4.1 (a)-(i)) show that, after the first vortex-antivortex pair has been emitted, the motion of the particle can be temporally chaotic, for heavy particle and light particles. This can be seen most easily from the time series of $f_{\rm o,x}$ and $f_{\rm o,y}$ (Figs. 4.1(d) and (f)) and their power spectra (Figs. 4.1(g) and (i)). By contrast, the temporal evolution of a neutral particle is periodic (see, e.g., the single peak in the power spectrum of Fig. 4.1 (h).

Neutral particle: To study the dynamics of a neutral particle in the superfluid, we use the initial configuration `ICP1`. We apply an external force $\mathbf{F}_{\rm ext} = 0.01\hat{\mathbf{x}}$ on the particle. In Figs. 4.2 (a)-(i) we show via pseudocolor plots the spatiotemporal evolution of the field $|\psi(\mathbf{x},t)|^2$; the particle appears as a large blue patch on these plots. The particle accelerates under the influence of the external force and its velocity reaches a maximum at $t \simeq 33$, before starting to decrease (see Fig. 4.1 (b)); this maximum of velocity is also the critical velocity $u_c \simeq 0.47$, where a vortex-antivortex pair is formed. Figure 4.2 (a) shows the vortex-antivortex pair still attached to the particle at $t = 38$, as an extension along the y-direction of the particle (blue patch). Subsequently, the vortex-antivortex pair is detached from the particle (Fig. 4.2 (b)); but the particle and the vortex-antivortex-pair assembly, henceforth PVA complex, becomes unstable with respect to the motion transverse to the direction of $\mathbf{F}_{\rm ext}$ at $t \simeq 54$ and oscillatory modes are excited, as we show in Fig. 4.1 (b) where the Cartesian components $u_{\rm o,x}$ and $u_{\rm o,y}$ of the particle velocity exhibit modulated oscillations. In Fig. 4.1 (h), the power spectra of both $u_{\rm o,x}$ and $u_{o,y}$ show one large peak and two or three small peaks; the former is associated with main temporal oscillation and the latter with the modulation. Figure 4.1 (e) shows that similar oscillations are present in the Cartesian components of the force exerted by the superfluid on the particle. As a result of this instability, at $t \simeq 64$ the particle is trapped on the positive (upper) vortex (Fig. 4.2 (c)); this is accompanied by an intense emission of sound waves. The particle trapped on the positive vortex and the negative (lower) vortex move together, with both aligned roughly perpendicular

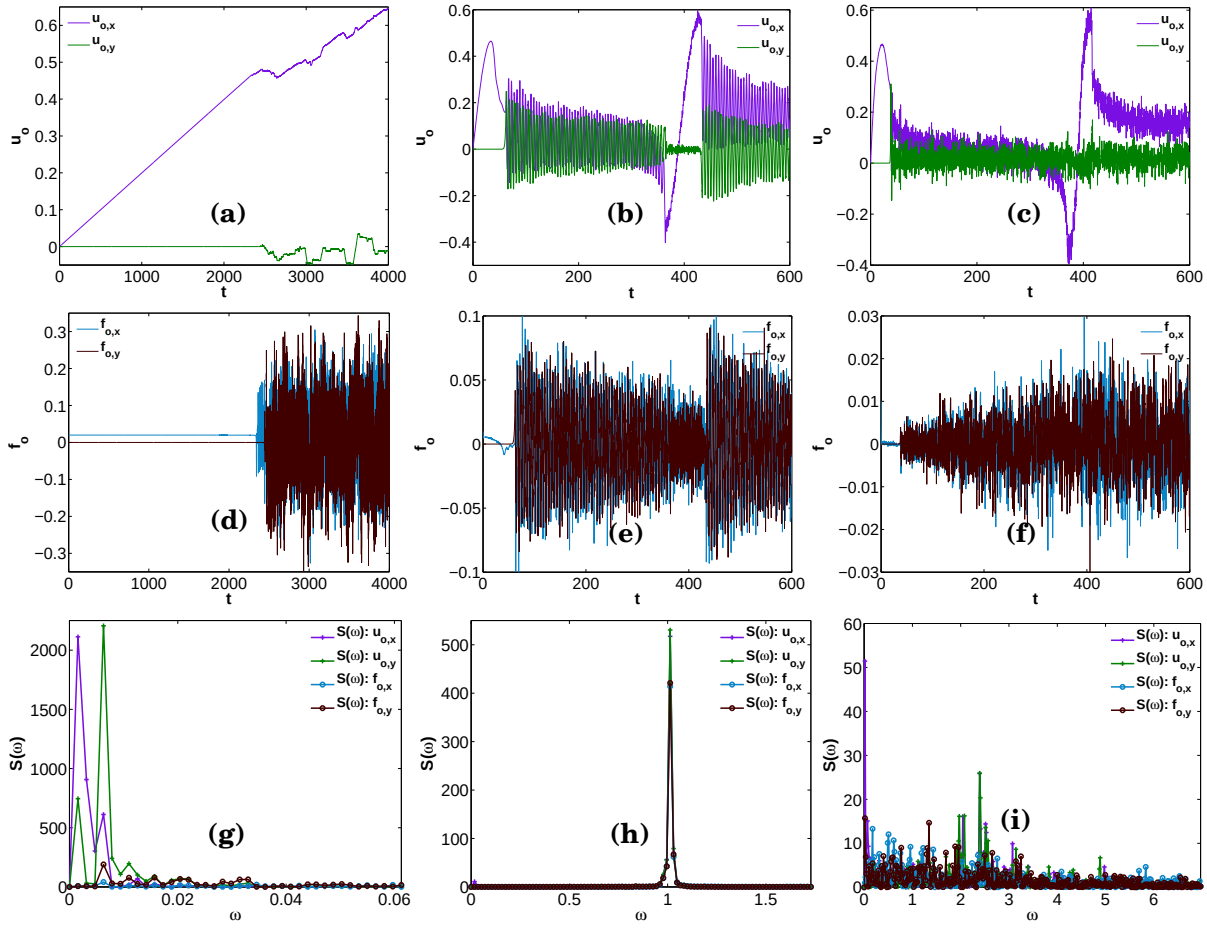

Figure 4.1: Plots of the Cartesian components $u_{\mathrm{o,x}}$ and $u_{\mathrm{o,y}}$ of the particle velocity $\mathbf{u}_{\mathrm{o}}$ for (a) heavy ($\mathcal{M} = 374$, $\mathbf{F}_{\mathrm{ext}} = 0.02\hat{\mathbf{x}}$), (b) neutral ($\mathcal{M} = 1$, $\mathbf{F}_{\mathrm{ext}} = 0.01\hat{\mathbf{x}}$), and (c) light ($\mathcal{M} = 0.0374$, $\mathbf{F}_{\mathrm{ext}} = 0.01\hat{\mathbf{x}}$) particles; (d), (e), and (f) are the analogs of (a), (b), and (c), respectively, for the Cartesian components $f_{\mathrm{o,x}}$ and $f_{\mathrm{o,y}}$ of the force $\mathbf{f}_{\mathrm{o}}$ on the particle. Power spectra, denoted generically by $S(\omega)$, of the time series of $u_{\mathrm{o,x}}$, $u_{\mathrm{o,y}}$, $f_{\mathrm{o,x}}$, and $f_{\mathrm{o,y}}$ are plotted versus the angular frequency ω for (g) heavy ($\mathcal{M} = 374$), (b) neutral ($\mathcal{M} = 1$), and light ($\mathcal{M} = 0.0374$) particles.

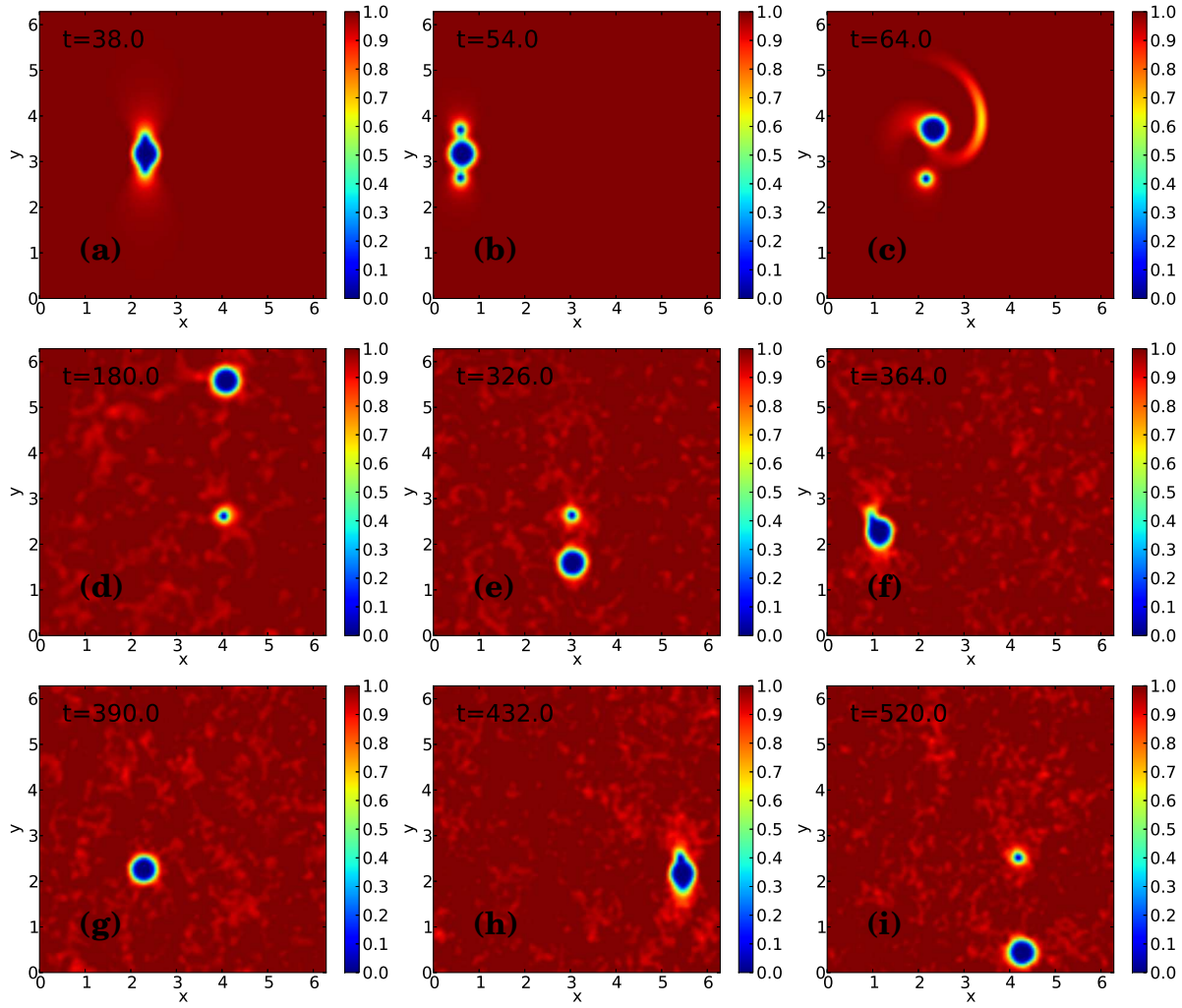

Figure 4.2: Spatiotemporal evolution of the field $|\psi(\mathbf{x},t)|^2$ shown via pseudocolor plots, illustrating the dynamics of a neutral particle, when a constant external force $\mathbf{F}_{\text{ext}} = 0.01\hat{\mathbf{x}}$ acts on it (initial configuration `ICP1`). The particle appears as a large blue patch and the vortices as blue dots (for details see text, subsection 4.3.1).

to the direction of motion (Fig. 4.2 (d)); the separation between the two increases, principally because the positive vortex moves away and takes the trapped particle along with it. Because of our periodic boundary conditions, the positive vortex (and the particle trapped by it) come back from below (the y-direction). The direction of the velocity field, in the small region in between the particle and the vortex, generated by the vortex-antivortex pair, is reversed (from $+\hat{\mathrm{x}}$ to $-\hat{\mathrm{x}}$). When the negative vortex and the positive vortex (and the trapped particle) are close enough to each other, that the field generated by the pair is strong enough that the PVA complex, traversing in the $+\hat{\mathrm{x}}$ direction, reverses its direction of motion at $t \simeq 350$. When the two vortices are very close together (see Fig. 4.2 (f)), they annihilate, while the particle moves predominantly in the $-\hat{\mathrm{x}}$ direction. Soon thereafter the acceleration, because of the external force, reverses the direction of motion once again and the particle begins to move predominantly in the $\hat{\mathrm{x}}$ direction as we show in Fig. 4.2 (g) at $t = 390$. The particle velocity increases, reaches a maximum value $u_{\mathrm{o,x}} = 0.57 > u_c$, and again a vortex-antivortex pair is formed, initially this pair is attached to the particle. At $t \simeq 434$ the particle gets trapped on the negative (lower) vortex and the cycle of particle and vortex motions, described above, is repeated again (see Fig. 4.1 (b) for $t \gtrsim 434$ and Fig. 4.2(i)). Video M2 gives the complete spatiotemporal evolution of the particle and $|\psi(\mathbf{x},t)|^2$.

Light particle: We study the dynamics of the light particle in the superfluid by using the initial configuration `ICP1`; the particle is accelerated by applying an external force $\mathbf{F}_{\mathrm{ext}} = 0.01\hat{\mathrm{x}}$ on it. Figures 4.3 (a)-(i) and Video M3 summarize the spatiotemporal evolution of the field $|\psi(\mathbf{x},t)|^2$ for the light-particle case. A comparison of the x-component of the particle velocity $u_{\mathrm{o,x}}$ (purple curve) in Figs. 4.1 (b) and (c), coupled with a comparison of the field $|\psi(\mathbf{x},t)|^2$ in Figs. 4.2 and 4.3, shows that the dynamics of the light particle is similar to, but not exactly the same as that of the neutral particle. A major feature which distinguishes their dynamics is the presence of a broad range of frequencies in the power spectra of $\mathbf{u}_{\mathrm{o}}$ and $\mathbf{f}_{\mathrm{o}}$ of the former; this indicates that the motion of the light particle is chaotic in contrast to that of the neutral particle whose dynamics is periodic in time.

The chaotic nature of the particle dynamics is enhanced when we increase the amplitude of the external force acting on the particle, as we show in Fig. 4.4; in particular now the power spectra of the Cartesian components of $\mathbf{u}_{\mathrm{o}}$ and $\mathbf{f}_{\mathrm{o}}$ have a broad range of frequencies for all the three types of particles. We can understand the motion of the particles by using the concept of the hydrodynamical mass (or effective mass) $m_* = \partial P_{\mathrm{ext}}/\partial u_{\mathrm{o}}$ ($P_{\mathrm{ext}} = F_{\mathrm{ext}}t$). To begin with there is no drag-force on the particle, but the particle still transfers momentum to the fluid by virtue of the

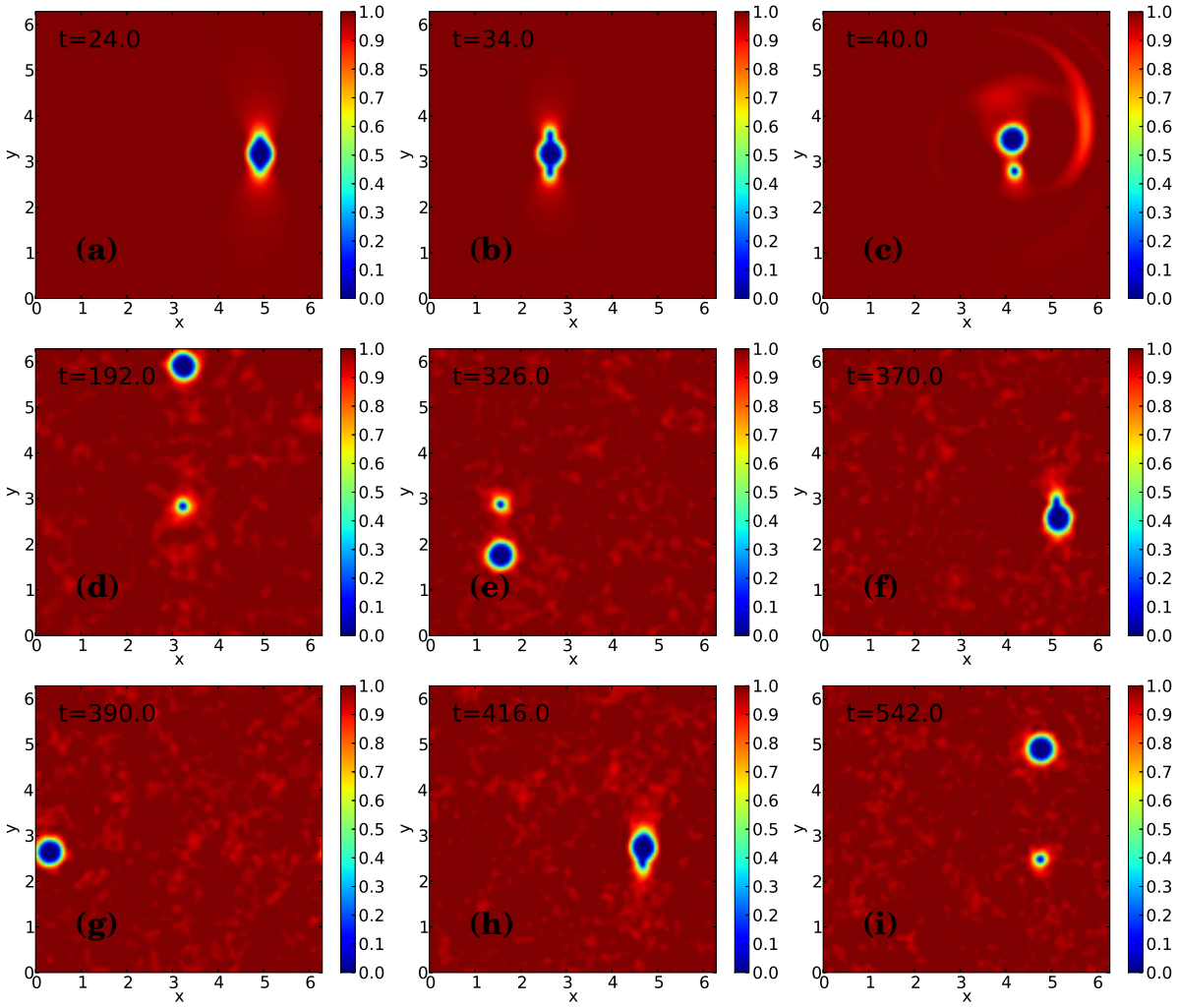

Figure 4.3: Spatiotemporal evolution of the field $|\psi(\mathbf{x},t)|^2$ shown via pseudocolor plots, illustrating the dynamics of a light particle, when a constant external force $\mathbf{F}_{\text{ext}} = 0.01\hat{\mathbf{x}}$ acts on it (initial configuration `ICP1`). The particle appears as a large blue patch and the vortices as blue dots (for details see text, subsection 4.3.1).

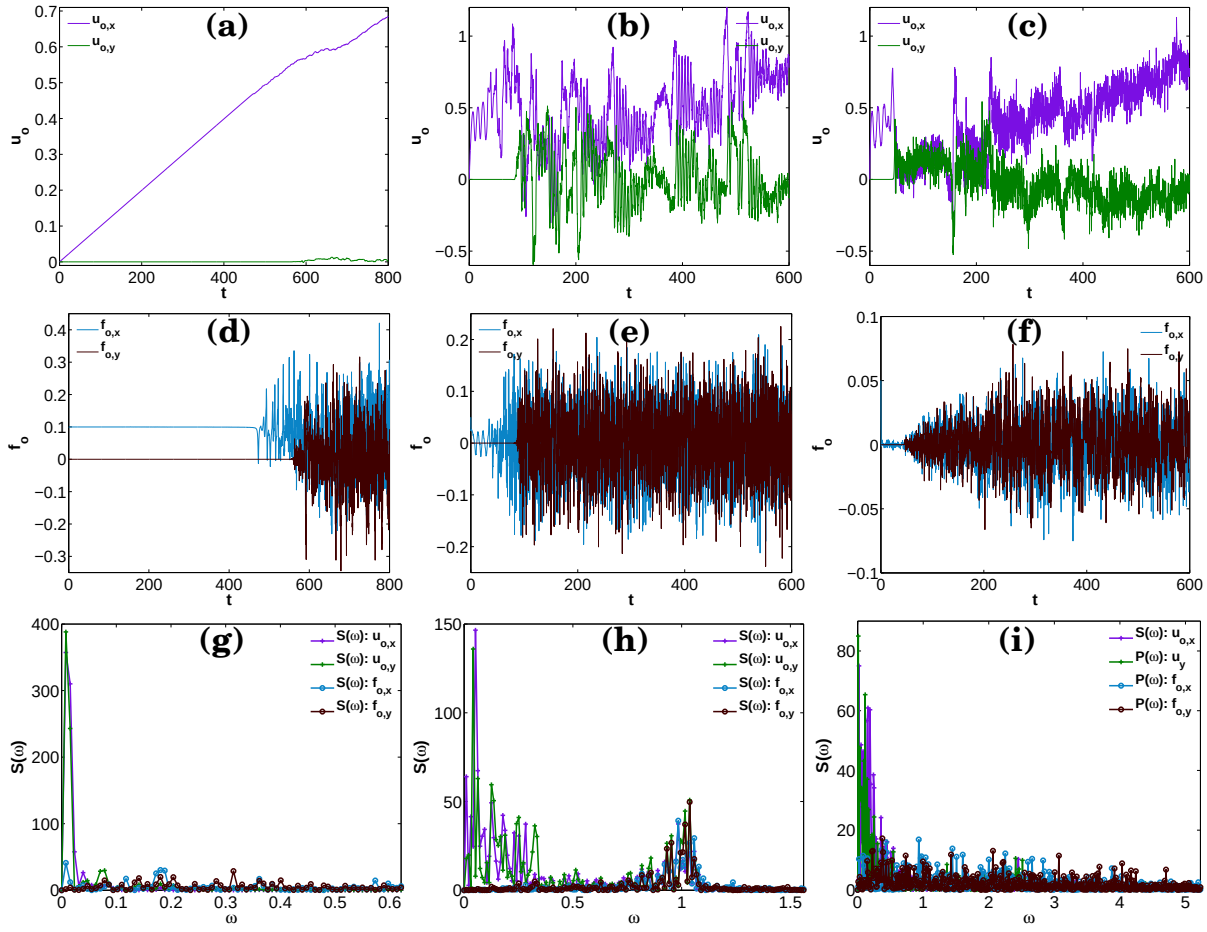

Figure 4.4: Plots of the Cartesian components $u_{\mathrm{o,x}}$ and $u_{\mathrm{o,y}}$ of the particle velocity $\mathbf{u}_{\mathrm{o}}$ for (a) heavy ($\mathcal{M} = 374$, $\mathbf{F}_{\mathrm{ext}} = 0.1\hat{\mathbf{x}}$), (b) neutral ($\mathcal{M} = 1$, $\mathbf{F}_{\mathrm{ext}} = 0.05\hat{\mathbf{x}}$), and (c) light ($\mathcal{M} = 0.0374$, $\mathbf{F}_{\mathrm{ext}} = 0.05\hat{\mathbf{x}}$) particles; (d), (e), and (f) are the analogs of (a), (b), and (c), respectively, for the Cartesian components $f_{\mathrm{o,x}}$ and $f_{\mathrm{o,y}}$ of the force $\mathbf{f}_{\mathrm{o}}$ on the particle. Power spectra, denoted generically by $S(\omega)$, of the time series of $u_{\mathrm{o,x}}$, $u_{\mathrm{o,y}}$, $f_{\mathrm{o,x}}$, and $f_{\mathrm{o,y}}$ are plotted versus the angular frequency ω for (g) heavy ($\mathcal{M} = 374$), (b) neutral ($\mathcal{M} = 1$), and light ($\mathcal{M} = 0.0374$) particles.

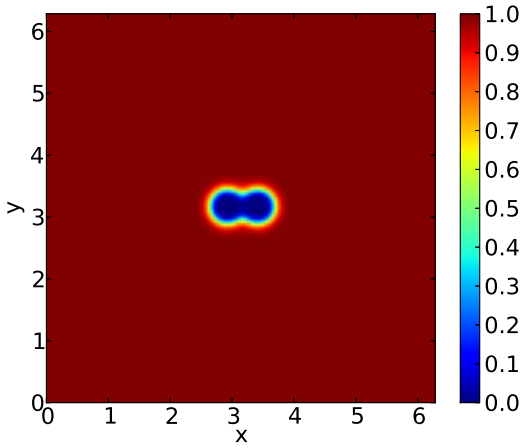

Figure 4.5: Pseudocolor plot of the field $|\psi(\mathbf{x},0)|^2$ showing two particles, separated by a distance $r_0 = 7\xi$, at rest (initial configuration `ICP2(a)`).

increase in its effective mass; this becomes very large (ideally infinity) at $u_{\rm o} = u_c$, where a vortex-antivortex pair is formed. Note that when a vortex-antivortex pair is formed, the plot of $u_{\rm o,x}$ versus time has a maximum (see Fig. 4.1(b)), i.e., the acceleration in the x direction vanishes even though the force $F_{\rm ext}$ is nonzero. Therefore, the effective mass m_* diverges when the vortex-antivortex pair is created. After this, m_* becomes negative and the particle slows down, this is more apparent in the cases of the neutral and the light particles than for a heavy particle.

4.3.2 Two-particle dynamics

In this Section we present the results from our study of the dynamics of two particles in the superfluid; first we describe the superfluid-mediated interaction, which is an effective attractive interaction between the particles. We then study head-on collision between two particles. The particles that we consider here are neutral.

Superfluid-mediated attractive interaction between particles

In Fig. 4.5 we show the initial configuration, which we use to demonstrate the existence of an effective, superfluid-mediated, attractive interaction between the particles; we prepare two particles, separated by a distance $r_0 = 7\xi$, at rest in the superfluid, by specifying the locations of the particle potentials $V_{\mathcal{P}}(\mathbf{x}_{\rm i})$ Eq. (4.9) in the ARGLE Eq. (4.10). The above initial configuration for two neutral particles is used in the TGPE Eq. (4.1). We study the following two cases: SR, repulsive interaction between the particles, is either (1) absent or (2) present. Figures 4.6 (a) and (b) show the displacement of the two particles, in units of ξ, with respect to the cen-

ter of the simulation box (π, π); the particles are initially placed at the coordinates $(\pi - r_0/2, \pi)/\xi$ and $(\pi + r_0/2, \pi)/\xi$ and their subsequent motion is tracked by following the purple curve (particle 1) and the green curve (particle 2), respectively. If there is no SR repulsion between the particles and they are released from rest, the two particles are accelerated towards each other if r_0 is sufficiently small ($r_0 \lesssim 10\xi$). When their centers are very close to or on top of each other, their respective velocities exceed the critical velocity u_c. However, the moment they cross each other, their velocities suddenly start to decrease and they are slowed-down until they come to rest; once again, the two particles start to move towards each other and their velocities reach maxima $u_{\mathrm{o,x}} < u_c$, when they are on top of each other. In the course of this sloshing motion of the particles, a large amount of acoustic energy is produced; moreover, the particles exchange energy with the superfluid, as we show in Fig. 4.7 (a), where $\delta E_{\mathrm{field}} = E_{\mathrm{field}}(t) - E_{\mathrm{field}}(0)$ (purple curve) is the energy change of the superfluid and E_{o} (green curve) the total kinetic energy of the particles; thus the energy for the motion of the two particles is supplied by the superfluid. This oscillatory motion of the particles continues but is damped (see Figs. 4.6 (a) and (c) and Fig. 4.7 (a)) because of the continued loss of energy, in the form of sound waves, thus, the particles form a bound pair. The Video M4 illustrates the sloshing motion of the two neutral particles in the absence of SR, repulsive interaction.

In Fig. 4.6 (b) we show the displacements of the two particles in the presence of the SR repulsion; when they are released from rest, the two particles accelerate towards each other, stop upon collision, when the separation between them $r \simeq r_{\mathrm{SR}}$, and then their direction of motion is reversed. The particles are unable to escape to infinity, as they are again pulled back and undergo multiple collisions; these are accompanied by the production of sound waves. Therefore, this inelastic collision between the two particles leads to the formation of a bound pair, even in the presence of the SR repulsion (for given ΔE and r_{SR} in Eqs. (4.5)). The Video M5 summarizes the collision dynamics of the two particles in the presence of SR, repulsion, when they are released from rest. Figure. 4.7 (b) shows the exchange of energy between the different energy components, here we plot versus time the change in superfluid energy $\delta E_{\mathrm{field}} = E_{\mathrm{field}}(t) - E_{\mathrm{field}}(0)$ (purple curve), the total kinetic energy of the particles E_{o} (green curve), and the SR-repulsion energy E_{SR} (sky-blue curve).

To characterize the superfluid-mediated, effective, attractive potential between the particles, we perform a series of simulations, in which we vary the initial distance between the two particles and obtain the minimum-energy states by using the ARGLE Eq. (4.10), in the absence of SR repulsive interaction. In Fig. 4.8 we

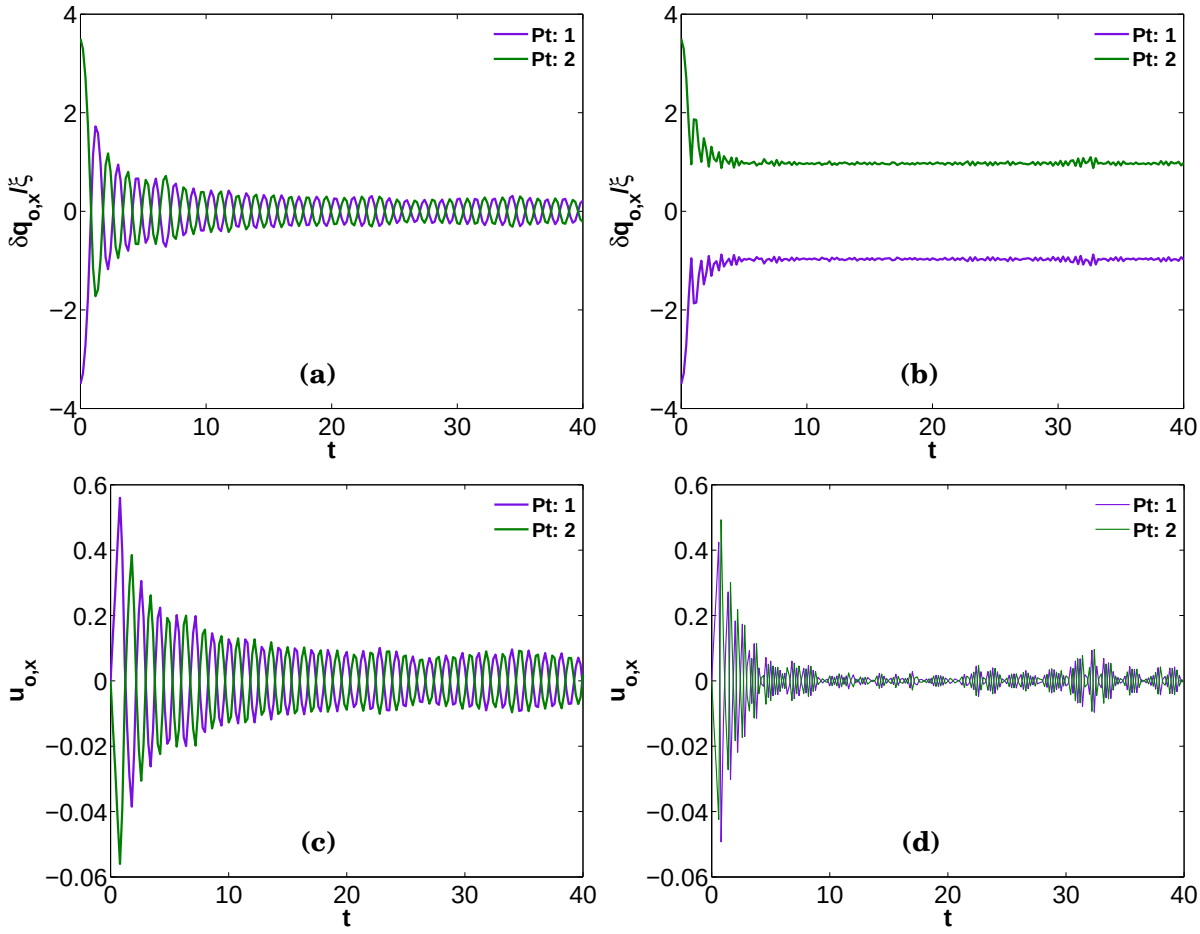

Figure 4.6: Plots versus time t of the displacement $\delta q_{\mathrm{o,x}}/\xi$ of the particles $Pt:1$ (purple curve) and $Pt:2$ (green curve), with respect to the center of the simulation box (π,π), when the SR-repulsive interaction between the particles is (a) absent (`ICP2(a)`) and (b) present (`ICP2(b)`). Plots of $u_{o,x}$ versus t for the particles $Pt:1$ (purple curve) and $Pt:2$ (green curve), when the SR-repulsive interaction between the particles is, (c) absent (`ICP2(a)`) and (d) present (`ICP2(b)`).

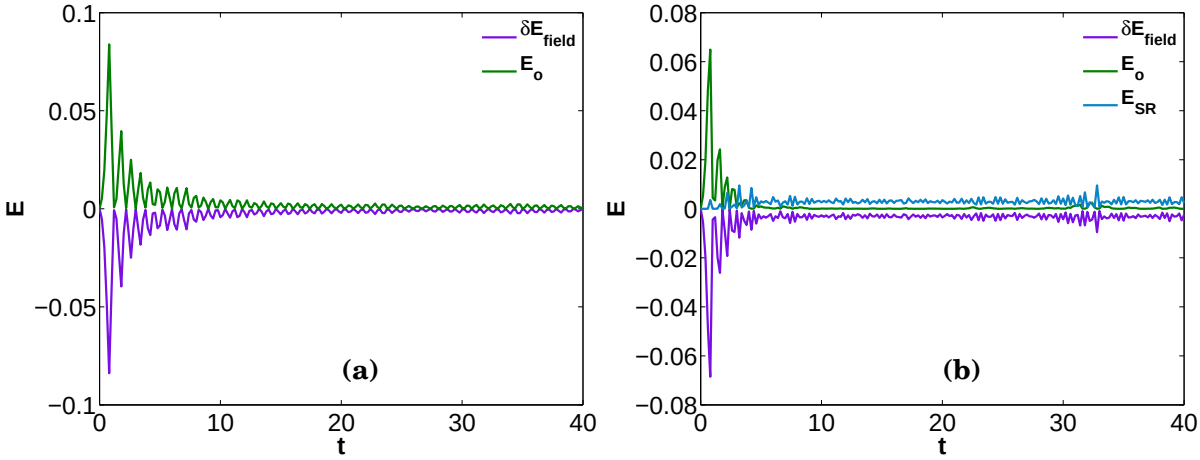

Figure 4.7: Plots versus time t of the energy components $\delta E_{\rm field} = E_{\rm field}(t) - E_{\rm field}(0)$ (purple curve), $E_{\rm o}$ (green curve), $E_{\rm SR}$ (sky-blue curve), when the SR-repulsive interaction between the particles is (a) absent (`ICP2(a)`) and (b) present (`ICP2(b)`).

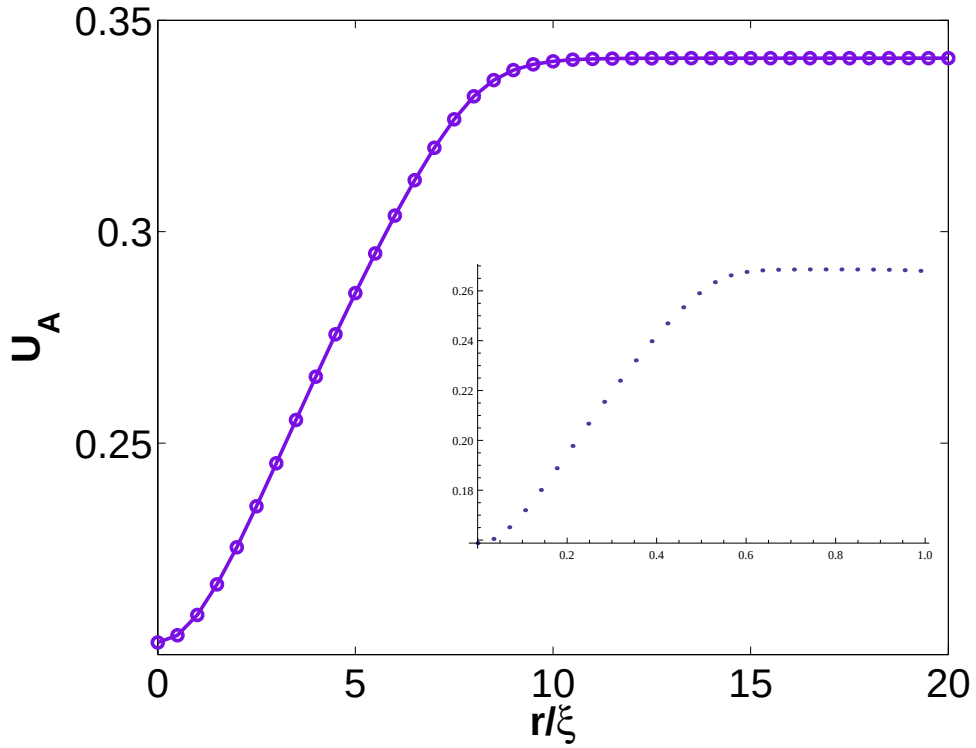

Figure 4.8: A Plot of $U_{\rm A}$ versus r/ξ, from our DNS run. The inset shows the same plot versus r and with $U_{\rm A}$ calculated from the Thomas-Fermi approximation (Eq. (4.14)).

plot the energy

$$U_{\rm A} = 2\alpha_0 \int_{\mathcal{A}} \left[\alpha_0 |\nabla\psi|^2 + \frac{1}{2} g|\psi|^4 - \mu|\psi|^2 + \sum\nolimits_{\rm i=1}^{\mathcal{N}_{\rm o}} V_{\mathcal{P}}(\mathbf{x}-\mathbf{q}_i)|\psi|^2 \right] d^2x + 2\alpha_0 (\frac{1}{2g}\mu^2\mathcal{A}) \quad (4.11)$$

as a function of the separation between the particles r/ξ. The potential $\Delta U_{\rm A} = U_{\rm A}(r) - U_{\rm A}(r=\infty)$ is negative, for small r, and vanishes in the limit $r/\xi \to \infty$; this shows the existence of an effective, superfluid-mediated, attractive interaction between the particles.

We can obtain a rough estimate of the energy $U_{\rm A}$ in the Thomas-Fermi (TF) approximation, where, by neglecting the kinetic energy term in the TGPE Eq. (4.1), we can write

$$|\psi(\mathbf{x})|^2 = \frac{(\mu - \mathcal{V}_{\rm P})\theta(\mu - \mathcal{V}_{\rm P})}{g}, \quad (4.12)$$

where

$$\mathcal{V}_{\rm P} = \sum\nolimits_{\rm i=1}^{\mathcal{N}_{\rm o}=2} V_{\mathcal{P}}(\mathbf{x} - \mathbf{q}_i), \quad (4.13)$$

and θ is the Heaviside function that ensures $|\psi|^2 > 0$. In this approximation,

$$U_{\rm A}^{\rm TF} = 2\alpha_0 \int_{\mathcal{A}} \left[\frac{\mu^2 - (\mu - \mathcal{V}_{\rm P})^2 \theta(\mu - \mathcal{V}_{\rm P})}{2g} \right] d^2x, \quad (4.14)$$

which we plot in the Fig. 4.8 (inset). A comparison of Fig. 4.8 and the inset shows that the values of $U_{\rm A}^{\rm TF}$ are in good agreement with those obtained from our DNS data.

Head-on collisions

The schematic diagram in Fig. 4.9 outlines the procedure, which we use to study the head-on collision between two particles. By using the ARGLE Eq. (4.10) we prepare an initial state with two stationary particles $Pt:1$ and $Pt:2$ at the coordinates $(\pi/2, \pi)$ and $(3\pi/2, \pi)$, respectively. We use this initial configuration in the TGPE Eq. (4.1) and apply the external forces $F_{\rm ext} = 0.01\hat{\mathbf{x}}$ and $F_{\rm ext} = -0.01\hat{\mathbf{x}}$ on the particles $Pt:1$ and $Pt:2$, respectively, so as to accelerate them; and then we turn off $F_{\rm ext}$ at $t_0 = 6$ (red vertical line). We study the head-on collision between the neutral particles, by varying the range $r_{\rm SR}$ of the SR repulsive interaction between the two particles, while keeping all the other parameters fixed.

In Figs. 4.10 (a) and (b) we show the trajectories of the two particles $Pt:1$ and $Pt:2$ undergoing a head-on collision by using solid and dashed lines, respectively. We use the following colors to indicate the values of $r_{\rm SR}$: (1) $r_{\rm SR} = 1.5\xi$ (purple), (2) $r_{\rm SR} = 6.5\xi$ (green), (3) $r_{\rm SR} = 7.0\xi$ (sky-blue), (4) $r_{\rm SR} = 8.0\xi$ (brown). We follow the same line-types and color-codes in Figs. 4.10 (c) and (d) to plot versus t the

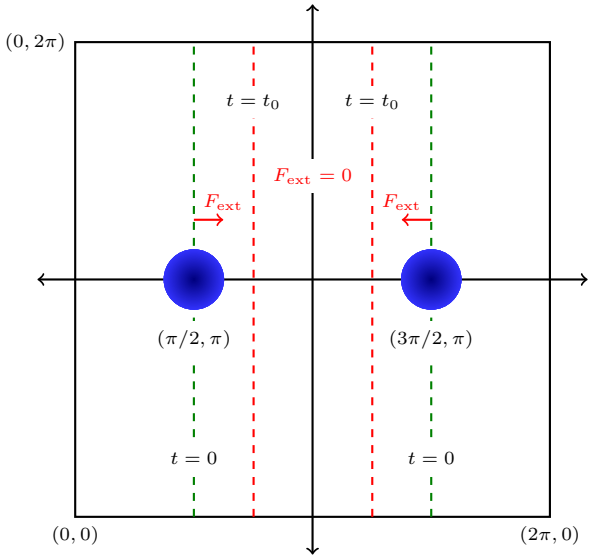

Figure 4.9: Schematic diagram outlining the initial configuration and the procedure, which we use to study the head-on collision between two particles (blue discs).

x-components of the velocities of the two particles. In Figs. 4.11 (a), (b), (c), and (d) we show the different energy components versus time for $r_{\rm SR} = 1.5\xi$, $r_{\rm SR} = 6.5\xi$, $r_{\rm SR} = 7.0\xi$, and $r_{\rm SR} = 8.0\xi$, respectively; here $\delta E_{\rm field} = E_{\rm field}(t) - E_{\rm field}(t_0)$ (purple curve) is the energy change of the superfluid, $E_{\rm o}$ (green curve) the total kinetic energy of the particles, and $E_{\rm SR}$ (sky-blue curve) the SR-repulsion energy.

For $r_{\rm SR} = 1.5\xi$, the collision between the two neutral particles is completely inelastic; they form a bound pair and the mean separation between their centers fluctuates around $r \simeq r_{\rm SR}$ (see Fig. 4.10(a), purple curves); the time average of the velocity of the particles is zero, after the collision (see Fig. 4.10(c), purple curves). Moreover, Fig. 4.11 (a) shows that, for this completely inelastic collision, initially, as the particles approach each other, the $E_{\rm o}$ shoots up at the cost of the $\delta E_{\rm field}$ and, thereafter, the energy exchanges are small; the subsequent exchanges occur between $E_{\rm SR}$ and $\delta E_{\rm field}$, whereas the $E_{\rm o}$ remains close to zero. Figure 4.10 (a) (green curves) shows that at $r_{\rm SR} = 6.5\xi$ the two particles rebound, with small, non-zero, mean velocities (see Fig. 4.10(c), green curves); the nature of the energy exchange between the different components is shown in Fig. 4.11 (b); at the time of the collision, $E_{\rm SR}$ shoots up at the combined cost of $\delta E_{\rm field}$ and $E_{\rm o}$. After the collision, most of the energy is transfered to the fluid and the particles have a small kinetic energy. For higher values of, e.g., $r_{\rm SR} = 7.0\xi$ and $r_{\rm SR} = 8.0\xi$, the head-on collision between neutral particles is nearly elastic and the particles rebound with velocities close to their values at incidence (see Fig. 4.10 (b) and (d)); as a consequence, the time averaged values of $E_{\rm o}$ before and after the collision (see

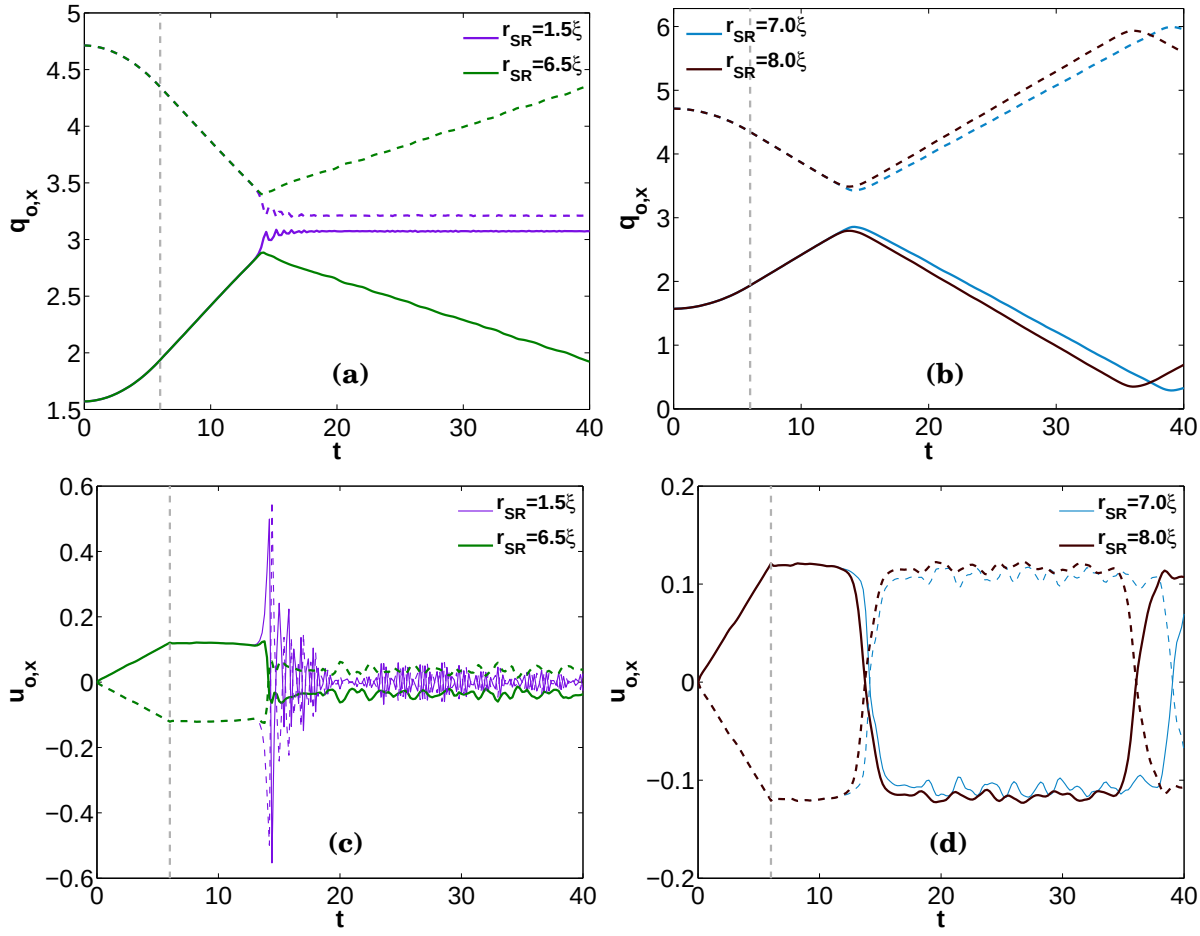

Figure 4.10: Head-on collisions between two neutral particles (initial configuration ICP2(c)): (a) particle trajectories shown via plots of $q_{o,x}$ versus time and $r_{\mathrm{SR}=1.5\xi}$ (purple curve) and $r_{\mathrm{SR}=6.5\xi}$ (green curve); (b) particle trajectories shown via plots of $q_{o,x}$ versus time and $r_{\mathrm{SR}=7.0\xi}$ (sky-blue curve) and $r_{\mathrm{SR}=8.0\xi}$ (brown curve); (c) $u_{\mathrm{o,x}}$ versus time for $r_{\mathrm{SR}=1.5\xi}$ (purple curve) and $r_{\mathrm{SR}=6.5\xi}$ (green curve); (d) $u_{\mathrm{o,x}}$ versus time for $r_{\mathrm{SR}=7.0\xi}$ (sky-blue curve) and $r_{\mathrm{SR}=8.0\xi}$ (brown curve).

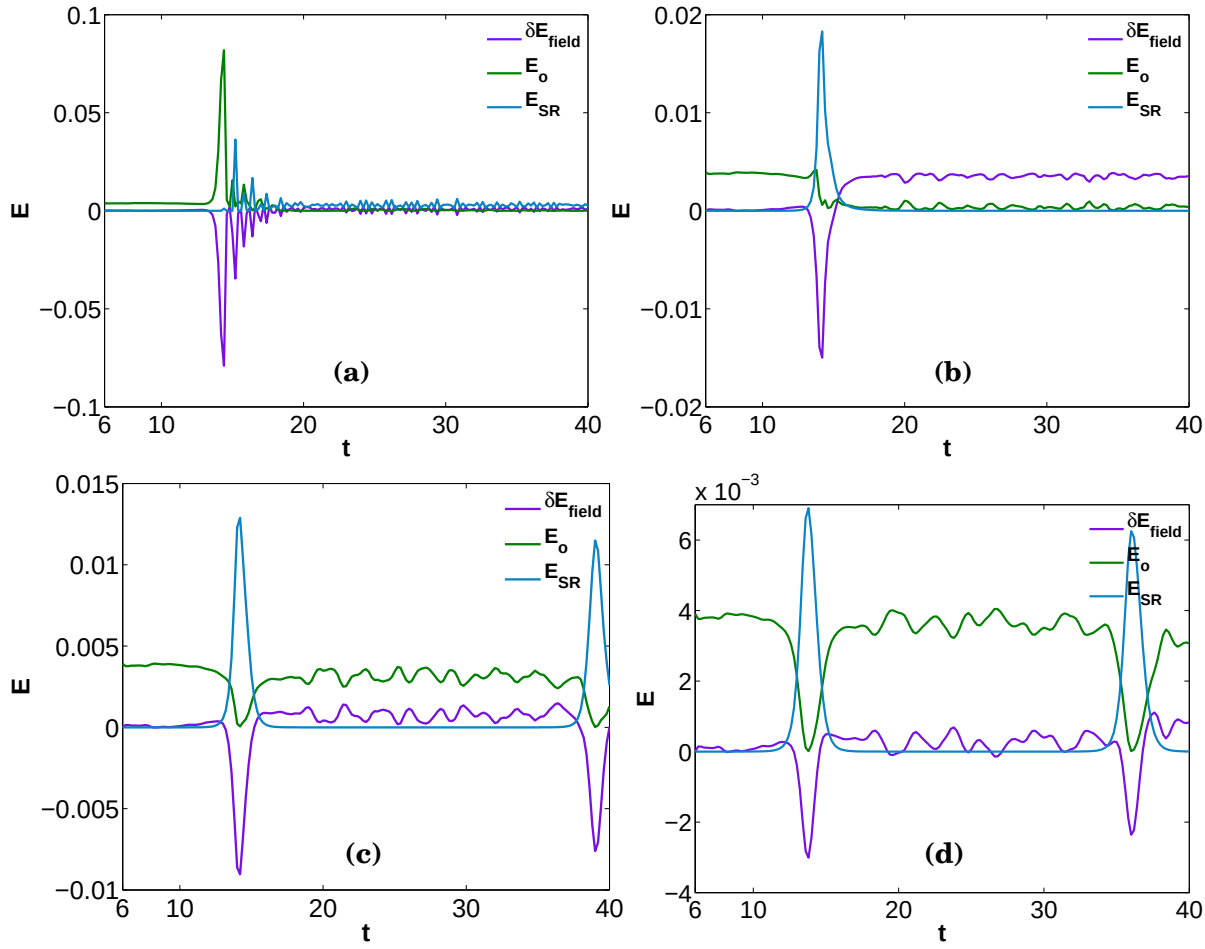

Figure 4.11: Head-on collisions between two neutral particles (initial configuration `ICP2(c)`): Plots versus time t of the energy components $\delta E_{\rm field} = E_{\rm field}(t) - E_{\rm field}(t_0)$ (purple curve), $E_{\rm o}$ (green curve), $E_{\rm SR}$ (sky-blue curve) for (a) $r_{\rm SR} = 1.5\xi$; (b) $r_{\rm SR} = 6.5\xi$; (c) $r_{\rm SR} = 7.0\xi$; (d) $r_{\rm SR} = 8.0\xi$. The external force driving the particles is turned off at $t_0 = 6$.

Figs. 4.11 (c) and (d), green curves) are comparable to each other. The Videos Video M6 and Video M7 illustrate the collision dynamics of two neutral particles for $r_{\rm SR} = 1.5\xi$ and $r_{\rm SR} = 7.0\xi$, respectively.

We have carried out similar, two-particle collision studies for the heavy and light particles. The head-on collision between two heavy particles is nearly elastic, for $r_{\rm SR} = 1.5\xi$ and the given velocities of incidence. For the collisions, which we have studied, the total kinetic energy of the particles is enough to overcome the superfluid-mediated, attractive potential. The Video M8 illustrates the collision dynamics of two heavy particles, for $r_{\rm SR} = 1.5$. However, the head-on collisions of light particles is similar to the case of neutral particles, for $r_{\rm SR} = 1.5\xi$ and similar initial conditions.

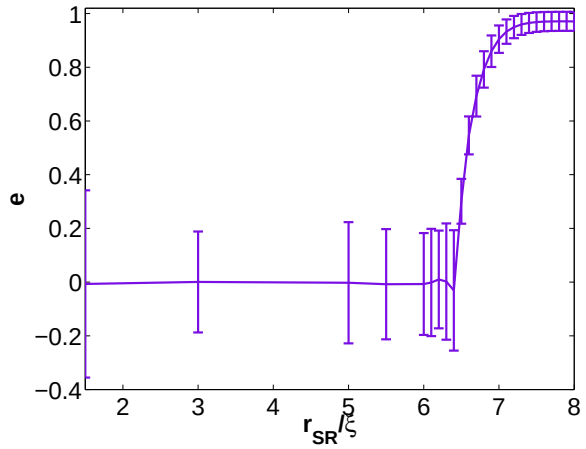

Figure 4.12: Plot of the coefficient of restitution e (Eq. (4.15)) versus $r_{\rm SR}/\xi$, for the head-on collision between two neutral particles (initial configuration `ICP2(c)`).

Coefficient of restitution: We characterise this transition from inelastic to elastic collisions by calculating the coefficient of restitution (for head-on collisions)

$$e = \frac{u_{2,\rm F} - u_{1,\rm F}}{u_{1,\rm I} - u_{2,\rm I}}, \tag{4.15}$$

where $u_{1,\rm I}$ and $u_{2,\rm I}$ are, respectively, the mean velocities of the particles $Pt:1$ and $Pt:2$ before the collision and $u_{1,\rm F}$ and $u_{2,\rm F}$ are the mean velocities of these particles after the collision. For the collisions described above, we find: (1) $e = 0$ for $r_{\rm SR}/\xi = 1.5$; (2) $e = 0.30 \pm .08$ for $r_{\rm SR}/\xi = 6.5$; (3) $e = 0.90 \pm .05$ for $r_{\rm SR}/\xi = 7.0$; and (4) $e = 0.97 \pm .04$ for $r_{\rm SR}/\xi = 8.0$. In Fig. 4.12 we plot e versus $r_{\rm SR}/\xi$ for head-on collision between two neutral particles. We find that, at low values of $r_{\rm SR}/\xi$, the particle collisions are inelastic with $e = 0$; and, as we increase $r_{\rm SR}/\xi$, e becomes finite at a critical value $r_{\rm SR}/\xi \sim 6.5$, and finally attains value close to 1, i.e., $e = 1$. Visually e seems to rise continuously from zero at this critical point; however, the error bars on our measurements of e do not permit us to obtain a reliable estimate for the precise manner in which e rises from zero at this critical point.

4.3.3 Many-particle dynamics

To illustrate the dynamics of the many particles in the superfluid, we study the dynamics of five particles by the using the initial configuration `ICP3`, which we describe below. Here we consider neutral particles. By using the ARGLE Eq. (4.10) we prepare an initial state with five stationary particles, $Pt:1$, $Pt:2$, $Pt:3$, $Pt:4$, and $Pt:5$ at the coordinates $(\pi/2, \pi/2)$, $(\pi/2, 3\pi/2)$, $(3\pi/2, \pi/2)$, $(3\pi/2, 3\pi/2)$, and (π, π), respectively. We use this initial configuration in the TGPE Eq. (4.1) and apply the external forces $\mathbf{F}_{\rm ext,1} = \frac{0.1}{\sqrt{2}}(1,1)$, $\mathbf{F}_{\rm ext,2} = \frac{0.1}{\sqrt{2}}(1,-1)$, $\mathbf{F}_{\rm ext,3} = \frac{0.1}{\sqrt{2}}(-1,1)$, and

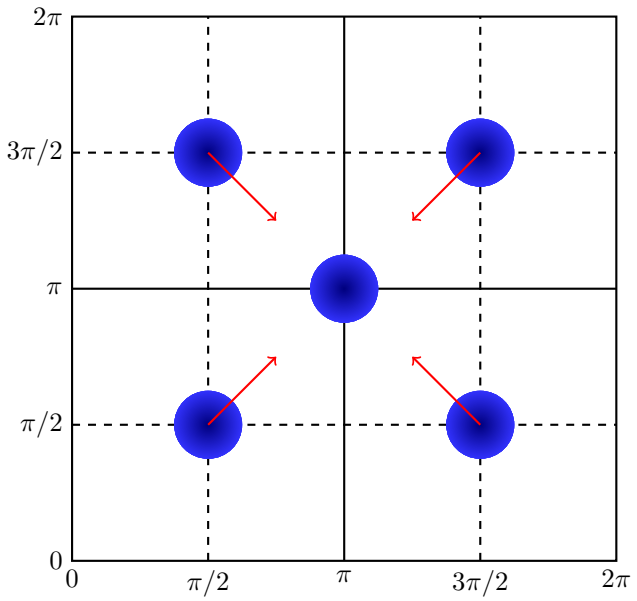

Figure 4.13: Schematic diagram with the initial configuration ICP3, which we use to study the dynamics of five particles in the superfluid. Red arrows indicate the direction of external forces $\mathbf{F}_{\rm ext}$, on the particles (blue discs); the forces are turned off at time $t_0 = 2$.

$\mathbf{F}_{\rm ext,4} = \frac{0.1}{\sqrt{2}}(-1,-1)$ on the particles $Pt:1$, $Pt:2$, $Pt:3$, $Pt:4$, respectively, until time $t_0 = 2$, so as to accelerate them towards the particle $Pt:5$ which is initially at rest. Figure 4.13 illustrates the initial configuration ICP3 and the red-arrows indicate the directions of the external forces. We use this initial configuration to study the ensuing five-particle-collision dynamics for two different values of, namely, (1) $r_{\rm SR} = 1.5\xi$ and (2) $r = 8.0\xi$.

For $r_{\rm SR} = 1.5\xi$, the five-particle collisions are completely inelastic and the particles stick-together to form a five-particle cluster. In Fig. 4.14 (a) we show the trajectories of the five colliding particles. After the collision, the cluster drifts slowly and the particles in the cluster trace out a randomly drifting, loop-like trajectories, as we show in Fig. 4.14 (b), where, over the time of our simulation, each particle trajectory shows roughly six loops; all the trajectories together span an area of size $\simeq 10\xi \times 10\xi$. The Video M9 illustrates the spatiotemporal evolution of the five colliding particles, for $r_{\rm SR} = 1.5\xi$.

We know from our study of head-on collisions between two neutral particles that, at $r_{\rm SR} = 8.0\xi$, these collisions are nearly elastic with $e = 0.97 \pm .04$. Similarly, the collisions between five particles are nearly elastic; the slight inelasiticity arises from the emission of sound waves. In Figs. 4.15 (a)-(i) we show via pseudocolor plots the spatiotemporal evolution of the field $|\psi(\mathbf{x},t)|^2$ and the five-particle-collision dynamics, for $r_{\rm SR} = 8.0\xi$. In Fig. 4.16 (a) we show the trajectories of the particles

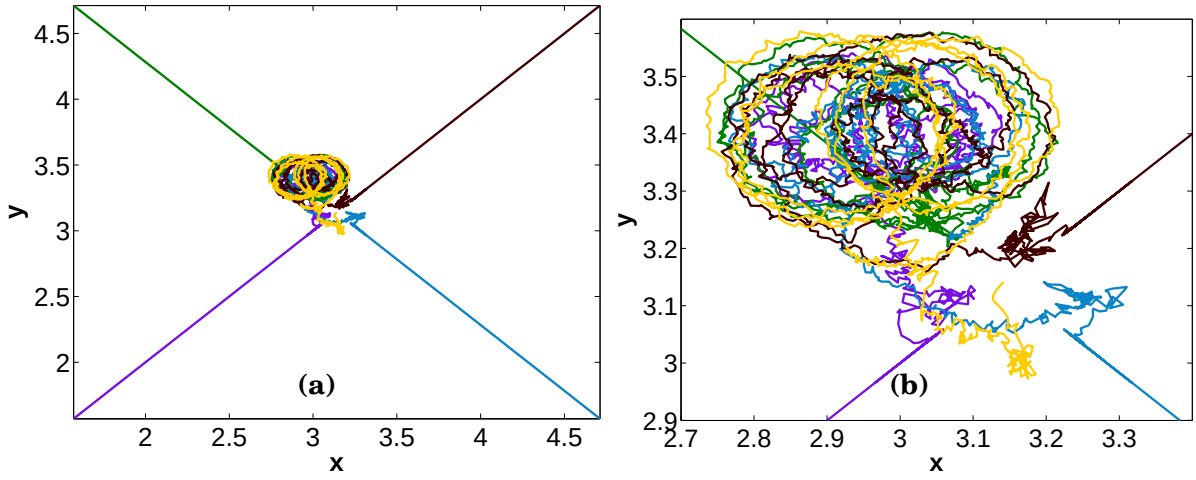

Figure 4.14: Trajectories of the five neutral particles $Pt:1$ (purple curve), $Pt:2$ (green curve), $Pt:3$ (sky-blue curve), $Pt:4$ (brown curve), and $Pt:5$ (yellow curve) undergoing inelastic collisions for $r_{\rm SR}=1.5\xi$ (initial configuration `ICP3(a)`) (a) full view; (b) magnified view.

$Pt:1$, $Pt:2$, $Pt:3$, $Pt:4$, and $Pt:5$ by using purple, green, sky-blue, brown, and yellow circles, respectively. To begin with, the particles $Pt:1$-$Pt:4$ move towards $Pt:5$ and rebound after the collisions with it, and, on their journey back, they collide with each other at the corners of the simulation domain because of our periodic boundary conditions; this process is repeated a few times, and the particles $Pt:1$-$Pt:4$ move back and forth along straight lines (see Fig. 4.16 (a)). During these symmetric repeated collisions, which are not perfectly elastic, the particles lose their kinetic energy to the fluid in the form the sound waves; this is also evident on the plots of the Cartesian components of the particle velocity $u_{\rm o}$ versus time, as we show in Fig. 4.16 (b)-(e), where the magnitude of the rebounding velocities decreases and keep decaying as the number of collision events increases. At around $t\simeq 130$, the stationary particle $Pt:5$ starts moving (see Fig. 4.16 (f)) and the symmetry imposed because of the initial configuration is lost; the particles now collide with each other in a random manner and their motion can become chaotic (see Fig. 4.16 (a)). The Video M10 gives the complete spatiotemporal evolution of the five particles undergoing collisions, for $r_{\rm SR}=8.0\xi$.

4.3.4 Interaction of a single particle with a vortex-antivortex pair

We study the interaction of a single particle with a vortex-antivortex pair for the heavy, neutral, and light particles. We use the initial configuration `ICP4`, in which a particle is placed at a distance, in front of the positive vortex of the translating vortex-antivortex pair. By using the ARGLE Eq. (4.10) we prepare a state with a stationary particle at $(1.5\pi, 1.257\pi)$, this is then combined with a state corre-

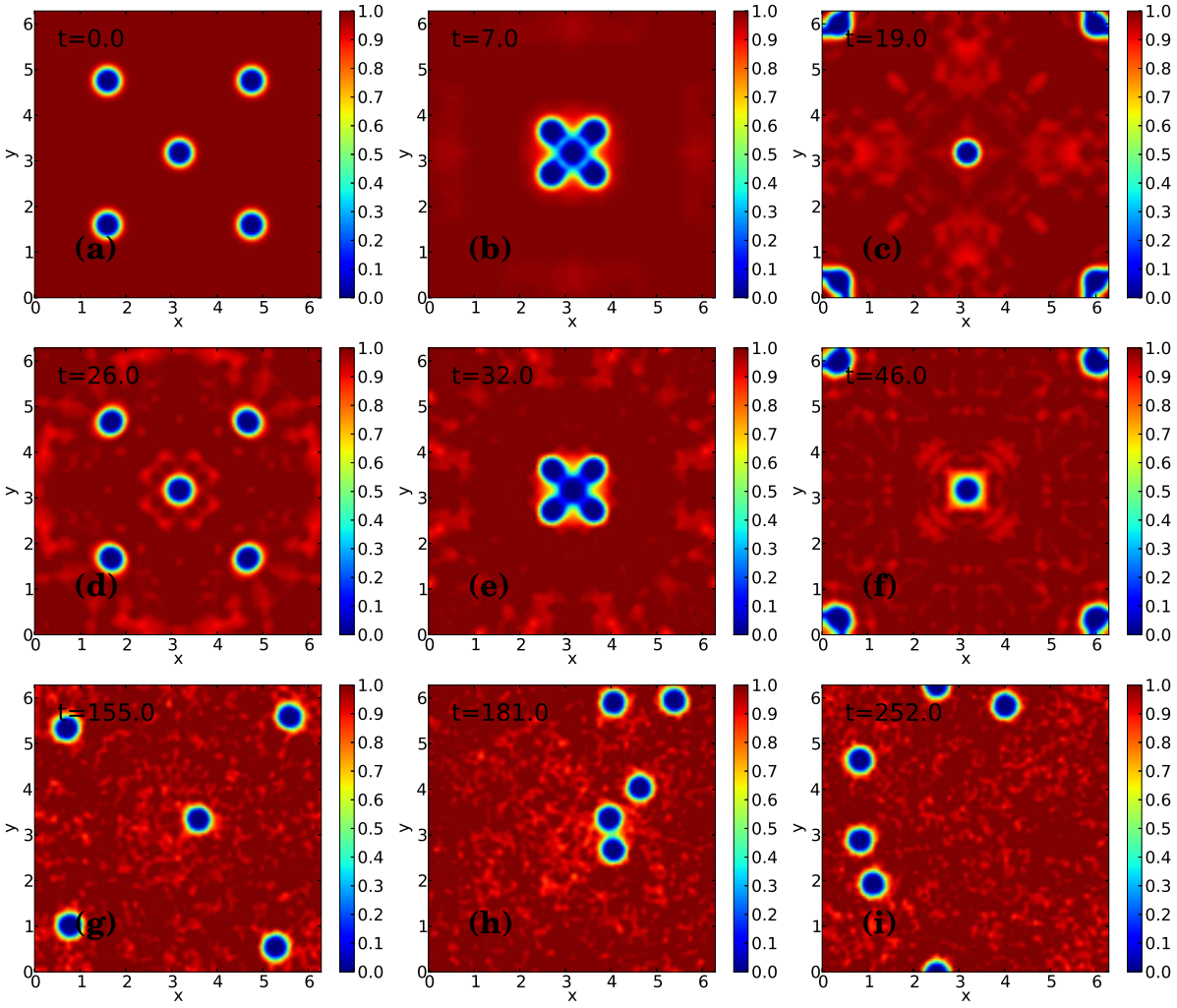

Figure 4.15: Spatiotemporal evolution of the field $|\psi(\mathbf{x},t)|^2$ shown via pseudocolor plots, for the collisions between five neutral particles ($r_{\mathrm{SR}} = 8.0\xi$, initial configuration `ICP3(b)`).

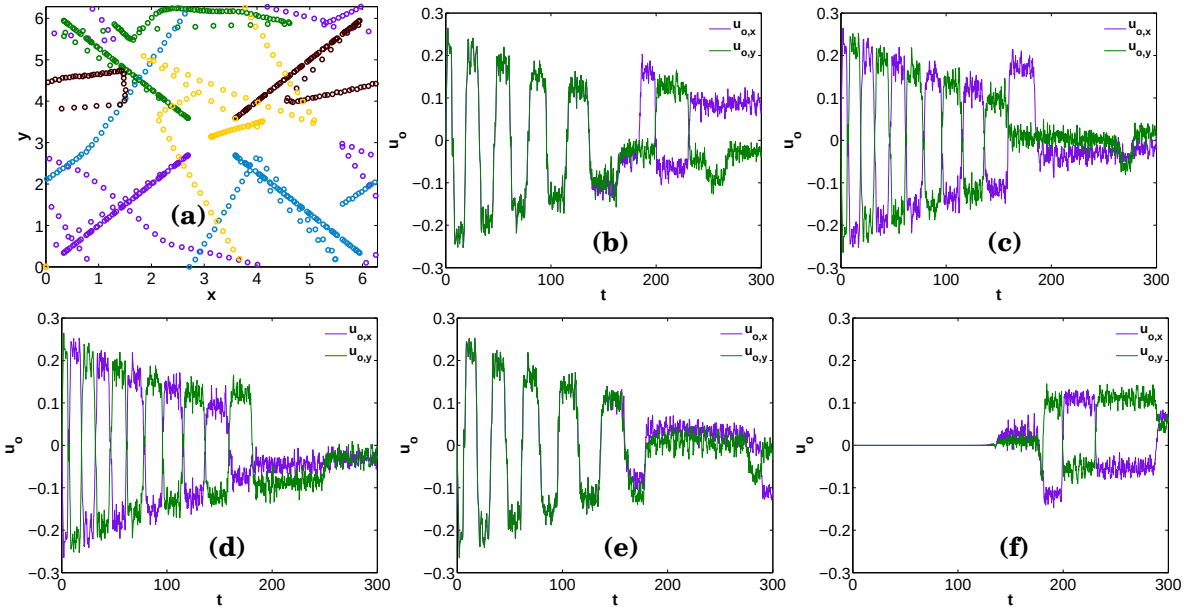

Figure 4.16: (a) Trajectories of the five neutral particles $Pt:1$ (purple curve), $Pt:2$ (green curve), $Pt:3$ (sky-blue curve), $Pt:4$ (brown curve), and $Pt:5$ (yellow curve) undergoing inelastic collisions ($r_{\rm SR}=8.0\xi$, initial configuration ICP3(b)); plots versus time t of $u_{o,x}$ (purple curve), $u_{o,y}$ (green curve) for the particles $Pt:1$-$Pt:5$ shown in (b)-(f), respectively.

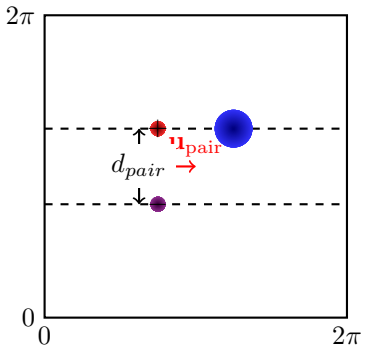

Figure 4.17: Schematic diagram illustrating the initial configuration ICP4, which we use to study the interaction of a single particle (blue disc), placed in front of a translating vortex-antivortex pair (represented by small red and purple discs).

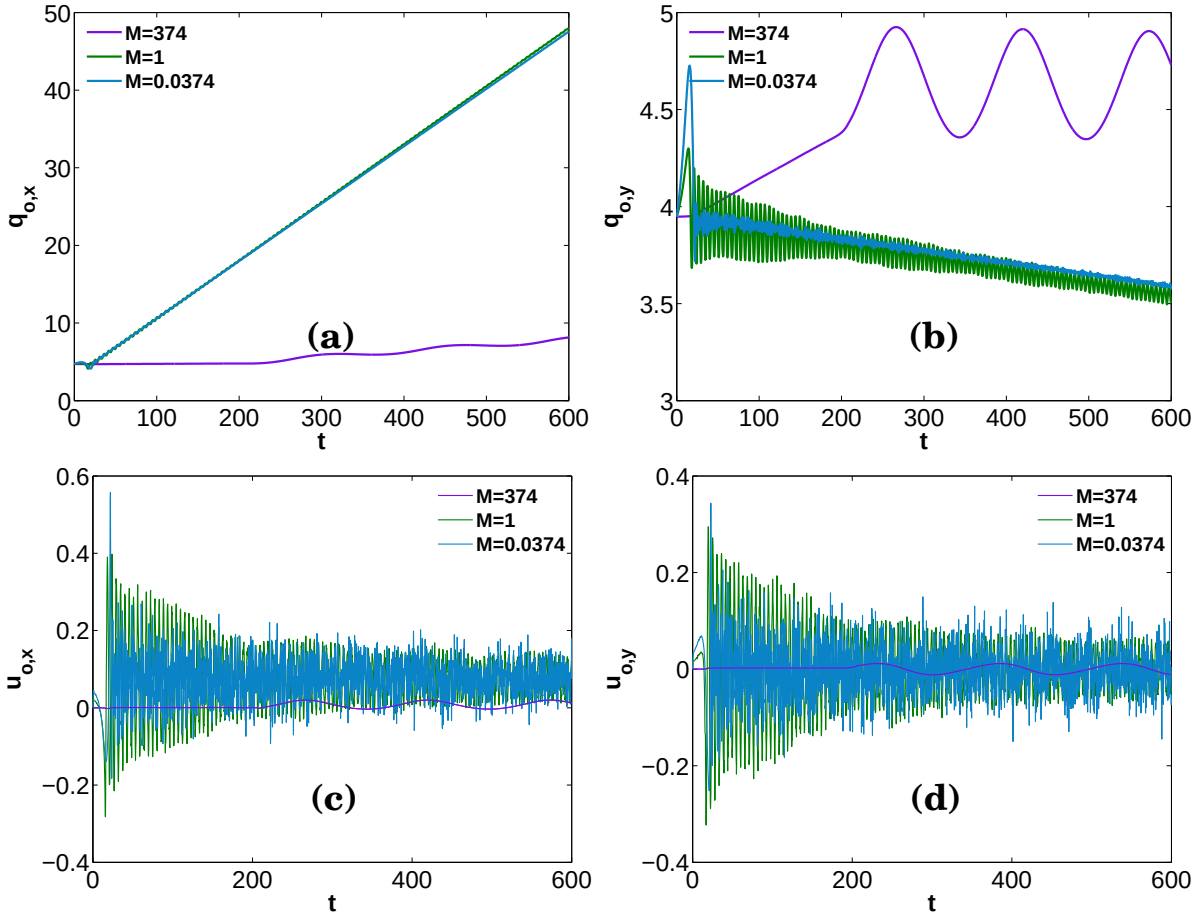

Figure 4.18: Plots versus time t of (a) $q_{\mathrm{o,x}}$, (b) $q_{\mathrm{o,y}}$, (c) $u_{\mathrm{o,x}}$, and (d) $u_{\mathrm{o,y}}$ for heavy ($\mathcal{M} = 374$, purple curve), neutral ($\mathcal{M} = 1$, green curve), and light ($\mathcal{M} = 0.0374$, sky-blue curve) particles, placed in the path of the positive (upper) vortex of a translating vortex-antivortex pair (initial configuration `ICP4`). In (a) and (b) the values of $q_{\mathrm{o,x}}$ and $q_{\mathrm{o,y}}$ are not mod2π; i.e., if particle goes around our periodic simulation domain once, say in the $\hat{\mathrm{x}}$ direction, then the values of $q_{\mathrm{o,x}}$ is its value in the box plus 2π.

sponding to a vortex-antivortex pair, of size $d_{\mathrm{pair}} \simeq 23\xi$ and which translates with a velocity $\mathbf{u}_{\mathrm{pair}} = 0.074\hat{\mathrm{x}}$ (see the schematic diagram in Fig. 4.17).

Figures 4.18 (a), (b), (c), and (d) show plots versus time of (a) $q_{\mathrm{o,x}}$, (b) $q_{\mathrm{o,y}}$, (c) $u_{\mathrm{o,x}}$, and (d) $u_{\mathrm{o,y}}$, respectively, for heavy, neutral, and light particles. When the vortex-antivortex pair approaches the heavy particle, the positive (upper) vortex glides over the particle, which leads to a momentum exchange, so the vortex-antivortex pair is deflected from its path, and it acquires a small velocity in the $-\hat{\mathrm{y}}$ direction. This interaction leads to the production of sound waves. Subsequently, while the negative vortex (of the vortex-antivortex pair) comes near the heavy particle and, in the presence of sound waves, this particle is finally trapped on the negative vortex. During the trapping of the particle on the negative vortex, a large amount of acoustic energy is released into the system. This sequence of events is illustrated

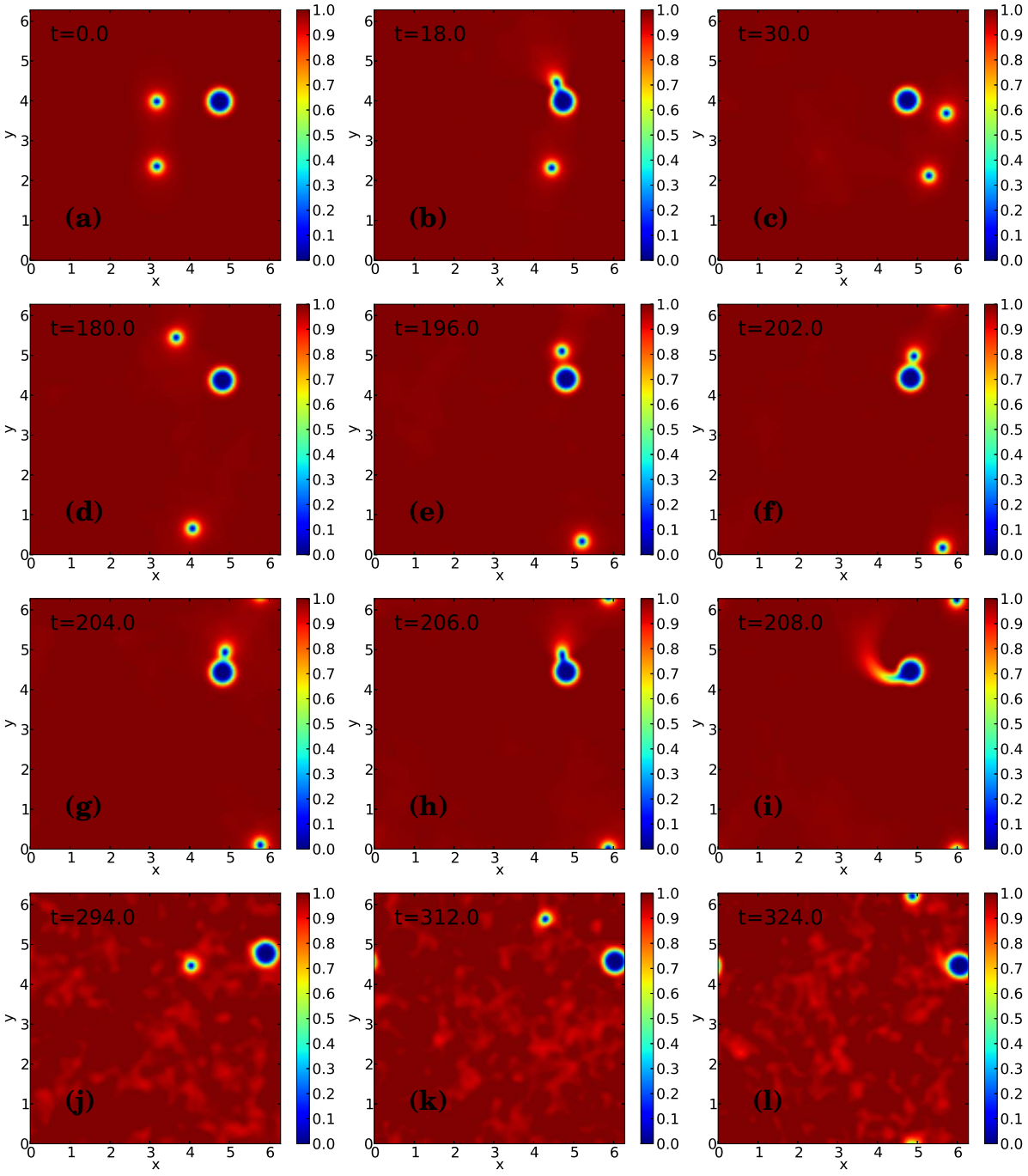

Figure 4.19: Spatiotemporal evolution of the field $|\psi(\mathbf{x},t)|^2$ shown via pseudocolor plots, for a heavy particle placed in the path of the positive (upper) vortex of a translating vortex-antivortex pair (initial configuration `ICP4`).

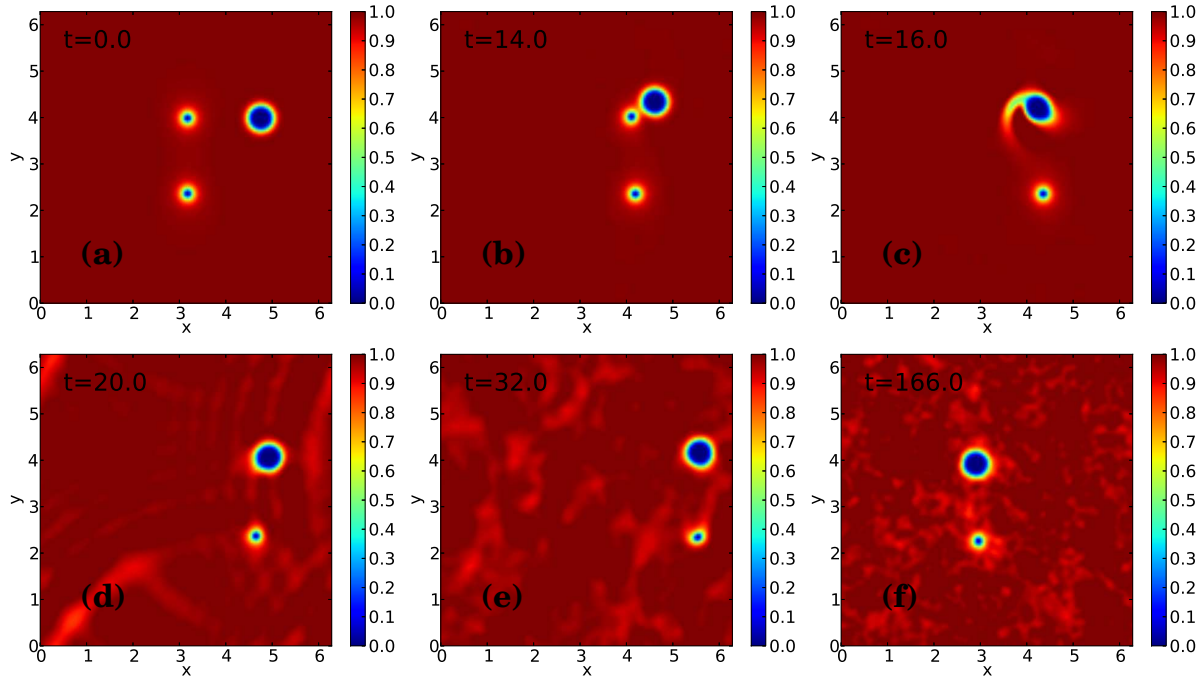

Figure 4.20: Spatiotemporal evolution of the field $|\psi(\mathbf{x},t)|^2$ shown via pseudocolor plots, for a neutral particle placed in the path of the positive (upper) vortex of a translating vortex-antivortex pair (initial configuration `ICP4`).

by the pseudocolor plots of Figs. 4.19 (a)-(i) and Video M11. The trapped particle executes oscillatory motion while drifting (see Fig. 4.18 purple curve for $t \gtrsim 200$) and the positive vortex now revolves around the particle trapped on the negative vortex.

When a translating vortex-antivortex pair approaches neutral or light particles, they feel the flow around the positive (upper) vortex more strongly than did the heavy particle; the neutral and light particles are pushed out and they move around the positive vortex before getting trapped on the positive vortex (see green and sky-blue curves Fig. 4.18 (a) and (b) for $t \lesssim 20$). The response of the light particle is most dramatic: while flowing around the positive vortex, it travels almost all the way to the back of the positive vortex $(t \simeq 20)$ before it is trapped on the vortex. The pseudocolor plots of Figs. 4.20 (a)-(i) and 4.21 (a)-(i) and the Videos M12 and M13 summarize the dynamics of the neutral and light particles, respectively. When the neutral and the light particle get trapped on the positive vortex, there is a sudden change in their velocities, as we show in Figs. 4.18 (c) and (d) at $t \simeq 20$; this results in the generation of large fluctuations. Neutral particles exhibit modulated oscillations, whereas light particles display chaotic temporal evolution. In Figs. 4.22 (a), (b), and (c) we plot energy time series to illustrate the exchange of energy between the particle and the superfluid field.

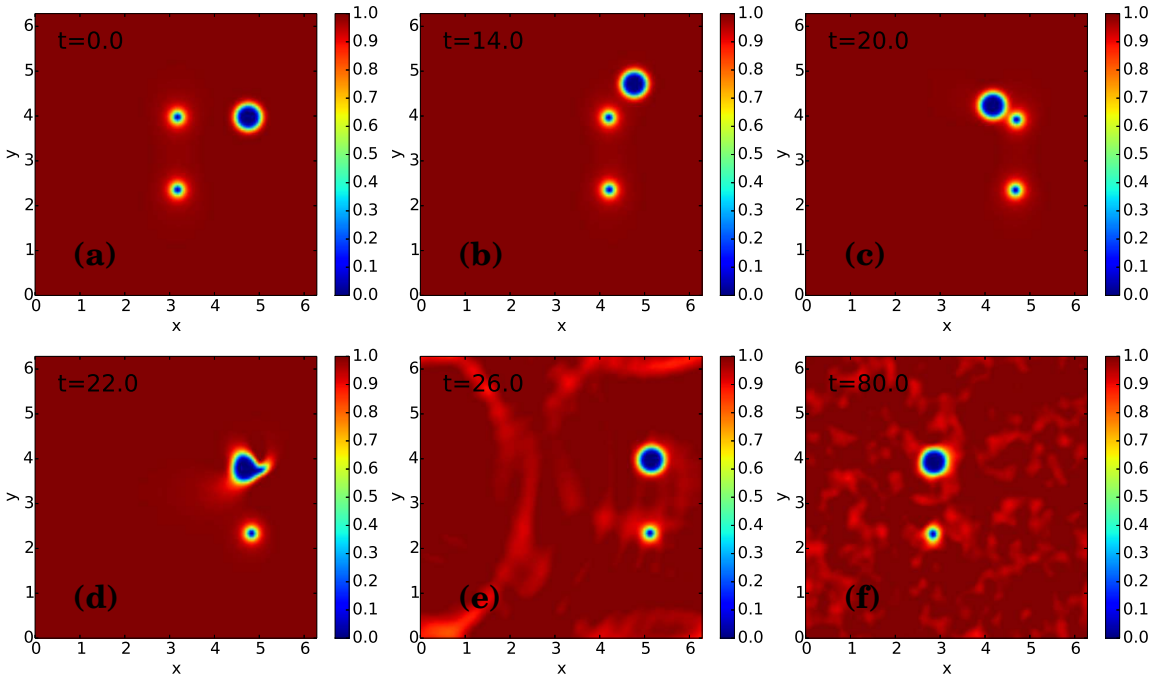

Figure 4.21: Spatiotemporal evolution of the field $|\psi(\mathbf{x},t)|^2$ shown via pseudocolor plots, for a light particle placed in the path of the positive (upper) vortex of a translating vortex-antivortex pair (initial configuration `ICP4`).

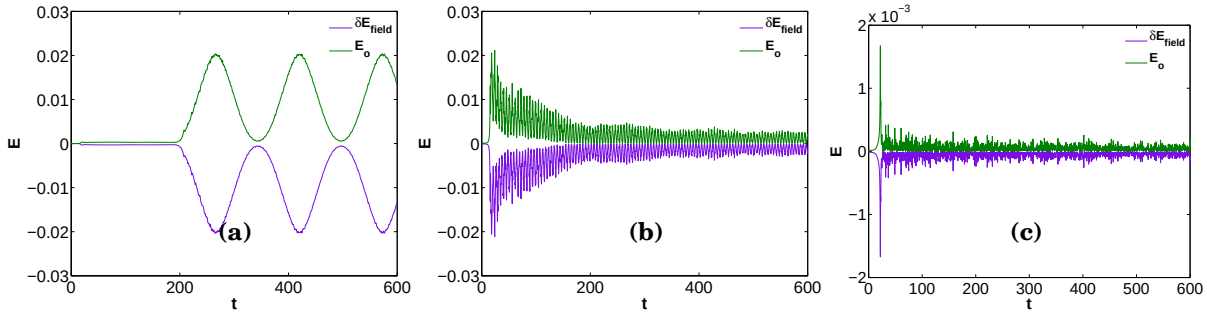

Figure 4.22: Plots versus time t of the energy components $\delta E_{\rm field}$ and $E_{\rm o}$ for (a) heavy, (b) neutral, and (c) light particles, placed in the path of the positive (upper) vortex of a translating vortex-antivortex pair (initial configuration `ICP4`).

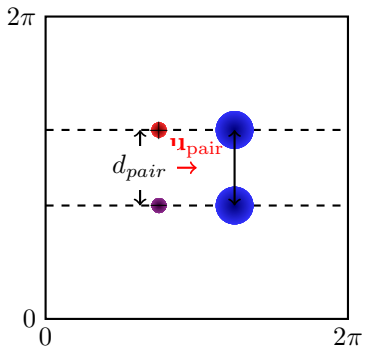

Figure 4.23: Schematic diagram showing the initial configuration ICP5, which we use to study the interaction of two particles (blue discs), placed in front of a translating vortex-antivortex pair (red and purple discs).

4.3.5 Interaction of two particles with a vortex-antivortex pair

We now study the interaction of two particles with a vortex-antivortex pair. For this we use the initial configuration ICP5, in which we place the two particles $Pt:1$ and $Pt:2$ at a distance, in front of the positive and the negative vortices of a translating vortex-antivortex pair (see the schematic diagram in Fig. 4.23). We use ARGLE Eq. (4.10) to prepare a state with two stationary particles $Pt:1$ and $Pt:2$ at $(1.5\pi, 1.257\pi)$ and $(1.5\pi, 0.743\pi)$, respectively; this state is then combined with a state corresponding to a vortex-antivortex pair of size $d_{\rm pair} \simeq 23\xi$ which translates with a velocity $\mathbf{u}_{\rm pair} = 0.074\hat{\mathbf{x}}$. We use the above initial configuration to study the interaction of the vortex-antivortex pair with heavy, neutral, and light particles.

In Figs. 4.24 (a)-(e) we show that, when the vortex-antivortex pair approaches the two symmetrically placed heavy particles, the positive (upper) vortex and the negative (lower) vortex glide along the circumferences of $Pt:1$ and $Pt:2$, respectively; thereafter, the vortex-antivortex pair continues to translate in the $\hat{\mathbf{x}}$ direction. The interaction of the vortex-antivortex pair with these particles leads to the transfer of momentum to the latter and they start moving slowy (see Figs. 4.25 (a)-(d) for $t \simeq 16$. Because of our periodic boundary conditions, the translating vortex-antivortex pair comes back and again glides along the particles, which are still in the path of translation of this pair (see Figs. 4.24 (f)-(i)). The particles move away from the vortices, as the vortex-antivortex pair moves beyond them (see Figs. 4.25 (a)-(d) for $t \gtrsim 100$). At later times, the separation between the particles is wide enough for the vortex-antivortex pair to pass through the region in between the particles without any significant obstruction (see Figs. 4.24 (j)-(l)). However, the plots of the particle-velocity components versus times show jumps when the vortex-antivortex pair passes through the region in between the particles. The

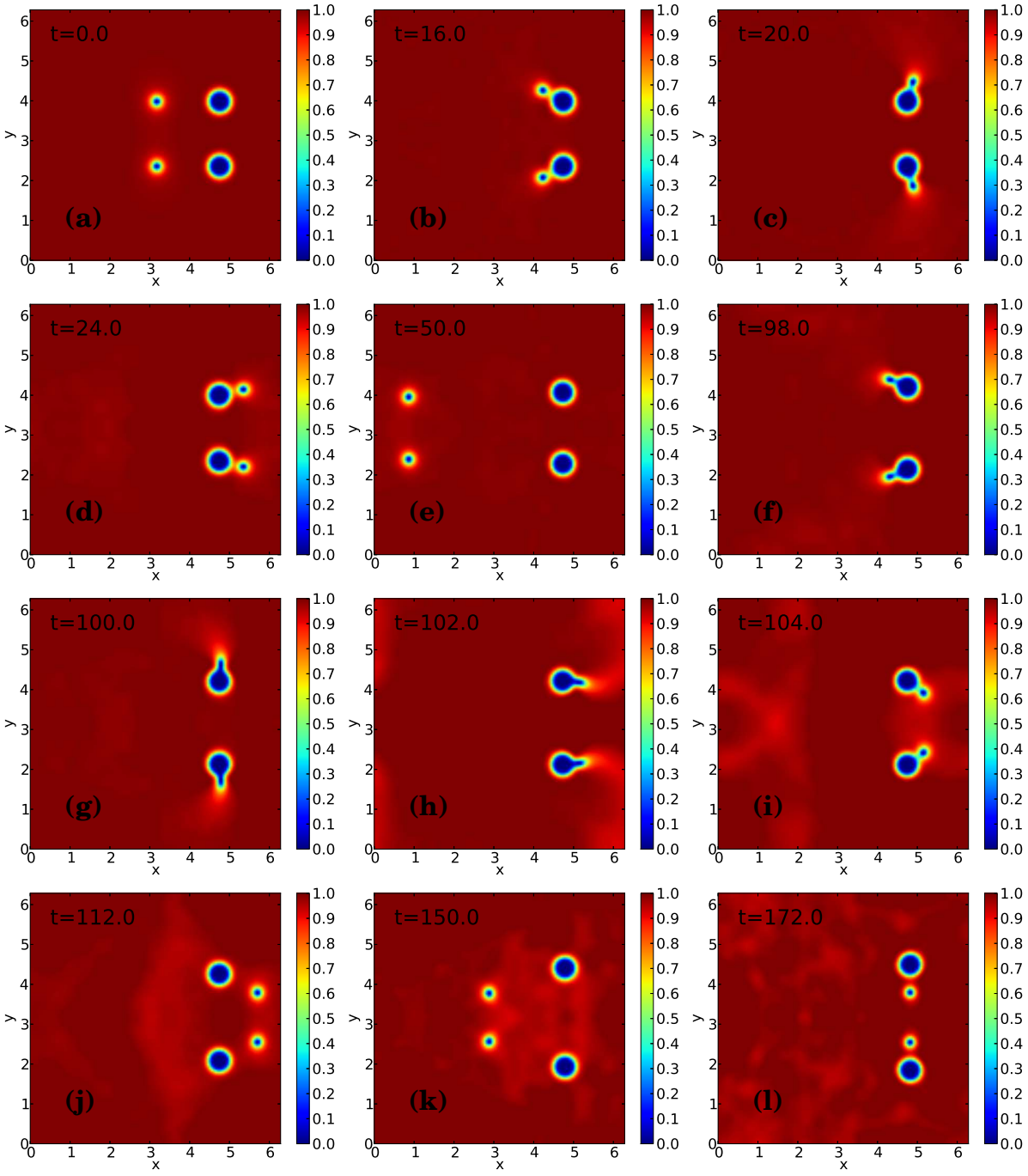

Figure 4.24: Spatiotemporal evolution of the field $|\psi(\mathbf{x},t)|^2$ shown via pseudocolor plots, for two heavy particle placed in the path of the positive (upper) and negative (lower) vortices, respectively, of a translating vortex-antivortex pair (initial configuration `ICP5`).

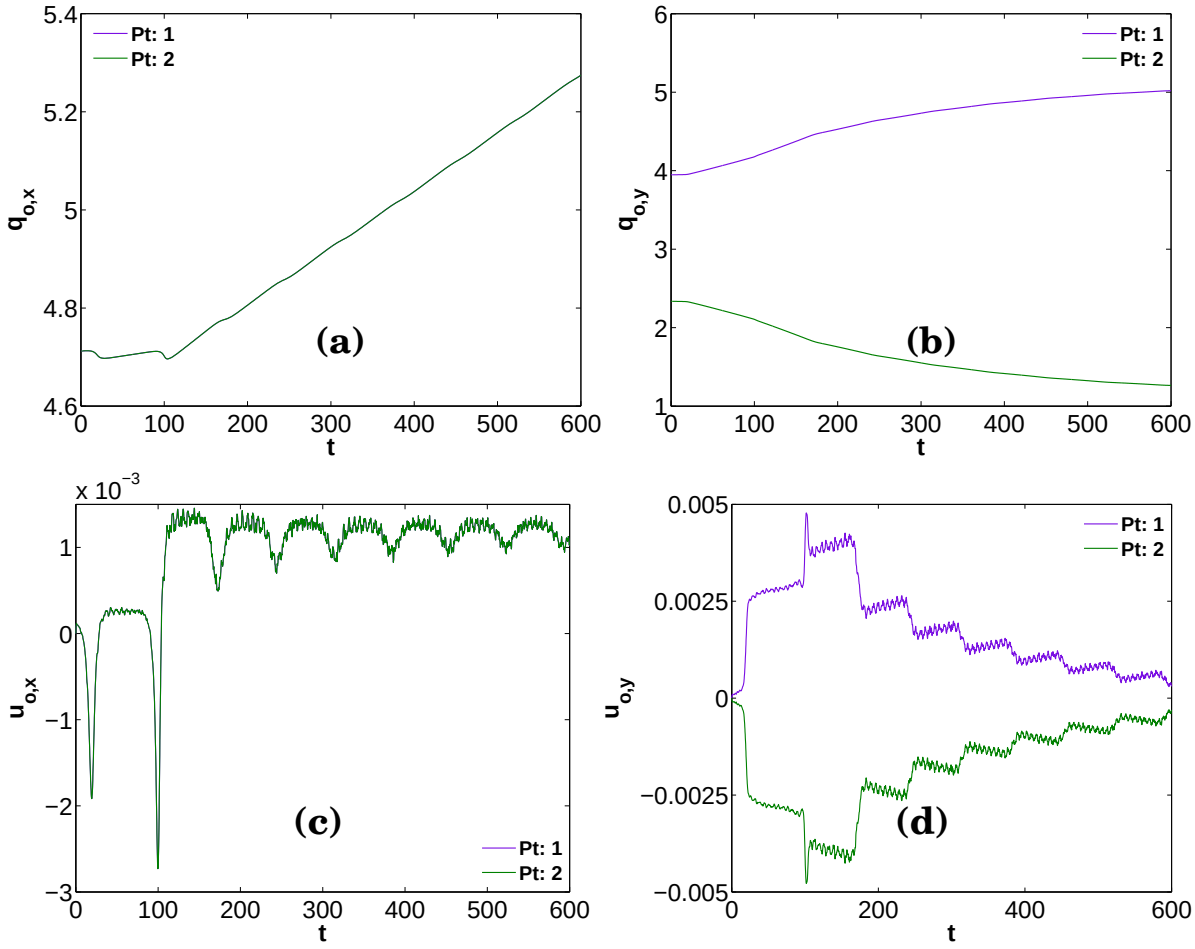

Figure 4.25: Plots versus time t of (a) $q_{\mathrm{o,x}}$, (b) $q_{\mathrm{o,y}}$, (c) $u_{\mathrm{o,x}}$, (d) $u_{\mathrm{o,y}}$ for two heavy particles $Pt:1$ (purple curve) and $Pt:2$ (green curve), placed in the path of the positive (upper) and negative (lower) vortices, respectively, of a translating vortex-antivortex pair (initial configuration `ICP5`). In (a) and (b) the values of $q_{\mathrm{o,x}}$ and $q_{\mathrm{o,y}}$ are not mod2π; i.e., if particle goes around our periodic simulation domain once, say in the $\hat{\mathrm{x}}$ direction, then the values of $q_{\mathrm{o,x}}$ is its value in the box plus 2π.

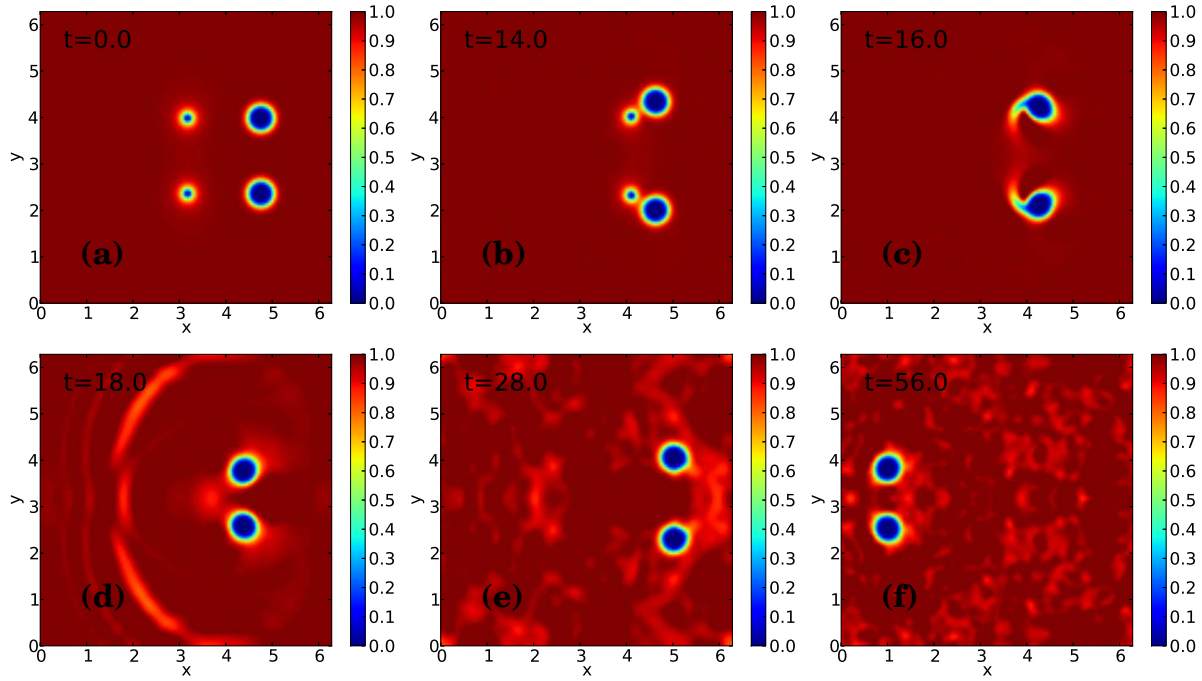

Figure 4.26: Spatiotemporal evolution of the field $|\psi(\mathbf{x},t)|^2$ shown via pseudocolor plots, for two neutral particle placed in the path of the positive (upper) and negative (lower) vortices, respectively, of a translating vortex-antivortex pair (initial configuration `ICP5`).

Video M14 illustrates the complete spatiotemporal evolution of the particle and field $|\psi(\mathbf{x},t)|^2$.

When the translating vortex-antivortex pair approaches symmetrically placed neutral or light particles, the particles $Pt:1$ and $Pt:2$ get trapped on the positive and the negative vortices, respectively. The trapping of the two neutral (light) particles here is similar to the trapping of a single neutral (light) particle placed in front of a translating vortex-antivortex pair (see subsection 4.3.4). After the particles are trapped on the vortices, the two-particle-vortex-antivortex-pair complex continues to translate in the $\hat{\mathrm{x}}$ direction, but the particles now exhibit fluctuations. The pseudocolor plots of Figs. 4.26 (a)-(f) and 4.27 (a)-(f) and the Videos M15 and M16 summarize the spatiotemporal evolution of the field $|\psi(\mathbf{x},t)|^2$ for the neutral and the light particles, respectively. The fluctuations in the case of the neutral particle are temporally periodic, with some modulation, whereas those in the case of the light particle are chaotic in nature (see Figs. 4.28 (a)-(d) (neutral particle) and 4.29 (a)-(d) (light particle) for details).

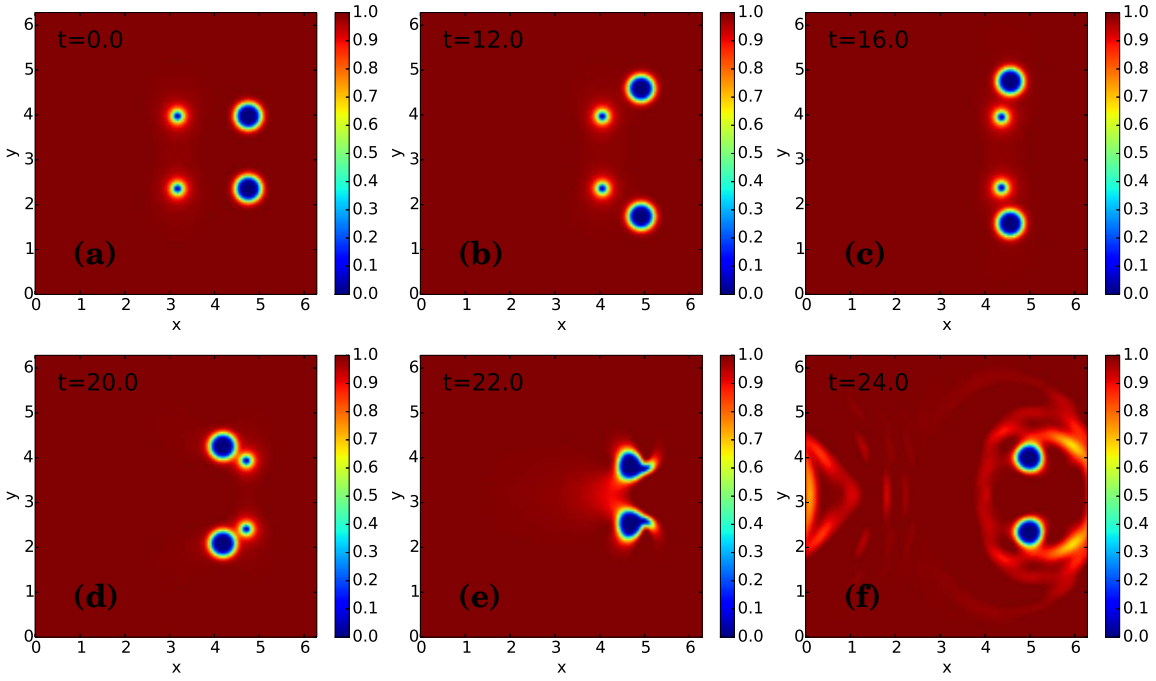

Figure 4.27: Spatiotemporal evolution of the field $|\psi(\mathbf{x},t)|^2$ shown via pseudocolor plots, for two heavy particle placed in the path of the positive (upper) and negative (lower) vortices, respectively, of a translating vortex-antivortex pair (initial configuration `ICP5`).

4.3.6 Single particle dynamics in the presence of counter-rotating vortex clusters

We study the dynamics of the single neutral particle in the presence of counter-rotating vortex clusters. We generate the initial configuration `ICP6` for this purpose in three steps: (1) we use the ARGLE Eq. (4.10) to prepare a state with a particle at (π,π) moving with velocity $0.1(1/\sqrt{2},-1/\sqrt{2})$; (2) we then use the ARGLE Eq. (4.10) to prepare two positive and two negative vortex clusters, where each cluster has 12 vortices of the same sign, and the positive and the negative clusters rotate in opposite directions (for preparation details see Appendix E.2); (3) the states obtained in the steps (1) and (2) are combined together, by multiplying their wave functions. The initial configuration so prepared is then used in the TGPE Eq. (4.1). We deliberately do not prepare the state with counter-rotating vortex clusters in its ground state, so under the TGPE dynamics the clusters expand and interact with the neighboring clusters, which results in a flow with a complex distribution of vortices. Thus, this initial state allows us to study a neutral particle in a state that displays superfluid turbulence.

In Figs. 4.30 (a)-(f) we show the spatiotemporal evolution of the filtered vorticity field; the particle is represented by a black disc here. Figures 4.30 (a)-(c) show that

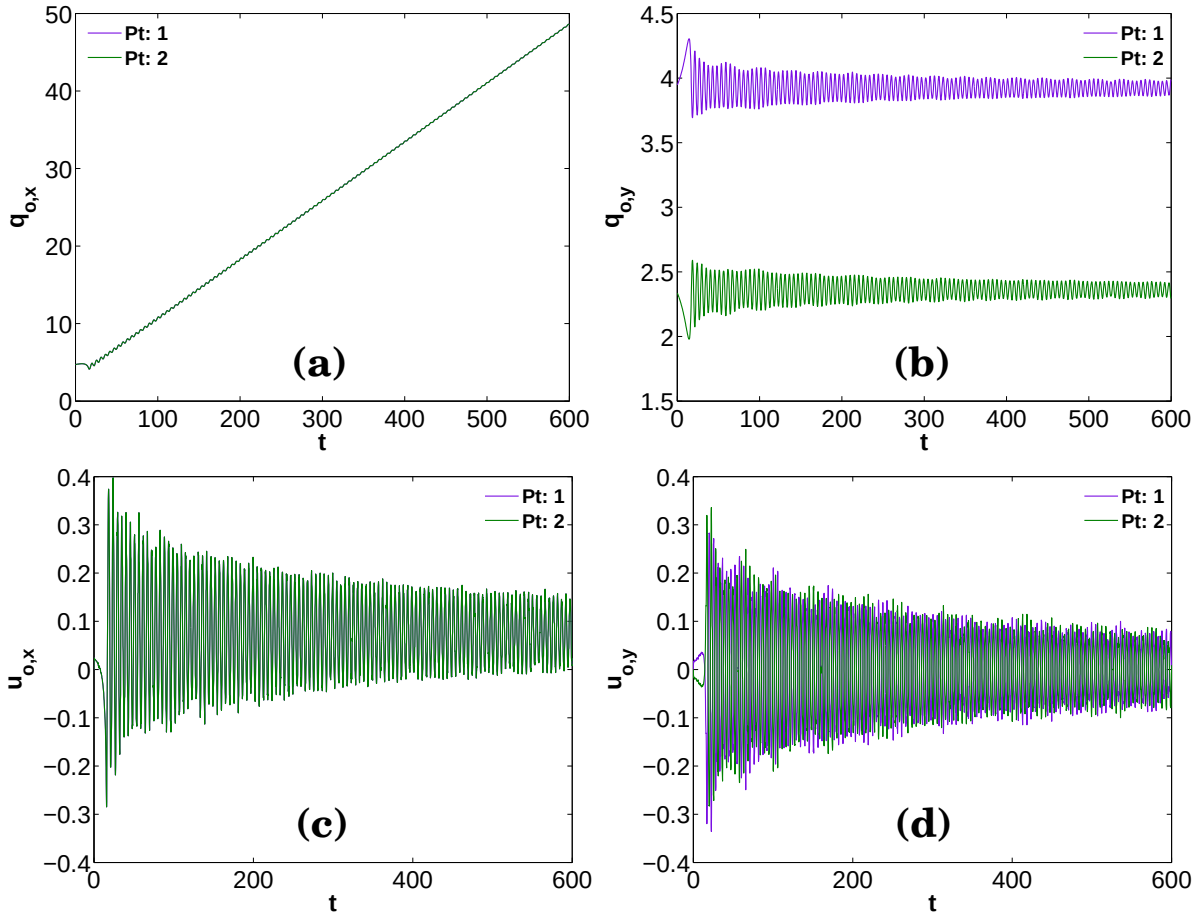

Figure 4.28: Plots versus time t of (a) $q_{\mathrm{o,x}}$, (b) $q_{\mathrm{o,y}}$, (c) $u_{\mathrm{o,x}}$, (d) $u_{\mathrm{o,y}}$ for two neutral particles $Pt : 1$ (purple curve) and $Pt : 2$ (green curve), placed in the path of the positive (upper) and negative (lower) vortices, respectively, of a translating vortex-antivortex pair (initial configuration `ICP5`). In (a) and (b) the values of $q_{\mathrm{o,x}}$ and $q_{\mathrm{o,y}}$ are not mod2π; i.e., if particle goes around our periodic simulation domain once, say in the $\hat{\mathrm{x}}$ direction, then the values of $q_{\mathrm{o,x}}$ is its value in the box plus 2π.

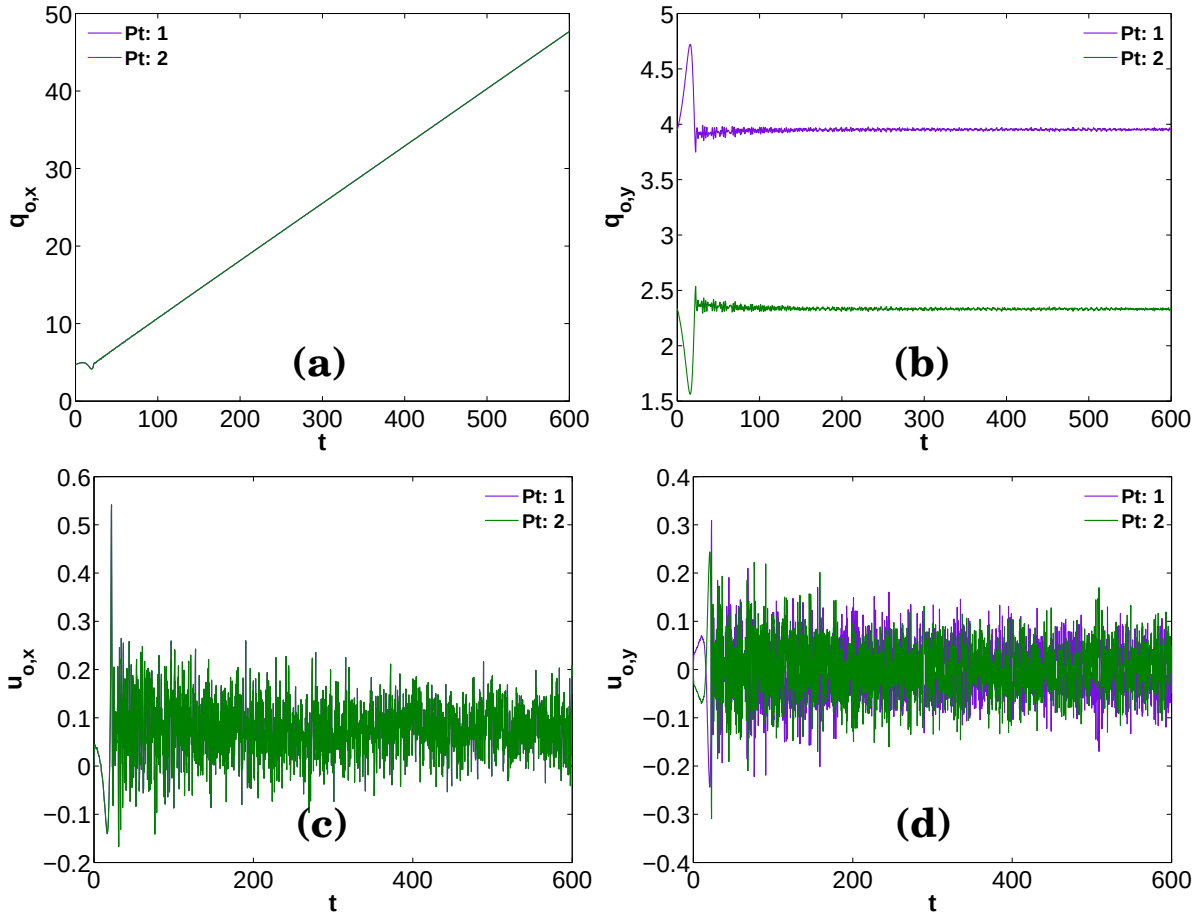

Figure 4.29: Plots versus time t of (a) $q_{\mathrm{o,x}}$, (b) $q_{\mathrm{o,y}}$, (c) $u_{\mathrm{o,x}}$, (d) $u_{\mathrm{o,y}}$ for two light particles $Pt:1$ (purple curve) and $Pt:2$ (green curve), placed in the path of the positive (upper) and negative (lower) vortices, respectively, of a translating vortex-antivortex pair (initial configuration `ICP5`). In (a) and (b) the values of $q_{\mathrm{o,x}}$ and $q_{\mathrm{o,y}}$ are not mod2π; i.e., if particle goes around our periodic simulation domain once, say in the $\hat{\mathrm{x}}$ direction, then the values of $q_{\mathrm{o,x}}$ is its value in the box plus 2π.

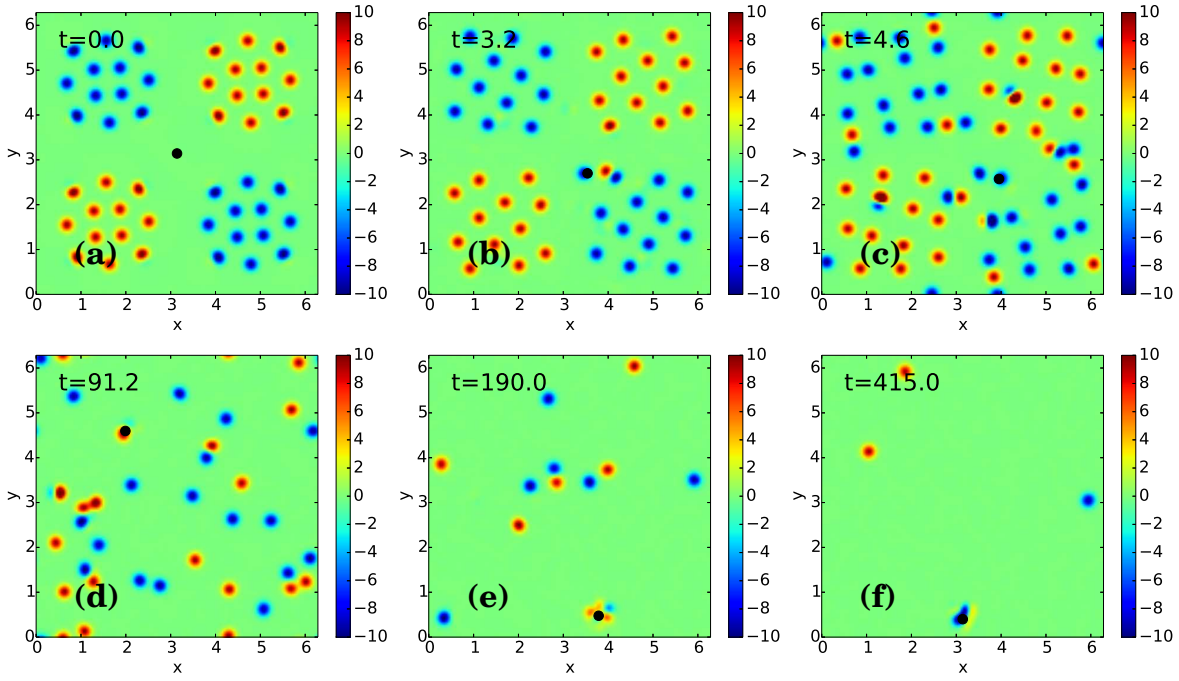

Figure 4.30: Spatiotemporal evolution of the filtered vorticity field (derived from the incompressible velocity field), for the neutral particle initially in the presence of counter-rotating vortex clusters (initial configuration `ICP6`). The instantaneous position of the particle is shown by a black disc.

the vortex clusters expand quickly and interact with their neighboring clusters. At $t \simeq 3.2$ the particle sheds a vortex-antivortex pair while moving towards the negative vortex cluster in the right bottom corner of the simulation domain; the particle gets trapped on a nearby negative-vortex and is dragged inside the cluster; at this time its velocity shoots up to $u_{\rm o} \sim 0.8$. The vortex density decreases as the system evolves because of the annihilation of the vortices and the anitvortices (see Figs. 4.30 (d)-(e)). The Video M17 illustrates the dynamics of a neutral particle in the presence of counter-rotating vortex clusters. Figure 4.31 shows that the trajectory of the particle (denoted by a series of purple circles), in the presence of vortices, is complex. The spacing between successive circles is large (small) when the particle velocity is large (small). During the motion the particle switches from one vortex to another and its direction of motion keeps changing because of its interactions with neighboring vortices. The regions with a high density of circles on the trajectory plot in Fig. 4.31 occur when the area around the particle is free of vortices or at late times when the overall vortex density has decreased considerably. Figure 4.32 (a) shows that $u_{\rm o,x}$ and $u_{\rm o,y}$ exhibit chaotic fluctuations; in Fig. 4.32 (b) we show plots of the energies that illustrate the exchange of energy between the particle and the superfluid field.

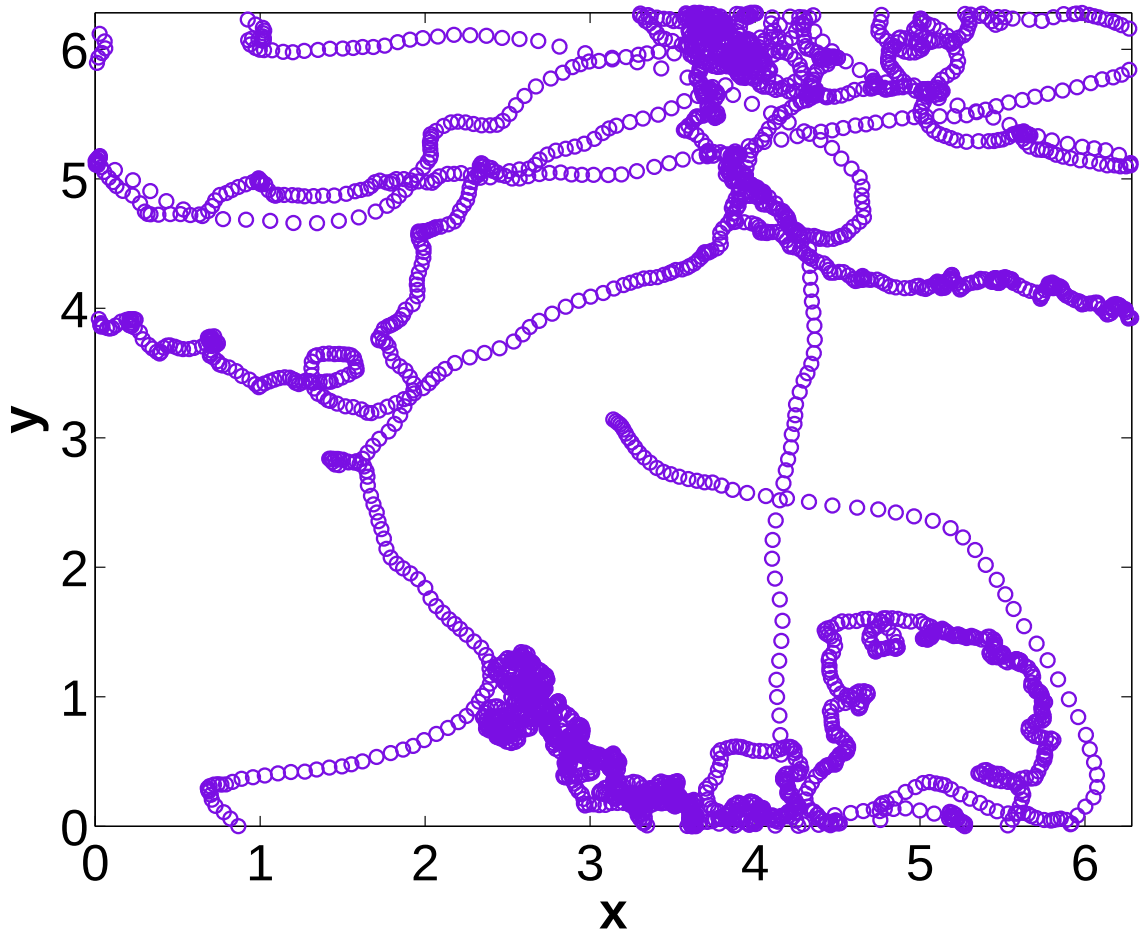

Figure 4.31: Trajectory of a neutral particle (denoted by purple circles), initially in the presence of counter-rotating vortex clusters (initial configuration `ICP6`).

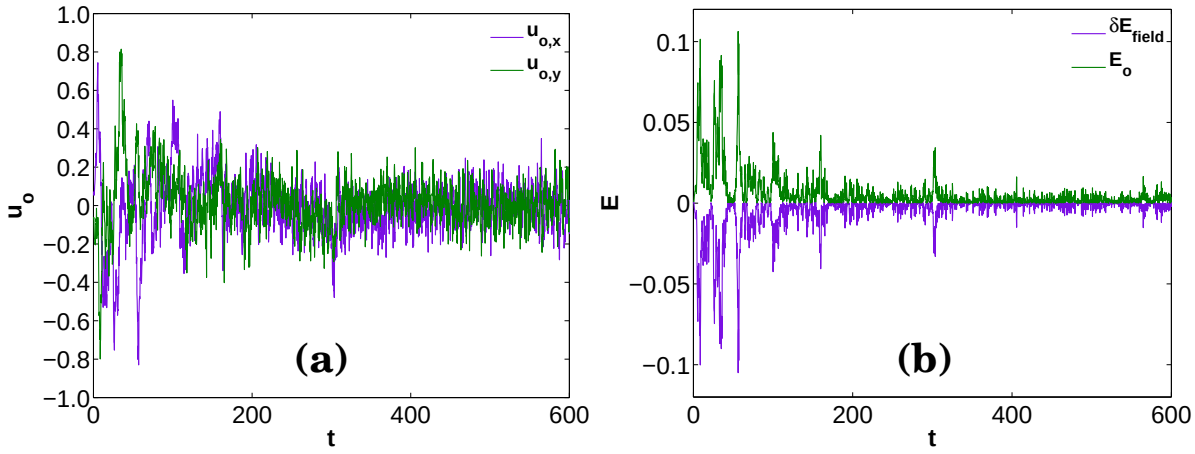

Figure 4.32: Plots versus time t of (a) $u_{\mathrm{o,x}}$ (purple curve) and $u_{\mathrm{o,y}}$; (b) $\delta E_{\mathrm{field}}$ (purple curve) and E_{o} (green curve); obtained from the dynamical evolution of the neutral particle in the presence of counter-rotating vortex clusters (initial configuration `ICP6`).

4.3.7 Many-particle dynamics in the presence of counter-rotating vortex clusters

We study the dynamics of four particles in the presence of small, counter-rotating vortex clusters as an illustrative example of many-particle dynamics in the presence of vortices. We generate the initial configuration `IPC7` for this purpose in three steps: (1) we use the ARGLE Eq. (4.10) to prepare a minimum-energy state with two clusters of positive and negative vortices; each cluster has 4 vortices of the same sign, and the positive and the negative clusters rotate in opposite directions (for preparation details see Appendix E.2). (2) We prepare a state with four stationary particles $Pt:1$, $Pt:2$, $Pt:3$, and $Pt:4$ at the coordinates $(3\pi/2,\pi/2)$, $(\pi/2,\pi/2)$, $(\pi/2,3\pi/2)$, and $(3\pi/2,3\pi/2)$, respectively, which correspond to the centers of vortex clusters; (3) the states obtained in the steps (1) and (2) are combined together, by multiplying their wave functions, for the initial configuration `ICP7` that is then used in the TGPE Eq. (4.1) to study the dynamics of this system.

In Figs. 4.33 (a)-(i) we show the spatiotemporal evolution of the field $|\psi(\mathbf{x},t)|^2$. In the initial stages of the dynamical evolution of the system, the particles $Pt:1$-$Pt:4$ remain stationary at the respective centers of the rotating-vortex clusters, because our initial configuration has four-fold symmetry (C_4) and we prepare it by using the ground state of the vortex clusters. (By contrast, in subsection 4.3.6 our initial configuration is not the ground of the vortex clusters.) However, at around $t=37$, an instability sets in as a result of which the particle $Pt:3$ starts to move out; it is then trapped by the negative vortex in front of it (see Fig. 4.33 (c), top-left vortex cluster); the trapped particle now rotates along with the other three vortices. Similarly, the motion of the other particles also becomes unstable and they are trapped in vortices, in their respective clusters; Fig. 4.33 (d) shows that the particle $Pt:2$ is trapped by a vortex at $t\simeq 40$ and the particles $Pt:1$ and $Pt:4$ are trapped by vortices at $t\simeq 42.4$ (see Fig. 4.33 (e)). Moreover, at $t\simeq 46.2$ the trapped particle $Pt:3$ and its vortex form a complex by including another negative vortex of the cluster (see Fig. 4.33 (f), top-left vortex cluster). In Fig. 4.34 (a) we show the phase of the wave function ψ; in such a plot, the vortices are the points around which the phase changes from 0 to 2π; the top-left quadrant still has four vortices, although two on the left are very close by and are held together in a particle-two-vortex complex. The particle-two-vortex complex and the trapped particles continue rotating along with the other vortices, in their respective clusters, over the rest of the simulation time, as we show in Figs. 4.33 (g)-(i). The Video M18 illustrates the spatiotemporal evolution of the four neutral particles and field $|\psi(\mathbf{x},t)|^2$.

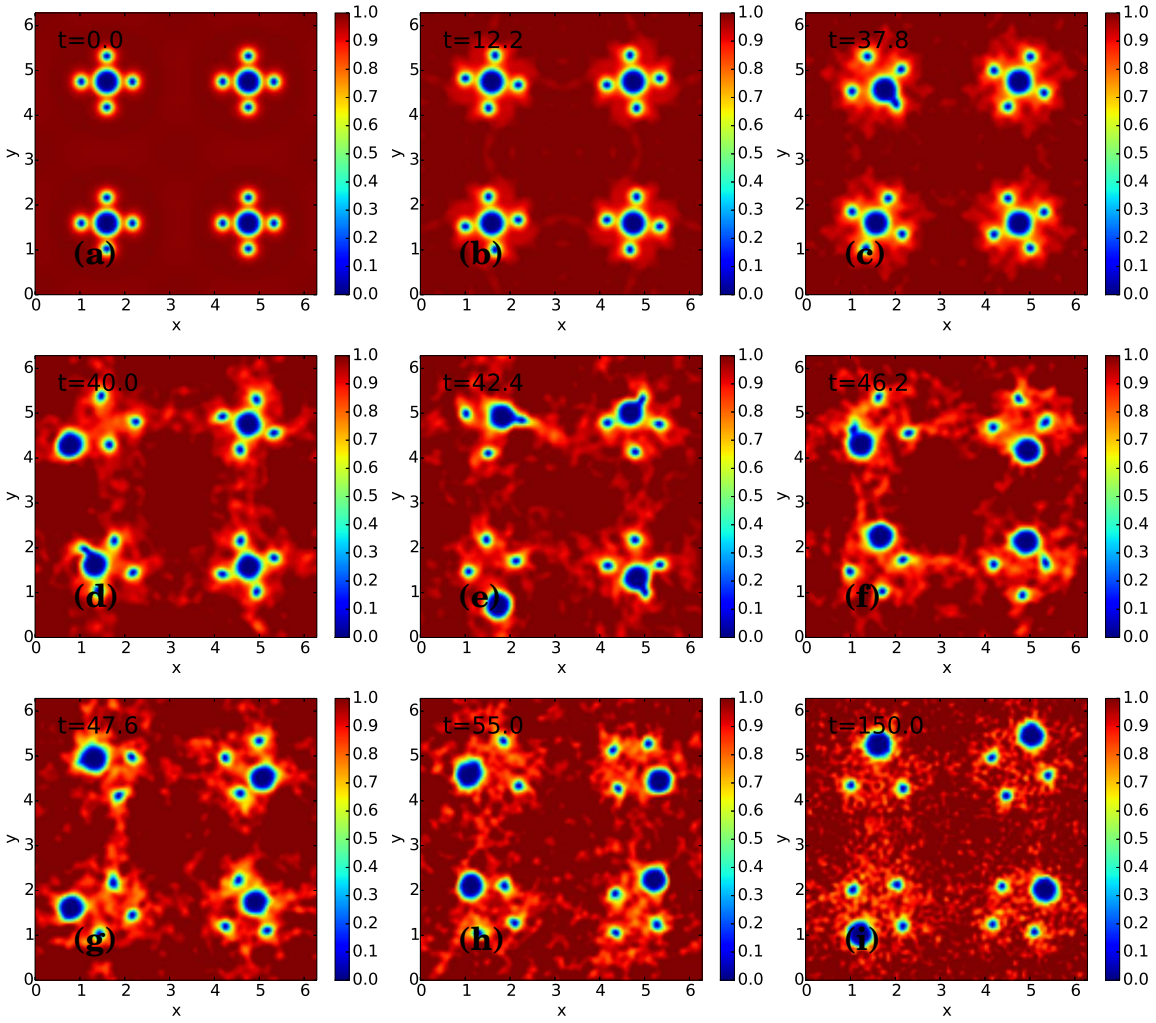

Figure 4.33: Spatiotemporal evolution of the field $|\psi(\mathbf{x},t)|^2$ shown via pseudocolor plots, for the four neutral particles (large blue patches), initially placed at the centers of the counter-rotating vortex clusters (initial configuration `ICP7`).

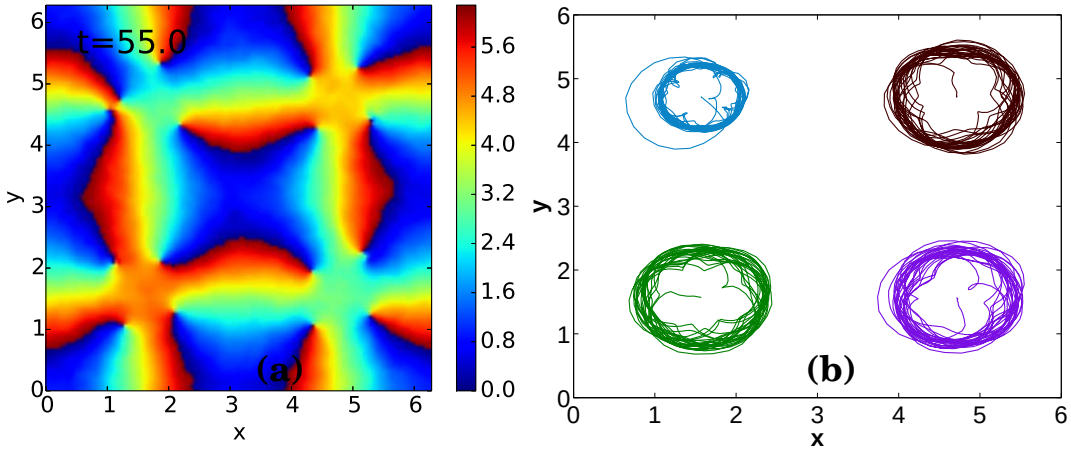

Figure 4.34: (a) Pseudocolor plot of the phase of $\psi(\mathbf{x}, t)$; (b) trajectories of four neutral particles $Pt : 1$ (purple curve), $Pt : 2$ (green curve) $Pt : 3$ (sky-blue curve), and $Pt : 4$ (brown curve), in the presence of counter-rotating vortex clusters (initial configuration ICP7).

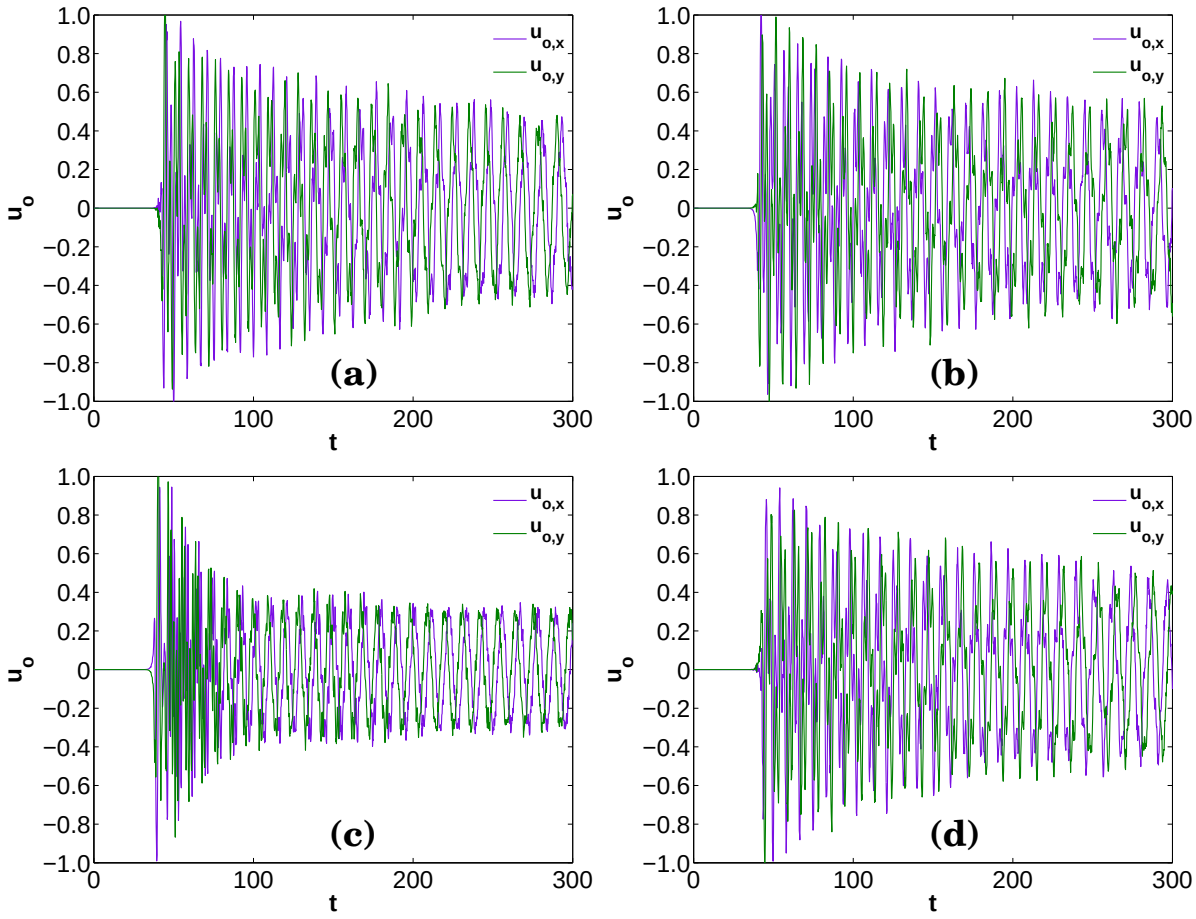

Figure 4.35: Plots versus time t of $u_{\mathrm{o,x}}$ (purple curve) and $u_{\mathrm{o,y}}$ (green curve) for the four neutral particles (a) $Pt : 1$, (b) $Pt : 2$, (c) $Pt : 3$, and (d) $Pt : 4$, in the presence of counter-rotating vortex clusters (initial configuration ICP7).

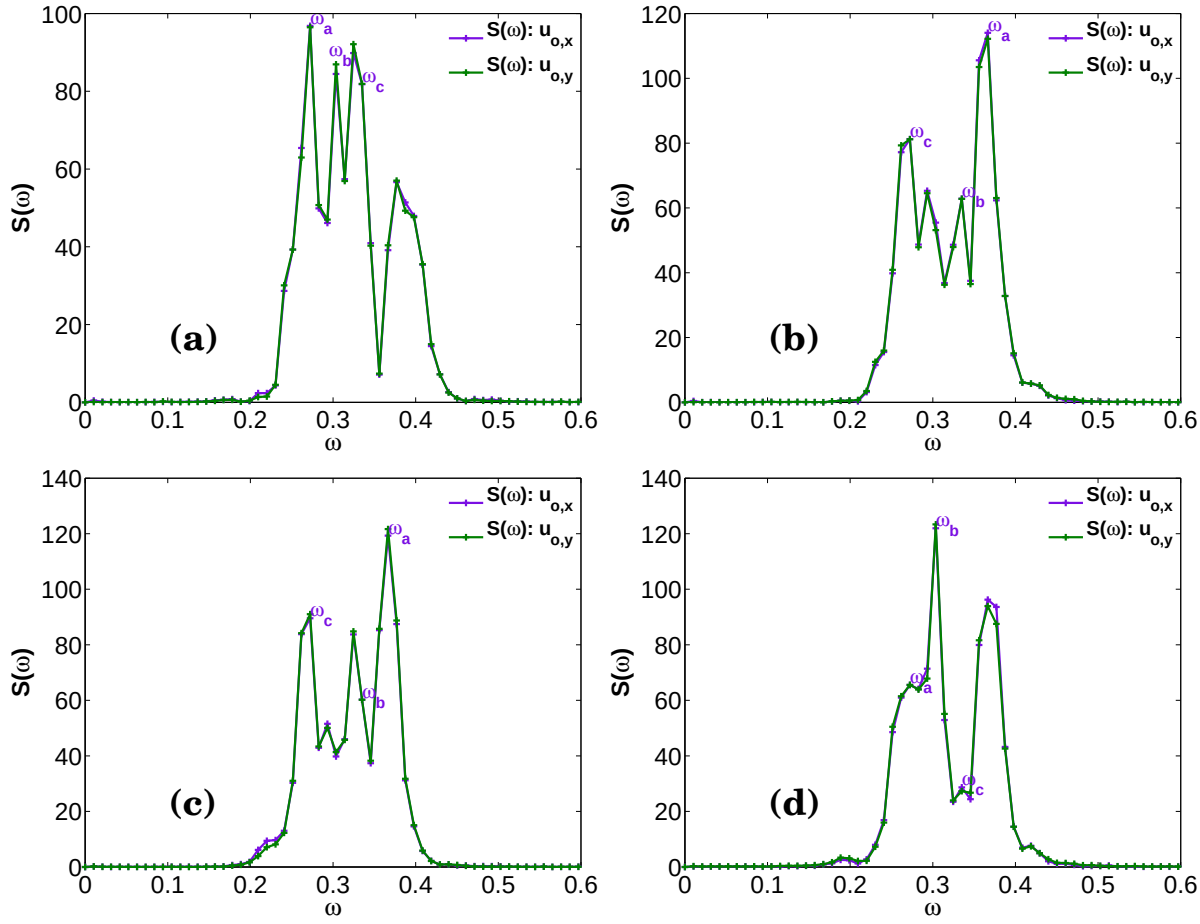

Figure 4.36: Plots of power spectra, denoted generically by $S(\omega)$, of the time series of $u_{\mathrm{o,x}}$ (purple curve), $u_{\mathrm{o,y}}$ (green curve) (see Figs. 4.35) for the four neutral particles (initial configuration `ICP7`) (a) $Pt:1$, $\omega_c = 2\omega_b - \omega_a$ ($\omega_a = 0.2723$, $\omega_b = 0.3037$, and $\omega_c = 0.3351$); (b) $Pt:2$, $\omega_c = 3\omega_b - 2\omega_a$ ($\omega_a = 0.3665$, $\omega_b = 0.3351$, and $\omega_c = 0.2723$); (c) $Pt:3$, $\omega_c = 3\omega_b - 2\omega_a$ ($\omega_a = 0.3665$, $\omega_b = 0.3351$, and $\omega_c = 0.2723$); (a) $Pt:4$, $\omega_c = 2\omega_b - \omega_a$ ($\omega_a = 0.2723$, $\omega_b = 0.3037$, and $\omega_c = 0.3351$). The frequencies ω_a, ω_b, and ω_c that we give are associated with $S(\omega)$ for $u_{\mathrm{o,x}}$ (purple curves).

We plot the trajectories of the centers of masses of the four particles $Pt : 1$ (purple curve), $Pt : 2$ (green curve), $Pt : 3$ (sky-blue curve), and $Pt : 4$ (brown curve) in Fig. 4.34 (b). These centers move along roughly circular trajectories; however, their motions are not completely periodic in time, so these trajectories meander away from perfectly closed curves and, therefore, fill out two-dimensional areas. This is a signature of either (a) ergodic behavior, e.g., with quasiperiodic temporal evolution or (b) chaotic time evolution. To distinguish between (a) and (b), we examine the time series of $u_{\mathrm{o,x}}$ and $u_{\mathrm{o,y}}$ for all the four particles in Figs. 4.35 (a)-(d). The principal peaks in these power spectra can be indexed as $n_a\omega_a + n_b\omega_b$, where n_a and n_b are integers and there are two main incommensurate frequencies ω_a and ω_b (i.e., ω_a/ω_b is an irrational number). For example, in Fig. 4.36 (a) the frequency ω_c, of one of the peaks in the power spectrum $S(\omega)$, can be written as $\omega_c = 2\omega_b - \omega_a$ (here $\omega_c = 0.3351$, $\omega_a = 0.2723$, and $\omega_b = 0.3037$). This labelling of peaks indicates clearly that the temporal evolution of $Pt : 1$ is quasiperiodic.

4.4 Conclusions

We have carried out an extensive study to understand the dynamics of particles in two-dimensional superfluids at $T = 0$. In our study, we have used the Galerkin-truncated GP equation to model the superfluid and we assume Newtonian dynamics for the particles, to carry out a systematic DNSs for a variety of initial configurations to elucidate the interplay of particles and fields in superfluids. We have used Gaussian potentials to represent particles in the TGPE. The study of particles in superfluids is an important problem, with a rich history [21, 22]. Early experimental and theoretical studies have been concerned with the mechanism of vortex nucleation by a moving impurity, e.g., $^4He^+$, in helium II [22]; moreover, the breakdown of superfluidity around ions moving with velocities greater than a critical velocity and the associated formation of vortex rings and loops constituted an important area [23, 24]. More recently, the studies of Refs. [25, 26] have investigated superfluid flow past an obstacle; in 2D the flow around a disc has been shown to become dissipative above a critical velocity because of the emission of vortex-antivortex pairs [25], whereas, in 3D, the appearance of vortices for a flow past a cylinder lead to the observation of dissipation [26]. The DNS studies of Refs. [11], based on the Gross-Pitaevskii equations, have shown that, for velocities greater than the critical velocity, the dominant mechanism of energy transfer between a moving particle and a superfluid is vortex formation; this study has also explored the link between vortex shedding and drag force on the particle. The

study of Ref. [10] investigated in 3D, the motion of a heavy particle through a superfluid, when a constant external force acts on the particle. This work has shown that, at $u_{\rm o} = u_c$ a vortex ring forms and the particle can get trapped within the vortex core if the applied force is less than a critical value. Reference [12] considered a point-like impurity and has calculated, analytically within the Gross-Pitaevskii framework, the induced mass of the particle and the drag force acting on it, in 1D, 2D, and 3D; it has also shown that the drag force appears for supersonic motion of the impurity. A recent study (Ref. [27]) has explored, asymptotically and numerically, the flow around a single impurity and a network of impurities by using a 2D Gross-Pitaevskii framework, it has suggested that the excitations of the superfluid depend sensitively on the potential representing the impurity.

In our comprehensive study, we have used active particles [10] to investigate the particle dynamics in superfluids, for a variety of interesting, initial configurations. From our study of the dynamics of a single particle in the superfluid, for the cases of light, neutral, and heavy particles, we find that the particle motion can become chaotic, even if the superfluid is not turbulent. Our study of the interaction of the particle(s) with vortices, shows that the ensuing dynamics depends sensitively on the particle characteristics. From our study of two-particle dynamics in superfluids, we have demonstrated the existence of an effective, superfluid-mediated, attractive interaction between the particles. Moreover, we have introduced a short-range repulsive interaction between particles and have studied the collisions of heavy, neutral, and light particles. Here, we find that, at low values of $r_{\rm SR}$, the collisions are completely inelastic with coefficient of restitution $e = 0$; as we increase $r_{\rm SR}$ e becomes finite at a critical point, and finally attains values close to unity, when the collisions are elastic. Furthermore, we find that many-particle collision dynamics also depends on $r_{\rm SR}$, where its low value results in the formation of a many-particle bound state. At large values of $r_{\rm SR}$, we obtain chaotic many-particle collision dynamics. Our studies of the assemblies of particles and vortices demonstrates that their dynamics show rich, turbulent spatiotemporal evolution.

4.5 Video Captions

Video M1 This video illustrates the spatiotemporal evolution of the heavy particle and the field $|\psi(\mathbf{x},t)|^2$, shown via pseudocolor plots, when a constant external force $\mathbf{F}_{\text{ext}} = 0.02\hat{\mathbf{x}}$ acts on the particle (initial configuration `ICP1`). The particle appears as a large blue patch and the vortices as blue dots.

Video M2 This video illustrates the spatiotemporal evolution of the neutral particle and the field $|\psi(\mathbf{x},t)|^2$, shown via pseudocolor plots, when a constant external force $\mathbf{F}_{\text{ext}} = 0.01\hat{\mathbf{x}}$ acts on the particle (initial configuration `ICP1`). The particle appears as a large blue patch and the vortices as blue dots.

Video M3 This video illustrates the spatiotemporal evolution of the light particle and the field $|\psi(\mathbf{x},t)|^2$, shown via pseudocolor plots, when a constant external force $\mathbf{F}_{\text{ext}} = 0.01\hat{\mathbf{x}}$ acts on the particle (initial configuration `ICP1`). The particle appears as a large blue patch and the vortices as blue dots.

Video M4 This video illustrates the collision dynamics of two neutral particles in the absence of a short-range, repulsive interaction (initial configuration `ICP2(a)`), when they are released from rest. The dynamics of the particles is illustrated by the spatiotemporal evolution of the field $|\psi(\mathbf{x},t)|^2$, shown via pseudocolor plots.

Video M5 This video illustrates the collision dynamics of two neutral particles in the presence of a short-range, repulsive interaction ($r_{\text{SR}} = 1.5\xi$, initial configuration `ICP2(b)`), when they are released from rest. The dynamics of the particles is illustrated by the spatiotemporal evolution of the field $|\psi(\mathbf{x},t)|^2$, shown via pseudocolor plots.

Video M6 This video illustrates the collision dynamics of two neutral particles for $r_{\text{SR}} = 1.5\xi$ (initial configuration `ICP2(c)`). The dynamics of the particles is illustrated by the spatiotemporal evolution of the field $|\psi(\mathbf{x},t)|^2$, shown via pseudocolor plots.

Video M7 This video illustrates the collision dynamics of two neutral particles for $r_{\text{SR}} = 7.0\xi$ (initial configuration `ICP2(c)`). The dynamics of the particles is illustrated by the spatiotemporal evolution of the field $|\psi(\mathbf{x},t)|^2$, shown via pseudocolor plots.

Video M8 This video illustrates the collision dynamics of two heavy particles for $r_{\rm SR} = 1.5\xi$ ($|\mathbf{F}_{\rm ext}| = 3.75$, $t_0 = 6.0$, and initial configuration `ICP2(c)` (see Fig. 4.9)). The dynamics of the particles is illustrated by the spatiotemporal evolution of the field $|\psi(\mathbf{x}, t)|^2$, shown via pseudocolor plots.

Video M9 This video illustrates the collision dynamics of five neutral particles for $r_{\rm SR} = 1.5\xi$ (initial configuration `ICP3`). The dynamics of the particles is illustrated by the spatiotemporal evolution of the field $|\psi(\mathbf{x}, t)|^2$, shown via pseudocolor plots.

Video M10 This video illustrates the collision dynamics of five neutral particles for $r_{\rm SR} = 8.0\xi$ (initial configuration `ICP3`). The dynamics of the particles is illustrated by the spatiotemporal evolution of the field $|\psi(\mathbf{x}, t)|^2$, shown via pseudocolor plots.

Video M11 This video illustrates the spatiotemporal evolution of the field $|\psi(\mathbf{x}, t)|^2$ shown via pseudocolor plots, for a heavy particle placed in the path of the positive (upper) vortex of a translating vortex-antivortex pair (initial configuration `ICP4`).

Video M12 This video illustrates the spatiotemporal evolution of the field $|\psi(\mathbf{x}, t)|^2$ shown via pseudocolor plots, for a neutral particle placed in the path of the positive (upper) vortex of a translating vortex-antivortex pair (initial configuration `ICP4`).

Video M13 This video illustrates the spatiotemporal evolution of the field $|\psi(\mathbf{x}, t)|^2$ shown via pseudocolor plots, for a light particle placed in the path of the positive (upper) vortex of a translating vortex-antivortex pair (initial configuration `ICP4`).

Video M14 This video illustrates the spatiotemporal evolution of the field $|\psi(\mathbf{x}, t)|^2$ shown via pseudocolor plots, for two heavy particles placed in the path of the positive (upper) and negative (lower) vortices, respectively, of a translating vortex-antivortex pair (initial configuration `ICP5`).

Video M15 This video illustrates the spatiotemporal evolution of the field $|\psi(\mathbf{x}, t)|^2$ shown via pseudocolor plots, for two neutral particles placed in the path of the positive (upper) and negative (lower) vortices, respectively, of a translating vortex-antivortex pair (initial configuration `ICP5`).

Video M16 This video illustrates the spatiotemporal evolution of the field $|\psi(\mathbf{x}, t)|^2$ shown via pseudocolor plots, for two light particles placed in the path of the pos-

itive (upper) and negative (lower) vortices, respectively, of a translating vortex-antivortex pair (initial configuration `ICP5`).

Video M17 This video illustrates the spatiotemporal evolution of the filtered vorticity field, for the neutral particle initially in the presence of counter-rotating vortex clusters (initial configuration `ICP6`). The instantaneous position of the particle is shown by a black disc.

Video M18 This video illustrates the spatiotemporal evolution of the field $|\psi(\mathbf{x}, t)|^2$ shown via pseudocolor plots, for the four neutral particles (large blue patches), initially placed at the centers of the counter-rotating vortex clusters (initial configuration `ICP7`).

Appendix E

E.1 Note on Units

The GP equation, which describes the dynamical evolution of the wave function $\psi(\mathbf{x},t)$ of a weakly interacting, 2D Bose gas at low temperatures, is

$$i\hbar\frac{\partial\psi(\mathbf{x},t)}{\partial t} = -\frac{\hbar^2}{2m}\nabla^2\psi(\mathbf{x},t) - \mu\psi(\mathbf{x},t) + g_{2\mathrm{D}}|\psi|^2\psi(\mathbf{x},t) + \sum\nolimits_{\mathrm{i}=1}^{\mathcal{N}_\circ} V_{\mathcal{P}}(\mathbf{x}-\mathbf{q}_i)\psi(\mathbf{x},t), \quad \textbf{(E.1)}$$

where $g_{2\mathrm{D}}$ is the effective interaction strength. As we have mentioned earlier, the GP equation conserves the energy, given by the Hamiltonian

$$H = \int_{\mathcal{A}} d^2x\Big(\frac{\hbar^2}{2m}|\nabla\psi|^2 + \frac{1}{2}g_{2\mathrm{D}}|\psi|^4 + \sum\nolimits_{\mathrm{i}=1}^{\mathcal{N}_\circ} V_{\mathcal{P}}(\mathbf{x}-\mathbf{q}_i)|\psi|^2\Big]d^2x\Big), \quad \textbf{(E.2)}$$

and the total number of particles $N = \int_{\mathcal{A}} d^2x|\psi|^2$. We can use the Madelung transformation to write $\psi(\mathbf{x},t) = \sqrt{\rho(\mathbf{x},t)/m}e^{i\phi(\mathbf{x},t)}$ and the total density is $\rho^* = N/\mathcal{A}$. To obtain Eq. (4.1), we first divide Eq. (E.1) by $\hbar$ and define $\mu = \mu/\hbar$, $g = g_{2\mathrm{D}}/\hbar$, and $V_{\mathcal{P}} = V_{\mathcal{P}}/\hbar$; we then set $\hbar/2m = \alpha_0$, with $m = 1$. In these units, the quantum of circulation is $h/m = 4\pi\alpha_0$, the sound velocity is $c = \sqrt{g|\psi_0|^2/m} = \sqrt{g\rho_0}$, and the healing length is $\xi = \sqrt{\hbar^2/2m|\psi_0|^2 g} = \sqrt{2\alpha_0^2/\rho_0 g}$, where $\rho_0 = m|\psi_0|^2$ is the condensate density. In our choice of units, the sound waves take time $t = (L/2)/c = \pi/c$, to travel from the center to the edge of the square, periodic simulation domain.

E.2 Preparation of counter-rotating vortex clusters

The steps involved in the preparation of ψ_{cluster} are outlined below:

1. Initialize $\psi_e(\lambda_1,\lambda_2) = \frac{(\lambda_1+\iota\lambda_2)}{A}\tanh\big(\frac{A}{\sqrt{2}\xi}\big)$, where $\lambda_1 = \sqrt{2}\cos x$, $\lambda_2 = \sqrt{2}\cos y$, and $A = \sqrt{\lambda_1^2+\lambda_2^2}$.
2. Prepare $\psi_4 = \psi_e(\lambda_1-\eta,\lambda_2)\psi_e(\lambda_1,\lambda_2-\eta)\psi_e(\lambda_1+\eta,\lambda_2)\psi_e(\lambda_1,\lambda_2+\eta)$, where $\eta = 1/\sqrt{2}$.

3. Prepare $\psi_{\text{cluster}} = (\psi_4)^{[\gamma_d/4]}$, where $\gamma_d = 8/(4\pi\alpha_0)$ and $[\cdot]$ denotes the integer part of a real number.

4. Evolve ψ_{cluster} by using ARGLE with $u_{\text{adv,x}} = \sin(x)\cos(y)$, $u_{\text{adv,y}} = -\cos(x)\sin(y)$ to minimize acoustic emission.

For more details on the preparation of a counter-rotating vortex clusters, we refer the reader to Ref. [20].

Bibliography

[1] G. Taylor. Diffusion by continuous movements. *Proc. London. Math. Soc.*, s2-20:196, 1922.

[2] J. Bec, L. Biferale, G. Boffetta, M. Cencini, S. Musacchio, and F. Toschi. Lyapunov exponents of heavy particles in turbulence. *Phys. Fluids*, 18(9):091702, 2006.

[3] R. A. Shaw. Particle-turbulence interactions in atmospheric clouds. *Annu. Rev. Fluid Mech.*, 35(1):183–227, 2003.

[4] W. W. Grabowski and L.-P. Wang. Growth of cloud droplets in a turbulent environment. *Annu. Rev. Fluid Mech.*, 45:293–324, 2013.

[5] G. Falkovich, A. Fouxon, and M. Stepanov. *Nature*, 419:151, 2002.

[6] P. J. Armitage. *Astrophysics of planet formation*. Cambridge University Press, UK, 2010.

[7] G. T. Csanady. *Turbulent diffusion in the environment*. Number 3 in Geophysics and Astrophysics Monographs. Springer, 1973.

[8] J. K. Eaton and J. R. Fessler. Preferential concentration of particles by turbulence. *Int. J. Multiphase Flow*, 20:169–209, 1994.

[9] S. L. Post and J. Abraham. Modeling the outcome of drop–drop collisions in diesel sprays. *Int. J. Multiphase Flow*, 28(6):997–1019, 2002.

[10] T. Winiecki and C. S. Adams. Motion of an object through a quantum fluid. *Europhys. Lett.*, 52(3):257, 2000.

[11] T. Winiecki, B. Jackson, J. F. McCann, and C. S. Adams. Vortex shedding and drag in dilute Bose-Einstein condensates. *J. Phys. B: At. Mol. and Opt. Phys.*, 33(19):4069, 2000.

[12] G. E. Astrakharchik and L. P. Pitaevskii. Motion of a heavy impurity through a bose-einstein condensate. *Phys. Rev. A*, 70:013608, Jul 2004.

[13] G. P. Bewley, D. P Lathrop, and K. R. Sreenivasan. Superfluid helium: Visualization of quantized vortices. *Nature*, 441(7093):588–588, 2006.

[14] G. P. Bewley, M. S. Paoletti, K. R. Sreenivasan, and D. P. Lathrop. Characterization of reconnecting vortices in superfluid helium. *Proc. Natl. Acad. Sci. USA*, 105(37):13707–13710, 2008.

[15] E. Fonda, D. P. Meichle, N. T. Ouellette, S. Hormoz, and D. P. Lathrop. Direct observation of Kelvin waves excited by quantized vortex reconnection. *Proc. Natl. Acad. Sci. USA*, 111(Supplement 1):4707–4710, 2014.

[16] N. G. Berloff, M. Brachet, and N. P. Proukakis. Modeling quantum fluid dynamics at nonzero temperatures. *Proc. Natl. Acad. Sci. USA*, 111(Supplement 1):4675–4682, 2014.

[17] V. Shukla, M. Brachet, and R. Pandit. Turbulence in the two-dimensional Fourier-truncated Gross-Pitaevskii equation. *New J. Phys.*, 15(11):113025, 2013.

[18] `http://www.fftw.org`.

[19] G. Krstulovic and M. Brachet. Energy cascade with small-scale thermalization, counterflow metastability, and anomalous velocity of vortex rings in Fourier-truncated Gross-Pitaevskii equation. *Phys. Rev. E*, 83:066311, Jun 2011.

[20] C. Nore, M. Abid, and M. E. Brachet. Decaying Kolmogorov turbulence in a model of superflow. *Phys. Fluids*, 9(9):2644–2669, 1997.

[21] D. R. Tilley and J. Tilley. *Superfluidity and superconductivity*. CRC Press, 1990.

[22] R. J. Donnelly. *Quantized vortices in helium II*, volume 2. Cambridge University Press, 1991.

[23] G. W. Rayfield and F. Reif. Quantized Vortex Rings in Superfluid Helium. *Phys. Rev.*, 136:A1194–A1208, Nov 1964.

[24] C. M. Muirhead, W. F. Vinen, and R. J. Donnelly. *Phil. Thans. Roy. Soc. Lond. A*, 3:3433, 1984.

[25] T. Frisch, Yv. Pomeau, and S. Rica. Transition to dissipation in a model of superflow. *Phys. Rev. Lett.*, 69(11):1644, 1992.

[26] C. Nore, C. Huepe, and M. E. Brachet. Subcritical dissipation in three-dimensional superflows. *Physical review letters*, 84(10):2191, 2000.

[27] F. Pinsker and N. G. Berloff. Transitions and excitations in a superfluid stream passing small impurities. *Phys. Rev. A*, 89:053605, May 2014.

Chapter 5

Homogeneous Isotropic Superfluid Turbulence in Two Dimensions: Inverse and Forward Cascades in the Hall-Vinen-Bekharevich-Khalatnikov model

In this Chapter we present the first direct-numerical-simulation of the statistical properties of two-dimensional superfluid turbulence in the Hall-Vinen-Bekharevich-Khalatnikov two-fluid model. We show that both normal fluid and superfluid energy spectra can exhibit two power-law regimes, the first associated with an inverse cascade of energy and the second with the forward cascade of enstrophy.

5.1 Introduction

Superfluid turbulence, which continues to provide challenges for experiments, theory, and numerical simulations [1–4], has been studied more often in three dimensions (3D) than in two dimensions (2D). It is well known that 2D and 3D *fluid* turbulence are qualitatively different [5–8]; similar differences have not been explored in detail for *superfluid* turbulence. Therefore, we study the statistical properties of 2D homogeneous, isotropic, superfluid turbulence, by using the Hall-Vinen-Bekharevich-Khalatnikov (HVBK), two-fluid model [4, 9–12], with the specific goal of elucidating the natures of inverse and forward cascades here, namely, the flow of energy from the energy-injection length scale to larger scales and the flux of enstrophy, the mean square vorticity, to small length scales. Homogeneous, isotropic, 2D and 3D fluid turbulence are essentially different because, in the former, both the energy and the enstrophy are conserved in the inviscid, unforced limit, whereas, in the latter, only the energy is conserved [5–8]. Therefore, in 2D fluid turbulence, energy, injected at a wave number $k_{\rm f}$, shows an inverse cascade towards large length scales (wave numbers $k < k_{\rm f}$), whereas the enstrophy displays a forward cascade to small length scales (wave numbers $k > k_{\rm f}$); these inverse and forward cascades

yield, respectively, energy spectra that scale as $E(k) \sim k^{-5/3}$ and $E(k) \sim k^{-\delta}$, where δ depends on the friction ($\delta = 3$ if there is no friction). By contrast, 3D fluid turbulence shows only a forward cascade of energy with $E(k) \sim k^{-5/3}$, at the level of Kolmogorov's (K41) phenomenological theory [5] and for $k_{\rm f} \ll k \ll k_d$, where k_d is the wave-number scale at which viscous dissipation becomes significant.

Our direct numerical simulation (DNS), which we have designed to study the statistical properties of inverse and forward cascades in the HVBK model, yields several interesting results that have not been anticipated hitherto: (1) Both normal-fluid and superfluid energy spectra, $E^n(k)$ and $E^s(k)$, respectively, show inverse- and forward-cascade regimes; the former is characterized by a power law $E^s(k) \sim E^n(k) \sim k^{-\alpha}$ whose exponent is consistent with $\alpha \simeq 5/3$. (2) The forward-cascade power law depends on (a) the friction coefficient, as in 2D fluid turbulence, and, in addition, on (b) ρ_n/ρ, where ρ_n and ρ are normal-fluid and total densities, respectively, and (c) the coefficient B of mutual friction, which couples normal and superfluid components. (3) As B increases, the normal and superfluid velocities, $\mathbf{u}_n$ and $\mathbf{u}_s$, respectively, get locked to each other, and, therefore, $E^s(k) \simeq E^n(k)$, especially in the inverse-cascade regime. (4) We quantify this locking tendency by calculating the probability distribution functions (PDFs) $\mathcal{P}(\cos(\theta))$ and $\mathcal{P}(\gamma)$, where the angle $\theta \equiv cos^{-1}((\mathbf{u}_{\rm n} \cdot \mathbf{u}_{\rm s})/(|\mathbf{u}_{\rm n}||\mathbf{u}_{\rm s}|))$ and the amplitude ratio $\gamma = |\mathbf{u}_{\rm n}|/|\mathbf{u}_{\rm s}|$; the former has a peak at $\cos(\theta) = 1$; and the latter exhibits a peak at $\gamma = 1$ and power-law tails on both sides of this peak. (4) This locking increases as we increase B, but the power-law exponents for the tails of $\mathcal{P}(\gamma)$ are universal, in so far as they do not depend on B, ρ_n/ρ, and the details of the energy-injection method. (5) We characterize the energy and enstrophy cascades by computing the energy and enstrophy fluxes and the mutual-friction transfer functions for all wave-number scales k.

The remaining part of this Chapter is organized as follows. In Sec. 5.2 we describe the HVBK model and the numerical methods we use. Section 5.3 is devoted to our results. We end with conclusions in Sec. 5.4.

5.2 Model and Numerical Methods

The incompressible, 2D HVBK equations can be written as [4, 9–12]

$$D_t \mathbf{u}_{\rm n} = -\frac{1}{\rho_{\rm n}} \nabla p_{\rm n} + \nu_{\rm n} \nabla^2 \mathbf{u}_{\rm n} - \mu_{\rm n} \mathbf{u}_{\rm n} + \mathbf{F}^{\rm n}_{\rm mf} + \mathbf{f}^{\rm n}_u, \tag{5.1a}$$

$$D_t \mathbf{u}_{\rm s} = -\frac{1}{\rho_{\rm s}} \nabla p_{\rm s} + \nu_{\rm s} \nabla^2 \mathbf{u}_{\rm s} - \mu_{\rm s} \mathbf{u}_{\rm s} + \mathbf{F}^{\rm s}_{\rm mf} + \mathbf{f}^{\rm s}_u, \tag{5.1b}$$

where $D_t \mathbf{u}_i \equiv \partial_t + \mathbf{u}_i \cdot \nabla$, $\nabla \cdot \mathbf{u}_i = 0$ is the incompressibility condition, and the subscript $i \in ({\rm n}, {\rm s})$ denotes the normal fluid (n) or the superfluid (s); ρ_i, p_i, and ν_i are

the density, partial pressure, and viscosity, respectively, of the component i. Linear-friction terms, with coefficients μ_i, model air-drag-induced or bottom friction. For the superfluid $\nu_{\rm s}$ and $\mu_{\rm s}$ are zero, but any DNS study must use $\nu_{\rm s}(\neq 0) \ll \nu_{\rm n}$ and $\mu_{\rm s} \ll \mu_{\rm n}$ to avoid numerical instabilities and to achieve a statistically steady state. The mutual-friction terms, which model the interaction between the normal and the superfluid components, can be written as $\mathbf{F}^{\rm n}_{\rm mf} = (\rho_s/\rho)\mathbf{f}_{\rm mf}$ and $\mathbf{F}^{\rm s}_{\rm mf} = -(\rho_n/\rho)\mathbf{f}_{\rm mf}$ in Eqs. (5.1a) and (5.1b), respectively, where

$$\mathbf{f}_{\rm mf} = \frac{B}{2}\frac{\omega_{\rm s}}{|\omega_{\rm s}|} \times (\omega_{\rm s} \times \mathbf{u}_{\rm ns}) + \frac{B'}{2}\omega_{\rm s} \times \mathbf{u}_{\rm ns}, \tag{5.2}$$

with $\mathbf{u}_{\rm ns} = (\mathbf{u}_{\rm n} - \mathbf{u}_{\rm s})$ the slip velocity, and B and B' the coefficients of mutual friction. In most of our studies we set $B' = 0$ so, in 2D, $\mathbf{f}_{\rm mf} = -\frac{B}{2}|\omega_{\rm s}|\mathbf{u}_{\rm ns}$. (We have checked in one representative case that our results do not change qualitatively if $B' > 0$.) In our DNS, we use the stream-function ψ_i and vorticity $\omega_i = \nabla \times \mathbf{u}_i = -\nabla^2\psi_i$ formulation [13]. To obtain a statistically steady state, we force the vorticity field with a Kolmogorov-type term $f^i_\omega = -f^i_0 k^i_{\rm f} \cos(k^i_{\rm f} x)$, where f^i_0 and $k^i_{\rm f}$ are the amplitude and the forcing wave number, respectively. We use (a) $k^i_{\rm f} = 2$ and (b) $k^i_{\rm f} = 50$; the former leads to energy spectra that are dominated by a forward cascade of enstrophy, whereas the latter yields spectra with an inverse cascade of energy and a forward cascade of enstrophy; we force the dominant component in case (b) (i.e., the normal-fluid (superfluid) component if $\rho_n/\rho > 0.5$ ($\rho_n/\rho \leq 0.5$)).

We perform a DNS of Eqs. (5.1a) and (5.1b) with periodic boundary conditions, on a square simulation domain with side $L = 2\pi$, by using a pseudospectral method with N_c^2 collocations points and the $2/3$ dealiasing rule. To evolve Eqs. (5.1a) and (5.1b) in time we use a second-order, exponential time differencing Runge-Kutta method [14]. The details of the parameters, which we use in our DNS runs, are given in the Table(5.1). We characterize our system by computing the spectra $E_n(k)$ and $E_s(k)$, $E_i(k) = \langle \sum_{k-\frac{1}{2}<k'\leq k+\frac{1}{2}} |\mathbf{u}_{\rm i}(\mathbf{k}', t)|^2 \rangle_t$ ($\langle\rangle_t$ denotes a time average), the probability distribution functions (PDFs) $P(\omega_i)$ of the vorticities and $P(\cos(\theta))$, the cumulative PDF $Q(\gamma)$ of γ, energy and enstrophy fluxes $\Pi_{\rm i}(k,t)$ and $Z_{\rm i}(k)$ ($i \in ({\rm n}, {\rm s})$), respectively, and the mutual-friction transfer function $M_{\rm i}(k)$, which we define below.

5.3 Results

We present the results of our DNS as follows. In Sec. 5.3.1 we present pseudocolor plots of normal-fluid and superfluid vorticities. Section 5.3.2 is devoted to energy spectra, Sec. 5.3.3 to fluxes, and Sec. 5.3.4 to probability distribution functions.

	N_c	ρ_n/ρ	B	ν_n	ν_s	μ_n	μ_s	k_f^n	k_f^s	f_0^n	f_0^s	ℓ_λ^n	ℓ_λ^s	Re_λ^n	Re_λ^s	$\tau_{\rm eddy}^n$	$\tau_{\rm eddy}^s$	$k_{\rm max}\eta_n$	$k_{\rm max}\eta_s$
R0	1024	–	–	10^{-4}	10^{-5}	10^{-2}	5×10^{-3}	2	2	10^{-3}	10^{-3}	0.36	0.38	92.77	1.25×10^3	51.1	45.8	17.7	5.16
R1	1024	0.1	1.0	10^{-4}	10^{-5}	10^{-2}	5×10^{-3}	2	2	10^{-3}	10^{-3}	0.371	0.378	112.9	1.3×10^3	46.3	42.3	16.8	5.01
R2a	1024	0.1	1.0	10^{-4}	10^{-5}	10^{-2}	5×10^{-3}	–	50	–	10^{-1}	0.062	0.049	108.4	876.7	5.43	5.12	2.89	0.82
R2b	1024	0.1	2.0	10^{-4}	10^{-5}	10^{-2}	5×10^{-3}	–	50	–	10^{-1}	0.058	0.05	100.6	876.8	5.23	5.05	2.80	0.82
R2c	1024	0.1	5.0	10^{-4}	10^{-5}	10^{-2}	5×10^{-3}	–	50	–	10^{-1}	0.054	0.05	94.3	876.5	5.12	5.04	2.7	0.82
R3	1024	0.05	1.0	10^{-4}	10^{-5}	10^{-2}	5×10^{-3}	–	50	–	10^{-1}	0.064	0.051	119.1	976.7	5.03	4.77	2.84	0.771
R4	1024	0.3	1.0	10^{-4}	10^{-5}	10^{-2}	5×10^{-3}	–	50	–	10^{-1}	0.052	0.039	62.9	487.6	5.72	5.14	3.18	0.868
R5	1024	0.5	1.0	10^{-5}	10^{-6}	10^{-2}	5×10^{-3}	–	50	–	10^{-1}	0.043	0.035	484.1	4.1×10^3	4.88	4.49	0.916	0.264
R6	1024	0.9	1.0	10^{-5}	10^{-6}	10^{-2}	5×10^{-3}	50	–	10^{-1}	–	0.039	0.047	617.0	7.19×10^3	3.50	3.84	0.771	0.268

Table 5.1: Parameters for our DNS runs R0-R6: ρ_n/ρ is the fraction of the normal fluid, B the mutual-friction coefficient, N_c^2 the number of collocation points, ν_n (ν_s) the normal-fluid (superfluid) kinematic viscosity, μ_n (μ_s) the coefficient of linear friction for the normal fluid (superfluid), and $k_{\rm f}^n$ ($k_{\rm f}^s$) and f_0^n (f_0^s) are the forcing wavevector and the forcing amplitude for the normal fluid (superfluid); ν_s and μ_s should vanish for a superfluid but they are included here for numerical stability, with $\nu_s \ll \nu_n$ and $\mu_s < \mu_n$. In runs R2a-R6 we force the dominant component (i.e., the normal-fluid (superfluid) component if $\rho_n/\rho > 0.5$ ($\rho_n/\rho \leq 0.5$)).

5.3.1 Vorticity fields

In Fig. 5.1 we present pseudocolor plots of ω_n and ω_s for runs R1 (panels (a) and (b)) and R2a (panels (c) and (d)) for $k_{\rm f} = 2$ and 50, respectively. The sizes of the vortical regions in these plots are $\sim k_{\rm f}^{-1}$ (as in 2D fluid turbulence with friction [7, 13]). Figures 5.1 (a) and (b) show that the normal and superfluid components are locked to each other; this is illustrated dramatically in Video M1, in which the lower two panels show the spatiotemporal evolution of Figs. 5.1 (a) and (b) and the top two panels show how ω_n and ω_s evolve in the absence of mutual friction (i.e., $B = B' = 0$); in the latter case, ω_n evolves to a frozen, stationary state; however, if $B > 0$, then the turbulence in the superfluid component is transferred to the normal component (top two panels of Video M1). Such a transfer of turbulence has been envisaged in 3D superfluid turbulence [15–17] but, to the best of our knowledge, never displayed as graphically as in our Video M1 for two-dimensional superfluid turbulence in the HVBK model.

5.3.2 Spectra

Figure 5.2 (a) compares energy spectra from runs R0 and R1, in which energy is injected at $k_{\rm f} = 2$, so there is no inverse-cascade regime in these spectra; this figure illustrates how the mutual-friction-induced interaction between the two components modifies the energy spectra $E_i(k,t)$. For the run R0, in which $B = 0$ and, therefore, the normal and superfluid components are uncoupled, $E^n(k)$ and $E^s(k)$ are shown in Fig. 5.2 (a) by full and dashed purple lines, respectively: not surprisingly, the region in which dissipation is significant is much larger in $E^n(k)$ than in $E^s(k)$; and the power-law regimes, more prominent in $E^s(k)$ than in $E^n(k)$, are

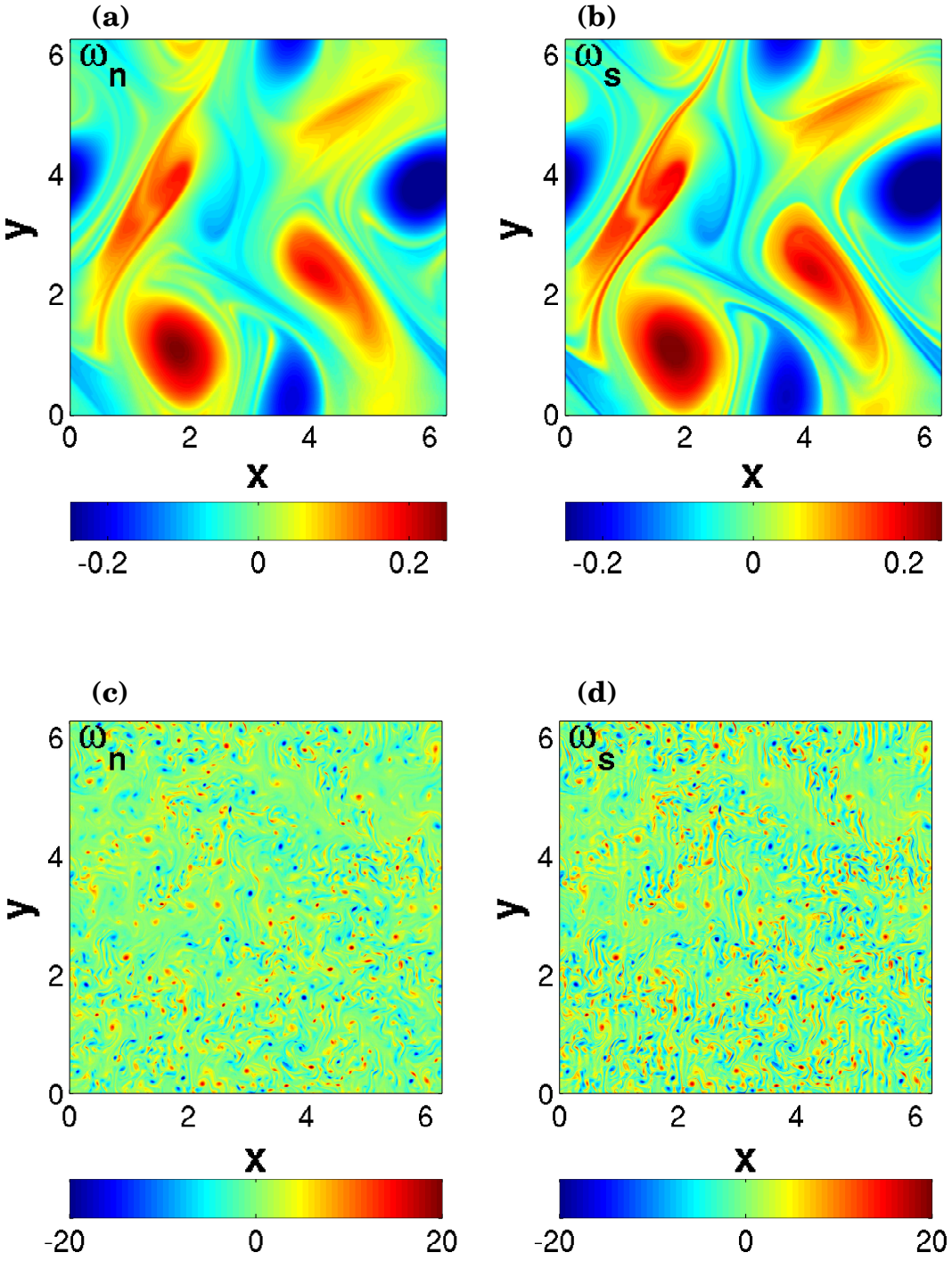

Figure 5.1: Pseudo-color plots of the vorticity fields, ω_n and ω_s, from our DNS runs `R1` at $t = 1720$ (panels (a) and (b), $k_{\rm f} = 2$) and `R2a` at $t = 1500$ (panels (c) and (d), $k_{\rm f} = 50$), respectively; show that the normal and superfluid component are locked to each other.

characterized by different, apparent scaling exponents, because the normal-fluid Reynolds number is too small for fully developed, normal-fluid turbulence. When we couple the normal and superfluid components, as in the run R1, $E^n(k)$ (green full curve in Fig. 5.2 (a)) is pulled up towards $E^s(k)$ (green dashed curve in Fig. 5.2 (a)), by virtue of the locking tendency that we have mentioned above; furthermore, both $E^n(k)$ and $E^s(k)$ now (i) display $k^{-\delta}$ forward-cascade, scaling ranges, with $\delta \simeq 4.2$, (ii) lie very close to each other at small wave numbers, and (iii) show dissipation regions at much higher wave numbers than in their counterparts when there is no coupling ($B = 0$ and run R0).

To study dual cascades, i.e., (i) an inverse cascade of energy for $k < k_{\rm f}$ and (ii) a direct cascade of enstrophy for $k > k_{\rm f}$, we use our DNS runs R2a-R6 (see Table 5.1). Figure 5.2 (b) shows $E^n(k)$ (full curves) and $E^s(k)$ (dashed curves) with dual cascades, for the runs R2a with $B = 1$ (purple curves), R2b with $B = 2$ (green curves), and R2c with $B = 5$ (blue curves). The inverse-cascade inertial ranges (with $k < k_{\rm f}$) of $E^n(k)$ and $E^s(k)$ exhibit scaling that is consistent with a $k^{-5/3}$ form (orange, dashed line), whereas the forward-cascade ranges (with $k > k_{\rm f}$) are consistent with $k^{-\delta}$ scaling, and $\delta \simeq 4.2$ (black, dashed line). In the forward-cascade regime of 2D fluid turbulence, the value of δ depends on the coefficient of linear friction [7, 13, 18, 19]; we find that, in the 2D HVBK model, δ depends not only on the coefficients of linear friction, but also on the mutual friction coefficients. Furthermore, the locking that we have discussed above makes $E^n(k)$ and $E^s(k)$ lie more-or-less on top of each other for a considerable range of wave numbers; not surprisingly, this range of overlap increases as B increases; for $B = 5$ it extends into the direct-cascade region. Figure 5.2 (c) shows inverse- and forward-cascade regimes in log-log plots of $E^n(k)$ (full curves) and $E^s(k)$ (dashed curves) versus k for five representative values of $\rho_{\rm n}/\rho$ (runs R2a (purple curves), R3 (green curves), R4 (blue curves), R5 (black curves), and R6 (yellow curves)), with $B = 1$ and $k < k_{\rm f} = 50$; the Reynolds numbers for these runs (see Table 5.1) are comparable, but not identical, to each other, because we force the normal-fluid (superfluid) if $\rho_n/\rho > 0.5$ ($\rho_n/\rho \leq 0.5$) to obtain a statistically steady state on the time scales of our DNS runs.

The HVBK model allows us to study the evolution of two-fluid turbulence as we change $\rho_{\rm n}/\rho$, which is small at low temperatures and increases as the temperature increases and approaches 1 at the superfluid transition temperature; if $\rho_{\rm n}/\rho = 0.05$, i.e., a 95% superfluid fraction, HVBK turbulence is close to that of a pure superfluid, on the length and Mach-number scales at which the HVBK model is valid; in contrast, HVBK turbulence at $\rho_{\rm n}/\rho = 0.9$ is close to that of a classical,

incompressible fluid. In Fig. 5.2 (c), the orange, dot-dashed line indicates a $k^{-5/3}$ power-law form that is visually close to the slopes (in log-log plots) of the energy spectra in the inverse-cascade scaling ranges; the black, dot-dashed line indicates a $k^{-4.2}$ power-law form that is visually close to the slope of the $E^n(k)$ spectrum in the forward-cascade scaling range for $\rho_{\rm n}/\rho = 0.9$; clearly, this forward-cascade spectral exponent depends on (a) the friction coefficient, as in 2D fluid turbulence, and, in addition, on (b) ρ_n/ρ, (c) and B; a complete study of this dependence requires extensive, and high-resolution DNS studies whose current computational cost is prohibitive.

5.3.3 Fluxes

To characterize fluxes in the inverse- and forward-cascade regimes we use the energy-transfer relations for 2D, homogeneous, isotropic, HVBK, turbulence, namely,

$$\partial_{\rm t} E_{\rm i}(k,t) = -\mathcal{D}_{\rm i}(k,t) + \mathcal{T}_{\rm i}(k,t) + \mathcal{M}_{\rm i}(k,t) + \mathcal{F}^{\rm i}_o(k), \tag{5.3}$$

where $i \in (n,s)$, $\mathcal{D}_{\rm i}(k,t) \equiv \sum_{k-\frac{1}{2}<k'\leq k+\frac{1}{2}} (\nu_{\rm i} k'^2 + \mu_{\rm i}) |\mathbf{u}_{\rm i}(\mathbf{k}')|^2$ is the transfer function, which combines the effects of viscous dissipation and the friction, $\mathcal{T}_{\rm i}(k,t)$ is the kinetic-energy transfer because of the triad interactions of the Fourier components of the velocities, and $\mathcal{F}^{\rm i}_o(k)$ is the energy-injection spectrum for the component $i \in (n,s)$. The transfer function $\mathcal{M}_{\rm i}(k)$, which accounts for the exchange of energy between the normal and the superfluid components, because of the mutual-friction coupling, is

$$\mathcal{M}_{\rm i}(k,t) \equiv \sum_{k-\frac{1}{2}<k'\leq k+\frac{1}{2}} \mathbf{F}^{\rm i}_{\rm mf}(\mathbf{k}',t) \cdot \mathbf{u}_{\rm i}(-\mathbf{k}',t). \tag{5.4}$$

Given $\mathcal{T}_{\rm i}(k,t)$, we can define the kinetic-energy fluxes, through the wave number k, as $\Pi_{\rm i}(k,t) = \langle \int_k^{\rm k_{max}} \mathcal{T}_{\rm i}(k',t) dk' \rangle_t$; and their analogs $Z_{\rm i}(k)$ ($i \in (n,s)$) for the enstrophy fluxes, which we plot versus k in Figs. 5.2 (d) and (e), respectively, for the same runs (`R2a` and `R3`-`R6`) and the same color codes as in Fig. 5.2 (c). In Fig. 5.2 (d), for each one of these runs, the energy fluxes $\Pi_{\rm i}(k,t) < 0$, for $k < k_{\rm f}$, which confirms that we have inverse cascades of energy; in contrast, the enstrophy fluxes $Z_{\rm i}(k) > 0$, for $k > k_{\rm f}$, in Fig. 5.2 (e), so we have forward cascades of enstrophy. For the runs `R2a` and `R3`-`R6` we plot, in Fig. 5.2 (f), the transfer functions $M_i(k) = \langle \mathcal{M}_{\rm i}(k,t) \rangle_t$; this function characterizes the energy exchange, because of the mutual friction B, between the normal and superfluid components.

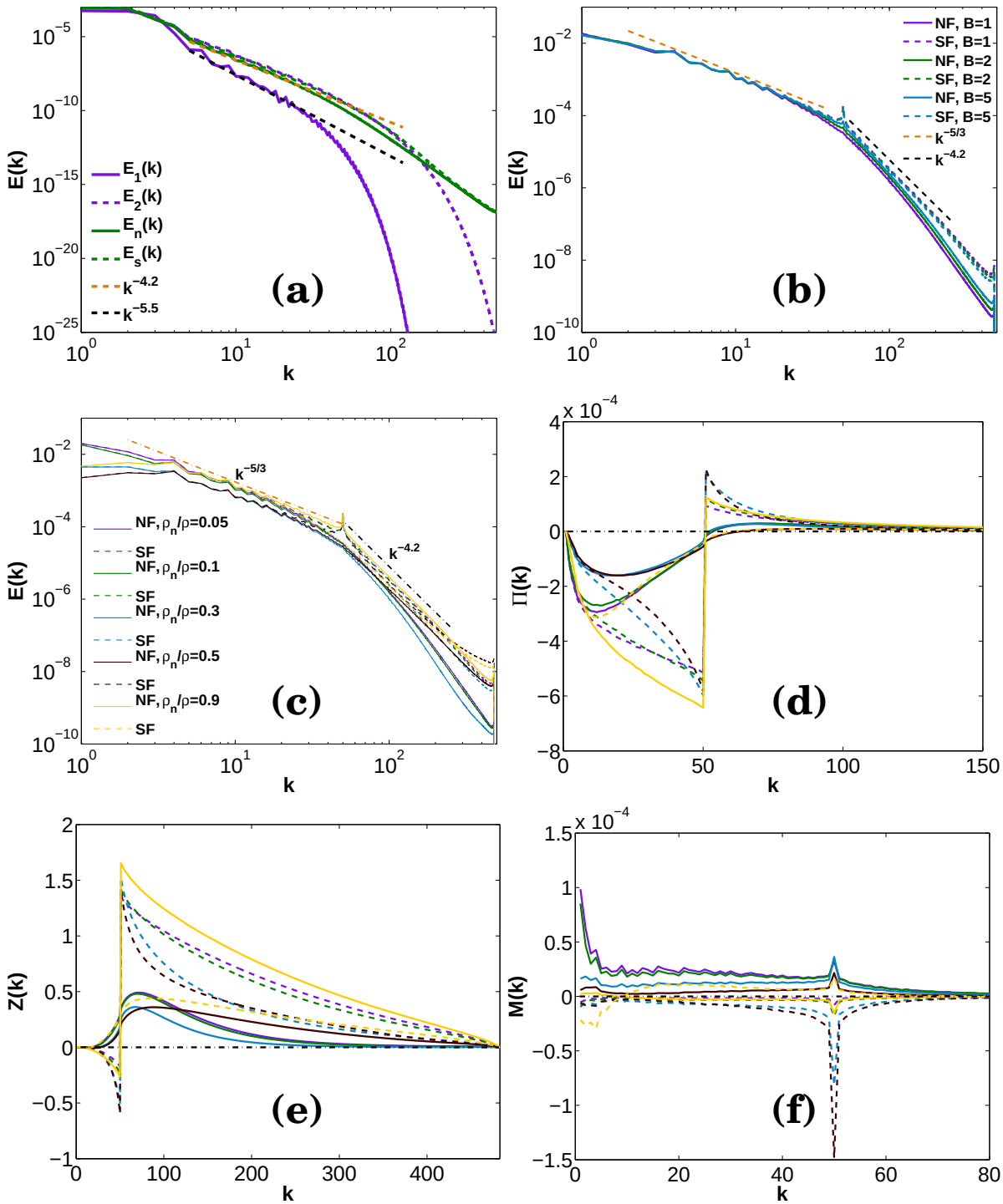

Figure 5.2: [Top panels] Log-log plots of the energy spectra $E_n(k)$ (full lines) and $E_s(k)$ (dashed lines) from our DNS runs: (a) R0 ($B = 0$, purple lines) and R1 ($B = 1$, green lines) with $k_{\rm f} = 2$; (b) R2a ($B = 1$, purple curves), R2b ($B = 2$, green curves), and R2c ($B = 5$, sky-blue curves) with $k_{\rm f}^s = 50$ and $\rho_n/\rho = 0.1$; (c) R2a (purple curves), R3 (green curves), R4 (sky-blue curves), R5 (black curves), and R6 (yellow curves), with $B = 1$ and we force the dominant component. [Lower panels] Plot of (d) energy flux $\Pi_{\rm i}(k)$; (e) enstrophy flux $Z_{\rm i}(k)$; and (f) mutual friction transfer function $M_i(k)$, for the DNS runs represented in the panel (c), as mentioned above.

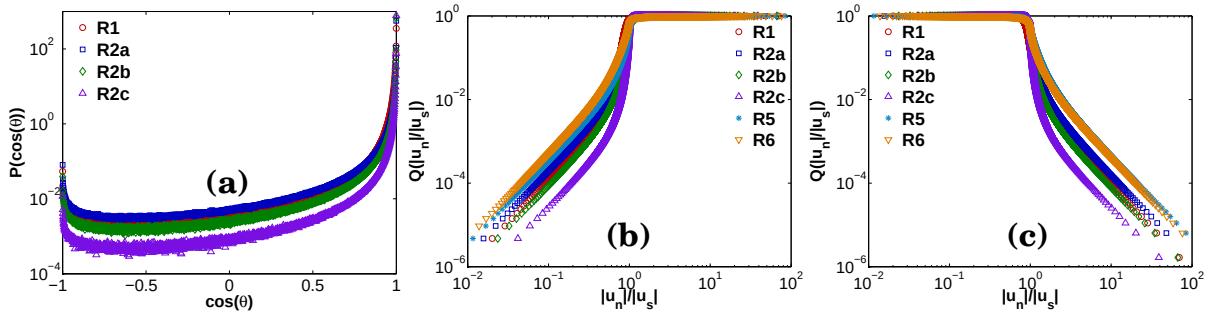

Figure 5.3: (a) Semilogarithmic (base 10) plots of the PDF $P(\cos(\theta))$ of the angle θ between $\mathbf{u}_n$ and $\mathbf{u}_s$ for runs `R1` (red circles), `R2a` ($B = 1$, blue squares), `R2b` ($B = 2$, green diamonds), and `R2c` ($B = 5$, purple triangles). Loglog (base 10) plots of (b) the cumulative distribution functions (CDF) $Q(\gamma)$ of $\gamma = |\mathbf{u}_n|/|\mathbf{u}_s|$ and (c) complementary CDFs $R(\gamma)$ for the runs `R1`, `R2a`-`R2c`, `R5`, and `R6`. CDFs show power-law tails $Q(\gamma) \sim \gamma^2$ and $R(\gamma) \sim \gamma^{-2}$, implying that the PDF $P(\gamma) \sim \gamma$, for $\gamma < 1$, and $P(\gamma) \sim \gamma^{-3}$, for $\gamma > 1$.

5.3.4 PDFs

We quantify the locking of the normal and superfluid velocities by plotting, in Fig. 5.3 (a), the PDF $P(\cos(\theta))$ of the angle θ between $\mathbf{u}_n$ and $\mathbf{u}_s$ for runs `R1` and `R2a`-`R2c`. $P(\cos(\theta))$ peaks at $\cos(\theta) = 1$ and falls rapidly with increasing θ; this indicates that $\mathbf{u}_n(\mathbf{r}, t)$ and $\mathbf{u}_s(\mathbf{r}, t)$ align preferentially along the same direction; the degree of alignment increases as we increase B.

In Figs. 5.3 (b) and (c) we show, respectively, plots of the cumulative distribution functions (CDFs) $Q(\gamma)$ of $\gamma = |\mathbf{u}_n|/|\mathbf{u}_s|$, and the complementary CDFs $R(\gamma)$, respectively, for the runs `R1`, `R2a`-`R2c`, `R5`, and `R6`. Both show power-law tails that imply that for the PDF $P(\gamma) \sim \gamma$, for $\gamma < 1$, and $P(\gamma) \sim \gamma^{-3}$, for $\gamma > 1$; the power-law exponents of these tails of $P(\gamma)$ are universal in the sense that they do not depend on B, ρ_n/ρ, and k_f.

In Figs. 5.4 and 5.5 we show that the PDFs of the Cartesian components of the normal and superfluid velocities in 2D HVBK turbulence are close to Gaussian (as in 2D turbulence). To obtain power-law tails in such PDFs, of the type that have been seen in some experiments in three-dimensional quantum turbulence [20], we must use either (a) the Gross-Pitaevskii equation [21–23], which can resolve quantum vortices or (b) Biot-Savart-type models [24]. Two-dimensional superfluid turbulence is now being studied numerically with such models [4,23,25,26]. In particular, some DNS studies have looked for inverse cascades in the 2D GP turbulence, which is forced and in which a dissipation term is used to obtain a statistically steady state. One such study [26] has obtained an inverse cascade, whereas another [25] has argued that a direct cascade occurs in the microcanonical evolution

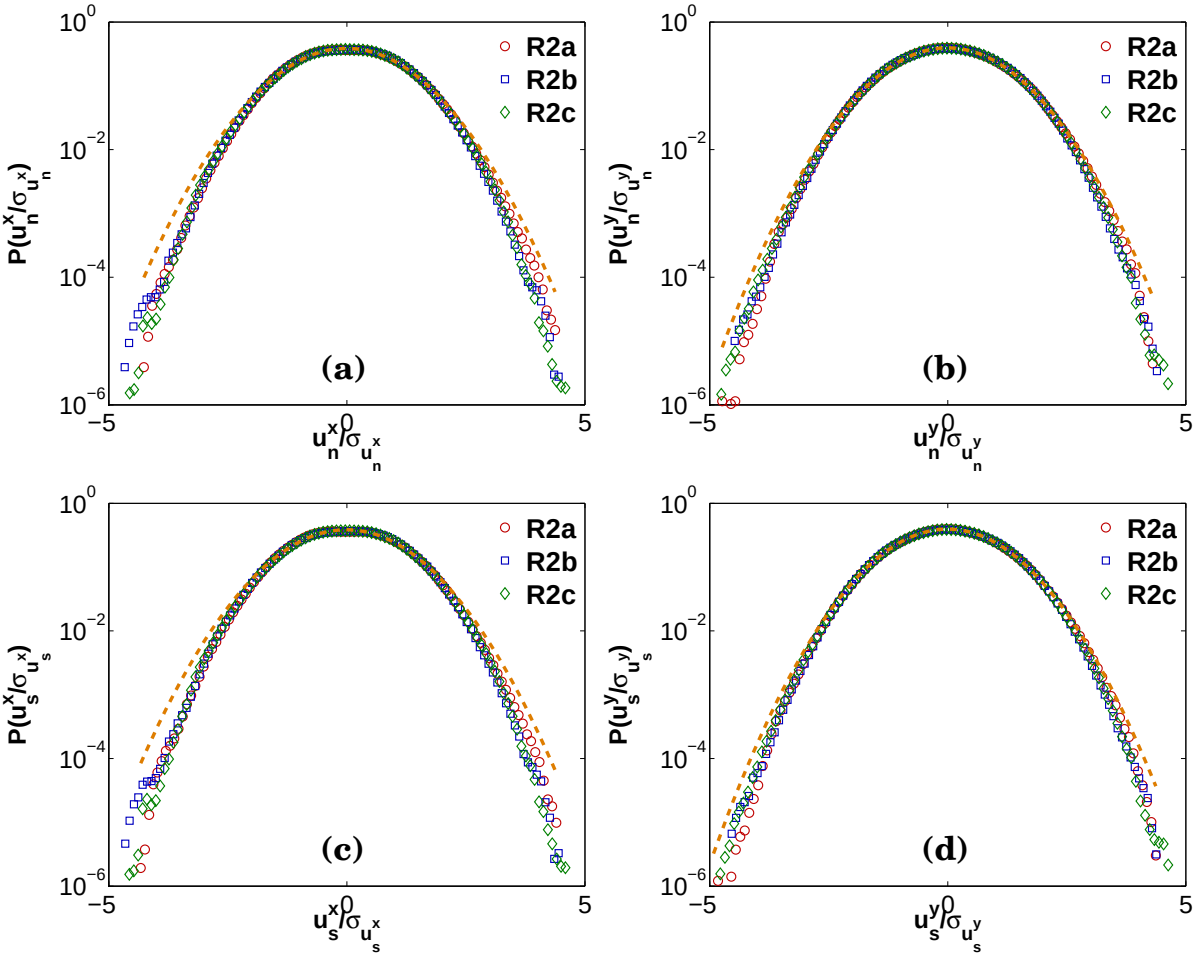

Figure 5.4: Semilogarithmic (base 10) plots of the PDFs of the (a) x component $\mathbf{u}_{\mathrm{n}}^{x}$ and (b) y component $\mathbf{u}_{\mathrm{n}}^{y}$ of the normal fluid velocity; PDFs of (c) x component $\mathbf{u}_{\mathrm{s}}^{x}$; (d) y component $\mathbf{u}_{\mathrm{s}}^{y}$ of the superfluid velocity. $\sigma_{\mathrm{u}_{\mathrm{i}}^{\mathrm{j}}}$ denotes the standard-deviation of the field $u_{\mathrm{i}}^{\mathrm{j}}$, here $i \in (\mathrm{n}, \mathrm{s})$ and $j \in (\mathrm{x}, \mathrm{y})$. These data are from our DNS runs `R2a` (red circles), `R2b` (blue squares), and `R2c` (green diamonds), respectively; the orange dashed line indicates a Gaussian fit.

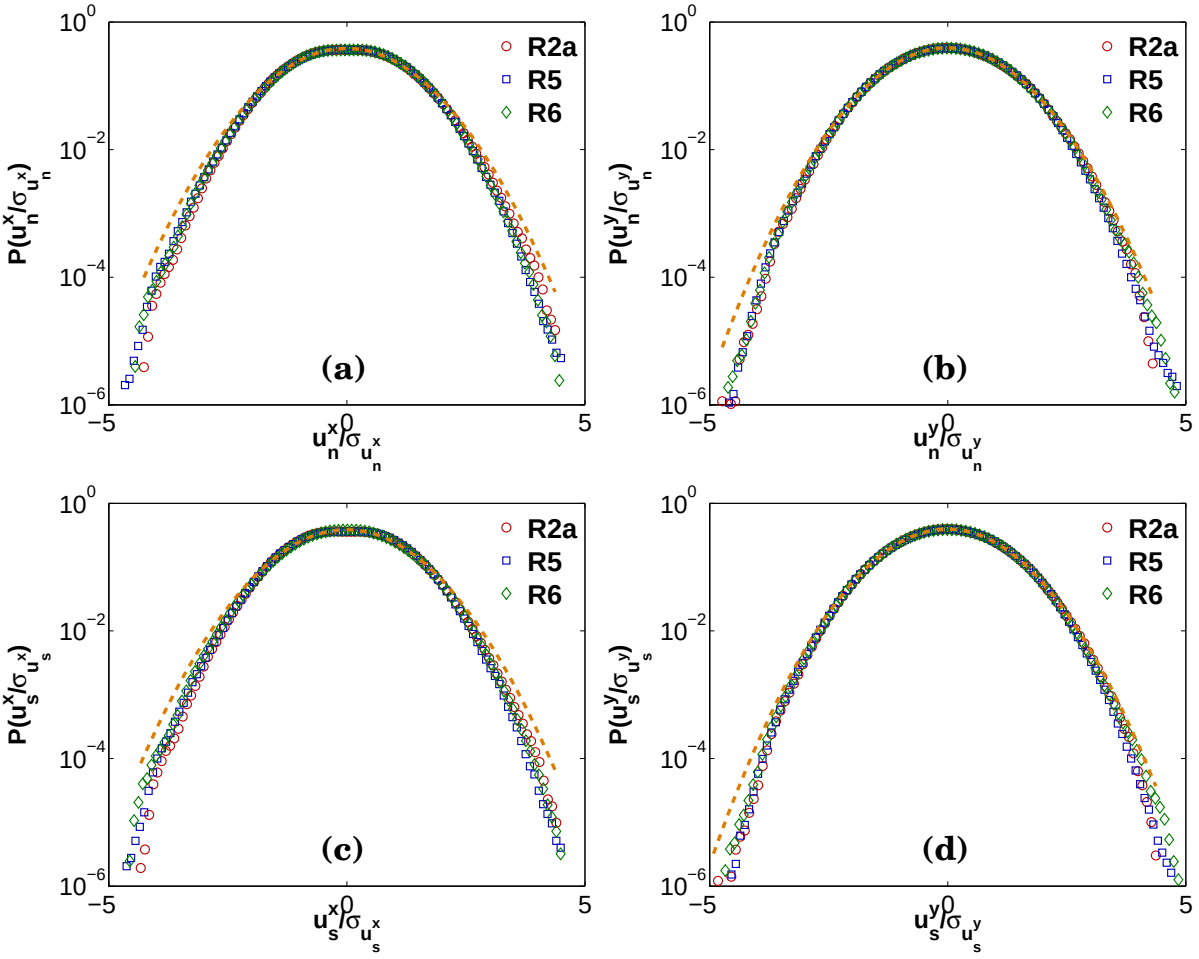

Figure 5.5: Semilogarithmic (base 10) plots of the PDFs of the (a) x component u_n^x and (b) y component u_n^y of the normal fluid velocity; PDFs of (c) x component u_s^x; (d) y component u_s^y of the superfluid velocity. $\sigma_{\mathrm{u}_\mathrm{i}^\mathrm{j}}$ denotes the standard-deviation of the field u_i^j, here $i \in (\mathrm{n},\mathrm{s})$ and $j \in (\mathrm{x},\mathrm{y})$. These data are from our DNS runs `R2a` (red circles), `R5` (blue squares), and `R6` (green diamonds), respectively; the orange dashed line indicates a Gaussian fit.

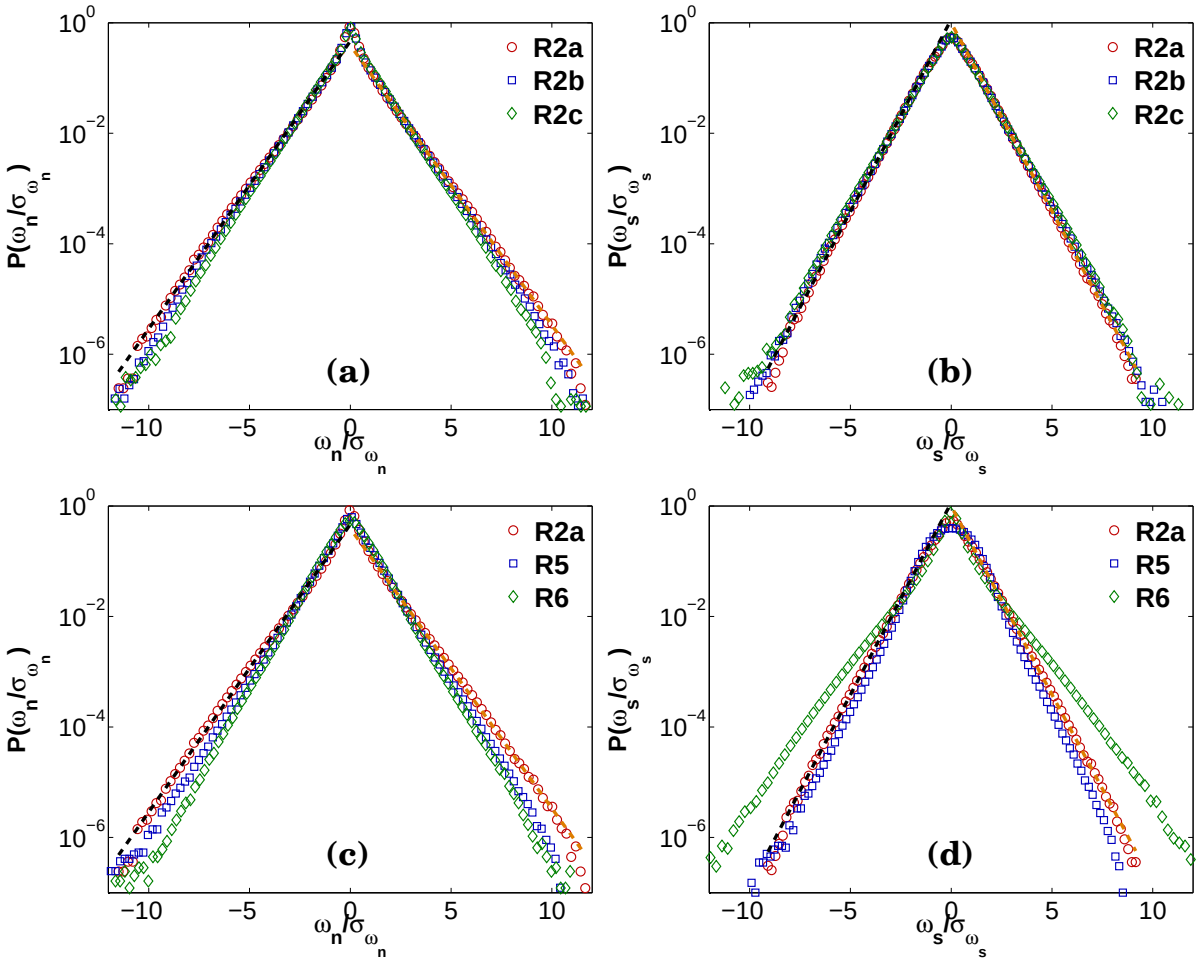

Figure 5.6: Semilogarithmic (base 10) plots of the PDFs of the vorticity of the (a) normal fluid ($\omega_{\rm n}$) from our DNS runs R2a (red circles), R2b (blue squares), and R2c (green diamonds); the black- and the orange-dashed lines indicate an exponential fit to the left (slope $= -0.5064$) and the right (slope $= 0.5207$) branches of the PDF $P(\omega_n/\sigma_{\omega_n})$ for the DNS run R2a; PDFs of the (b) superfluid ($\omega_{\rm s}$) from our DNS runs R2a (red circles), R2b (blue squares), and R2c (green diamonds); the black- and the orange-dashed lines indicate an exponential fit to the left (slope $= -0.6818$) and the right (slope $= 0.6951$) branches of the PDF $P(\omega_s/\sigma_{\omega_s})$ for the DNS run R2a; PDFs of the (c) normal fluid ($\omega_{\rm n}$) from our DNS runs R2a (red circles), R5 (blue squares), and R6 (green diamonds); the black- and the orange-dashed lines indicate an exponential fit to the left (slope $= -0.5064$) and the right (slope $= 0.5207$) branches of the PDF $P(\omega_n/\sigma_{\omega_n})$ for the DNS run R2a; PDFs of the (d) superfluid ($\omega_{\rm s}$) from our DNS runs R2a (red circles), R5 (blue squares), and R6 (green diamonds); the black- and the orange-dashed lines indicate an exponential fit to the left (slope $= -0.6818$) and the right (slope $= 0.6951$) branches of the PDF $P(\omega_s/\sigma_{\omega_s})$ for the DNS run R2a. $\sigma_{\omega_{\rm i}}$ denotes the standard-deviation of the field $\omega_{\rm i}$, here $i \in ({\rm n}, {\rm s})$.

of the GPE. On scales that are much larger than the mean separation between quantum vortices, and when quantum vortices of the same sign cluster, we expect superfluids to be described by the HVBK equations, if we restrict ourselves to low-Mach-number flows [4, 9, 10]; and the extraction of HVBK-model parameters from Gross-Pitaevskii studies is just beginning to be studied in three [27–29] and two [30, 31] dimensions. Figure 5.6 shows that the PDFs of the normal and superfluid vorticity in 2D HVBK turbulence are close to exponentials, as in the case of 2D fluid turbulence.

5.4 Conclusions

Our DNS of homogeneous, isotropic turbulence in the 2D HVBK model has led to the first elucidation of inverse and forward cascades, in this system, has contrasted them with their counterparts in 2D fluid turbulence, and led to the following results that await experimental confirmation. We have shown that both $E^n(k)$ and $E^s(k)$ exhibit inverse- and forward-cascade regimes, the former with $E^s(k) \sim E^n(k) \sim k^{-\alpha}$ and $\alpha \simeq -5/3$, and the latter with spectral exponents that depend on the friction coefficient, ρ_n/ρ, and B. We have demonstrated that, as B increases, $\mathbf{u}_n$ and $\mathbf{u}_s$ tend to align with each other: the PDF $\mathcal{P}(\cos(\theta))$ has a peak at $\cos(\theta) = 1$ and $\mathcal{P}(\gamma)$ displays power-law tails with universal exponents, which do not depend on B, ρ_n/ρ, and k_f. Furthermore, we have shown how energy and enstrophy fluxes depend on B, ρ_n/ρ, and the wavenumber k. The parameters B and ρ_n/ρ depend on the temperature; and this dependence has been measured in experiments [32] in three dimensions; such experimental studies have not been carried out in 2D.

5.5 Video Captions

Video M1 This video illustrates the spatiotemporal evolution, via pseudocolor plots, of ω_n (left panels) and ω_s (right panels) in which the mutual friction is (a) absent in the top two panels (DNS run `R0`) and (b) present in the lower two panels (DNS run `R1`).

Bibliography

[1] R. J. Donnelly. *Quantized vortices in helium II*, volume 2. Cambridge University Press, 1991.

[2] M. S. Paoletti and D. P. Lathrop. Quantum turbulence. *Annu. Rev. Condens. Matter Phys.*, 2(1):213–234, 2011.

[3] L. Skrbek and K. R. Sreenivasan. Developed quantum turbulence and its decay. *Phys. Fluids*, 24(1):011301, 2012.

[4] N. G. Berloff, M. Brachet, and N. P. Proukakis. Modeling quantum fluid dynamics at nonzero temperatures. *Proc. Natl. Acad. Sci. USA*, 111(Supplement 1):4675–4682, 2014.

[5] U. Frisch. *Turbulence*, volume 1. Cambridge University Press, Cambridge, UK, 1996.

[6] M. Lesieur. *Turbulence in fluids*, volume 3. Kluwer academic publishers Dordrecht, 1997.

[7] G. Boffetta and R. E. Ecke. Two-dimensional turbulence. *Annual Review of Fluid Mechanics*, 44:427–451, 2012.

[8] R. Pandit, P. Perlekar, and S. S. Ray. Statistical properties of turbulence: An overview. *Pramana*, 73(1):157–191, 2009.

[9] R. J. Donnelly. Cryogenic fluid dynamics. *J. Phys.: Condensed Matter*, 11(40):7783, 1999.

[10] C. F. Barenghi, R. J. Donnelly, and W. F. Vinen. Friction on quantized vortices in helium II. A review. *J. Low Temp. Phys.*, 52(3-4):189–247, 1983.

[11] H. E. Hall and W. F. Vinen. The rotation of liquid helium II. II. The theory of mutual friction in uniformly rotating helium II. *Proceedings of the Royal Society of London. Series A. Mathematical and Physical Sciences*, 238(1213):215–234, 1956.

[12] I. M. Khalatnikov. *An introduction to the theory of superfluidity*. WA Benjamin New York, 1965.

[13] P. Perlekar and R. Pandit. Statistically steady turbulence in thin films: direct numerical simulations with Ekman friction. *New J. Phys.*, 11(7):073003, 2009.

[14] S. M. Cox and P. C. Matthews. Exponential time differencing for stiff systems. *J. Comput. Phys.*, 176(2):430–455, March 2002.

[15] P. E. Roche, C. F. Barenghi, and E. Lévêque. Quantum turbulence at finite temperature: The two-fluids cascade. *Europhys. Lett.*, 87(5):54006, 2009.

[16] K. Morris, J. Koplik, and D. W. I. Rouson. Vortex locking in direct numerical simulations of quantum turbulence. *Phys. Rev. Lett.*, 101(1):015301, 2008.

[17] D. H. Wacks and C. F. Barenghi. Shell model of superfluid turbulence. *Phys. Rev. B*, 84(18):184505, 2011.

[18] K. Nam, E. Ott, T. M. Antonsen, and P. N. Guzdar. Lagrangian Chaos and the Effect of Drag on the Enstrophy Cascade in Two-Dimensional Turbulence. *Phys. Rev. Lett.*, 84:5134–5137, May 2000.

[19] G. Boffetta, A. Cenedese, S. Espa, and S. Musacchio. Effects of friction on 2D turbulence: An experimental study of the direct cascade. *Europhys. Lett.*, 71(4):590, 2005.

[20] M. S. Paoletti, M. E. Fisher, K. R. Sreenivasan, and D. P. Lathrop. Velocity statistics distinguish quantum turbulence from classical turbulence. *Phys. Rev. Lett.*, 101(15):154501, 2008.

[21] A. C. White, C. F. Barenghi, N. P. Proukakis, A. J. Youd, and D. H. Wacks. Nonclassical velocity statistics in a turbulent atomic Bose-Einstein condensate. *Phys. Rev. Lett.*, 104(7):075301, 2010.

[22] B. Nowak, J. Schole, D. Sexty, and T. Gasenzer. Nonthermal fixed points, vortex statistics, and superfluid turbulence in an ultracold Bose gas. *Phys. Rev. A*, 85(4):043627, 2012.

[23] V. Shukla, M. Brachet, and R. Pandit. Turbulence in the two-dimensional Fourier-truncated Gross-Pitaevskii equation. *New J. Phys.*, 15(11):113025, 2013.

[24] H. Adachi and M. Tsubota. Numerical study of velocity statistics in steady counterflow quantum turbulence. *Phys. Rev. B*, 83(13):132503, 2011.

[25] R. Numasato, M. Tsubota, and V. S. L'vov. Direct energy cascade in two-dimensional compressible quantum turbulence. *Phys. Rev. A*, 81(6):063630, 2010.

[26] M. T. Reeves, T. P. Billam, B. P. Anderson, and A. S. Bradley. Inverse Energy Cascade in Forced Two-Dimensional Quantum Turbulence. *Phys. Rev. Lett.*, 110(10):104501, 2013.

[27] N. G. Berloff and A. J. Youd. Dissipative Dynamics of Superfluid Vortices at Nonzero Temperatures. *Phys. Rev. Lett.*, 99:145301, Oct 2007.

[28] G. Krstulovic and M. Brachet. Anomalous vortex-ring velocities induced by thermally excited kelvin waves and counterflow effects in superfluids. *Phys. Rev. B*, 83:132506, Apr 2011.

[29] G. Krstulovic and M. Brachet. Energy cascade with small-scale thermalization, counterflow metastability, and anomalous velocity of vortex rings in Fourier-truncated Gross-Pitaevskii equation. *Phys. Rev. E*, 83:066311, Jun 2011.

[30] B. Jackson, N. P. Proukakis, C. F. Barenghi, and E. Zaremba. Finite-temperature vortex dynamics in Bose-Einstein condensates. *Phys. Rev. A*, 79:053615, May 2009.

[31] V. Shukla, M. Brachet, and R. Pandit. Superfluid Mutual-friction Coefficients from Vortex Dynamics in the Two-dimensional Galerkin-truncated Gross-Pitaevskii Equation. To be published.

[32] R. J. Donnelly and C. F. Barenghi. The observed properties of liquid helium at the saturated vapor pressure. *J. Phys. Chem. Ref. Data*, 27(6):1217–1274, 1998.

Chapter 6

Superfluid turbulence: A shell-model approach

In this Chapter we examine the multiscaling behavior of the velocity structure functions in three-dimensional superfluid turbulence by using a shell-model for the three-dimensional Hall-Vinen-Bekharevich-Khalatnikov (HVBK) equations. Our HVBK shell model is based on the Gledzer-Okhitani-Yamada (GOY) shell model. In particular, we examine the dependence of multiscaling on the normal-fluid fraction and the mutual-friction coefficients. Our extensive study of the 3D HVBK-shell-model shows that the multiscaling behavior of the velocity structure functions in superfluid turbulence is more complex than what has been reported so far.

6.1 Introduction

The characterization of the multiscaling properties of velocity structure functions [1] occupies a central place in the elucidation of the statistical properties of turbulence, in general, and superfluid turbulence, in particular. Direct numerical simulations (DNSs) play an important role in such studies in fluid turbulence [1–3]; such DNSs have achieved impressive spatial resolutions (see, e.g., Ref. [1]). By contrast, DNS studies of superfluid turbulence, whether at the level of the Gross-Pitaevskii (GP) equation (Chapters 2-3 and references therein) or via the Hall-Vinen-Bekharevich-Khalatnikov (HVBK) equations (Chapter 5 and references therein), have only achieved modest spatial resolutions. Futhermore, the large number of parameters in these equations, e.g., the mutual-friction coefficients, the ratio of the normal-fluid density to the superfluid density, and the Reynolds number, pose a significant challenge for systematic studies of the multiscaling of nomal-fluid- and superfluid-velocity structure functions. It has been suggested, therefore, that shell models for the HVBK equations [4–6] be used first to study such multiscaling in detail. This is because, ever since their introduction in the early work of Obukhov [7], Desnyansky and Novikov [8], Gledzer, and Ohkitani and Yamada [9, 10], shell models have

played valuable roles in elucidating the multiscaling properties of structure functions of fluid turbulence [1, 11–18]. Over the years, such shell models have been used to study magnetohydrodynamic (MHD) turbulence [19–24], Hall-MHD turbulence [25–28], fluid turbulence with polymer additives [29], fluid turbulence in two dimensions [30], fluid turbulence in dimensions in between two and three [31], turbulence in binary-fluid mixtures [32] and in rotating systems [33], and, as we have mentioned above, turbulence in superfluids [4–6]. Shell models have also been used to initiate studies of the dynamic multiscaling of time-dependent structure functions [34–36].

In this Chapter we build on the shell-model studies of Refs. [4–6] to explore the dependence of the multiscaling exponents here on the parameters of the HVBK model. It has been noted in Ref. [6] that, given current computational resources, a systematic study of this parameter dependence lies beyond the scope of a well-resolved DNS of the three-dimensional (3D) HVBK equations; however, such a study is possible if we use shell models for the 3D HVBK equations. Our study extends the work of Refs. [4–6] by obtaining a variety of results that we summarize before we present the details of our study.

Our extensive study of the 3D HVBK-shell-model shows that the multiscaling behavior of the velocity structure functions in superfluid turbulence is more complex than that reported in Ref. [6]; however, they agree with those of Ref. [6] in that, in the limit when the normal-fluid fraction, is either small (pure superfluid) or large, the equal-time multiscaling exponents are close to the pure-fluid values. Moreover, we find that there are two regions, with intermediate values of the normal-fluid fraction, in which the multiscaling exponents are larger than those observed for the pure fluid and Kolmogorov's 1941 (K41) predictions [1]; separating the above two intermediate ranges is the region in which the multiscaling exponents are close to the K41 prediction. We have also investigated the dependence of the multiscaling exponents on the mutual-friction coefficient, with equal proportions of superfluid and normal-fluid components; here, our results show that, for small (weak-coupling limit) and large (strong-coupling limit) values of the mutual-friction coefficient, the multiscaling exponents tend to their pure-fluid values, whereas, in an intermediate range, there are deviations from the pure-fluid behavior; in particular, the multiscaling exponents are larger than their pure-fluid counterparts for high-order structure functions (order $p \geq 3$).

The rest of this Chapter is organized as follows. In Sec. 6.2 we describe the model and the numerical methods we use. Section 6.3 is devoted to our results. We end with conclusions in Sec. 6.4.

6.2 Models and Numerical Simulations

The GOY shell model for the Navier-Stokes equation [9, 10] is defined through the equations

$$\left[\frac{d}{dt}+\nu k_m^2\right]u_m = \iota[ak_m u_{m+1}u_{m+2}+bk_{m-1}u_{m-1}u_{m+1}+ck_{m-2}u_{m-1}u_{m-2}]^* + f_m, \quad (6.1)$$

on a logarithmically discretized Fourier space labelled by scalar wave vectors $k = k_0\lambda^m$, with $k_0 = 2^{-4}$ and $\lambda = 2$, that are associated with the shell m; $*$ denotes complex conjugation and ν the fluid viscosity. The dynamical variables are the complex scalar shell velocities $u_m(k_m)$, and the coefficients $a = 1, b = -\delta, c = -(1-\delta)$ are chosen to conserve the shell-model analogs of energy and helicity in the limit of vanishing viscosity and absence of external forcing. The standard value of $\delta = 1/2$. N is the total number of shells. f_m is the external forcing that is used to drive the system into a statistically steady state. The logarithmic discretization of Fourier space allows us to achieve very high Reynolds numbers, even with a moderate number of shells. In the GOY-shell-model equations, direct interactions are limited to the nearest- and next-nearest-neighbour shells, whereas, in the Navier-Stokes equation in Fourier space, every Fourier mode of the velocity is directly coupled to every other Fourier mode.

The incompressible, 3D HVBK equations [37] can be written as

$$\rho_s\Big(\frac{\partial \mathbf{u}^s}{\partial t}+\mathbf{u}^s\cdot\nabla\mathbf{u}^s\Big) = -\frac{\rho_s}{\rho}\nabla p+\rho_s\sigma\nabla T+\mathbf{F}^s_{mf}, \quad (6.2a)$$

$$\rho_n\Big(\frac{\partial \mathbf{u}^n}{\partial t}+\mathbf{u}^n\cdot\nabla\mathbf{u}^n\Big) = -\frac{\rho_n}{\rho}\nabla p-\rho_n\sigma\nabla T+\mathbf{F}^n_{mf}+\nu_n\nabla^2\mathbf{u}^n, \quad (6.2b)$$

with the incompressibility condition $\nabla\cdot\mathbf{u}^i = 0$, the subscript $i \in (n, s)$ denotes the normal fluid (n) or the superfluid (s); p, σ and T are the pressure, specific entropy, and temperature, respectively; ρ_n (ρ_s) is the normal-fluid (superfluid) density; ν_i is the normal fluid viscosity. The mutual-friction terms, which model the interaction between the normal and superfluid components, can be written as $\mathbf{F}^s_{mf} = -(\rho_n/\rho)\mathbf{f}_{mf}$ and $\mathbf{F}^n_{mf} = (\rho_s/\rho)\mathbf{f}_{mf}$ in Eqs. (6.2a) and (6.2a), respectively, where

$$\mathbf{f}_{\rm mf} = \frac{B}{2}\frac{\omega_{\rm s}}{|\omega_{\rm s}|}\times(\omega_{\rm s}\times\mathbf{u}_{\rm ns})+\frac{B'}{2}\omega_{\rm s}\times\mathbf{u}_{\rm ns}, \quad (6.3)$$

with $\mathbf{u}_{\rm ns} = (\mathbf{u}_{\rm n}-\mathbf{u}_{\rm s})$ the slip velocity, and B and B' the coefficients of mutual friction. In most of our studies we set $B' = 0$ so, $\mathbf{f}_{\rm mf} = -\frac{B}{2}|\omega_{\rm s}|\mathbf{u}_{\rm ns}$ (Gorter-Mellink form [38]).

The shell model for the HVBK equations, based on the GOY shell model, is [4]

$$\left[\frac{d}{dt}+\nu^n k_m^2\right]u_m^n = \mathrm{NL}[u_m^n]+F_m^n+f_m^n, \quad (6.4)$$

$$\left[\frac{d}{dt} + \nu^s k_m^2\right] u_m^s = \mathrm{NL}[u_m^s] + F_m^s + f_m^s, \tag{6.5}$$

where

$$\mathrm{NL}[u_m] = i[ak_m u_{m+1}u_{m+2} + bk_{m-1}u_{m-1}u_{m+1} + ck_{m-2}u_{m-1}u_{m-2}]^*. \tag{6.6}$$

It is defined on a logarithmically discretized Fourier space labelled by scalar wave vectors $k = k_0\lambda^m$ with $k_0 = 2^{-4}$ and $\lambda = 2$, that are associated with the shells m. ν^n and ν^s are the normal fluid and the superfluid viscosities, respectively. The dynamical variables are the complex scalar shell velocities $u_m^n(k_m)$ and $u_m^s(k_m)$, defined for the normal fluid and the superfluid, respectively. The coefficients $a = 1$, $b = -1/2$, $c = -1/2$ are chosen to conserve the shell-model analogues of energy and helicity in the limit of vanishing viscosity and the absence of external forcing. f_m^n (f_m^s) is the external forcing that we use to drive the system into a statistically steady state. The shell-model analogs of the mutual-friction terms, which models the interaction between the normal and the superfluid components, are

$$F_m^s = \frac{\rho_n B\Omega_s^{1/2}}{2\rho}(u_m^n - u_m^s) \tag{6.7}$$

and

$$F_m^n = -\frac{\rho_s B\Omega_s^{1/2}}{2\rho}(u_m^n - u_m^s). \tag{6.8}$$

The superfluid and normal-fluid enstrophies, respectively, are defined by

$$\Omega_s = \sum_{m=1}^{N} \frac{1}{2}k_m^2|u_m^s|^2 \tag{6.9}$$

and

$$\Omega_n = \sum_{m=1}^{N} \frac{1}{2}k_m^2|u_m^n|^2. \tag{6.10}$$

The total energy is

$$E_T = E_n + E_s \equiv \frac{1}{2}\sum_{m=1}^{N}\left(|u_m^n|^2 + |u_m^s|^2\right), \tag{6.11}$$

where E_n and E_s are the normal-fluid and superfluid energies, respectively. Now we define the shell-model analogs of the statistical quantities, which we use in our study. The helicity is

$$H_i = \sum_{m=1}^{N} \frac{1}{2}\left(\frac{a}{c}\right)^m \frac{|u_m^i|^2}{k_m}; \tag{6.12}$$

the energy spectra are

$$E_i(k_m) = \frac{1}{2}\frac{|u_m^i|^2}{k_m}; \tag{6.13}$$

the root-mean-square velocity is

$$u^i_{\rm rms} = \Big(\sum_m |u^i_m|^2\Big)^{1/2}; \tag{6.14}$$

the Taylor microscale is

$$\lambda_i = \left[\frac{\sum_m E^i(k_m)}{\sum_m k_m^2 E^i(k_m)}\right]^{1/2}; \tag{6.15}$$

the Taylor-microscale Reynold's number is

$$Re^i_\lambda = u_{\rm rms}\lambda_i/\nu_i; \tag{6.16}$$

the integral length scale is

$$\ell_I = \frac{\sum_m E^i(k_m)/k_m}{\sum_m E^i(k_m)}; \tag{6.17}$$

large-eddy-turnover time is

$$T^i_{eddy} = \frac{1}{k_1 u^i_1}; \tag{6.18}$$

here $i \in (n, s)$.

The equal-time, order-p structure functions for the shell model are

$$S^i_p(k_m) \equiv \Big\langle \big[u^i_m(t)u^{i*}_m(t)\big]^{p/2}\Big\rangle \sim k_m^{-\zeta^i_p}, \tag{6.19}$$

where the power-law dependence is obtained only if k_m^{-1} lies in the inertial range and $i \in (n, s)$. The structure functions, as defined above, show period-three oscillations because of three cycles in the static solutions of the GOY model for the Navier-Stokes equation [13]. Therefore, we use the modified structure functions [12, 13]

$$\Sigma^i_p \equiv \left\langle \left|\Im\big[u^i_{m+2}u^i_{m+1}u^i_m - \frac{1}{4}u^i_{m-1}u^i_m u^i_{m+1}\big]\right|^{p/3}\right\rangle \sim k_m^{-\zeta^i_p}, \tag{6.20}$$

which filters out these oscillations effectively, $i \in (n, s)$. The Sabra-model variant of the HVBK equations do not show such oscillations. The multiscaling exponents ζ^i_p, $i \in (n, s)$ must satisfy the convexity inequality for any three positive integers $p_1 \le p_2 \le p_3$ [1]

$$(p_3 - p_1)\zeta^i_{2p_2} \ge (p_3 - p_2)\zeta^i_{2p_1} + (p_2 - p_1)\zeta^i_{2p_3}. \tag{6.21}$$

We obtain a smooth energy spectrum, without period-3 oscillations, by using $E_i(k_m) = \Sigma^i_2(k_m)/k_m$, $i \in (n, s)$.

To obtain a statistically steady state, we force both the components, the superfluid and normal fluid, with a force of the form

$$f^{n,s}_m = (1 + i) \times 5 \times 10^{-3}\delta_{1,m}, \tag{6.22}$$

	ρ_n/ρ	B	ν_n	ν_s	Δt
PG1	–	–	10^{-7}	–	10^{-5}
PG2	–	–	10^{-9}	–	10^{-5}
G1a	0.0450	1.5260	10^{-7}	10^{-10}	5.0×10^{-6}
G1	0.0450	1.5260	10^{-7}	10^{-9}	10^{-5}
G2	0.0998	1.3255	10^{-7}	10^{-9}	10^{-5}
G3	0.2503	1.0765	10^{-7}	10^{-9}	10^{-5}
G4	0.4004	0.9838	10^{-7}	10^{-9}	10^{-5}
G5	0.4994	0.9848	10^{-7}	10^{-9}	10^{-5}
G6	0.6003	1.0447	10^{-7}	10^{-9}	10^{-5}
G7	0.6493	1.1034	10^{-7}	10^{-9}	10^{-5}
G8	0.6995	1.1924	10^{-7}	10^{-9}	10^{-5}
G9	0.7501	1.3267	10^{-7}	10^{-9}	10^{-5}

Table 6.1: Parameters for our 3D shell-model runs (pure-fluid) PG1, PG2 and (HVBK) G1a-G9: ρ_n/ρ is the normal-fluid density fraction; B is the mutual-friction coefficient; ν_n (ν_s) is the normal-fluid (superfluid) viscosity; Δt is the incremental time step; we use $N = 36$ shells in our simulations.

where δ is the Kronecker-delta. We use the second-order, slaved Adams-Bashforth scheme to integrate the 3D HVBK-GOY-shell-model Eqs. (6.4) and (6.5) [12,39]. To study the multiscaling behavior of structure functions in the 3D HVBK-GOY-shell-model, we design three sets of runs.

1. G1a-G9: In these runs, we input the values of ρ_n/ρ and B at different temperatures measured in experiments on helium II [40]. We use suitable values of ν_n and ν_s, which, along with other parameters, are summarized in the Table 6.1.

2. B1-B19: We vary ρ_n/ρ between $0.05 - 0.95$ and keep $B = 1.5$ fixed.

3. R1-R12: We vary B between $0.1 - 10$ and keep $\rho_n/\rho = 0.5$ fixed.

In the runs B1-B19 and R1-R12 we use $\nu_n = 10^{-7}$, $\nu_s = 10^{-9}$, and the time step $\Delta t = 10^{-5}$.

We use the initial condition $u_m^{n,s} = (1+i)k_m e^{-k_m^2}$, for $1 \le m \le N$ in the runs G1a-G9, PG1, and PG2; the GOY-shell-model runs PG1 ($\nu_n = 10^{-7}$) and PG2 ($\nu_n = 10^{-9}$) are included for the purpose of comparison with the runs G1a-G9. In the runs B1-B19 and R1-R12, we use the initial values $u_m^{n,s} = u_0^{n,s} k_m^{1/2} e^{-k_m^2} e^{i\vartheta_m}$, for $1 \le m \le N$, where ϑ_m is a random phase distributed uniformly on $[0, 2\pi)$. In our shell-model runs, we use the boundary conditions $u_{-2}^i = u_{-1}^i = u_0^i = 0$ and $u_{N+1}^i = u_{N+2}^i = 0$, $i \in (n, s)$. We report for $N = 36$ shells; Ref. [4] uses $N = 18$ and Ref. [6] presents data with $N = 36$.

	λ_n	λ_s	$Re^n_\lambda(\times 10^6)$	$Re^s_\lambda(\times 10^8)$	T^n_{eddy}	T^s_{eddy}
PG1	0.95	–	7.2	–	14.50	–
PG2	0.50	–	310	–	20.33	–
G1a	0.42	0.28	2.3	15	45.61	45.61
G1	0.70	0.51	4.2	3.1	21.80	21.80
G2	0.73	0.54	4.4	3.2	22.03	22.03
G3	0.82	0.61	5.2	3.9	19.83	19.83
G4	0.71	0.54	4.4	3.4	18.41	18.41
G5	0.89	0.70	6.2	4.9	17.15	17.15
G6	0.94	0.77	6.9	5.6	15.45	15.45
G7	0.94	0.78	7.0	5.9	14.94	14.94
G8	0.95	0.80	7.2	6.1	14.51	14.51
G9	0.95	0.82	7.3	6.3	14.42	14.42

Table 6.2: Parameters determined in our shell-model runs PG1, PG2 and G1a-G9: λ_n (λ_s) is the Taylor microscale for the normal-fluid (superfluid); Re^n_λ (Re^s_λ) is the Taylor-microscale Reynold's number for the normal-fluid (superfluid); T^n_{eddy} (T^s_{eddy}) is the large-eddy-turnover time for the normal-fluid (superfluid).

6.3 Results

In Table 6.2 we list the values of the λ_i, Re^i_λ, and T^i_{eddy} that we obtain from our 3D HVBK-Goy-shell-model simulations PG1, PG2, and G1a-G9. Figure 6.1 compares $E_n(k_m)$ (full curves) and $E_s(k_m)$ (dashed curves) for four representative values of ρ_n/ρ (runs G1 (purple curves), G2 (green curves), G5 (sky-blue curves), and G9 (brown curves)). The inertial ranges of $E_n(k_m)$ and $E_s(k_m)$ exhibit scaling that is consistent with a $k^{-5/3}$ power-law form (orange, dashed line). The runs PG1 and PG2 together can be regarded as uncoupled ($B = 0$) normal fluid and superfluid, respectively; we use them for the sake of comparison with other runs to show how the mutual friction modifies the energy spectra. When we couple the normal and superfluid components, as in the run G1, $E_n(k_m)$ is pulled up towards $E_s(k_m)$, by virtue of the tendency of locking between u_n and u_s (see Chapter 5); in contrast, in the absence of coupling, the spectra $E(k_m)$ for the runs PG1 (yellow, full curves) and PG2 (yellow, dashed curves) lie far apart especially in the dissipation range.

We study the multiscaling behaviors of the velocity structure functions Eqs. (6.20) for the normal fluid and superfluid, obtained from the 3D HVBK-Goy-shell-model. We extract the multiscaling exponents ζ^n_p and ζ^s_p for the normal fluid and superfluid components, respectively, by using the Eqs. (6.20). In Table 6.3 we list the values of these exponents, which we have obtained from Σ^i_p, for $p = 1$ to 6, $i \in (n, s)$; each row of this Table has two lines, the first and second lines contain, respectively, the values of ζ^n_p and ζ^s_p. The Table 6.3 shows that $\zeta^n_p = \zeta^s_p$, for $p = 1$ to 6, for the runs G1-G9,

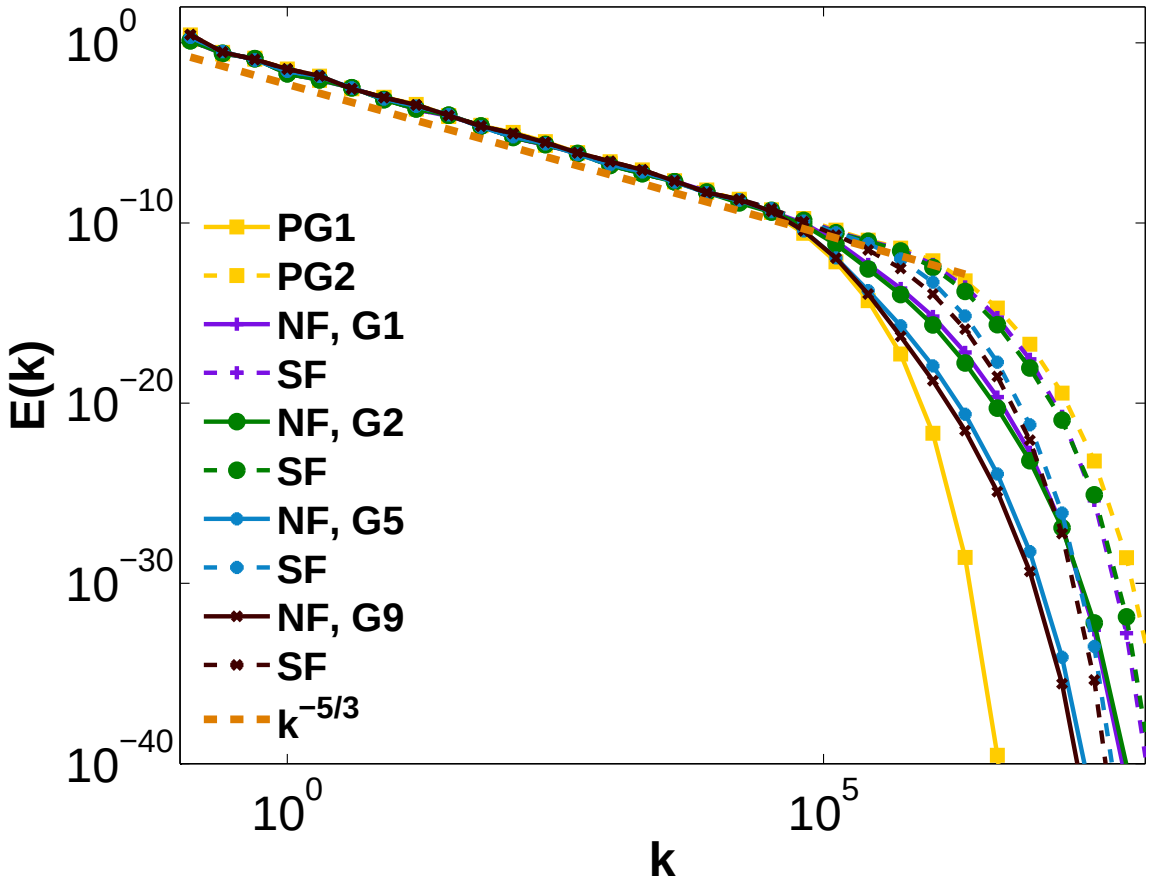

Figure 6.1: Log-log (base 10) plots of the spectra $E_n(k_m)$ (full curves) and $E_s(k_m)$ (dashed curves) from our shell-model runs: `PG1` and `PG2` (yellow curves); `G1` (purple curves); `G2` (green curves); `G5` (sky-blue curves); `G9` (brown curves); a $k^{-5/3}$ power-law is shown by the orange-dashed line. The abbreviation NF (SF) stands for normal-fluid (superfluid).

	ρ_n/ρ (B)	ζ_1^n ζ_1^s	ζ_2^n ζ_2^s	ζ_3^n ζ_3^s	ζ_4^n ζ_4^s	ζ_5^n ζ_5^s	ζ_6^n ζ_6^s
PG1	–	0.378 ± 0.004	0.704 ± 0.006	0.996 ± 0.009	1.26 ± 0.01	1.51 ± 0.02	1.74 ± 0.03
PG2	–	0.383 ± 0.003	0.714 ± 0.005	1.007 ± 0.007	1.27 ± 0.01	1.52 ± 0.02	1.75 ± 0.02
G1a	0.0450	0.378 ± 0.008	0.70 ± 0.01	0.99 ± 0.02	1.26 ± 0.03	1.50 ± 0.05	1.73 ± 0.07
	(1.5260)	0.378 ± 0.008	0.70 ± 0.01	0.99 ± 0.02	1.26 ± 0.03	1.50 ± 0.05	1.73 ± 0.07
G1	0.0450	0.387 ± 0.003	0.723 ± 0.004	1.024 ± 0.006	1.300 ± 0.008	1.56 ± 0.01	1.80 ± 0.02
	(1.5260)	0.384 ± 0.003	0.721 ± 0.004	1.022 ± 0.006	1.300 ± 0.008	1.55 ± 0.01	1.80 ± 0.02
G2	0.0998	0.390 ± 0.003	0.732 ± 0.005	1.040 ± 0.007	1.32 ± 0.01	1.58 ± 0.02	1.83 ± 0.03
	(1.3255)	0.389 ± 0.003	0.731 ± 0.005	1.040 ± 0.007	1.32 ± 0.01	1.58 ± 0.02	1.83 ± 0.03
G3	0.2503	0.372 ± 0.006	0.71 ± 0.01	1.02 ± 0.01	1.32 ± 0.02	1.60 ± 0.02	1.86 ± 0.04
	(1.0765)	0.372 ± 0.006	0.71 ± 0.01	1.02 ± 0.01	1.32 ± 0.02	1.60 ± 0.02	1.86 ± 0.04
G4	0.4004	0.3309 ± 0.0001	0.6663 ± 0.0001	1.0046 ± 0.0001	1.3446 ± 0.0001	1.6858 ± 0.0002	2.0276 ± 0.0003
	(0.9838)	0.3310 ± 0.0001	0.6664 ± 0.0001	1.0044 ± 0.0001	1.3441 ± 0.0001	1.6847 ± 0.0002	2.0259 ± 0.0002
G5	0.4994	0.375 ± 0.004	0.732 ± 0.005	1.079 ± 0.006	1.418 ± 0.008	1.75 ± 0.01	2.06 ± 0.02
	(0.9848)	0.374 ± 0.003	0.732 ± 0.005	1.079 ± 0.006	1.417 ± 0.008	1.74 ± 0.01	2.06 ± 0.02
G6	0.6003	0.386 ± 0.003	0.737 ± 0.005	1.065 ± 0.007	1.37 ± 0.01	1.67 ± 0.02	1.94 ± 0.03
	(1.0447)	0.385 ± 0.003	0.737 ± 0.005	1.064 ± 0.007	1.37 ± 0.01	1.66 ± 0.02	1.94 ± 0.03
G7	0.6493	0.384 ± 0.003	0.734 ± 0.005	1.060 ± 0.006	1.37 ± 0.01	1.66 ± 0.02	1.94 ± 0.03
	(1.1034)	0.384 ± 0.003	0.734 ± 0.004	1.060 ± 0.006	1.37 ± 0.01	1.66 ± 0.02	1.94 ± 0.03
G8	0.6995	0.383 ± 0.003	0.728 ± 0.004	1.047 ± 0.007	1.35 ± 0.01	1.63 ± 0.02	1.90 ± 0.03
	(1.1924)	0.383 ± 0.003	0.728 ± 0.004	1.046 ± 0.007	1.35 ± 0.01	1.63 ± 0.02	1.90 ± 0.03
G9	0.7501	0.381 ± 0.004	0.718 ± 0.006	1.027 ± 0.008	1.32 ± 0.01	1.59 ± 0.02	1.85 ± 0.03
	(1.3267)	0.380 ± 0.004	0.718 ± 0.006	1.027 ± 0.008	1.32 ± 0.01	1.59 ± 0.02	1.85 ± 0.03

Table 6.3: Multiscaling exponents ζ_p from our shell-model runs PG1, PG2, and G1 – G9; each row of the Table has two lines; the first and second lines contain, respectively, the values of ζ_p^n and ζ_p^s. In the second column, ρ_n/ρ is the normal-fluid density fraction (first line) and B is the mutual-friction coefficient (second line, in parentheses).

because of the mutual-friction-induced locking of the normal fluid and superfluid velocities in the inertial range.

Figures 6.2 (a) and (b) show plots of ζ_p^n and ζ_p^s versus order p, respectively; in these plots the orange line is the K41 prediction $\zeta_p^{K41} = p/3$ and the yellow line shows the multiscaling behavior of the pure fluid (classical turbulence) ζ_p^c. We find that the multiscaling exponents ζ_p^i, $i \in (n, s)$, determined from the 3D HVBK-GOY-shell-model, show deviations from the pure-fluid behavior ζ_p^c; these deviations depend on the values of ρ_n/ρ and B. Moreover, for the run G4 ($\rho_n/\rho = 0.4$, $B = 0.9838$) the ζ_p^i's (green lines in Figs. 6.2 (a) and (b)) are close to $\zeta_p^{K41} = p/3$. For the run G3 ($\rho_n/\rho = 0.25$, $B = 1.08$), the ζ_p^i's (purple lines in Figs. 6.2 (a) and (b)) lie roughly between ζ_p^{K41} and ζ_p^c; whereas, for the runs G5-G7, the behavior of ζ_p^i, relative to ζ_p^{K41} and ζ_p^c, depends on the order p.

To understand the dependence of the multiscaling exponents ζ_p^i, $i \in (n, s)$, on ρ_n/ρ (which includes the variation of B with temperature), we plot, in Fig. 6.3, ζ_p^n, for $p = 1$ to 6, versus ρ_n/ρ from our runs G1-G9. Figure 6.3 shows that, depending on

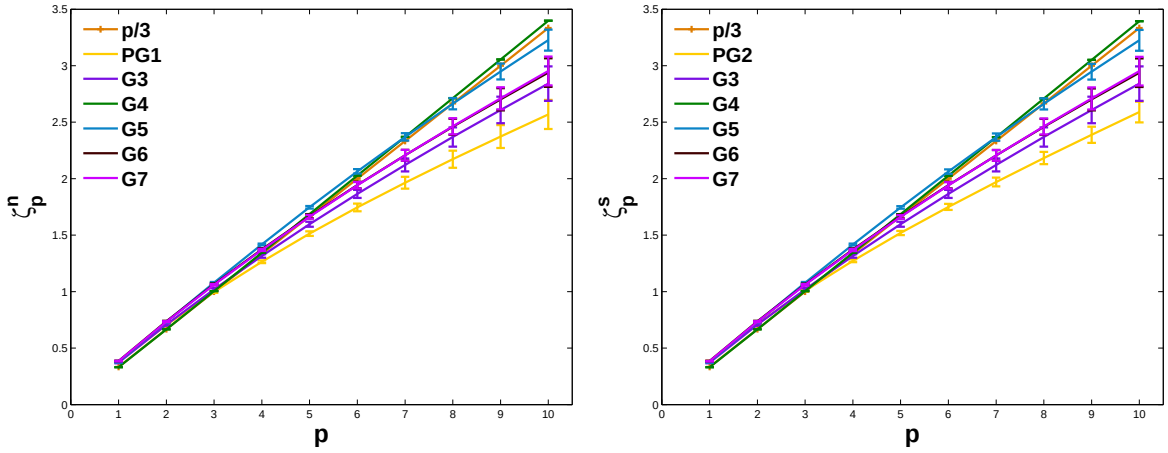

Figure 6.2: Plots versus order p of the multiscaling exponents: (a) ζ_p^n and (b) ζ_p^s, for the shell-model runs `G3` (purple curve), `G4` (green curve), `G5` (sky-blue curve), `G6` (brown curve), and `G7` (magenta curve). `PG1`, `PG2` are the pure-fluid runs (yellow curve) and $\zeta^{K41} = p/3$ is denoted by the orange line.

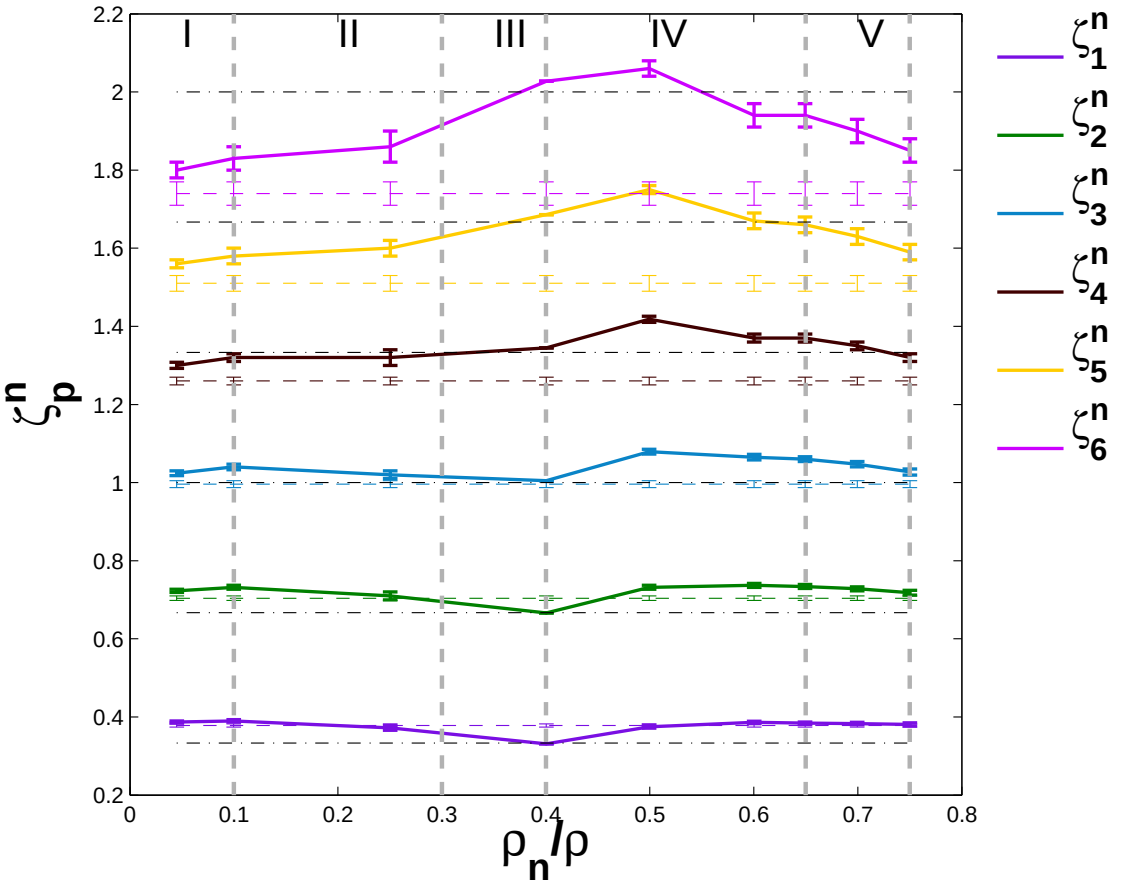

Figure 6.3: Plots of ζ_p^n, for $p = 1$ to 6, versus ρ_n/ρ, from our shell-model runs `G1`-`G9`. For the purpose of reference, we show the value of a pure-fluid exponent ζ_p^c, for order p, by a horizontal, dashed line; different colors indicate different values of the order p. The black, dot-dashed lines indicates $\zeta_p^{K41} = p/3$.

the values of ρ_n/ρ, the behavior of the exponents ζ_p^n can be classified *roughly* into five categories I-V (demarcated by grey, dashed, vertical lines on the plot), which we describe below.

1. Region I ($\rho_n/\rho \lesssim 0.1$): The values of ζ_p^n are close to the pure-fluid exponents ζ_p^c.
2. Region II ($0.1 < \rho_n/\rho < 0.3$): $\zeta_p^n > \zeta_p^c$, for $p \geq 3$ and, for $p = 1, 2$, $\zeta_p^n \simeq \zeta_p^c$.
3. Region III ($0.3 \lesssim \rho_n/\rho \lesssim 0.4$): $\zeta_p^n \simeq \zeta_p^{K41}$.
4. Region IV ($0.4 < \rho_n/\rho \lesssim 0.65$): ζ_p^n show significant deviations from both ζ_p^c and ζ_p^{K41}.
5. Region V ($\rho_n/\rho > 0.65$): ζ_p^n show a tendency to move towards ζ_n^c.

To determine the dependence of the multiscaling exponents ζ_p^i, $i \in (n, s)$, on ρ_n/ρ, while keeping the coefficient of mutual friction $B = 1.5$ fixed, we perform a set of 3D-HVBK-GOY-shell-model runs `B1-B19`, where we systematically scan across the values of ρ_n/ρ. These runs allow us to classify the behavior of ζ_p^i, $i \in (n, s)$, as a function of ρ_n/ρ, more clearly than the runs `G1-G9`. In Table 6.4 we present the values of the ζ_p^i, $i \in (n, s)$, which we extract from Σ_p^i (Eq. 6.20), for $p = 1$ to 6, $i \in (n, s)$; each row of this Table has two lines; the first and second lines contain the values of ζ_p^n and ζ_p^s, respectively. For these runs $\zeta_p^n \simeq \zeta_p^s$. In Fig. 6.4 we plot, versus ρ_n/ρ ζ_p^n, for $p = 1$ to 6, which we have obtained from the runs `B1-B19`. The plots of ζ_p^n versus ρ_n/ρ show two regions ($0.1 < \rho_n/\rho < 0.3$ and $0.4 < \rho_n/\rho < 0.65$) with clear bumps, where the values of ζ_p^n deviate significantly from both $\zeta_p^{K41} < \zeta_p^n$ and $\zeta_p^c < \zeta_p^n$. We classify *roughly* the behavior of these ζ_p^n into six categories I-VI (demarcated by grey, dashed, vertical lines on the plot), which we describe below:

1. Region I ($\rho_n/\rho \lesssim 0.1$): $\zeta_p^n \simeq \zeta_p^c$.
2. Region II ($0.1 < \rho_n/\rho < 0.3$): ζ_p^n show significant deviations from both $\zeta_p^c < \zeta_p^n$ and $\zeta_p^{K41} < \zeta_p^n$.
3. Region III ($0.3 \lesssim \rho_n/\rho \lesssim 0.4$): $\zeta_p^n \simeq \zeta_p^{K41}$.
4. Region IV ($0.4 < \rho_n/\rho < 0.65$): ζ_p^n show significant deviations from both $\zeta_p^c < \zeta_p^n$ and $\zeta_p^{K41} < \zeta_p^n$.
5. Region V ($0.65 \gtrsim \rho_n/\rho < 0.75$): ζ_p^n show a tendency to move towards ζ_n^c values.
6. Region VI ($\rho_n/\rho \gtrsim 0.75$): $\zeta_p^n \simeq \zeta_p^c$.

We also explore the dependence of the multiscaling exponents ζ_p^i, $i \in (n, s)$, on the mutual-friction coefficient B, while keeping the normal-fluid-density fraction

	ρ_n/ρ	ζ_1	ζ_2	ζ_3	ζ_4	ζ_5	ζ_6
B1	0.05	0.387 ± 0.002	0.724 ± 0.004	1.026 ± 0.006	1.303 ± 0.009	1.56 ± 0.02	1.80 ± 0.03
		0.384 ± 0.002	0.720 ± 0.004	1.023 ± 0.006	1.301 ± 0.009	1.56 ± 0.02	1.80 ± 0.03
B2	0.10	0.389 ± 0.003	0.732 ± 0.004	1.042 ± 0.006	1.328 ± 0.009	1.59 ± 0.02	1.84 ± 0.02
		0.388 ± 0.003	0.733 ± 0.004	1.045 ± 0.005	1.333 ± 0.008	1.60 ± 0.01	1.85 ± 0.02
B3	0.15	0.402 ± 0.002	0.766 ± 0.004	1.111 ± 0.006	1.44 ± 0.01	1.75 ± 0.02	2.05 ± 0.03
		0.395 ± 0.002	0.761 ± 0.004	1.107 ± 0.006	1.44 ± 0.01	1.75 ± 0.02	2.05 ± 0.03
B4	0.20	0.380 ± 0.003	0.733 ± 0.005	1.071 ± 0.006	1.399 ± 0.008	1.72 ± 0.01	2.02 ± 0.02
		0.376 ± 0.003	0.730 ± 0.005	1.069 ± 0.006	1.397 ± 0.008	1.71 ± 0.01	2.02 ± 0.02
B5	0.025	0.364 ± 0.002	0.711 ± 0.004	1.053 ± 0.005	1.392 ± 0.009	1.73 ± 0.01	2.05 ± 0.02
		0.360 ± 0.002	0.708 ± 0.004	1.051 ± 0.005	1.390 ± 0.007	1.72 ± 0.01	2.05 ± 0.02
B6	0.30	0.334 ± 0.002	0.672 ± 0.002	1.011 ± 0.002	1.351 ± 0.002	1.690 ± 0.003	2.024 ± 0.09
		0.334 ± 0.002	0.671 ± 0.002	1.010 ± 0.002	1.350 ± 0.002	1.688 ± 0.003	2.01 ± 0.009
B7	0.35	0.345 ± 0.001	0.683 ± 0.002	1.021 ± 0.002	1.359 ± 0.003	1.696 ± 0.005	2.03 ± 0.01
		0.3385 ± 0.0009	0.677 ± 0.001	1.015 ± 0.002	1.355 ± 0.003	1.693 ± 0.005	2.02 ± 0.01
B8	0.40	0.340 ± 0.002	0.679 ± 0.002	1.019 ± 0.003	1.359 ± 0.003	1.695 ± 0.006	2.03 ± 0.01
		0.339 ± 0.001	0.680 ± 0.002	1.021 ± 0.002	1.361 ± 0.002	1.699 ± 0.006	2.03 ± 0.01
B9	0.45	0.365 ± 0.002	0.712 ± 0.002	1.057 ± 0.003	1.397 ± 0.006	1.73 ± 0.01	2.05 ± 0.02
		0.353 ± 0.001	0.699 ± 0.002	1.046 ± 0.003	1.389 ± 0.005	1.72 ± 0.01	2.05 ± 0.03
B10	0.50	0.376 ± 0.002	0.727 ± 0.002	1.072 ± 0.004	1.410 ± 0.007	1.74 ± 0.01	2.06 ± 0.03
		0.365 ± 0.002	0.720 ± 0.002	1.068 ± 0.004	1.408 ± 0.007	1.74 ± 0.01	2.05 ± 0.03
B11	0.55	0.382 ± 0.002	0.734 ± 0.003	1.078 ± 0.004	1.415 ± 0.006	1.74 ± 0.01	2.05 ± 0.03
		0.370 ± 0.002	0.727 ± 0.003	1.075 ± 0.004	1.414 ± 0.007	1.74 ± 0.01	2.06 ± 0.03
B12	0.60	0.380 ± 0.003	0.735 ± 0.005	1.074 ± 0.008	1.40 ± 0.01	1.72 ± 0.02	2.03 ± 0.03
		0.379 ± 0.003	0.734 ± 0.005	1.073 ± 0.008	1.40 ± 0.01	1.72 ± 0.02	2.03 ± 0.03
B13	0.65	0.379 ± 0.003	0.724 ± 0.004	1.048 ± 0.006	1.36 ± 0.01	1.65 ± 0.02	1.93 ± 0.03
		0.378 ± 0.003	0.723 ± 0.004	1.047 ± 0.006	1.36 ± 0.01	1.65 ± 0.02	1.93 ± 0.03
B14	0.70	0.375 ± 0.004	0.714 ± 0.007	1.02 ± 0.01	1.31 ± 0.02	1.58 ± 0.03	1.82 ± 0.05
		0.375 ± 0.005	0.714 ± 0.007	1.02 ± 0.01	1.31 ± 0.02	1.58 ± 0.03	1.82 ± 0.05
B15	0.75	0.371 ± 0.004	0.706 ± 0.006	1.012 ± 0.009	1.30 ± 0.02	1.56 ± 0.03	1.80 ± 0.04
		0.371 ± 0.004	0.705 ± 0.006	1.012 ± 0.009	1.30 ± 0.02	1.56 ± 0.03	1.80 ± 0.04
B16	0.80	0.370 ± 0.004	0.697 ± 0.006	0.998 ± 0.009	1.28 ± 0.01	1.54 ± 0.02	1.80 ± 0.04
		0.369 ± 0.004	0.697 ± 0.006	0.998 ± 0.009	1.28 ± 0.01	1.54 ± 0.02	1.80 ± 0.04
B17	0.85	0.371 ± 0.003	0.698 ± 0.005	0.998 ± 0.007	1.28 ± 0.01	1.54 ± 0.02	1.79 ± 0.03
		0.371 ± 0.003	0.698 ± 0.005	0.998 ± 0.007	1.28 ± 0.01	1.54 ± 0.02	1.79 ± 0.03
B18	0.90	0.372 ± 0.004	0.699 ± 0.006	0.996 ± 0.008	1.27 ± 0.01	1.53 ± 0.02	1.77 ± 0.04
		0.372 ± 0.004	0.698 ± 0.006	0.996 ± 0.008	1.27 ± 0.01	1.53 ± 0.02	1.77 ± 0.04
B19	0.95	0.374 ± 0.004	0.700 ± 0.006	0.994 ± 0.008	1.266 ± 0.01	1.52 ± 0.02	1.75 ± 0.03
		0.374 ± 0.004	0.699 ± 0.006	0.994 ± 0.008	1.265 ± 0.01	1.52 ± 0.02	1.75 ± 0.03

Table 6.4: Multiscaling exponents ζ_p from our shell-model runs B1-B19; each row of the Table has two lines; the first and second lines contain, respectively, the values of ζ_p^n and ζ_p^s. ρ_n/ρ is the normal-fluid density fraction; we keep the mutual-friction coefficient $B = 1.5$ fixed.

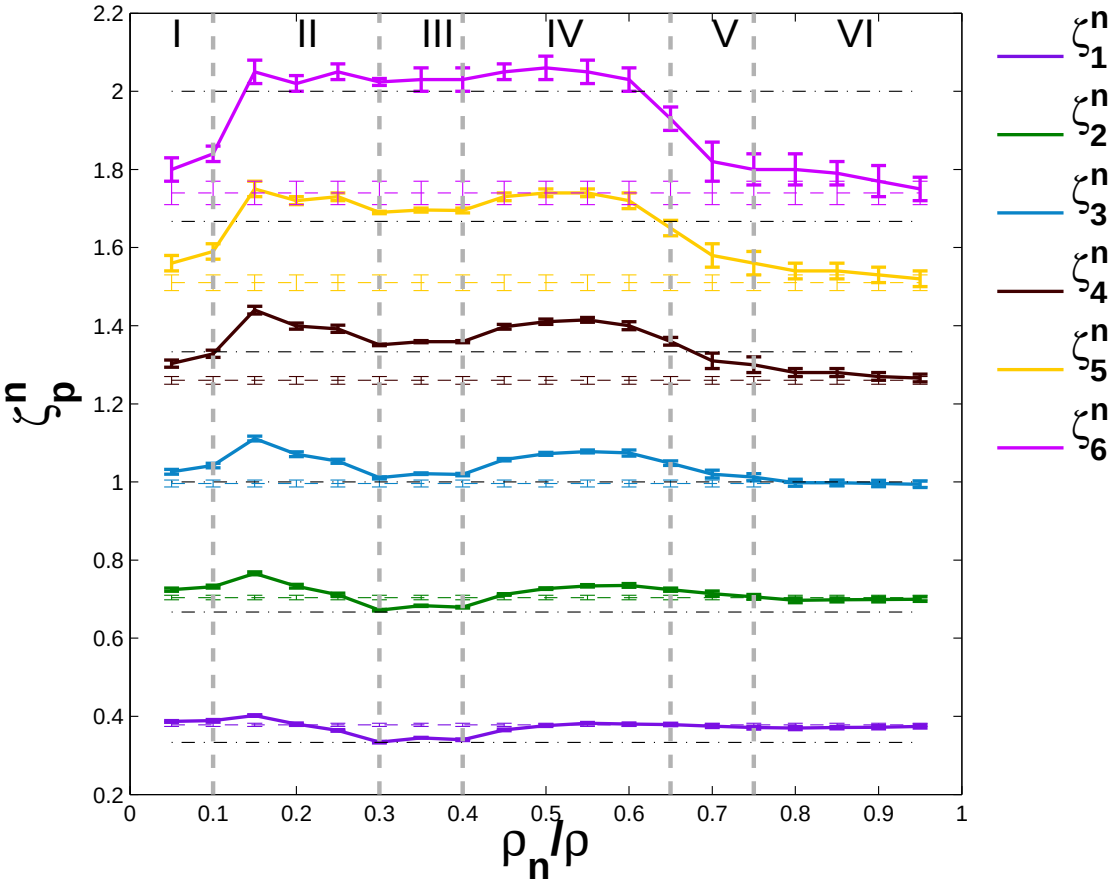

Figure 6.4: Plots of ζ_p^n, for $p = 1$ to 6, versus ρ_n/ρ, from our shell-model runs B1-B19. For the purpose of reference, we show the value of a pure-fluid exponent ζ_p^c, for order p, by a horizontal, dashed line; different colors indicate different values of the order p. The black, dot-dashed lines indicates $\zeta_p^{K41} = p/3$. In the shell-model runs B1-B19, we keep the mutual-friction coefficient $B = 1.5$ fixed.

	B	ζ_1	ζ_2	ζ_3	ζ_4	ζ_5	ζ_6
R1	0.10	0.371 ± 0.007	0.71 ± 0.01	1.03 ± 0.02	1.33 ± 0.03	1.61 ± 0.04	1.89 ± 0.06
		0.370 ± 0.007	0.71 ± 0.01	1.03 ± 0.02	1.33 ± 0.03	1.61 ± 0.04	1.89 ± 0.06
R2	0.50	0.366 ± 0.007	0.708 ± 0.01	1.04 ± 0.02	1.36 ± 0.02	1.67 ± 0.04	1.98 ± 0.05
		0.366 ± 0.007	0.708 ± 0.01	1.04 ± 0.02	1.36 ± 0.02	1.67 ± 0.04	1.98 ± 0.05
R3	0.80	0.348 ± 0.002	0.691 ± 0.002	1.034 ± 0.003	1.376 ± 0.004	1.715 ± 0.007	2.05 ± 0.01
		0.347 ± 0.002	0.691 ± 0.002	1.033 ± 0.003	1.374 ± 0.004	1.712 ± 0.007	2.04 ± 0.01
R4	1.00	0.346 ± 0.001	0.688 ± 0.002	1.031 ± 0.002	1.370 ± 0.004	1.704 ± 0.008	2.03 ± 0.02
		0.345 ± 0.001	0.688 ± 0.002	1.030 ± 0.002	1.368 ± 0.004	1.700 ± 0.008	2.02 ± 0.02
R5	1.25	0.361 ± 0.002	0.711 ± 0.002	1.057 ± 0.004	1.397 ± 0.006	1.73 ± 0.01	2.05 ± 0.02
		0.359 ± 0.002	0.710 ± 0.002	1.056 ± 0.004	1.394 ± 0.006	1.72 ± 0.01	2.04 ± 0.02
R6	1.50	0.372 ± 0.002	0.727 ± 0.003	1.072 ± 0.005	1.408 ± 0.008	1.73 ± 0.01	2.04 ± 0.03
		0.370 ± 0.002	0.725 ± 0.003	1.070 ± 0.005	1.405 ± 0.008	1.73 ± 0.01	2.04 ± 0.03
R7	1.75	0.384 ± 0.002	0.743 ± 0.004	1.086 ± 0.006	1.418 ± 0.009	1.74 ± 0.002	2.04 ± 0.03
		0.382 ± 0.002	0.742 ± 0.004	1.086 ± 0.006	1.417 ± 0.009	1.73 ± 0.002	2.04 ± 0.03
R8	2.00	0.382 ± 0.003	0.738 ± 0.004	1.078 ± 0.006	1.404 ± 0.009	1.72 ± 0.02	2.01 ± 0.03
		0.382 ± 0.003	0.738 ± 0.004	1.077 ± 0.006	1.403 ± 0.009	1.73 ± 0.02	2.01 ± 0.03
R9	4.00	0.376 ± 0.004	0.720 ± 0.007	1.04 ± 0.01	1.34 ± 0.02	1.61 ± 0.03	1.87 ± 0.05
		0.376 ± 0.004	0.720 ± 0.007	1.04 ± 0.01	1.34 ± 0.02	1.61 ± 0.03	1.87 ± 0.05
R10	6.00	0.368 ± 0.004	0.699 ± 0.006	1.008 ± 0.008	1.30 ± 0.01	1.58 ± 0.02	1.84 ± 0.04
		0.368 ± 0.004	0.699 ± 0.006	1.008 ± 0.008	1.30 ± 0.01	1.58 ± 0.02	1.84 ± 0.04
R11	8.00	0.370 ± 0.004	0.699 ± 0.006	1.000 ± 0.009	1.28 ± 0.02	1.54 ± 0.02	1.79 ± 0.04
		0.370 ± 0.004	0.699 ± 0.006	1.000 ± 0.009	1.28 ± 0.01	1.54 ± 0.02	1.79 ± 0.04
R12	10.0	0.370 ± 0.004	0.696 ± 0.006	0.993 ± 0.009	1.27 ± 0.01	1.52 ± 0.02	1.76 ± 0.04
		0.370 ± 0.004	0.696 ± 0.006	0.992 ± 0.009	1.27 ± 0.01	1.52 ± 0.02	1.76 ± 0.04

Table 6.5: Multiscaling exponents ζ_p from our shell-model runs R1-R12; each row of the Table has two lines; the first and second lines contain, respectively, the values of ζ_p^n and ζ_p^s. B is the mutual-friction coefficient; we keep the normal-fluid-density fraction $\rho_n/\rho = 0.5$ fixed.

$\rho_n/\rho = 0.5$ fixed. In the 3D-HVBK-GOY-shell-model runs R1-R12, we systematically vary the values of B; we list the values of ζ_p^i, $i \in (n, s)$ obtained from Σ_p^i (Eq. 6.20), for $p = 1$ to 6, $i \in (n, s)$, in Table 6.5; each row of this Table has two lines; the first and second lines contain, respectively, the values of ζ_p^n and ζ_p^s. In Fig. 6.5 we plot versus B ζ_p^n, for $p = 1$ to 6, which we have obtained from the runs R1-R12. We find that ζ_p^n deviate from their pure-fluid counterparts ζ_p^c significantly, in the range $1 \leq B \leq 3$, with $\zeta_p^n > \zeta_p^c$, for $p \geq 3$; in the above range, $\zeta_1^n < \zeta_1^c$, whereas ζ_2^n is marginally larger than ζ_2^c. As $B \to 0.1$ (small values) and $B \to 10$ (large values) the multiscaling exponents $\zeta_p^n \simeq \zeta_p^c$, because, in the limit $B \to 0$, the normal fluid and superfluid are uncoupled; and for very large values of B, the coupling is so strong that single-fluid behavior emerges.

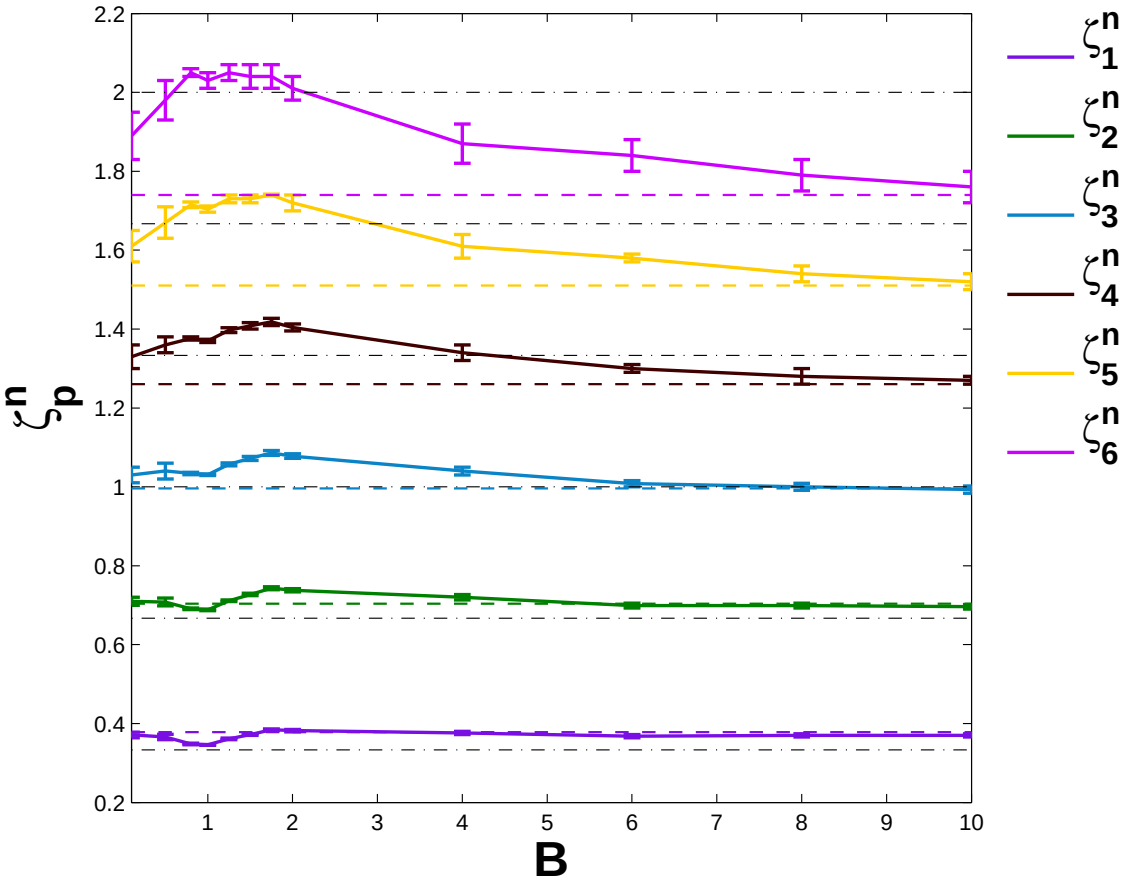

Figure 6.5: Plot of ζ_p^n, for $p = 1$ to 6, versus ρ_n/ρ, from the shell-model runs R1-R12. For the purpose of reference, we show the value of a pure-fluid exponent ζ_p^c, for order p, by a horizontal, dashed line; different colors indicate different values of order p. The black, dot-dashed lines indicates $\zeta_p^{K41} = p/3$. In the shell-model runs R1-R12, we keep the normal-fluid density fraction $\rho_n/\rho = 0.5$ fixed.

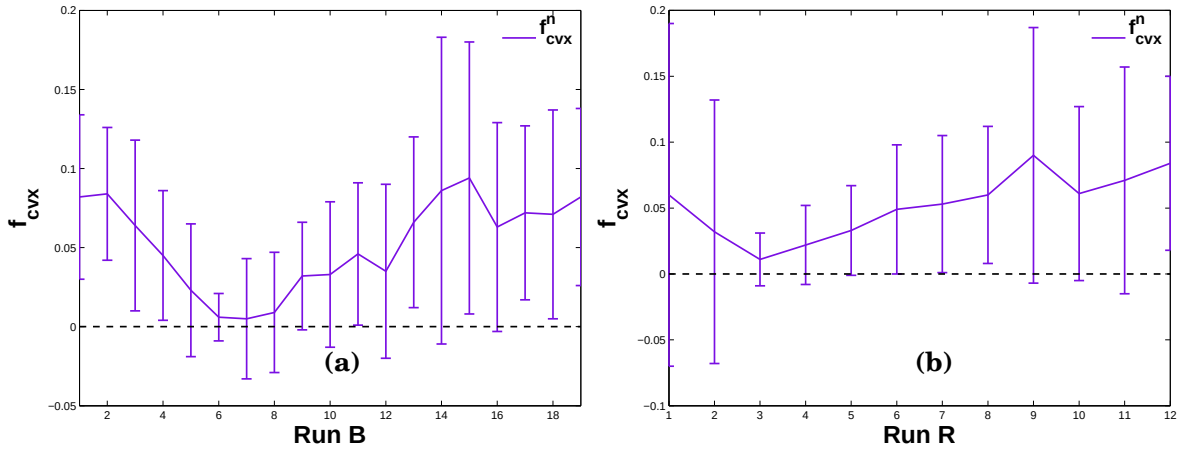

Figure 6.6: Plots of (a) $f^n_{\rm cvx}$ for the runs B1-B19 ($B = 1.5$); (b) $f^n_{\rm cvx}$ for the runs R1-R12 ($\rho_n/\rho = 0.5$); where $f^i_{\rm cvx} = (p_3 - p_1)\zeta^i_{2p_2} - (p_3 - p_2)\zeta^i_{2p_1} - (p_2 - p_1)\zeta^i_{2p_3}$, $i \in (n, s)$, and we take $p_1 = 1$, $p_2 = 2$, and $p_3 = 3$. The multiscaling exponents ζ^i_p, $i \in (n, s)$, satisfy the convexity constraint, if $f^i_{\rm cvx} > 0$, for any three positive integers $p_1 \leq p_2 \leq p_3$. The x-axis label in the above plots indicates the run index, e.g., B1.

We have checked explicitly that all the values of ζ^n_p and ζ^s_p, which we have reported above, satisfy the convexity inequality Eq. (6.21). We illustrate this in the plots of Fig. 6.6.

6.4 Conclusions

We have carried out extensive numerical simulations of the 3D-HVBK-GOY-shell-model, specifically to study the multiscaling behavior of the structure functions in superfluid turbulence. The study of the multiscaling of structure functions, is still in its infancy in superfluid turbulence; however, it has benefited from experimental investigations in liquid helium, which have shown the existence of multiscaling, in the inertial range, below the superfluid transition temperature T_λ [41–43]. The experimental observation of multiscaling of the structure functions, provides the motivation to carry out detailed theoretical and numerical investigations of the multiscaling behavior of structure functions in superfluid turbulence. The DNS studies based on the phenomenological models, such as, the Gross-Pitaevskii equation and the HVBK two-fluid equations, have not been able to cover the large range of length scales that are required to obtain reliable data for high-order structure functions. The shell models based on the HVBK two-fluid equations have already been used to study the statistical properties of 3D superfluid turbulence in both ^{4}He [4,6] and ^{3}He-B [4,5]; these studies have elucidated the nature of energy spectra and fluxes, in the case of both forced and decaying superfluid turbulence. The only detailed investigation of the multiscaling behavior of structure functions, is

an HVBK-shell-model study [6]; this study has shown that, for $\rho_n/\rho \leq 0.1$ and $\rho_n/\rho \leq 0.9$, the multiscaling exponents are close to those of a pure-fluid, whereas, in the range $0.25 \leq \rho_n/\rho \leq 0.5$, the high-order mutliscaling exponents deviate significantly from, and are smaller than, their pure-fluid counterparts.

Our extensive study of the 3D HVBK-GOY-shell-model shows that the multiscaling behavior of the structure functions in superfluid turbulence is more complex than that reported in Ref. [6]. However, our results agree with those of Ref. [6] in that, for $\rho_n/\rho \lesssim 0.1$ and $\rho_n/\rho \gtrsim 0.75$, the multiscaling exponents are close to the pure-fluid values. Moreover, we find that there are two regions, with $0.1 < \rho_n/\rho < 0.3$ and $0.4 < \rho_n/\rho < 0.65$, where the multiscaling exponents are larger than the pure-fluid and K41 values, i.e., $\zeta_p^i > \zeta_p^c$ and $\zeta_p^i > \zeta_p^{K41}$, $i \in (n, s)$; also, in the range $0.3 \lesssim \rho_n/\rho \lesssim 0.4$, the multiscaling exponents are close to the K41 prediction $\zeta_p^i \simeq \zeta_p^{K41}$. We have also investigated the dependence of the multiscaling exponents on the mutual friction coefficient B, while keeping $\rho_n/\rho = 0.5$ fixed; here, our results, show that, for small (weak-coupling limit) and large (strong-coupling limit) values of B, the multiscaling exponents tend to their pure-fluid values, whereas, in the range $1 \lesssim B \lesssim 3$, there are deviations from the pure-fluid behavior $\zeta_p^i > \zeta_p^c$, for $p \geq 3$, $i \in (n, s)$. We hope our extensive study of the multiscaling of structure functions in the 3D-HVBK-GOY shell model will stimulate detailed experimental and DNS studies of such multiscaling.

Bibliography

[1] U. Frisch. *Turbulence*, volume 1. Cambridge University Press, Cambridge, UK, 1996.

[2] T. Ishihara, T. Gotoh, and Y. Kaneda. Study of high-Reynolds number isotropic turbulence by direct numerical simulation. *Annu. Rev. Fluid Mech.*, 41:165–180, 2009.

[3] A. Arnèodo, R. Benzi, J. Berg, L. Biferale, E. Bodenschatz, A. Busse, E. Calzavarini, B. Castaing, M. Cencini, L. Chevillard, R. T. Fisher, R. Grauer, H. Homann, D. Lamb, A. S. Lanotte, E. Lévèque, B. Lüthi, J. Mann, N. Mordant, W.-C. Müller, S. Ott, N. T. Ouellette, J.-F. Pinton, S. B. Pope, S. G. Roux, F. Toschi, H. Xu, and P. K. Yeung. Universal intermittent properties of particle trajectories in highly turbulent flows. *Phys. Rev. Lett.*, 100:254504, Jun 2008.

[4] D. H. Wacks and C. F. Barenghi. Shell model of superfluid turbulence. *Phys. Rev. B*, 84(18):184505, 2011.

[5] L. Boué, V. L'vov, A. Pomyalov, and I. Procaccia. Energy spectra of superfluid turbulence in ^{3}He. *Phys. Rev. B*, 85:104502, Mar 2012.

[6] L. Boué, V. L'vov, A. Pomyalov, and I. Procaccia. Enhancement of intermittency in superfluid turbulence. *Phys. Rev. Lett.*, 110:014502, Jan 2013.

[7] A. M. Obukhov. *Atmos. Oceanic Phys.*, 10:127, 1974.

[8] V. N. Desnyansky and E. A. Novikov. *Prikl. Mat. Mekh.*, 38:507, 1974.

[9] E. B. Gledzer. System of hydrodynamic type admitting two quadratic integrals of motion. *Sov. Phys. Dokl. SSSR*, 18:216–7, 1973.

[10] K. Ohkitani and M. Yamada. Temporal intermittency in the energy cascade process and local Lyapunov analysis in fully developed model of turbulence. *Prog. Theor. Phys.*, 81:32941, 1982.

[11] M. H. Jensen, G. Paladin, and A. Vulpiani. Intermittency in a cascade model for three-dimensional turbulence. *Phys. Rev. A*, 43:798–805, Jan 1991.

[12] D. Pisarenko, L. Biferale, D. Courvoisier, U. Frisch, and M. Vergassola. Further results on multifractality in shell models. *Phys. Fluids A*, 5(10):2533–2538, 1993.

[13] S. Dhar, A. Sain, A. Pande, and R. Pandit. Recent advances in the theory of homogeneous isotropic turbulence. *Pramana J. Phys.: Special Issue on Nonlinearity and Chaos in the Physical Sciences*, 48:325, 1997.

[14] Sujan K. Dhar, Anirban Sain, and Rahul Pandit. Inertial- and dissipation-range asymptotics in fluid turbulence. *Phys. Rev. Lett.*, 78:2964–2967, Apr 1997.

[15] L. Biferale. Shell models of energy cascade in turbulence. *Annu. Rev. Fluid Mech.*, 35(1):441–468, 2003.

[16] T. Bohr, M. H. Jensen, G. Paladin, and A. Vulpiani. *Dynamical systems approach to turbulence*. Cambridge Nonlinear Science Series. Cambridge University Press, UK, 2005.

[17] P. D. Ditlevsen. *Turbulence and shell models*. Cambridge University Press, UK, 2010.

[18] V. S. L'vov, E. Podivilov, A. Pomyalov, I. Procaccia, and D. Vandembroucq. Improved shell model of turbulence. *Phys. Rev. E*, 58:1811–1822, Aug 1998.

[19] A. Basu, A. Sain, S. K. Dhar, and R. Pandit. Multiscaling in Models of Magnetohydrodynamic Turbulence. *Phys. Rev. Lett.*, 81:2687–2690, Sep 1998.

[20] C. Kalelkar and R. Pandit. Decay of magnetohydrodynamic turbulence from power-law initial conditions. *Phys. Rev. E*, 69:046304, Apr 2004.

[21] G. Sahoo, D. Mitra, and R. Pandit. Dynamo onset as a first-order transition: Lessons from a shell model for magnetohydrodynamics. *Phys. Rev. E*, 81:036317, Mar 2010.

[22] P. Frick and D. Sokoloff. Cascade and dynamo action in a shell model of magnetohydrodynamic turbulence. *Phys. Rev. E*, 57:4155–4164, Apr 1998.

[23] A. Brandenburg, K. Enqvist, and P. Olesen. Large-scale magnetic fields from hydromagnetic turbulence in the very early universe. *Phys. Rev. D*, 54:1291–1300, Jul 1996.

[24] P. Giuliani and V. Carbone. A note on shell models for MHD turbulence. *Europhys. Lett.*, 43(5):527, 1998.

[25] D. Hori, M. Furukawa, S. Ohsaki, and Z. Yoshida. A shell model for the hall MHD system. *J. Plasma Fusion Res.*, 81(3):141–142, 2005.

[26] D. Hori and H. Miura. Spectrum properties of hall MHD turbulence. *J. Plasma Fusion Res.*, 3:S1053–S1053, 2008.

[27] Sébastien Galtier. von kármán-howarth equations for Hall magnetohydrodynamic flows. *Phys. Rev. E*, 77:015302, Jan 2008.

[28] D. Banerjee, S. S. Ray, G. Sahoo, and R. Pandit. Multiscaling in Hall-Magnetohydrodynamic Turbulence: Insights from a Shell Model. *Phys. Rev. Lett.*, 111:174501, Oct 2013.

[29] C. Kalelkar, R. Govindarajan, and R. Pandit. Drag reduction by polymer additives in decaying turbulence. *Phys. Rev. E*, 72:017301, Jul 2005.

[30] E. Aurell, G. Boffetta, A. Crisanti, P. Frick, G. Paladin, and A. Vulpiani. Statistical mechanics of shell models for two-dimensional turbulence. *Phys. Rev. E*, 50:4705–4715, Dec 1994.

[31] P. Giuliani, M. H. Jensen, and V. Yakhot. Critical "dimension" in shell model turbulence. *Phys. Rev. E*, 65:036305, Feb 2002.

[32] S. S. Ray and A. Basu. Universality of scaling and multiscaling in turbulent symmetric binary fluids. *Phys. Rev. E*, 84:036316, Sep 2011.

[33] Y. Hattori, R. Rubinstein, and A. Ishizawa. Shell model for rotating turbulence. *Phys. Rev. E*, 70:046311, Oct 2004.

[34] D. Mitra and R. Pandit. Varieties of dynamic multiscaling in fluid turbulence. *Phys. Rev. Lett.*, 93:024501, Jul 2004.

[35] D. Mitra, S. S. Ray, and R. Pandit. Dynamic multiscaling in turbulence. *Eur. Phys. J. B*, 64:463–469, 2008.

[36] S. S. Ray and R. Pandit. The universality of dynamic multiscaling in homogeneous, isotropic Navier–Stokes and passive-scalar turbulence. *New J. Phys.*, 10:033003, 2008.

[37] R. J. Donnelly. *Quantized vortices in helium II*, volume 2. Cambridge University Press, 1991.

[38] C. J. Gorter and J. H. Mellink. On the irreversible processes in liquid helium II. *Physica*, 15(3):285–304, 1949.

[39] S. M. Cox and P. C. Matthews. Exponential time differencing for stiff systems. *J. Comput. Phys.*, 176(2):430–455, 2002.

[40] R. J. Donnelly and C. F. Barenghi. The observed properties of liquid helium at the saturated vapor pressure. *J. Phys. Chem. Ref. Data*, 27(6):1217–1274, 1998.

[41] J. Maurer and P. Tabeling. Local investigation of superfluid turbulence. *Europhys. Lett.*, 43(1):29, 1998.

[42] J. Salort, B. Chabaud, E. Lévêque, and P.-E. Roche. Investigation of intermittency in superfluid turbulence. In *J. Phys. Conf. Ser.*, volume 318, page 042014. IOP Publishing, 2011.

[43] J. Salort, B. Chabaud, E. Lévêque, and P.-E. Roche. Energy cascade and the four-fifths law in superfluid turbulence. *Europhys. Lett.*, 97(3):34006, 2012.